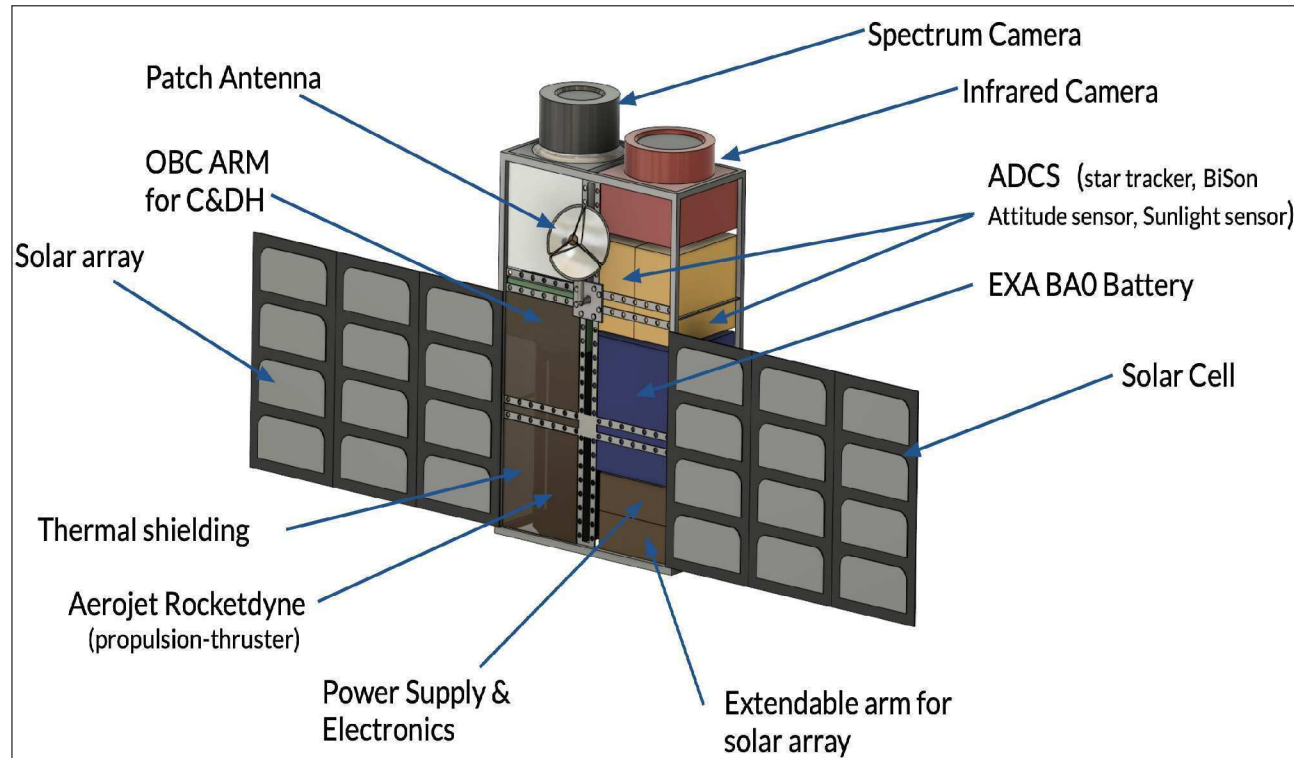


# PROJECT HURRISAT

---



ILLINOIS INSTITUTE OF TECHNOLOGY  
ARMOUR COLLEGE OF ENGINEERING  
SPACECRAFT DESIGN PROPOSAL  
THE NASA CSLI INITIATIVE

*Project Hurrusat*  
March 12<sup>th</sup>, 2022

## PROJECT HURRISAT

---

### Team Structure

<sup>1</sup>Eyob Ghebreiesus, <sup>2</sup>Jake McMahon, <sup>3</sup>Kiril Bachiyski, <sup>4</sup>Liam Palmatier, <sup>5</sup>Tewodros Assefa

<sup>1</sup> M.Sc. Aerospace Engineering. Project Manager, Systems engineer for Mission analysis and operations

<sup>2</sup> B.Sc. Aerospace Engineering. Project Requirements, Constraints, and Risk Assessments

<sup>3</sup> B.Sc. Aerospace Engineering. Payload delivery design and Communication Architecture

<sup>4</sup> M.Sc. Aerospace Engineering. Power design, Thermal design and Shielding

<sup>5</sup> M.Sc. Aerospace. Structures, Propulsion and Thrusters design

Homepage: *Project HurriSat*

Contact: ehgberejesus@hawk.iit.edu

Published on *March 12<sup>th</sup>, 2022*

Copyright © 2022

All rights reserved. This Lab report or any portion thereof may not be reproduced or used in any manner whatsoever without the express written permission of the publisher except for the use of referencing for educational purposes.

The above copyright notice and this permission notice shall be included in all copies or substantial portions of the document.

Produced via LaTeX, Inc U.S.A.

MIT License for the GitHub Project, 2022

*github.com/eyobghiday/project-hurrisat*

Department of Mechanical, Materials and Aerospace Engineering  
ILLINOIS INSTITUTE OF TECHNOLOGY

# Contents

<b>1</b>	<b>Introduction</b>	<b>1</b>
1.1	Mission Statement . . . . .	1
1.2	Mission Relevance to NASA . . . . .	1
1.3	Background in Hurricanes . . . . .	1
1.4	Stakeholders and Customers . . . . .	2
<b>2</b>	<b>Mission Exploration</b>	<b>2</b>
2.1	Mission Objectives . . . . .	2
2.2	Requirements . . . . .	3
2.3	Analysis and Trade Studies . . . . .	4
2.4	Risk Assessment . . . . .	6
<b>3</b>	<b>Mission Design Architecture</b>	<b>7</b>
3.1	Mission Operation . . . . .	7
3.2	Mission Architecture . . . . .	8
3.3	Mission Life . . . . .	9
3.4	Launch Vehicle interface . . . . .	10
3.5	Orbital parameters . . . . .	10
3.6	Payload . . . . .	12
<b>4</b>	<b>Cubesat Budget</b>	<b>13</b>
4.1	Mass Budget . . . . .	13
4.2	Power Budget . . . . .	14
4.3	$\Delta V_{design}$ Budget . . . . .	14
4.4	Cost Budget . . . . .	15
4.5	Cubesat Sizing . . . . .	16
4.6	Cubesat Configuration . . . . .	16
<b>5</b>	<b>Subsystem Design</b>	<b>18</b>
5.1	Communications . . . . .	18
5.2	Command and Data Handling . . . . .	19
5.3	Electrical . . . . .	19
5.4	ADCS . . . . .	20
5.5	Control System . . . . .	20
5.6	Thermal . . . . .	20
5.7	Propulsion . . . . .	21
5.8	Structure . . . . .	22

<b>6</b>	<b>Mission Feasibility</b>	<b>23</b>
6.1	Feasibility and Success Criteria . . . . .	23
6.2	Risk Control . . . . .	24
6.3	Alternatives . . . . .	25
6.4	Technology Gaps and Trades . . . . .	26
<b>7</b>	<b>Conclusion</b>	<b>26</b>
<b>8</b>	<b>Appendix</b>	<b>27</b>
8.1	ADCS Components . . . . .	27
8.2	Electrical Components . . . . .	28
8.3	CAD Drawings . . . . .	28
8.4	Fact Sheet . . . . .	30
8.5	Codes and Scripts . . . . .	31
8.6	Keywords . . . . .	34
8.7	List of Tables . . . . .	34
8.8	List of Figures . . . . .	35
	<b>References</b>	<b>36</b>

# 1 Introduction

## 1.1 Mission Statement

The mission of this project is to propose a Low Earth Orbit, 6U sized Cubesat to monitor and track down hurricanes across the South-Atlantic U.S. Region. This Cubesat should be able to measure small to big scale hurricanes across the required region with greater accuracy. It should also be able to record the size of a hurricane, speed, impact area, changes in temperature, pressure, and other details successfully. By doing so, it has to communicate and transmit data back and forth between local stations effectively. Furthermore, it will ensure the collected data is processed and used as per the contract agreement with the NASA and its interested parties effectively.

## 1.2 Mission Relevance to NASA

HurriSat's mission is in accordance with the first objective of NASA's Strategic plan [8] listed in sections 1.1, 1.2, and 3. Its main goal is to study the causes effects of severe space weather events, and prevent potential damage. Additional criteria in addressing the National Challenges and Catalyze economic growth for space sustainability. Climate change greatly increases the severity and frequency of hurricanes and other extreme weather. This has led to a significant need for fast and accurate weather data in order to prevent and reduce catastrophic damages. This feasibility report ensures HurriSat meets the requirements and objective outlined by NASA in the CSLI [10] initiative.

This document provides a refined look at the mission analysis and concept of operations for HurriSat. The mission goals and objectives are laid out, and the analysis plan is discussed in detail. The conceptual design and analysis takes a scientific approach towards the concept of operations. Here the criteria from the NASA CLSI missions are analyzed and turned into either requirements or constraints. Alternate plans for the mission are also discussed in later section. Furthermore, a brief evaluation is conducted for each subsystem and its purpose in the mission according to the project plan.

## 1.3 Background in Hurricanes

Hurricanes are among the most destructive weather phenomena that are caused by strong winds and surge effects. They can be fatal, and usually cause destruction of infrastructures. In 2012, Hurricane Sandy led to about \$65 billion damage in the northeastern coastal region of the USA and in the Ontario Province of Canada [3]. The severity of the consequences,

Category	Speed (mph)	Severity
1	74 – 95	Minimal damage
2	96 – 110	Considerable damage
3	111 – 129	Extreme damage
4	130 – 156	Devastating
5	> 156	Catastrophic

**Table 1.1 – Hurricane Severity**

associates with hurricane activity, has motivated several investigations, attempting to forecast hurricane activity in both near and distant future. Hurricanes are primarily classified based on their speed as seen in Table 1.1, with Category 5 being the most severe. This serves as one of the many reasons that led us bring forward project HurriSat to NASA and its affiliates. Therefore, HurriSat's sole mission will be dedicated to tracking, monitoring and possibly avoiding fatal devastation caused by hurricanes. Additionally, HurriSat will be equipped with high-tech cameras and faster processor to provide accurate weather data with little to zero maintenance cost.

## 1.4 Stakeholders and Customers

The stake holders partly consist of with an interest with the enterprise of NASA and its affiliates. They are divided into two main categories, Primary and Secondary stakeholders as listed in Table ???. Those stakeholders may include those listed but not limited to:

**Table 1.2 – Stakeholders**

Primary Stakeholders	Secondary Stakeholders
NASA	Department of Education
National Weather Service	National Environmental Satellit
Federal Emergency Management Agency	NOAA
Department of Defense	Others: Public Safety, Health and Red cross

## 2 Mission Exploration

The mission of this project is to propose a Low Earth Orbit 6U sized Cubesat in order to track down the hurricanes across the South-Atlantic U.S. Region. The primary target coverage area is about 110,000 square miles across the South East-cost. This Cubesat should be able to track small to big size hurricanes across the given region. This is mainly achieved using high-tech dual cameras. It will try to collect the speed, impact area, changes in temperature, pressure, and air composition of earth's atmosphere for a given radius in miles. By doing so, it has to communicate and transmit data back and forth between local stations effectively. Furthermore, we must ensure the recorded data is shared with the outlined stakeholders and interested parties effectively.

### 2.1 Mission Objectives

Our primary and secondary mission objectives are as follows.

#### 2.1.1 Primary Objectives

- Data recording (Wind speed, hurricane trajectory, impact radius) and analysis.
- Transmission of data to and from ground station up to 10 external entities.
- Cubesat autonomous tasking if necessary, and warning category level for immediate action.

- Navigation and monitoring hurricane impacted areas. Assessing damage on infrastructures to a certain degree.
- Updating locations using on board GPS or grounds station.

### 2.1.2 Secondary Objectives

- Recording relevant data (Temperature, Pressure, Humidity) for scientific study .
- Maintaining communication with weather stations every 15 – 20m minutes.
- Guidance and Navigation of hurricane free zones.
- Remote sensing capabilities and effective communication with nearby satellites to avoid debris and collision course.

## 2.2 Requirements

### 2.2.1 Functional Requirements

- Cubesat shall coverage a minimum of 2400x1300 square km (110,00 square miles) ground area for hurricane monitoring.
- Cubesat shall provide 2 visible spectrum images with up to 10m/pixel or lower for narrow field, and upto 100m-200m/pixel or max for a wide range of hurricane resolution.
- Spacecraft shall provide temperature, relative speed, atmospheric readings of hurricane (use infrared cam).
- Must able to transmit to ground station without having to rotate the spacecraft.
- Responsiveness: Transmitting 3 24-bit color depth images to the ground station over a single pass spanning 15 minutes.

### 2.2.2 Operational Requirements

- Duration: Will have a mission life of at least 15-20 years
- Availability: 12-hour maximum outage provided space weather conditions.
- Reliable: Provided no external and uncontrolled space phenomenon.
- Communication: Updates every 15-20 min per by pass.
- Data content: Images, location, relative speed, hurricane radius, impact area, atmospheric data, weather prediction and forecast.

### 2.2.3 Subsystem Requirements and Constraints

After going over the mission requirements, the subsystem components are inspected and checked to see if they can meet the mission purpose. Figure 2.1 goes over all our subsystem designs and lists whether that specific component's requirement and constraint. This in return shapes our design and component selection process.

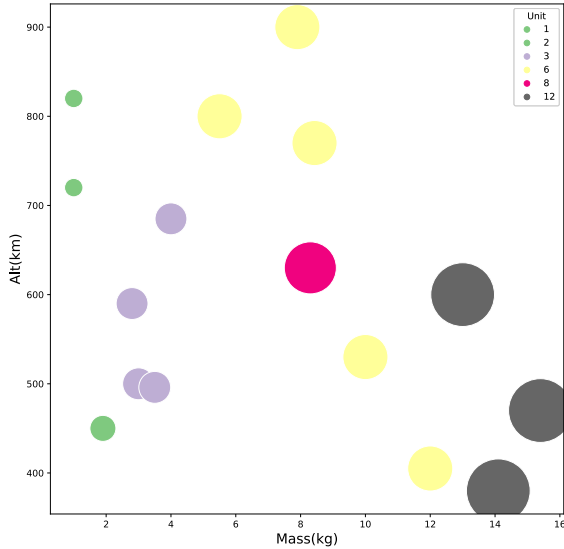
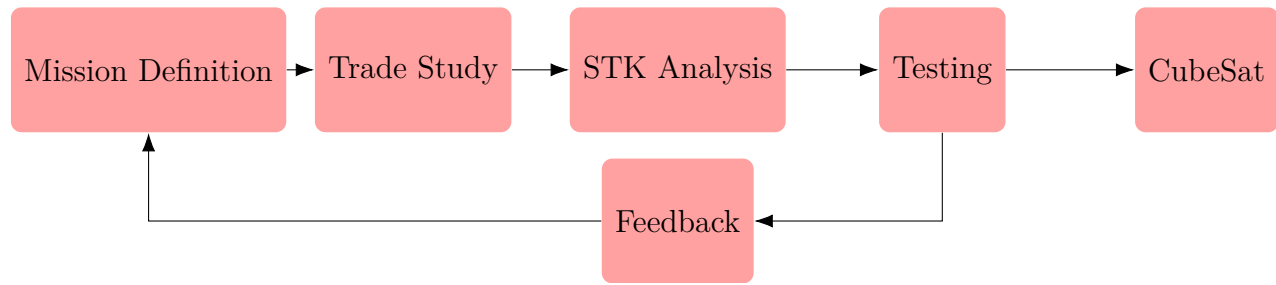
Subsystem	Subsystem Inputs (Requirements)	Components selected (Output)	( Component requirement and constraint)
<b>Imaging</b>	Coverage: 2400x1300km Resolution: 10m/pixel Provides temperature readings for air pressure and cloud formations.	Spectral Camera (for wide and narrow image)	Average size of 4MB per picture. Mass 35g, Operational Ttemp: -30C to +85C.
		Infrared camera ( Infrared will be used for temperature readings for air pressure and cloud formations.)	Infrared image with average size of 2.5MB per picture, OBC will require considerable storage and power. Mass is 45g. Operational Temp: -40C to +70C, Power: 1.6-4.2W
<b>ADCS</b>	Needs to maintain and regulate spacecraft altitude, direction, and position relative to the purpose CubeSat needs to track hurricanes/extreme weather and provide accurate graphs	BiSon64-ET	operation Temp: -125C to 125C Mass: <24g Radiation: 8.1^14
		Arcsec Sagitta Star tracker	Mass: 65g, power < 1.4W, availability > 99% of the night sky. On-board calibration algorithm
		nanoSSOC-D60 digital sun sensor	Mass: 275g, Operational Temp: -30C to +85C.
<b>C&amp;DH</b>	For uploading, downloading and exchanging bits of information to and from ground station. Possible comms between cubesats is needed.	Patch antenna option 2 (S-Band)	Minimum line loss, about 1.5W power.
		S-Band High Data Rate Transmitter	Signal bandwidth of 1Mbps
		Onboard computer (ARM Cortex)	Central Computer main frame, must have RAM or SD slot for files storage. Mass: 130g, 8 Mbit, 2MB RAM and 32 GB.
<b>Power</b>	Support for life time about 15 years.	DHV-CS-10 Solar Panel	Energy source Mass: 7 grams, Operational Temp: -65C to +125C
		EXA BAOx High Energy Density Battery Array	4.5 per battery of total of about 44 W/hr
<b>Propulsion</b>	Is needed to propel to operational orbit, and attitude control. Delta v around 400m/s.	Modular Propulsion System 130-2U	3 Dimensional propulsion, for estimated mass 1.4-2.4
<b>Structure</b>	Able to fit all the subsystem components	Custom Structure	Thermal resistant, well equipped, and balanced axis of symmetry
<b>Ground Station</b>	Average access time with the ground station is 15 minutes.	ISIS Full Ground Station Kit for S-band	Minimum line loss, about 1.5W power.

**Figure 2.1 – Subsystem Requirements and Constraints**

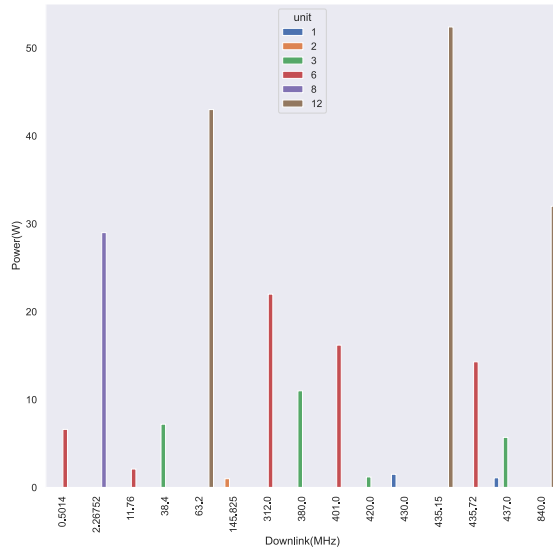
## 2.3 Analysis and Trade Studies

To ensure our project results in designing an effective and efficient cubesat, we have made a project plan to provide the best output parameters in Figure 2.2. After initial mission definition the project is closely followed by trade studies. Numerous data for previous successful missions were collected firsthand. The Japanese XI [5] cubesat, the Freja [12] cubesat, and the Firesat from the Space mission and design [7] reference were used as a basis. Those projects solely match our functionality requirements for a 1U-12U cubesat. Figure 2.3(a) is the volume (density) of cubesats at various altitude. It shows 6U-sats are commonly used for a wide range of altitude. If HurriSat is to be equipped with a faster imaging cameras, and max transfer (bandwidth) frequency as shown in Figure 2.3(b), it will require high throughput (red-accent) power. The tradeoff is an increase in mass size as shown in Figure 2.3(c). The inclination distribution of cubesats is graphed in Figure 2.3(d) in order to provide some insight on satellite footprint with mass and altitude. Once we select the performance metrics, we use STK [1] software analysis to test the values in the simulation. After reading the feedback from the simulation; if the findings are feasible, we proceed to component design phase. If not, we go back to refine our mission definition and operational requirements. This is an agile project managing system where we select the performance parameters and perceive the coverage, operation orbit and bypass simultaneously to decide the best fit. This allows us to be flexible with the little time provided.

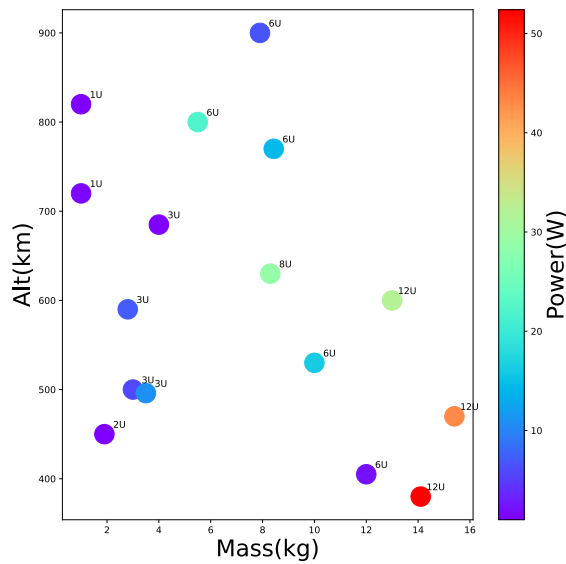
**Figure 2.2 – Mission Analysis**



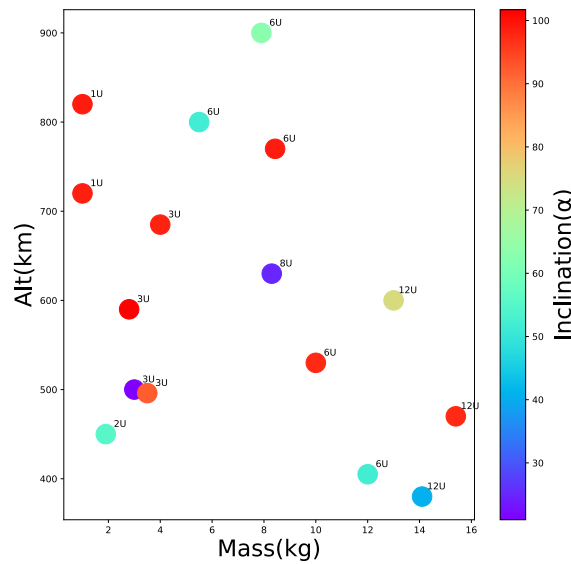
(a) Cubesat size scatter vs altitude.



(b) Downlink Freq over power per unit size.



(c) Power Loading



(d) Inclination

**Figure 2.3 – Trade Studies**

## 2.4 Risk Assessment

Risk assessment assures the stakeholders whether our cubesat is on track to be hazard free, secure, safe, and scientifically feasible. It is impossible to avoid risks completely. Thus, the team has provided a risk assessment definition in Table 2.1. Those definitions are basic guideline to help assessing the risks and provide some mitigation mechanisms. They are divided in to two sections: probability and severity. Probability is the likelihood of risk to occur, while severity is the effect of the risk. To determine the risk assessments a color grading scale is provided in Table 2.2. Bright red is a high probability and extremely severe. This risk will definitely hinder all types of operation and may even lead to complete failure of the mission. Green on the other hand is quite the opposite.

**Table 2.1** – Risk Definitions

Risk Probability	Description
Frequent	Consistent threat to mission. Requires deliberate and active planning.
Occasional	May occur a couple-three times.
Improbable	Highly unlikely to occur.
Risk Severity	Description
Catastrophic	Would cause complete mission failure. It's a no-go situation.
Major	Would cause significant complication to mission.
Minor	Would causes a minor hindrance to mission.
Negligible	Minimal effect on mission.

**Table 2.2** – Risk Color-grading

Risk Probability	Risk Severity			
		Catastrophic (4)	Major (3)	Minor (2)
Frequent (A)	A4	A3	A2	A1
Occasional (B)	B4	B3	B2	B1
Improbable (C)	C4	C3	C2	C1

Updated risk assessment are shown below. Risk assessment assures the stakeholders whether our cubesat is on track to be hazard free, secure, safe, and scientifically feasible. It is impossible to avoid risks completely. Table 2.3 is where we listed out every possible risk. While most of the risks are accounted for, there might still be an unforeseeable event due to sudden radiation exposure or unaccounted space debris. HurriSat will still be utilizing its propulsion driven ADCS guided by the active software tracking to avoid debris. It will also feature a double wall bumper in the structures to sustain slight damage. Similarly, some parts of the IC transistors will have to be embedded with carbon Teflon shielding to resist radiation and thermal exposure.

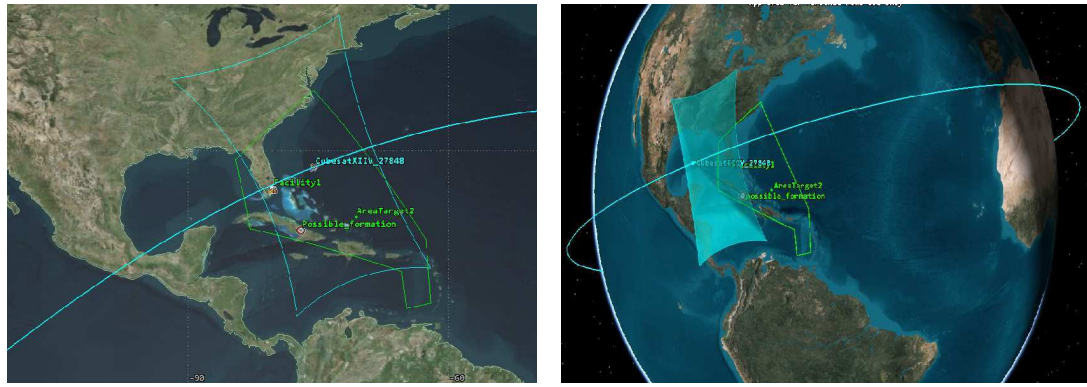
**Table 2.3 – Risk Assessment**

Hazard	Assessment	Risk	Mitigation
<b>Pre Launch</b>			
Operational Cost	B3	Delayed project timeline	Clear focus on fund acquisition
Environmental (Dust, Humidity, Weather)	A1	Hinder launch-day, minor damage to Cubesat	Controlled and designated-construction environment
Transportation	A1	Damage to CubSat or team	Route Planning, safe access to traffic
Team injury	B1	Damage to team member and legal liability	Safe workspace guidelines
Technology Limitation	B1	Longer time and overhead	Mindful design
<b>Post Launch</b>			
Space Debris and Micrometeoroids	B4	Fatal destruction or damage of the Cubesat	Double Wall Bumper, Active space debris tracking software
Radiation Exposure	A3	Electronic systems, causing circuit damage or system shut downs	Transistors, IC's and circuits will be embedded with carbon nanotubes.
Thermal Damage	A2	Electrical, mechanical component damage	Selecting the best Thermal resistant shield
Solar Flares	C3	Damage or destruction of CubSat	Active tracking of solar threats. Selective Solar flare resistant design, Course correction mechanisms.
Foreign Satellites	C4	Longer time and overhead	Active tracking of other Satellites
<b>Launch</b>			
Initial Acceleration	B2	Damage due to increasing drag and friction	Minimized induced drag, using thrusters and controllers
Mechanical Vibration	B3	Structural and payload damage	Incorporate shock observant if possible. Distribute static loads.
Acoustic Energy	B2	Structural damage	Use sound suppression system and pressurized leveling.

## 3 Mission Design Architecture

### 3.1 Mission Operation

HurriSat is designated to cover ground area of 100,000 square miles as in Figure 3.1a. The target area is highlighted in neon blue ticker from STK [1] simulation. Now if there is any possible high or low wind formation present in the targeted area (see possibleFormation point in the map), it is first picked up by the spectral camera we have, and is logged by the on board computer processor. Once the image is processed and if indeed there's a high wind formation at the target area; the ground station is signaled, and heat signatures picked up by the infrared camera is transmitted. The cubesat then adjusts it self via its ADCS navigation system. This is where the narrow camera gets triggered to actively follow the hurricane. It's purpose is to narrowly focus on target area 2 (see highlighted in green) and taking detailed images of 10m/pixel or less for possible hurricane size, relative speed, and impact area. A typical hurricane will travel across the ocean at a speed of about 250 miles (400 kilometers) per day, or about 10 to 15 miles (16 to 24 kilometers) per hour [15]. Thus, for an area of that size HurriSat is able to pick it up all in one bypass without having to use any thrust. Should the hurricane linger or move faster than expected (which is highly unlikely), HurriSat can get an update after making 15-20 min orbital journey seen in Figure 3.1b. This map shows the actual operation orbit for HurriSat using STK. It's inclined at 35 degree, at 800km to get a more closer and detailed view of hurricane sizes. This also helps reduce any signal loss from the ISIS antenna, whilst updating to ground station every now and then.



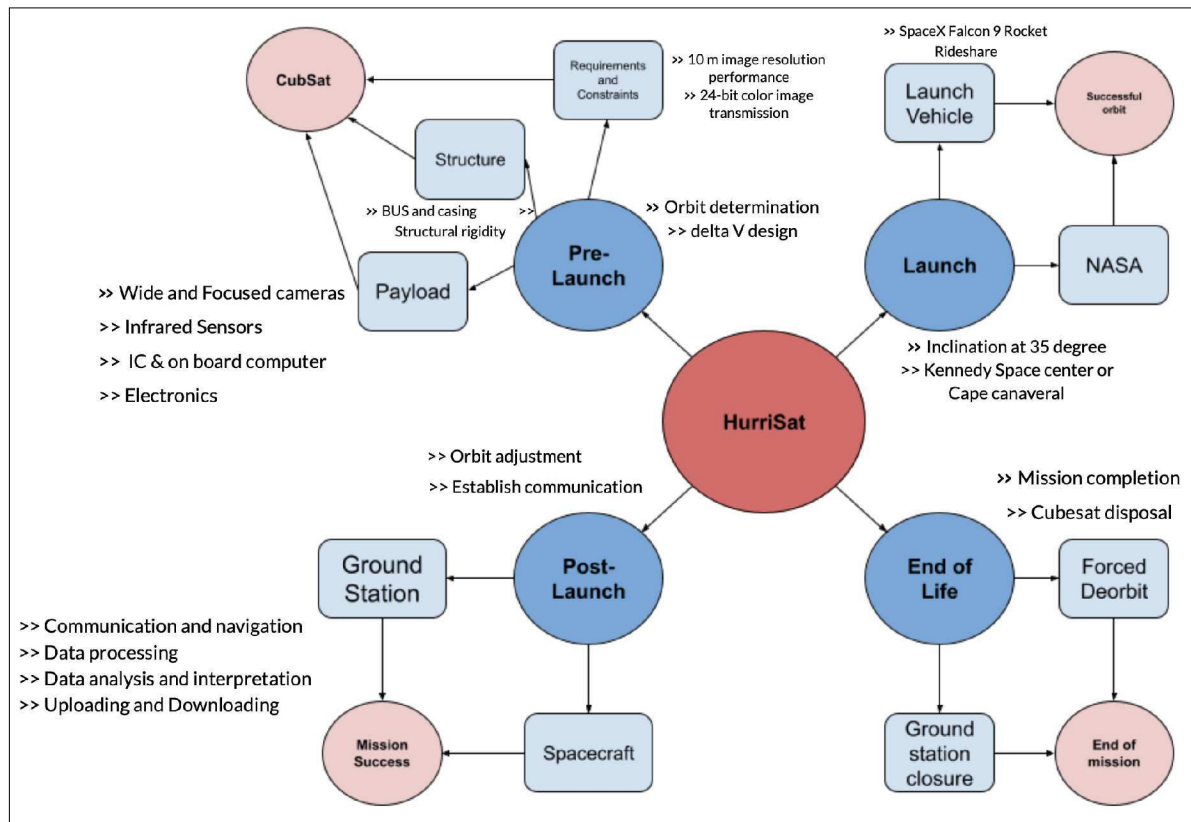
(a) Ground Coverage

(b) HurriSat Orbit

**Figure 3.1 – HurriSat Orbit and Ground Coverage**

### 3.2 Mission Architecture

Figure 3.2 is the overall mission architecture diagram. This diagram shows a high-level summary of the HurriSat project relative to its purpose and mission life. For easier exploration we have divided it into four main phases. The pre-launch, launch, post-launch, and end of life. Light blue blocks in the diagram outlines who or what entity will be involved, and the light red circle blocks indicate the ultimate mission (goal) for each section.

**Figure 3.2 – Mission Architecture**

### 3.3 Mission Life

The outline of the mission timeline for HurriSat is illustrated in Table 3.1. The preliminary design includes all the work completed within this report. Final Design will be the remaining design time used to complete design of the system and all supporting infrastructure to allow for execution of the strategic mission. Production and NASA integration will include the time to get approval from NASA, completion of all required documentations and licenses, and the construction of all required mission systems. Finally operation will include the time from launch until the eventual end of mission that will conclude with a force deorbit of the HurriSat system. In total, the HurriSat project is expected to have a total operation time of 17 years.

Additionally Figure 3.3 shows the life cycle block diagram. This diagram shows the expected timeline of HurriSat broken down into the Design, Production, Launch, Operation, and end of life phase. It also compares how the high level Spacecraft (s/c), ground, and launch vehicles operate at the 5 phases of the cubesat's life cycle.

**Table 3.1 – Mission Life Summary**

Mission timeline	Expected
Preliminary design	0.25 year
Final design	0.75 year
Production and NASA integration	1 year
Operation	15 years
<b>Total</b>	<b>17 years</b>

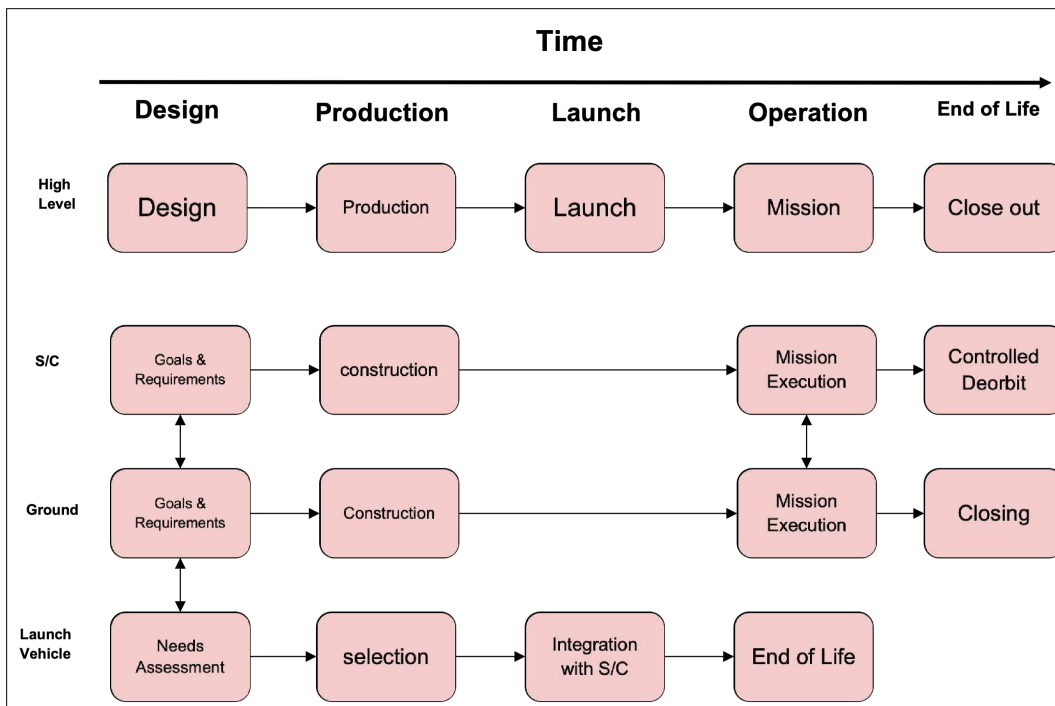


**Figure 3.3 – HurriSat Timeline**

Similarly Figure 3.4 is the sub-component functions block diagram. It is an interconnected functional overview for each subsystem in the cubesat. The main components in the payload (2 cameras) provide imagery function, while the on board computer process the data. The power is distributed as needed to all the components from the solar panels. The ADSC, propulsion all work together to help manage the cubesat's movement according to the ground stations needs.

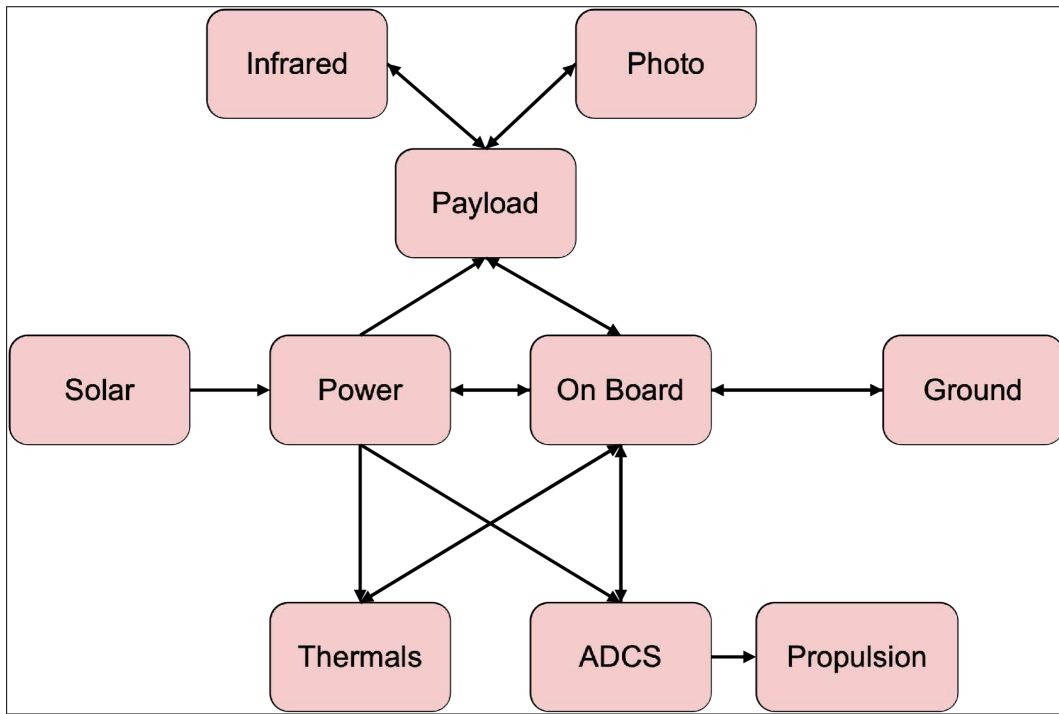


**Figure 3.4 – Block Diagram**

### 3.4 Launch Vehicle interface

Considering all of the possible launch vehicles (see Table 3.2) available to NASA, the Falcon 9 Rocket (highlighted in red) is chosen as the best candidate. This is because SpaceX [14] is able to launch materials at a rate of \$1.1 million for up to 200kg per ride share. Additionally SpaceX has a frequent launch rate of roughly a launch every 4 months. HurriSat will integrate with the Falcon 9 rocket using SpaceX's 157.5 cm diameter bolted interface. These factors will allow HurriSat to be launched in a timely manner at an affordable price.

### 3.5 Orbital parameters

The trade studies from initial report shows that GEO satellites are more than double the weight of LEO satellite. This is typically because of that additional propellant they carry in order to transfer. The reason we chose a LEO orbit satellite is so that it's cheaper to operate and maintain at that altitude, cheaper to launch, light weight and utilizes that strong signal for communication.

**Table 3.2 – Launch Vehicles Compared**

Launcher	Company	Launch Cost (usd Million)	Rocket Mass (kg)	Stages	Payload (kg)	Isp (sec)
Minotaur	Northrop Grumman	\$50	73,000	4	1,458	286
Delta II	McDonnel Douglas	\$51	286,000	3	6,140	319
Falcon 9	SpaceX	\$67	549054	2	22800	275
Falcon 9 Heavy	SpaceX	\$100	1,420,788	3	63,800	282
Atlas V	United Launch Alliance	\$125	590,000	2	18,850	280

Hurrisat will be sharing a ride amongst other cubesats or shuttles heading to ISS or other missions. Typically it is cheaper (about \$1 million) compared to single launch at \$67 million. This incentives requires selecting best orbital parameters and launch sites. Launch sites for previous missions include Cape Canaveral Air Force Station, Pacific Missile Range Facility, Kennedy Space Center, Mojave Air and Space Port, and Rocket Lab Launch Complex [11]. After careful observation and study [2] we have chosen the Kennedy Space center ( $28.573^{\circ}\text{N}$  and  $80.649^{\circ}\text{W}$ ) in Florida as our launch site. It's also where SpaceX uses to launch our choice of rocket; the Falcon 9.

### 3.5.1 Hohmann Transfer

The Falcon 9 will be releasing it at around 400Km (closer to ISS altitude) [9]. Since HurriSat will be sharing a launch vehicle amongst other it will need a Hohmann transfer. To transfer to its operational orbit of 800Km, it utilizes the propulsion and ADSC system. The Hohmann transfer values are shown in Table 3.3. These values are calculated with some marginal error for the actual weight and propulsion specific impulse provided by actual the manufacturer using a script, then simulated to STK. The orbital transfer is shown in Figure 3.5(a and b).

**Table 3.3 – Transfer Values**

Initial Orbital Parameters	
Inclination	35 degrees
Eccentricity	0 degrees
Altitude	400 km
Hohmann Transfer: 400km to 800km	
Delta V	0.217 km/s
Transfer time	2900 s / 0.8 Hr
Eccentricity	0.514 degrees
Inclination	35 degrees
Radius of Periapsis	6778.1 km
Radius of Apoapsis	7175.1 km
Semi-Major Axis	13956.3 km
Final Orbital Parameters	
Inclination	35 degrees
Eccentricity	0 degrees
Altitude	800 km

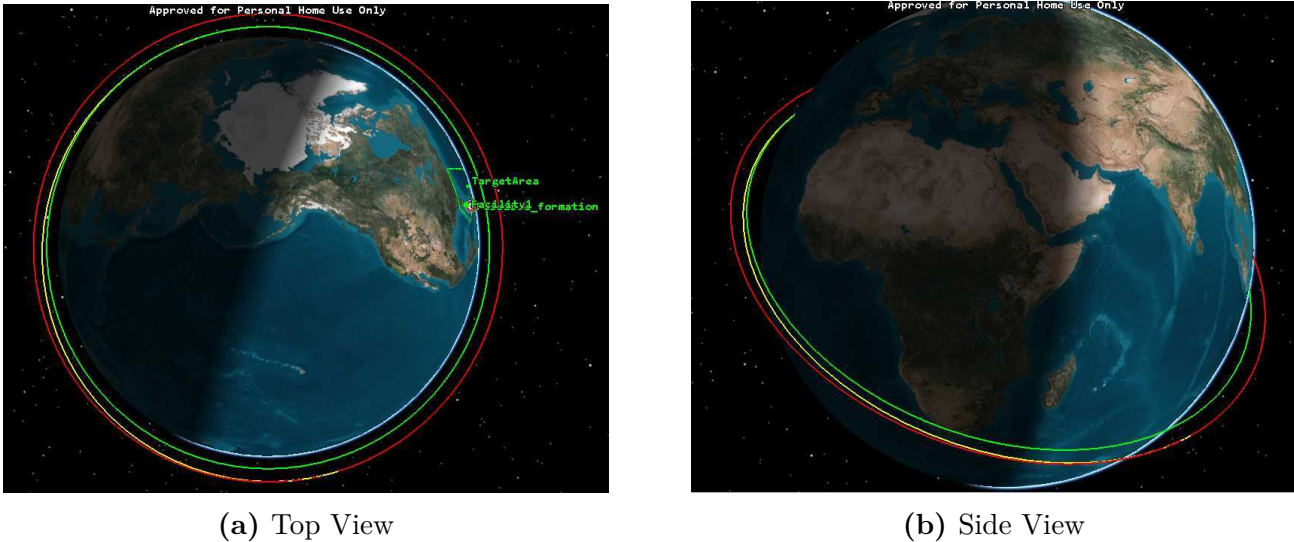


**Figure 3.5** – Hohman Transfer simulated using STK

### 3.6 Payload

The payload is equipped with all the components needed for the mission. These components listed in Table 3.4 are selected specifically in order to meet the requirements. The payload comprises one visible spectrum image sensors behind a 2 setting variable zoom lens, one setting to detect possible hurricane formations alongside another to acquire detailed images, and an infrared spectrum sensor to provide hurricane characteristics. All fixed in orientation on the spacecraft. Camera and electronics weigh around 600*grams* and the infrared sensor weighs around 45*grams*.

**Table 3.4 – Payload Characteristics**

Component	Function	Characteristics	Requirements Met
IR camera	Gather Atmospheric data	640x512 pixels	Temperature, atmospheric readings
Imaging sensor	capture images	4112x2248 pixels	Provide visible spectrum images
Camera wide	Detect hurricane formations	2400x1300km; 548m/pixel	Yes, since $200\text{m}/\text{pixel} \leq 548\text{m}/\text{pixel}$
Camera narrow	Detailed hurricane imaging	26x14km coverage; 10m/pixel	Yes since $10\text{m}/\text{pixel} \geq 6.5\text{m}/\text{pixel}$
Antenna	Transmission & Comms	1 Mbps	Yes, can transmit 3 images per passs
OBC ARM	Data Processing	4112x2248 pixels	Provide visible spectrum

To achieve the ground coverage requirement of at least 10m/pixel the camera sensor has a resolution of  $4112 \times 2248$  pixels and a size of  $3 \times 2\text{mm}$  with a pixel size of  $0.64\text{m}$ . The Spectral Camera's 3.6(a) pixel size was selected based on the smallest available scale pixel technology and commercial availability. Narrow setting lens focal length was selected to equal  $90\text{mm}$  to achieve a zoomed in

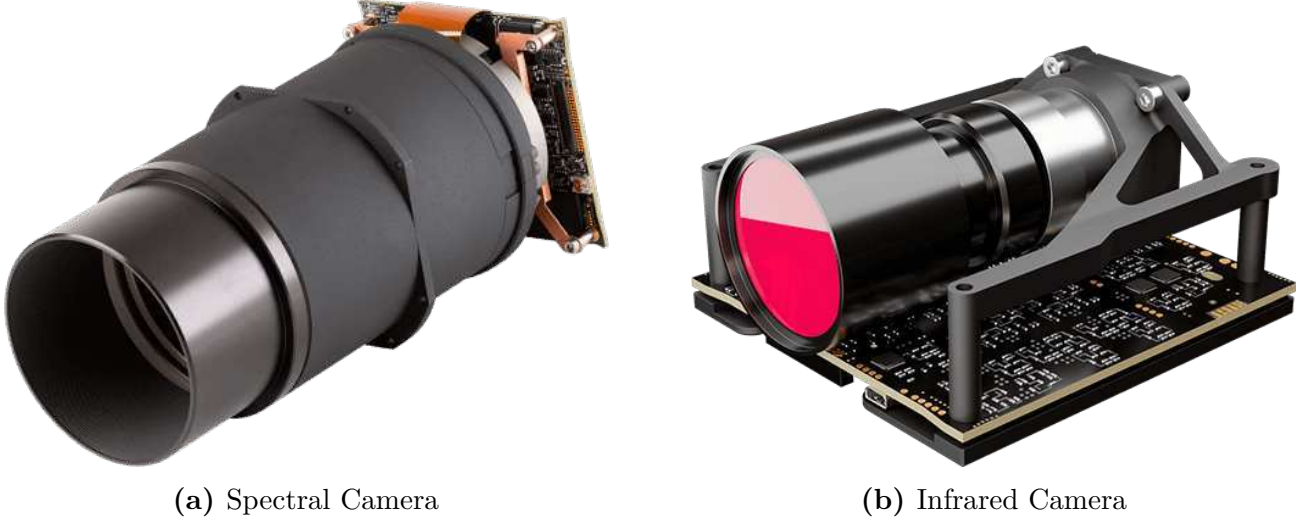
**Figure 3.6** – Required Cameras

image to sufficient ground resolution. With these specifications overall narrow camera lens ground resolution is  $6.5\text{m/pixel}$  which exceeds the initial requirement of  $10\text{m/pixel}$ . Ground coverage is as required and equal to  $26 \times 14\text{km}$ . The second lens setting is set at focal length of  $1\text{mm}$  which results in a large half cone angle. This camera lens setting has the purpose of locating possible hurricane formations' location and relative speed. It has a ground resolution of  $584\text{m/pixel}$ . Area coverage on this setting is  $2400 \times 1312\text{km}$  which means that in most cases the satellite can cover the entire target area with a single pass.

The infrared camera in Figure 3.6(b) is used to collect hurricane formation characteristics to the ground station. It's used to capture infrared pictures of could formation, temperature readings and other atmospheric readings with a configurable scan. It has a lower lens resolution compared to the visible spectrum cameras, however it is sufficient given that it only needs to give average temperature readings for a massive hurricane.

## 4 Cubesat Budget

### 4.1 Mass Budget

The mass estimate for HurriSat is based on previous successful 6U cubesat missions and commercial data sheet for sub-components weights [2]. Typically a 6U CubeSat is  $20\text{ cm} \times 10\text{ cm} \times 34.05\text{ cm}$ . After listing every single component in the payload, the total weight is determined by summing them all at once. Then the rest of subsystem sections are determined based on percentage values from reference sheets [8]. Table 4.2 shows the mass sizing based on the total payload mass. Payload is estimated to be approximately 3.1kg after sizing. This includes dual high-tech cameras, LiDAR, IC electronics, and censors outlined in the payload section.

## 4.2 Power Budget

The power budget placed on each subsystem is shown in Table 4.1 and a 30% margin is taken into account. This specific values are obtained based on the components the payload houses first. Each component's power is summed up and determined before to estimate the total payload power consummation. It's from then that each of subsystem's power are determined.

Element	Power (W)
Payload	5.8
ADCS	8
C&DH	1
Power	9
Propulsion	12
Structure	0
Thermal	0
Communication	1
Margin	30%
Total	47.84

Table 4.1 – Power Sizing

Subsystem	Mass (kg)
Payload	0.172
ADCS	0.284
C&D	0.13
Power	1.283
Propulsion	3.49
Structure	1.2
Thermal	1.757
Margin	10%
Total	7.2325

Table 4.2 – Mass Sizing

## 4.3 $\Delta V_{design}$ Budget

The delta-v budget is an estimate of the total change in velocity required for the space mission. It is calculated as the sum of the delta-v required to perform each propulsive maneuver needed during the mission. It also determines the propellant is required for HurriSat at a given given empty mass and propulsion system. The Delta V design required for the spacecraft was observed over a range of possible altitudes and inclination angles. The range was selected after a thorough research of LEO Cubesats (see Figure 2.3 for more trade studies) that operate on the optimum orbit. Table 4.3 shows the values with the best parameters listed. The intersection cell (highlighted cell in bright red) is our optimum  $\Delta v_{design} = 11.729 \text{ km/s}$ . Selected choice of altitude is  $h = 800 \text{ km}$ , and the inclination angle is  $\alpha = 35^\circ$ .

Table 4.3 –  $\Delta V_{design}$  in (km/s)

Altitude (km)	Inclination Angle $\alpha$ (degrees)					
	30	32	35	40	45	52
800	11.709	11.717	11.729	11.752	11.778	11.817
850	11.836	11.843	11.856	11.879	11.904	11.943
900	11.958	11.966	11.978	12.001	12.026	12.065
950	12.077	12.084	12.097	12.119	12.144	12.183
1000	12.191	12.199	12.211	12.234	12.258	12.297
1100	12.410	12.418	12.430	12.452	12.476	12.514
1200	12.617	12.624	12.636	12.658	12.682	12.720

## 4.4 Cost Budget

Cost budget is a financial plan exhibiting the expected costs related to running a business or undertaking a project or for developing a product. Cost budget are prepared for those expenses which are significant for the project. The maximum cost budget for CSLI missions is capped at *300,000 USD* by NASA. It's still difficult to accurately provide the cost for HurriSat. This is mostly because the technology and commercialization of these satellites is still in its infancy stages. Based on the findings from Space Flight [6] HurriSat is estimated to cost around *48 – 50k USD* per unit excluding labor costs. Every other component cost is listed in Figure 4.1. The stake holders should know that cost is driven by supply and demand, and thus a steeper price change is expected given the manufacturing challenges.

Component	Association	Function	Quantity	Total Cost	Source
<b>BiSon64-ET</b>	ADCS	Attitude Sensor	1	\$9,740	CubeSatShop
<b>Arcsec Sagitta Star tracker</b>	ADCS	Star Tracking	1	\$44,000	CubeSatShop
<b>nanoSSOC-D60 digital sun sensor</b>	ADCS	Sun Sensor	1	\$4,500	CubeSatShop
<b>Patch antenna option 2 (S-Band)</b>	Comms	Antenna	1	\$2,330	CubeSatShop
<b>S-Band High Data Rate Transmitter</b>	Comms	Transmitter	1	\$18	ISIspace
<b>onboard computer</b>	C&DH	Central Computer	1	\$10,000	EnduroSat
<b>Infrared camera</b>	Imaging	Infrared Imaging	1	\$5,000*	Sensors Unlimited
<b>Camera narrow</b>	Payload	Wide Imaging	1	\$3,500*	Custom Optics
<b>Camera wide</b>	Payload	Focus Imaging	1	\$3,500*	Edmund Optics
<b>Deployable Multifunction Solar Array</b>	Power	Support array for solar panel	4	\$56,000	CubeSatShop
<b>DHV-CS-10 Solar Panel</b>	Power	Provide Power to CubeSat	14	\$22,000	CubeSatShop
<b>EXA BAOx High Energy Density Battery Array - 44 W/Hr</b>	Power	Power Storage	2	\$12,600	CubeSatShop
<b>Modular Propulsion System 130-2U</b>	Propulsion	3 Dimensional Propulsion	1	\$130,000	Aerojet Rocketdyne
<b>Framing Structure</b>	Structure	Structure	1	\$7,500	Custom Build
<b>ISIS Full Ground Station Kit for S-band</b>	Ground Station	Receiver	1	\$72,250	CubeSatShop

**Figure 4.1 – Cost Budget**

Based on previous research done at PRICE, it's obvious planetary missions tend to cost more than similar ones that stay near the Earth. NASA's attempt at a planetary CubeSat demonstrates that these unique satellites are becoming a permanent part of space exploration. The sum of each component listed in the figure comes to about *251,000 USD* cost. There are still installation, maintenance and testing overheads to account for. But those can only be estimated once the manufacturing phase starts.

## 4.5 Cubesat Sizing

HurriSat's sizing is represented in Figure 4.2 down below. The main components are laid out, and labeled. Note that actual sized may vary upon manufacturing and delivery. But the figure is to show how the components are aligned in a manner that's able to fit the cubesat's purpose whilst keeping it's axis of symmetry intact. The subsystem components are shown as boxed figures for place holding. All these components are estimated from the dimensions provided in the commercial manufacturing data sheet. It should be noted that the main frame casing is custom built with Aluminum Alloy. The number of solar panels and solar cells are designed in such a way to reflect the values proposed as per the power budget.

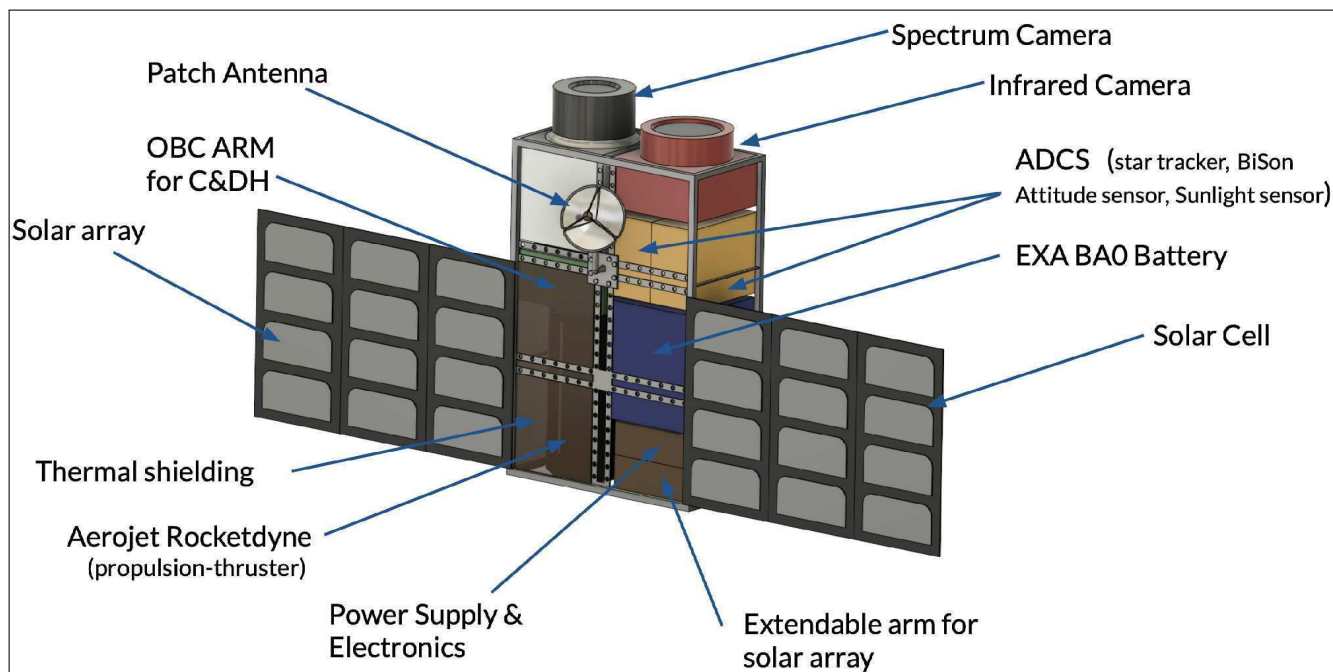
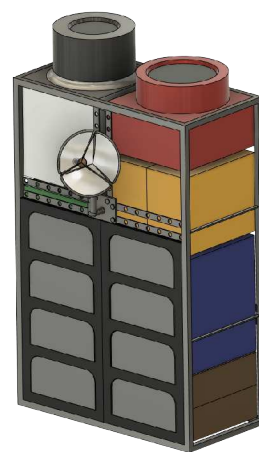


**Figure 4.2 – HurriSat and its Components**

## 4.6 Cubesat Configuration

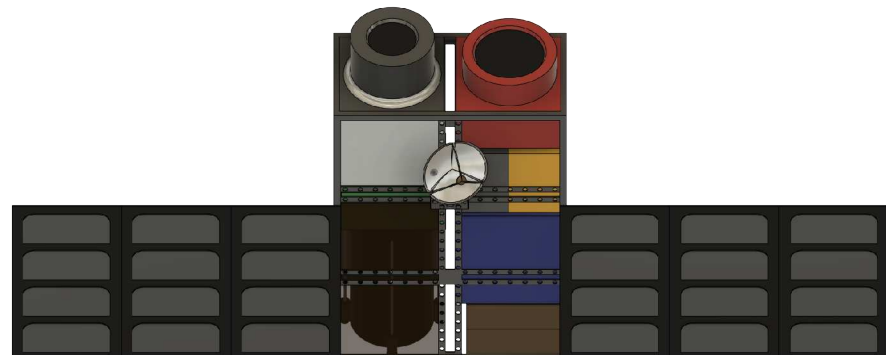
HurriSat is designed to easily accommodate in the launch vehicle. In Figure 4.3a it is fully closed for transportation and the Falcon 9 launching phase. This easy packaging helps minimize collision impact and prevent any launch associated risks, like mechanical, vibrational, electrical or acoustic energy. The Semi folded 4.3b shows how the solar arrays for cubesat extend during the transition from parking to operational orbit in order to gain some solar power. This sets up the satellite ready for operation. Mechanical lever arms are utilized to push the folded panels away from the unit without any hydraulic system. Figure 4.3c is a fully extended HurriSat during and on operation at the desired orbit. Cold thrustures can be used to maneuver the cubesat with the aid of the ADSC and thrusters at hand.



(a) Clothed and Intact



(b) Unfolding Phase



(c) Fully Stretched

**Figure 4.3 –** HurriSat Launch Configuration

## 5 Subsystem Design

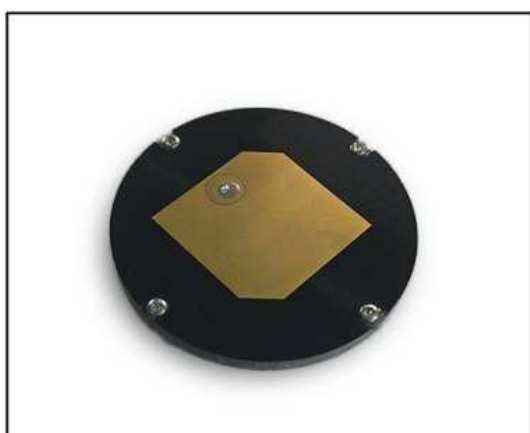
### 5.1 Communications

The satellite communication system will consist of a single patch antenna (Figure 5.1 a) set in the S band at 2.2GHz frequency and BPSK modulation. Given the wide signal spread of the antenna and the fact that the proposed ground station (Figure 5.1 b) receiver is well within close proximity to the target area. The satellite will not have to adjust orientation to transmit data or receive instructions.

The antenna is expected to transmit no more than 3 images per pass, 2 of which have an average size of ***4MB*** and one infrared image with a size of ***2.5MB***. Given that the average access time with the ground station is 15 minutes, a signal bandwidth of ***1Mbps*** was selected. With the selected antenna characteristics, the communication system power requirement is estimated at ***1.5W***.

**Table 5.1** – Communications Table

Parameter	Value	Units
Power	1.5	W
Line loss	-3	dB
Frequency	2.29	GHz
Transmitter gain	6.5	dB
Atmospheric losses	-0.99	dB
Receiver gain	36	dB
Operating temperature	260	K
Bit rate	1	Mbps
Link budget	27.02	dB
Link margin	16.25	dB



(a) Cubesat Path Antenna



(b) Ground Station Receiver

**Figure 5.1** – Communication Mechanism

## 5.2 Command and Data Handling

Data handling will be managed by the ARM Cortex on board compared manufactured by Endu-oSat [4]. This command and control computer shown in Figure 5.2 has an excellent M7 processor that provides many great features at an estimated cost of \$10,000. This includes an ARM Cortex M7 processor and a 2 MB of memory for caching. Additionally the computer offers a built-in clock, 3-axis magnetometer, and MicroSD card slots (see Table 5.2). Finally the computer has many interfaces including 4x RS-485, 2x RS-422, 3x UART, 2x I2C, SPI, USB, and CAN. These features allow for Hurrisat to manage all of its computing requirements and stay within the power budget requirements.

**Table 5.2 – OBC Data Handling**

Parameter	Value	Units
Processor	ARM Cortex M7	N/A
Program Memory	2	MB
Storage expansion slot	MicroSD	8-bit pin up to 32GB
SRAM	1	MB
External FRAM Memory	8	Mbit
Mass	130	g
Interfaces	2x RS-422, 3x UART, SPI, USB, CAN	N/A



**Figure 5.2 – On Board Computer**

## 5.3 Electrical

The average power drawn throughout the mission is approximately  $47.8W$ , which is a reasonable power requirement for a 6U cubesat. It is calculated using a python script for accuracy and precision 8.5. The most cost-effective and sustainable option for the power source is solar photovoltaic cells with a required surface area of  $0.44m^2$ . Since this is greater than the total surface area of the 6U cubesat, a deployable solar array is required in addition to arrays across the external surface of the structure. The EXA DMSA (Deployable Multifunction Solar Array) in Figure 8.2b was selected for the deployable array due to its thin structure and deployment mechanism while the DVH-CS-10 (Figure 8.2a) was selected for the surface panels due to the size and high efficiency.

The HurriSat will utilize two EXA BA01/D high density battery arrays (see Figure 8.2c). These battery arrays were chosen due to their high energy storage and small size. They meet the energy storage requirements to keep HurriSat operational throughout its orbit period.

## 5.4 ADCS

Altitude determination and control subsystem will be managed using a Arcse Sagitta start tracker (Figure 8.1a), BiSon64-ET attitude sensor (Figure 8.1c), and a nanoSSOC-D60 (Figure 8.1b) digital sun sensor. In combination, these sensors will allow us to receive accurate attitude information at an affordable cost of 58,240. With this information the on board computer will be able to give the appropriate commands to the propulsion system to make appropriate changes to the orbit and attitude.

### 5.4.1 Attitude Determination

The HurriSat utilizes three attitude determination systems in order to accurately determine its attitude. These systems were selected for their small size, accuracy, and large field of view. The nanoSSOC-D60 is a sun sensor that has a FOV of +/-60 degrees with an accuracy of within 0.5 degrees and precision within 0.1 degree. The Bison64-ET-B is an attitude sensor with a FOV of +/-64 degrees with a calibrated accuracy within 0.5 degrees. The arcsec Sagitta star tracker has a FOV of 25.4 degrees X 25.4 degrees as well as successful flight heritage.

## 5.5 Control System

In order to control the attitude of the HurriSat a reaction wheel is needed. The small CubeWheel (Figure 8.1d) was selected due to its small size and compatible interfaces with the attitude determination hardware. This reaction wheel will have a speed range of +/- 8000 RPM with a control accuracy of 5 RPM and a maximum torque of 0.23 mNm.

## 5.6 Thermal

Thermal design requires a thorough analysis and data from the manufacturing companies. In order to leverage thermodynamics to design technologies and products, the operational temperature of each subsystem had to be determined firsthand. The temperature at an altitude of 800km is estimated to be 420C while the thermal limitations of HurriSat's components lie between -150C and 250C 5.3. Thermal shielding is required to keep these components within their operational limits. To mitigate the impact of heat due to solar rays on the components we will use silver-coated teflon due to its reflective properties (see Figure 5.3). The propulsion system will be insulated to minimize its impact on internal heating. Thermostats and thermistors will be used to monitor the temperature in areas of the HurriSat structure to ensure all components are kept within their operational temperature.

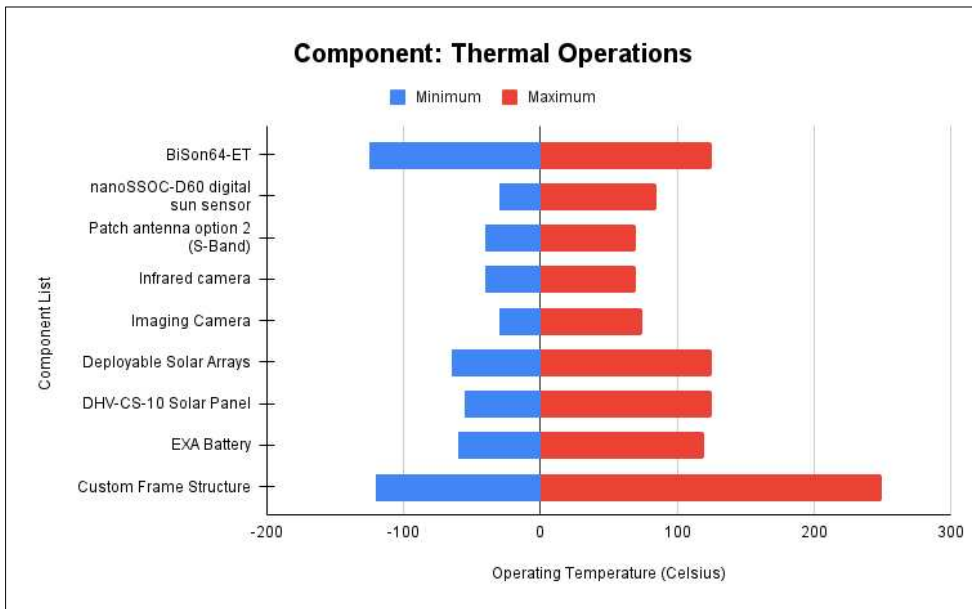


**Figure 5.3 – Thermal Limitations**

## 5.7 Propulsion

The general analysis conducted to identify a comprehensive list of propulsion methodologies involves identifying the set of maneuvers necessary to reach orbit altitude and adjust the inclination when necessary. Primary propulsion technologies would be used for orbit adjustment including shaping, changing, and maintaining altitude before and after reaching target orbit. Optimizing the orbit will determine the rate of propellant use and how long it can maintain its orbit, and by extension its lifetime. To reduce the consumption of propellant and the need for high powered propulsion systems, unnecessary and costly maneuvers must be avoided. Inclination change is one such reason; that requires significant propellant and thruster firings to manage. STK and python scripts were utilized to estimate the required total-Impulse for the Hohmann transfer from the departure orbit of CubeSat at an altitude of 400 km to the designated orbit of 800 km at a similar inclination of 35°.

The maneuver to change altitude is conducted with a green monopropellant propulsion systems produced by Aerojet Rocketdyne [16]. The total Impulse managed by this propulsion system using an AF-M315E propellant blend for better performance and safety is sufficient for the maneuver with an estimated Delta V of 400 m/s for the wet mass of the designed CubeSat (See Figure (5.4)a). The MPS-130-2U piston [13] fed modular propulsion system utilizes a non-toxic green monopropellant delivering up to a 50% increase in density specific impulse while having a reduced footprint compared to similar velocity impulse systems operated with Hydrazine (Table 5.3). Green Monopropellant (highlighted red in the table) is chosen because it reduces fire hazards, has less equipment overhead, and weighs less compared to Hydrazine based propulsion systems.

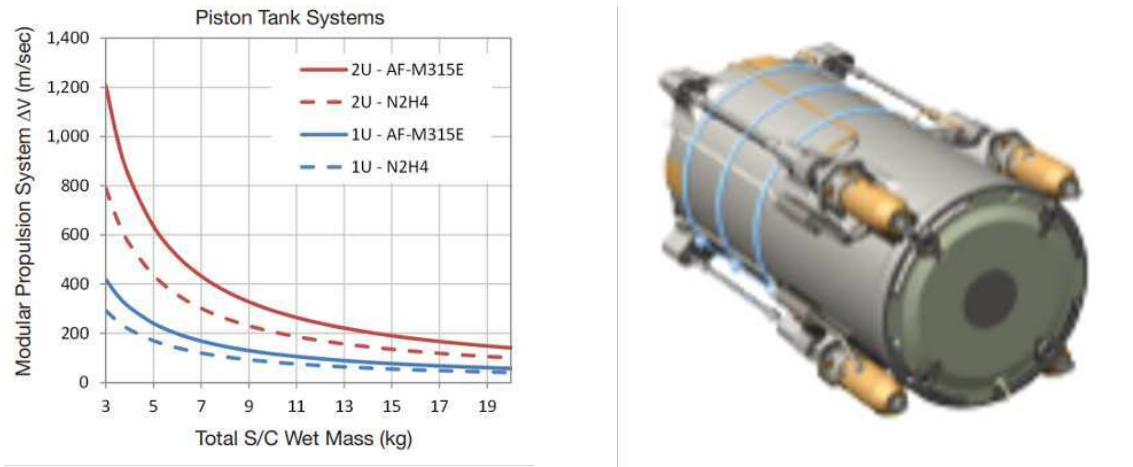


**Figure 5.4 – Aerojet Rocketdyne Piston Tank Modular Propulsion System**

**Table 5.3 – Propellant Comparison**

Propulsion System	MPS-130-2U	
Dimensions (cm)	10x10x20	
Thrust (N)	0.25 - 1.0	
Propellant	Green Monopropellant (AF-M315E)	Hydrazine
Dry Mass (kg)	1.4	1.5
Wet Mass (kg)	2.5	2.8
Estimated Delta V (m/s)	400	300
Total Impulse (N-s)	2720	1960

## 5.8 Structure

Structure configuration for any CubeSat requires a lightweight material capable of withstanding the environmental elements it would be exposed to such as aerodynamic, gravitational, and solar torques that could arise during liftoff and transonic periods. The prevalence of electronic components onboard requires as little interference as possible, as such a non-magnetic 7000 series Aluminum alloy is commonly utilized [17]. These alloys are tempered through multiple processes such as solution heat-treated by homogenizing the 7075-alloy cast for several hours, quenching for stress relief, then artificially aged to stabilize the microstructure and meet process requirements. This process allows the materials to obtain desirable characteristics such as improved strength, low density, corrosion resistance, better crack, and fatigue resistance. The T651 alloy was found to have better overall mechanical properties as shown in Table 5.4 and was the choice of material for the 6U casing design .

All structures have natural frequencies of vibration which create large amplitudes that can lead to fatigue failure, undesirable noises, and reduced performance. A modal analysis for the natural frequency and mode shape is therefore conducted on the designed casing structure (Figure 8.3) to

understand how the model reacts to external disturbances in a free vibration simulation, where more than one node participates in the system response. This analysis helps identify peak frequencies at or near structure natural frequency that may affect the performance of the structure. A sample of this response at a peak frequency of 127.1 Hz has a maximum deformation of about 0.46 mm as shown in Figure 5.5.

**Table 5.4 – Aluminum Alloy Comparison**

Aluminum Alloy	Al7075-T651	Al7075-T7351
Yield Strength (MPa)	505	435
Ultimate Tensile Strength (MPa)	570	510
Modulus of Elasticity (GPa)	72	70
Brinell Hardness	150	140
Density (g/cc)	2.81	
Poisson's Ratio	0.32	
Coefficient of Thermal Expansion @20-100°C (μm/m°C)	23.4	

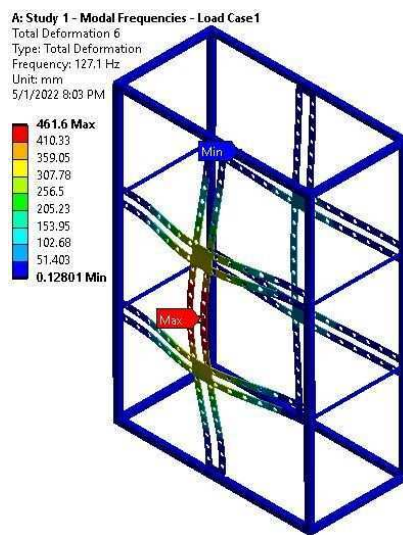


**Figure 5.5 – Modal analysis of structure at peak frequency of 127.1 Hz**

## 6 Mission Feasibility

### 6.1 Feasibility and Success Criteria

The success of this project depends on meeting the performance metrics and thereby achieving the goals mentioned in the mission statement. Table 6.1 indicates how those metrics will be measured and whether the proposal holds true during testing phase.

Based on feasibility Table on the right and the project analysis provided shows the importance of orbital flight for weather satellites. Highlighting the severity of the consequences associated with hurricane activity, not only is orbital flight beneficial but crucial to the likes of NASA in order

to mitigate alert public safety from a catastrophic weather. Project Hurrisat proves it is indeed possible to tackle down hurricanes effectively and perhaps avoiding them in an efficient manner for years to come.

**Table 6.1 – Mission Success Criteria**

Objective	Effective Measure	Control Method
Coverage of 110000 square miles (2400x1300 square km)	Variable setting camera lens (Wide and Narrow)	STK Simulation
Hurricane recognizing, Tracking and Alerting	Active tracking using Arcse Sagitta star tracker from ADCS	STK Simulation
Project Lifetime (15 years)	DHV-CS Solar Arrays and EXA BA0 high energy battery. Al 7075-t Support structure casing	STK Simulation, Solidworks for stress analysis
Updating every 15-20 min	ISIS S band, BPSK Modulation	STK Simulation
Data content (Image, Location, velocity)	ARM Cortex M7 OBC	STK Simulation
Atmospheric Data (Temp, Humidity, Wind)	Infrared Spectrum Camera	Sentinel toolbox, STK simulation

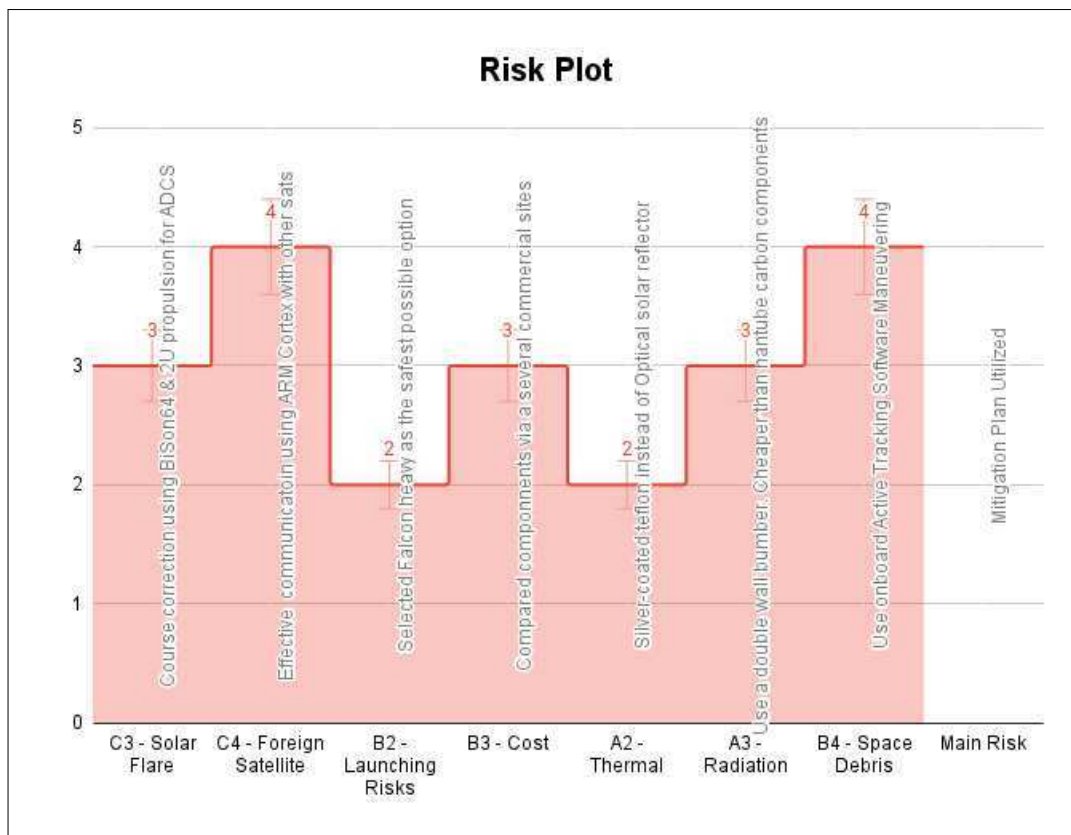
## 6.2 Risk Control

HurriSat is designed by taking the main anticipated risks in to account. The components are designed and selected in a manner they can mitigate ad avoid the potential risk as listed in Figure 6.2. The Risks anticipated column are color graded based on probability of that hazard occurring. (i.e. Red is frequent, while yellow is less likely to occur). The values how ever are assigned based on that specific risk severity.(i.e. 4 is catastrophic while 2 is minor). The risk plot Graph 6.1 the weights (risk severity) of those risks and what we did to mitigate them. Our two main catastrophic hazard concerns are space Debris and radiation. Those can penetrate cubesat's components and cause a major failure . However we can counter space-debris using active tracking software mechanism installed on the OBC computer and maneuvering using propelled thruster. A double wall bumper is also installed around the casing that can potentially shield most of the radiation and flares.

Of course there's a trade off of slight weight increase and steeper price for OBC processor. But those were the main reason that were chosen first hand. Other small scale risks are also anticipated but not shown (such as mechanical vibration, overhead and launching risks). Those however were found severe enough to halt the mission.

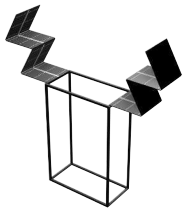
**Table 6.2 – Mission Risks**

Main Risks anticipated	Mitigation Plan Utilized	Value
B4 - Space Debris	Use onboard active tracking software maneuvering	4
A3 - Radiation	Use a double wall bumper. Cheaper than carbon nanotube components	3
A2 - Thermal	Silver-coated teflon instead of optical solar reflector	2
B3 - Cost	Compared components over several commercial sites	3
B2 - Launching Risks	Selected Falcon heavy as the safest possible option	2
C4 - Foreign Satellite	Effective communication using ARM Cortex with other satellites	4
C3 - Solar Flare	Course correction using BiSon64 and 2U propulsion for ADCS	3

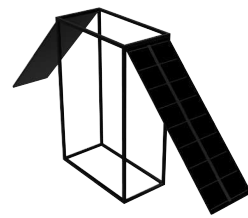

**Figure 6.1 – Risk Control**

### 6.3 Alternatives

- Optical solar reflector to counter solar flares can be used as cheaper alternatives instead of nanotube coating.
- Double wall bumpers were considered be used to further avoid thermal limitations.



(a) Set up 1



(b) Set up 2

**Figure 6.2** – Alternative frames considered

- Alternate possible design considered as seen in Figure 6.2. Even if they can be used by switching up the axis of symmetry, there isn't enough area to put the solar cells on the side of frame. It can be possible considering lowering down the power budget for the cubesat.

## 6.4 Technology Gaps and Trades

Project HurriSat is designed by focusing on detailed component requirement and constraint in mind. Although goal is to aim for the safest and efficient spacecraft design possible, we are very limited on basis of cost and technological gap. The trade off is finding cheap yet good enough components, ride sharing for launch, and not nano-carbon framing and such. The list below highlights some of the challenges faced during this project.

- Launching mechanisms can only be determined by NASA and SpaceX mechanics.
- The ADCS and OBC can be combined for a an advanced all in one components, had there been no halt in electronics production due to the pandemic.
- Actual stress, thermal and radiation values may vary since we're not manufacturing the cubesats.
- Prices are subject to change based on demand and supply

## 7 Conclusion

This concludes our design report for the project HurriSat. This low-earth orbit weather satellite will be used to study, monitor, and track hurricanes and other extreme weather across the east coast. This satellite meets the complete NASA's strategic goal as shown earlier. i.e. to study the cause effect of severe space weather events, and prevent potential damage. Hurrisat will also accomplish NASA's strategic goal to address national challenges and catalyze economic growth for space sustainability. This report outlines the mission exploration, architecture, the subsystem design, mission feasibility, and the further work needed for NASA's cubesat initiative project.

## 8 Appendix

### 8.1 ADCS Components



(a) Arcse Sagitta star tracker



(b) nanoSSOC-D60



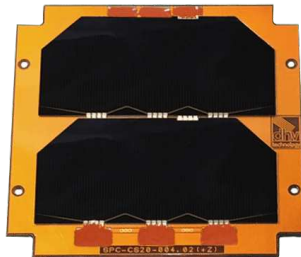
(c) BiSon64-ET



(d) Momentum Wheel

**Figure 8.1 – ADCS Components**

## 8.2 Electrical Components



(a) DHV-CS-10 CubeSat Solar Panel



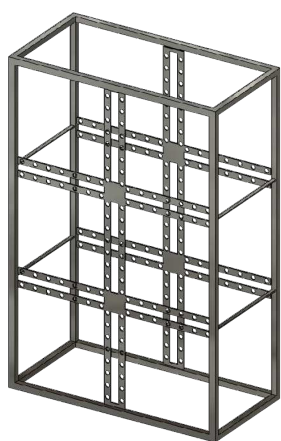
(b) EXA Deployable Multifunction Solar Array



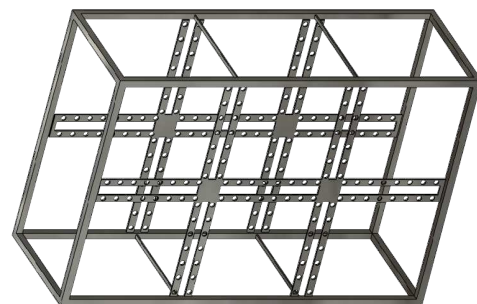
(c) EXA BA01 Battery Array

Figure 8.2 – Electrical Components

## 8.3 CAD Drawings

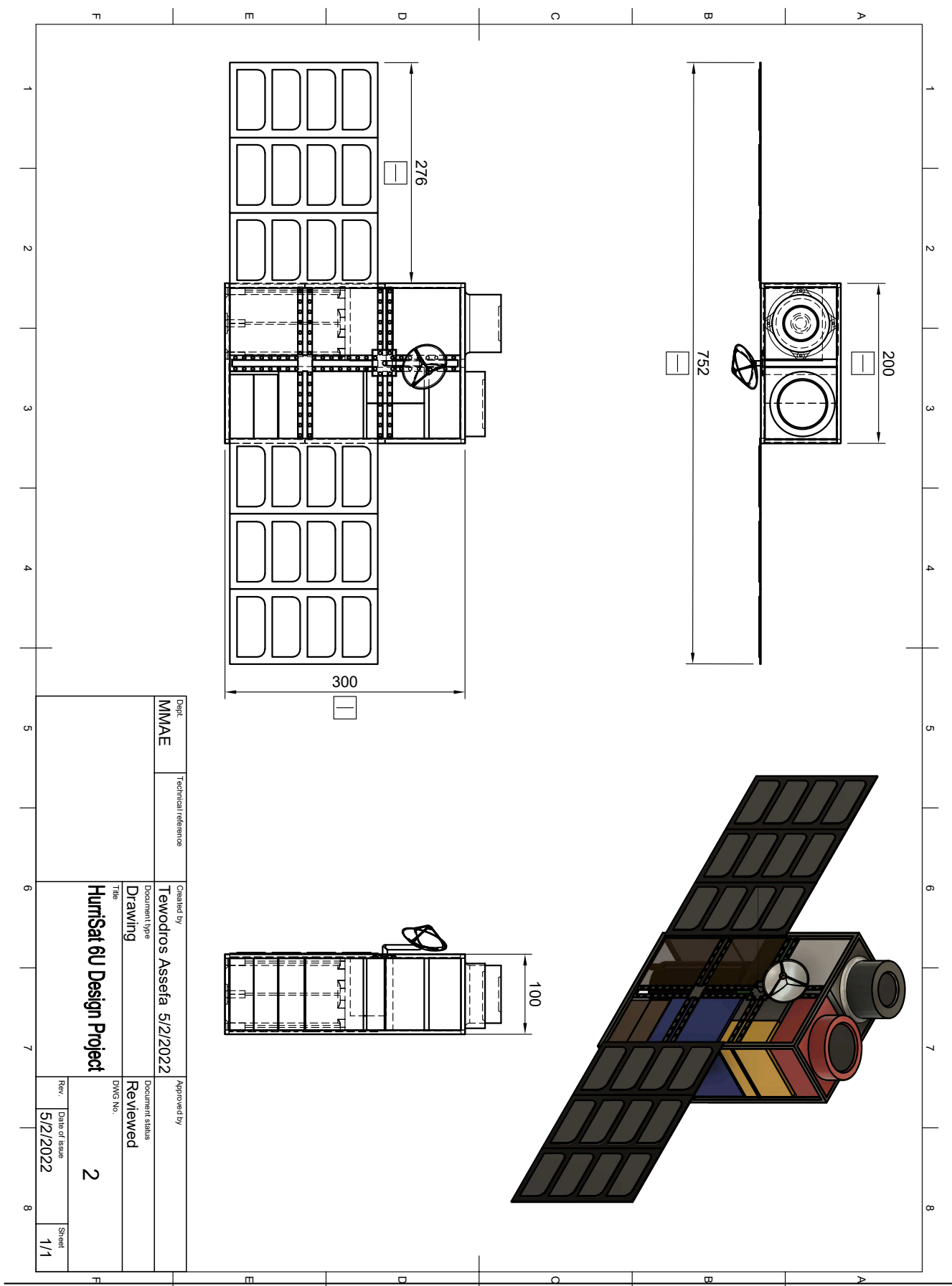


(a) Frame: Side View



(b) Frame: Iso View

Figure 8.3 – Al7075-T651 Cubesat Frame



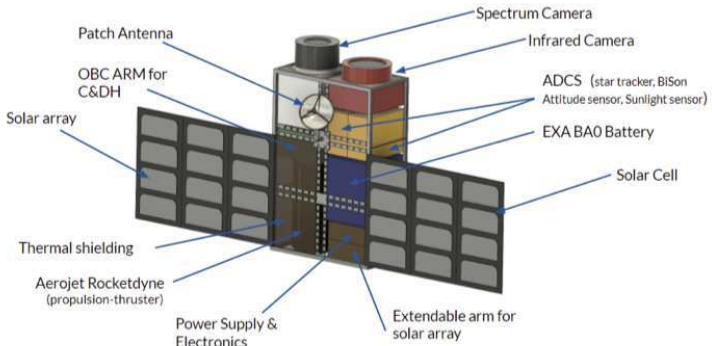
## 8.4 Fact Sheet

# HurriSat Fact Sheet

May 1st 2022

## HurriSat Overview

The mission of this project is to propose a Low Earth Orbit 6U sized Cubesat in order to track down the hurricanes across the South-Atlantic U.S. Region. This Cubesat should be able to track small to big size hurricanes across the required region with greater accuracy. Cubesat will collect the size of hurricane, speed, impact area, changes in temperature, pressure, and other details successfully. By doing so, it has to communicate and transmit data back and forth between local stations effectively. Furthermore, we must ensure the collected data is used as per the contract agreement with NASA and its interested parties effectively.



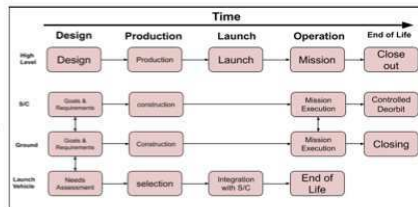
## Requirements

- 2400x1300 km<sup>2</sup> ground coverage
- 2 visible spectrum image
- Communicate with ground station
- Mission life of ≥15 years
- Reliable under ideal conditions

- Provide temperature, relative speed, and atmospheric reading
- Communication every 15-20 min
- Data content: Images, location, relative velocity, atmospheric data

## Life Cycle

HurriSat life cycle is expected to be 17 years. Design phase of 1 year, production phase of 1 year, and a launch/mission phase of 15 years. A summary of the life cycle can be seen in the figure to the left.



## Component and Cost List

The Table to the left lists the components, subsystem association, function, cost, source, and required quantity for all expected components of the HurriSat design. The total cost of the design is expected to be \$382,938. It is expected that with these components HurriSat will be able to meet the mission requirements at the lowest possible cost.

Component	Association	Function	Quantity	Total Cost	Source
BiSon64-ET	ADCS	Attitude Sensor	1	\$9,740	CubeSatShop
Arcsec Sagitta Star tracker	ADCS	Star Tracking	1	\$44,000	CubeSatShop
nanoSSOC-D60 digital sun sensor	ADCS	Sun Sensor	1	\$4,500	CubeSatShop
Patch antenna option 2 (S-Band)	Comms	Antenna	1	\$2,330	CubeSatShop
S-Band High Data Rate Transmitter	Comms	Transmitter	1	\$18	ISIspace
onboard computer	C&DH	Central Computer	1	\$10,000	EnduroSat
Infrared camera	Imaging	Infrared Imaging	1	\$5,000*	Sensors Unlimited
Camera narrow	Payload	Wide Imaging	1	\$3,500*	Custom*
Camera wide	Payload	Focus Imaging	1	\$3,500*	Custom*
Deployable Multifunction Solar Array	Power	Support array for solar panel	4	\$56,000	CubeSatShop
DHV-CS-10 Solar Panel	Power	Provide Power to CubeSat	14	\$22,000	CubeSatShop
EXA BAOx High Energy Density Battery Array - 44 W/Hr	Power	Power Storage	2	\$12,600	CubeSatShop
Modular Propulsion System 130-2U	Propulsion	3 Dimensional Propulsion	1	\$130,000	Aerojet Rocketdyne
Custom Structure	Structure	Structure	1	\$7,500	Custom Build
ISIS Full Ground Station Kit for S-band	Ground Station	Receiver	1	\$72,250	CubeSatShop

## 8.5 Codes and Scripts

### 8.5.1 Script for Mass Sizing

```

import numpy as np

pay_m=0.605 #initial mass of payload in kg using trade studies
dry_m=pay_m/(.3)
print("Dry mass is:", round(dry_m,4))
str_m=.11*dry_m
print("str_m=",round(str_m,3))
the_m=.02*dry_m
print("the_m=",round(the_m,3))
pow_m=.17*dry_m
print("pow_m=",round(pow_m,3))
tt_m=.15*dry_m
print("tt_m=",round(tt_m,3))
adcs_m=.08*dry_m
print("adcs_m=",round(adcs_m,3))
pro_m=.17*dry_m #we add three more to make it to 100%
print("pro_m=",round(pro_m,3))
mar_m=.1*dry_m
print("mar_m=",round(mar_m,3))
Tot_m=pay_m+str_m+the_m+pow_m+tt_m+adcs_m+pro_m+mar_m
print("Total Mass inlcuding the 10% margin (kg):", round(Tot_m,4))

```

### 8.5.2 Script for Delta V ( $\Delta v_{design}$ )

```

import numpy as np
import sympy as sp
import math

def deltaV_design(phi, alpha, altitude, launchsite, losses):
    mu_e = 398600.5
    r_e = 6378.137
    V_bo = np.sqrt(mu_e/(r_e+altitude))
    beta = np.degrees(np.arcsin(np.cos(np.radians(alpha))/np.cos(np.radians(launchsite))))
    V_ls = 465.1*np.cos(np.radians(launchsite))/1000
    dV_g1 = np.sqrt((2*mu_e*altitude)/(r_e*(r_e+altitude)))
    dV_needed = np.array([-V_bo*np.cos(np.radians(phi))*np.cos(np.radians(beta)), V_bo*np.

```

```

dV_design = np.linalg.norm(dV_needed) + losses
return dV_design

alt=[800, 850, 900, 950, 1000, 1100, 1200]
alpha=[30, 32, 35, 40, 45, 52, 52] #inclination
phi=0 #circular orbit so flight path angle is assumed close to zero
launchsite=28 #kenedy space center
loss=.9
for k in range(np.size(alt)):
    print("\nFor altitude = ", alt[k])
    for i in range(np.size(alpha)):
        print('If alpha(inclination) is:', alpha[i], 'then Vdeesign is:', round(deltaV_desi)

```

### 8.5.3 Script for Attitude Determination and Control

```

import numpy as np
import sympy as sp
import math

Imax = 55
Imin = 30
MomentArm = 0.3
ResidualDipole = 2
FrontalSA = 1
mu_e = 398600.5
r_e = 6378.137
Altitude = 700
R = Altitude + r_e
magLat = 10
VrelativeX = -1.006320
VrelativeY = -1.225255
VrelativeZ = 7.427699
Vrelative = np.sqrt(VrelativeX**2 + VrelativeY**2 + VrelativeZ**2)

Tg = 3 * mu_e * (Imax - Imin) / (R**3)
print(f'The maximum gravity gradient torque per degree is {Tg}')

AD = 1.47e-13
Cd = 3

```

```
F = 0.5 * AD * Cd * FrontalSA * Vrelative
Ta = MomentArm * F
print(f'The magnitude of the maximum drag torque is {Ta}')
```

```
B0 = 3.12e-5
B = B0 * ((r_e / R)**3) * np.sqrt(1 + (3 * (np.sin(np.radians(magLat))**2)))
Tm = ResidualDipole * B
print(f'The magnitude of the maximum magnetic torque is {Tm}')
```

```
Fs = 1378
c = 3e8
As =
q = 0.6
i =
F2 = (Fs * As * (1 + q) * np.cos(np.radians(i))) / c
Ts = MomentArm * F2
print(f'The magnitude of the maximum solar pressure torque is {Ts}')
```

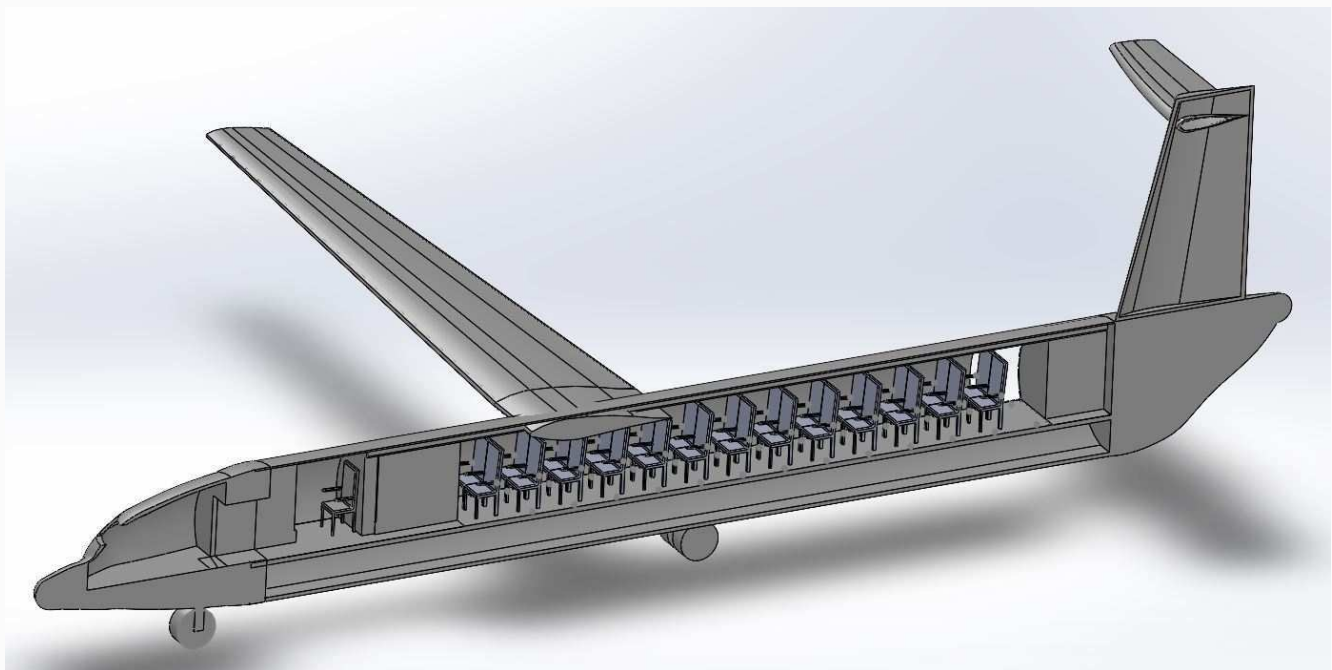
## References

- [1] AGI Solutions. *Systems Tool Kit ( STK )*. 2021. URL: <https://licensing.agi.com/stk/>.
- [2] Daniel Cipera. “Comparison of Traditional Versus Cubesat Remote Sensing: a Model-Based Systems Engineering Approach”. In: (2018).
- [3] Wei Cui and Luca Caracoglia. “Exploring hurricane wind speed along US Atlantic coast in warming climate and effects on predictions of structural damage and intervention costs”. In: *Engineering Structures* 122 (2016), pp. 209–225. ISSN: 18737323. DOI: 10.1016/j.engstruct.2016.05.003. URL: <http://dx.doi.org/10.1016/j.engstruct.2016.05.003>.
- [4] Endurosat. *Onboard Computer (OBC) — CubeSat by EnduroSat*. URL: <https://www.endurosat.com/cubesat-store/cubesat-obc/onboard-computer-obc/> (visited on 05/04/2022).
- [5] EoPortal. “CubeSat - Launch 1”. In: (2002), pp. 1–13. URL: <https://earth.esa.int/web/eoportal/satellite-missions/c-missions/cubesat-launch-1>.
- [6] Space Flight. “Commerical Space Launch Schedule and Pricing”. In: *Space Flight* (). URL: <https://web.archive.org/web/20151016001943/http://www.spaceflightindustries.com/schedule-pricing/>.
- [7] Wiley J Larson and James R. Wertz. *Spacecraft Mission Analysis and Design*. 1999, p. 1008. ISBN: 1881883108. URL: [https://the-eye.eu/public/WorldTracker.org/Space/Space%20Engineering/Space\\_Mission\\_Analysis\\_and\\_Design.pdf](https://the-eye.eu/public/WorldTracker.org/Space/Space%20Engineering/Space_Mission_Analysis_and_Design.pdf).
- [8] NASA. “2018 NASA Strategic Plan”. In: (2018), Strategic Goal 1. URL: <https://www.nasa.gov/image-feature/us-flag-in-the-cupola>.
- [9] NASA. “Cubesat. 101: Basic Concepts and Processes for First-Time CubeSat Developers”. In: *NASA and California Polytechnic State University* October (2017), p. 86.
- [10] NASA. “NASA Cubesat Launch Initiative CLI”. In: *Space Operations* (2013), pp. 1–13. URL: [https://www.nasa.gov/directorates/somd/home/CubeSats\\_initiative.html](https://www.nasa.gov/directorates/somd/home/CubeSats_initiative.html).
- [11] NASA. “Past Elana CubeSat Launches”. In: (2022). URL: <https://www.nasa.gov/content/past-elana-cubesat-launches>.
- [12] Swedish Weather Sat. “Freja 6U Sat”. In: (1986). URL: <http://www.svengrahn.pp.se/histind/Swefirst/Satellitedetails/Freja/FrejaFacts.htm>.
- [13] SatCatalog. *MPS-130-2U - Monopropellant System — SatCatalog*. URL: <https://www.satcatalog.com/component/mps-130-2u/> (visited on 05/02/2022).
- [14] SpaceX Flacon-9. “Falcon-9-Users-Guide-2021-09-3”. In: [www.spacex.com](http://www.spacex.com) 09-3 (2021).

# PROJECT TWO

# PROJECT MORBIUS

---



## AIAA 50-PASSENGER HYBRID ELECTRIC TURBOPROP

*Proposal for the American Institute of Aeronautics and Astronautics*  
October 20<sup>th</sup>, 2022

# PROJECT MORBIUS

---

## Team Structure

<sup>1</sup>Eyob Ghebreiesus <sup>2</sup>James Szewczyk <sup>3</sup>Marek Jelen <sup>4</sup>Matt Tobin

<sup>1</sup> Lead Systems Engineer, Aerodynamics, Trade Studies & Optimization, Dynamic Stability & Control.

<sup>2</sup> Propulsion Lead, Avionics, Deputy for Structures & Integration

<sup>3</sup> Cost Analysis Lead, Efficiency Merit & Quality Control

<sup>4</sup> Structures Lead, CAD Drawing, Landing Gear & Material Selection.

Homepage: *Project Morbius*

Created on *August 25<sup>th</sup>, 2022*

Published on *October 20<sup>th</sup>, 2022*

Copyright © 2022

All rights reserved. This Lab report or any portion thereof may not be reproduced or used in any manner whatsoever without the express written permission of the publisher except for the use of referencing for educational purposes.

The above copyright notice and this permission notice shall be included in all copies or substantial portions of the document.

Produced via LaTeX, Inc U.S.A.

MIT License for the GitHub Project, 2022

*github.com/eyobghiday/project-morbius*

Department of Mechanical, Materials and Aerospace Engineering

ILLINOIS INSTITUTE OF TECHNOLOGY

# Contents

<b>1</b>	<b>Introduction</b>	<b>1</b>
1.1	Project Summary . . . . .	1
1.2	Team Organisation . . . . .	1
<b>2</b>	<b>Mission Overview</b>	<b>1</b>
2.1	Mission Requirements . . . . .	2
2.2	Initial Sizing . . . . .	2
2.3	Baseline Plane Dimension . . . . .	5
<b>3</b>	<b>Trade Study</b>	<b>5</b>
3.1	Aspect Ratio and Wing Loading . . . . .	5
3.2	T-W vs W-S Optimization . . . . .	6
3.3	VN Diagram . . . . .	6
<b>4</b>	<b>Aerodynamics</b>	<b>9</b>
4.1	Airfoil Selection . . . . .	9
4.2	Main Wing . . . . .	9
4.3	Flaps and Slats . . . . .	10
4.4	Tail Configuration . . . . .	11
4.5	Optimization . . . . .	13
<b>5</b>	<b>Propulsion</b>	<b>13</b>
5.1	Hybrid Engine Configuration . . . . .	13
5.2	Battery Sizing . . . . .	15
5.3	Efficiencies . . . . .	16
5.4	Integration . . . . .	18
5.5	Engines . . . . .	19
<b>6</b>	<b>Stability &amp; Control</b>	<b>19</b>
6.1	Weight & Balance . . . . .	19
6.2	Static Margin . . . . .	20
6.3	Longitudinal Stability . . . . .	20
6.4	Lateral Stability . . . . .	21
6.5	Empty vs Full Weight . . . . .	22
<b>7</b>	<b>Structures</b>	<b>23</b>
7.1	Material Selection . . . . .	23
7.2	Fuselage . . . . .	24

7.3	Landing Gear . . . . .	24
7.4	CAD Drawing . . . . .	24
<b>8</b>	<b>Cost Analysis</b>	<b>30</b>
8.1	2022 Adjustments . . . . .	30
8.2	R&D Cost . . . . .	30
8.3	Operation & Maintenance . . . . .	30
8.4	Pricing and Revenue . . . . .	31
<b>9</b>	<b>Conclusion</b>	<b>32</b>
9.1	Efficiency Merit . . . . .	32
9.2	Conclusion . . . . .	32
<b>10</b>	<b>Appendix</b>	<b>33</b>
10.1	Codes and Scripts . . . . .	33
<b>List of Figures</b>		<b>36</b>
<b>List of Tables</b>		<b>36</b>
<b>Abbreviations</b>		<b>37</b>
<b>References</b>		<b>37</b>

# 1 Introduction

This report contains the conceptual design, analysis, and preliminary design of a hybrid engine turboprop aircraft. World renowned aircraft maker, Embraer released its most recent market outlook on turboprops and has estimated a demand for 1,080 turboprops around the world. This demand was seen to be led by Asia Pacific China, and US, with 490 aircraft allocated there [3]. Europe was the next largest segment, with 190 aircraft forecasted. For its own aircraft, due to enter into service in 2027-2028, it estimated demand of around 500 units alone from the company.

## 1.1 Project Summary

This project dubbed "IMT-22" short for It's Morbin Time 2022, is a hybrid turboprop aircraft designed for commercial air travel at an economic fare. Turboprop's generally strike a balance between the features of both piston-prop and turbojet airplanes. The specifications for this airplane design is carefully chosen, keeping with the guidelines proposed under the FAA 14 Part-25, ICOA Code-B and Code-C. This conceptual design report details each step of the design, analysis and optimizing process. Here the aerodynamic performances are explored, followed by stability, propulsion, and structural integrity to produce an optimal aircraft. The IMT-22 is expected to enter the market by 2035.

## 1.2 Team Organisation

The team is made of four members in total and their roles are shown in Table 4.1. Each role has a lead and a deputy that represent their significance and the tasks delegated.

**Table 1.1 – Team Organization Chart**

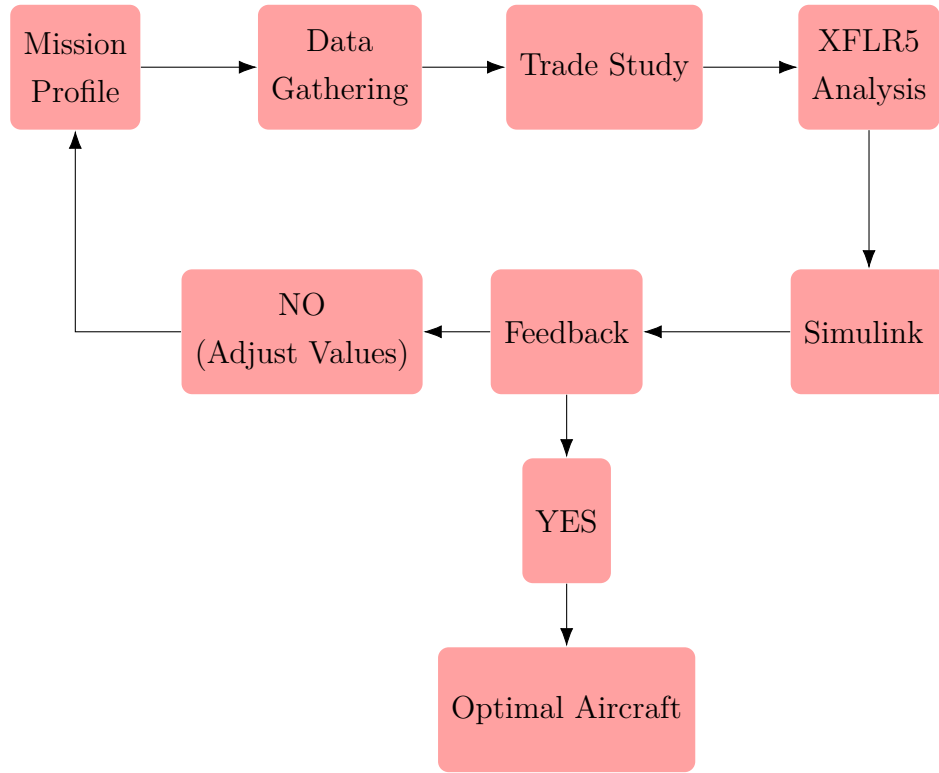
Subsystem	Lead	Deputy
Spokesperson	James Szewczyk	–
Aerodynamics	Eyob Ghebreiesus	James Szewczyk
Propulsion	James Szewczyk	Matthew Tobin
Structures	Matthew Tobin	James Szewczyk
Stability	Eyob Ghebreiesus	James Szewczyk
Cost Analysis	Marek Jelen	Eyob Ghebreiesus
Trade Studies	Eyob Ghebreiesus	James Szewczyk

# 2 Mission Overview

To ensure our project results in designing an effective and efficient aircraft, we have made a project plan to provide the best output parameters in Figure 2.1. After initial mission definition, and requirements the project is closely followed by historical studies. Numerous data for existing turboprop aircrafts were collected firsthand. This data will be used to compare performance metrics of IMT-22 with existing planes. Once we select the design metrics like Aspect Ratio,

Take off Weight, Wing Loading, we use Python scripts, Initial sizing Matrix and other methods to graph the data and see where we land. After that we proceed into XFLR5 Airfoil analysis to test the values in the simulation. After reading the feedback from the simulation; if the findings are feasible, we proceed to component design phase. If not, we go back to refine our mission definition and operational requirements. This is an agile project managing system where we select the performance parameters and perceive the coverage, operation orbit and bypass simultaneously to decide the best fit. This allows us to be flexible with the little time provided.

**Figure 2.1 – Project Flow**



## 2.1 Mission Requirements

Our mission begins with developing new regional aircraft to satisfy the 50-seat portion of the market that meets the US domestic that has significantly better fuel burn and economics than existing options. The overall goal is to be at least 20% better than existing 50 seat regional turboprops in 500nmi block fuel per seat with a cost to build that is comparable to the existing aircraft, including the hybrid propulsion system. The specific requirements are listed below in Table 2.1.

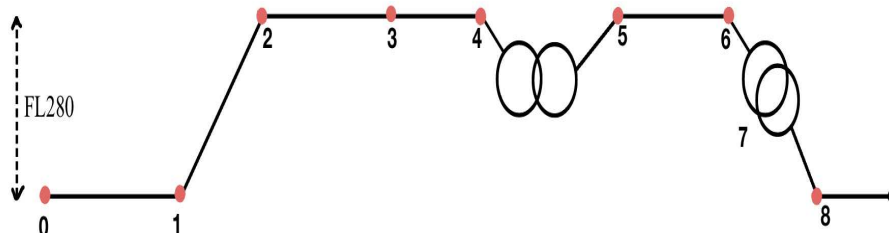
## 2.2 Initial Sizing

As per the requirements listed in Table 2.1, the team proceeded on to look at currently existing turboprops to understand their performances. In order to improve the efficiency of hybrid engines,

**Table 2.1 – Specification Requirements**

Requirements	Value
Passengers	50+/-4
Range (R)	1000nmi
Distance to Climb to Cruise Altitude	200nmi
Crew (2 pilots + 1 member)	3
Approach Speed ( $V_{app}$ )	141KN
Min Cruise ( $V_{cruise}$ )	275KTAS
Target Cruise ( $V_{cruise}$ )	350KTAS
Max Takeoff Distance( $S_{TO}$ )	4500ft
Max Landing Distance( $S_{Landing}$ )	4500ft
Loiter Time	45min
Flying Altitude (FL280)	28,000ft
Pressurization Altitude	5,000ft
Min Seat Width	17.2in
Target Seat Width	18in
Max Wing Span (ICAO Code B)	78.8ft
Max Wing Span (ICAO Code C)	118.11ft
Carbon Reduction amount	20%
Entry Into Service (EIS)	2035
Certification Base	FAA-14 Part 25

and attain the required target, a mission profile is defined in Figure 2.2 to estimate weight fractions.

**Figure 2.2 – Mission Profile**

Where:

- 0 - 1: Engine Taxi/Takeoff
- 1 - 2: Climb
- 2 - 3: Cruise (Turbine Powered)
- 3 - 4: Cruise (Electric Powered)
- 4 - 5: Loiter (45m minute)
- 5 - 6: Diversion Cruise
- 6 - 7: Diversion Loiter (20 min)
- 7 - 8: Land

The mission profile accounts for additional diversion in case a first landing attempt is deemed

impossible. It also serves as a safety factor, providing better aircraft analysis for commercial purposes. The electric cruise section is placed at the end of the expected cruise segment to maximize range from the electric propulsion. The segment cannot be done before the diversion, as the crew would not have knowledge of the additional cruise section prior to the diversion.

Now that we have our mission profile, the weight fractions are calculated for each mission profile in Table 2.2. Note that since the aircraft is hybrid, some of the coefficients had to be adjusted instead of just using Raymer's values. A more detailed explanation of the electrical values is found in the Propulsion 5 section.

**Table 2.2 – Mission Weight Fractions**

Section	Fraction	Value	Notes
Taxi/Takeoff	$\frac{w_1}{w_0}$	1	Fully Electric
Climb	$\frac{w_2}{w_1}$	0.985	Raymer
Main Cruise	$\frac{w_3}{w_2}$	0.946	55.7% Turboprop Engine
Electric Cruise	$\frac{w_4}{w_3}$	1.00	44.3% Fully Electric
Loiter for Planned Landing	$\frac{w_5}{w_4}$	0.978	Raymer
Diversion Cruise	$\frac{w_6}{w_5}$	0.986	Breguet's Range
Diversion Loiter	$\frac{w_7}{w_6}$	0.99	Breguet's Endurance
Landing	$\frac{w_8}{w_7}$	1.00	Fully Electric
Hybrid Efficiency	$\eta_{hyb}$	0.91	Empirical
Fuel Mass Fraction	$\frac{w_f}{w_0}$	0.201	Multiplying Fractions

Data from current existing turboprop regional transports average a cruise SFC of 0.477. The SFC target is around 0.3816 lb/hr for cruise and an SFC of .32 for loiter. This SFC follows the expected increase in fuel efficiency of the recent Pratt and Whittney 127XT series turboprops. The 127XT series are already 18% more efficient than the current regional turboprop engines, with most using the PW150 series. With a 2% further increase in efficiency expected in the next decade, the SFC's targeted should be attainable before the 2035 delivery date.

$$SFC_{target} = 0.80 * SFC_{known} = 0.80 * 0.477 = 0.3816$$

From Raymer's Table 3.1, the empty weight fraction for a twin turboprop aircraft accounted for composite material structure (factor of 0.95) is:

$$\frac{W_e}{W_0} = 0.95 * 0.96 * W_0^{-0.05}$$

Now using Raymer's Equation 3.4, accommodating our battery and crew as total payload our estimated  $W_0$  becomes:

$$W_0 = \frac{W_{crew} + W_{battery}}{1 - \frac{W_f}{W_0} - \frac{W_e}{W_0}} = \frac{12260 + 6288}{1 - 0.201 - 0.95 * 0.96(W_0)^{-0.05}} = 68343 \text{lb}$$

With the mission weight fraction listed in Table 2.2 the summary of the calculated value is listed below.

**Table 2.3 – Summary of Weights**

Category	Note	lbf
Crew Weight	$w_{crew}$	660
Passenger Payload	$w_{pass}$	12000
Fuel Weight	$w_{fuel}$	13941
Battery Weight	$w_{bat}$	6288
Empty Weight	$w_e$	35723
Max Gross Takeoff	$w_0$	68343

## 2.3 Baseline Plane Dimension

Therefore our baseline plane dimension will be as shown in Table 2.4.

**Table 2.4 – Baseline Plane Dimensions**

Category	Note	lbf
Crew Weight	$w_{crew}$	660
Passenger Payload	$w_{pass}$	12000
Fuel Weight	$w_{fuel}$	13941
Battery Weight	$w_{bat}$	6288
Empty Weight	$w_e$	35723
Max Gross Takeoff	$w_0$	68343
Aspect Ratio	$AR$	11.5
Thrust to Weight	$\frac{T}{W_0}$	0.205

## 3 Trade Study

### 3.1 Aspect Ratio and Wing Loading

It is known that Aspect Ratio greatly affects the wing loading and lifting capability. Aspect ratio is wing span divided by the wing area. But to determine the best AR (greater than 9 at least – Raymer [8]) we need to determine our wing loading. Raymer's Table 5.4 provides wing loading for turbo prop ( $40 \frac{lbf}{ft^2}$ ), but those values are based on very old data and are low when compared to currently existing turboprops. First hand most older turboprops are flying at Mach=0.44, However the required cruise Mach for this design is 0.53-0.58 @ 28,000 altitude. Thus in order to meet the required specification we plotted *Span* vs  $W_0$  to study the *Wingloading* for several existing turboprop planes (see Figure 3.1a). For the baseline maximum gross take off weight of  $W_0 = 68343 \text{ lbs}$  and an AR of 12 we got around ( $80 \frac{lbf}{ft^2}$ ) wing loading. This in return sets our wing span to be about  $b = 102 \text{ ft} (30 \text{ m})$  or which is within the limits of ICOA Code-C requirement. This way we can relieve some of the wing loading (green shade) overhead without having to increase the

overall cost of the plane.

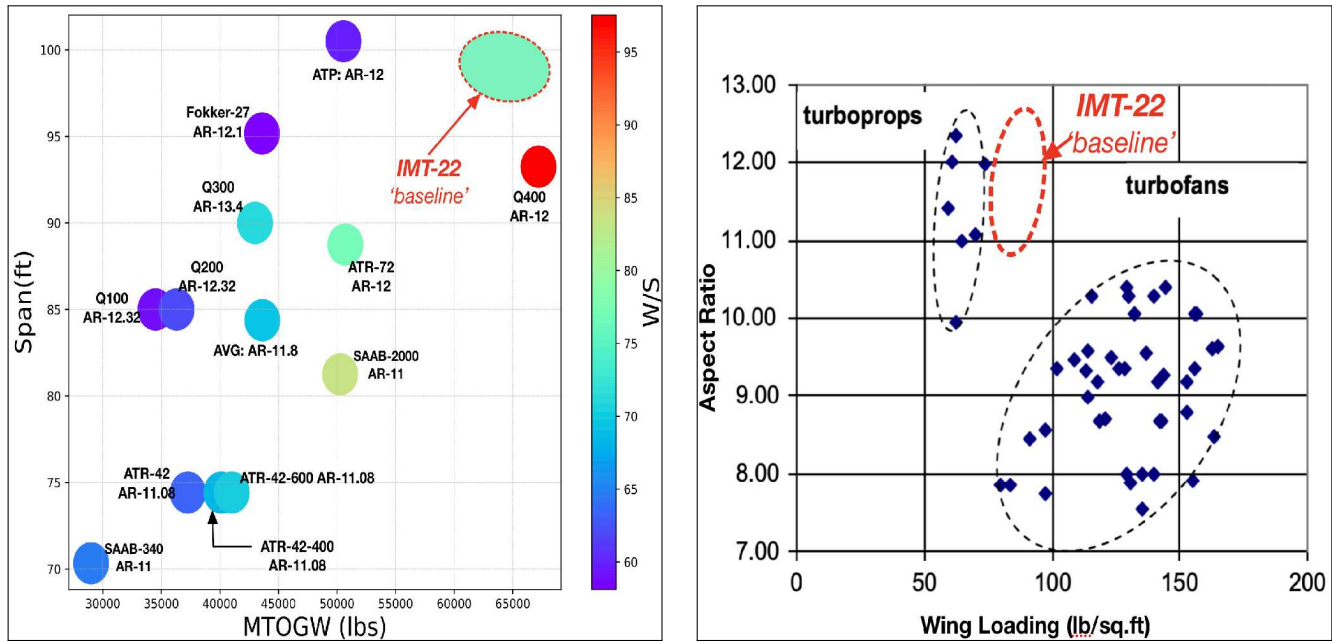


Figure 3.1 – Aspect Ratio and Wing loading

### 3.2 T-W vs W-S Optimization

Like Raymer said, the  $\frac{T}{W}$  vs  $\frac{W}{S}$  is the "granddaddy" of the trade studies [8]. For this design trade, the approach speed ( $V_{app} \leq 141kn$ ), take off distance  $S_{to} \leq 4500ft$  and fuel reduction  $F_{red} \geq 20\%$  are used as constraints based on the report specification (see Table 3.1). The baseline highlighted in center is obtained from the initial trade studies, the rest are computed iteratively by varying the wing loading and thrust to weight values. Refer to the codes in the Appendix 10 section.

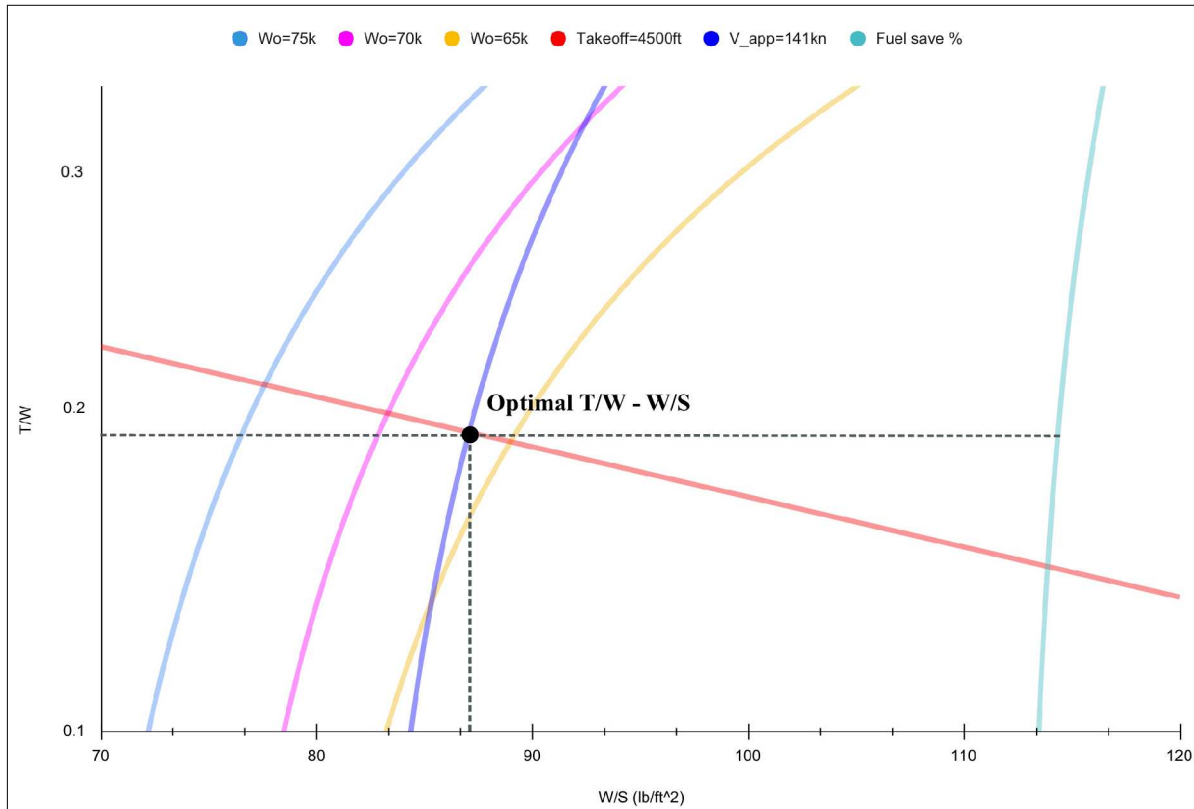
Now that we plot our design trade studies in Figure 4.3, the optimal combination of T/W and W/S is found from the intersection of the constraints. It shows that the initial estimation were shy away from the optimal values.

### 3.3 VN Diagram

The flight envelope defines operational limits for an aerial platform with respect to maximum speed and load factor given a particular atmospheric density. For the IMT-22 an aircraft cruises at 590ft/s (180m/s) as seen in the Figure 3.3. If it's flying anywhere outside the envelope lines it may suffer some structural damage, thus the limits should therefore never be exceeded. The blue dashed line represents the the limit of vertical gust load during cruise and the red dashed line indicates the limit of vertical gust at dive speed.

**Table 3.1 – Optimization Parameters**

$\frac{T}{W} = 0.255$	$W_0 = 61419/lb$ $V_{app} = 130.0/kn$ $S_{to} = 2356/ft$ $F_{red} = 28.6\%$	$W_0 = 69752/lb$ $V_{app} = 137.7/kn$ $S_{to} = 2675/ft$ $F_{red} = 27.7\%$	$W_0 = 78086/lb$ $V_{app} = 145.7/kn$ $S_{to} = 2995/ft$ $F_{red} = 26.9\%$
$\frac{T}{W} = 0.205$	$W_0 = 60009/lb$ $V_{app} = 127.7/kn$ $S_{to} = 2961/ft$ $F_{red} = 20.8\%$	$W_0 = 68343/lb$ $V_{app} = 136.3/kn$ $S_{to} = 3372/ft$ $F_{red} = 27.8\%$	$W_0 = 76676/lb$ $V_{app} = 144.4/kn$ $S_{to} = 3783/ft$ $F_{red} = 27.0\%$
$\frac{T}{W} = 0.155$	$W_0 = 58612/lb$ $V_{app} = 126.2/kn$ $S_{to} = 4053/ft$ $F_{red} = 28.9\%$	$W_0 = 66947/lb$ $V_{app} = 135.0/kn$ $S_{to} = 4630/ft$ $F_{red} = 27.9\%$	$W_0 = 75279/lb$ $V_{app} = 143.1/kn$ $S_{to} = 5206/ft$ $F_{red} = 27.2\%$
	$\frac{W}{S} = 72 \frac{lb}{ft^2}$	$\frac{W}{S} = 82 \frac{lb}{ft^2}$	$\frac{W}{S} = 92 \frac{lb}{ft^2}$

**Figure 3.2 – Design Trade  $\frac{T}{W} - \frac{W}{S}$** 

Now that we have our optimal configuration listed in Table 3.2, we move forward to the detail design phase.

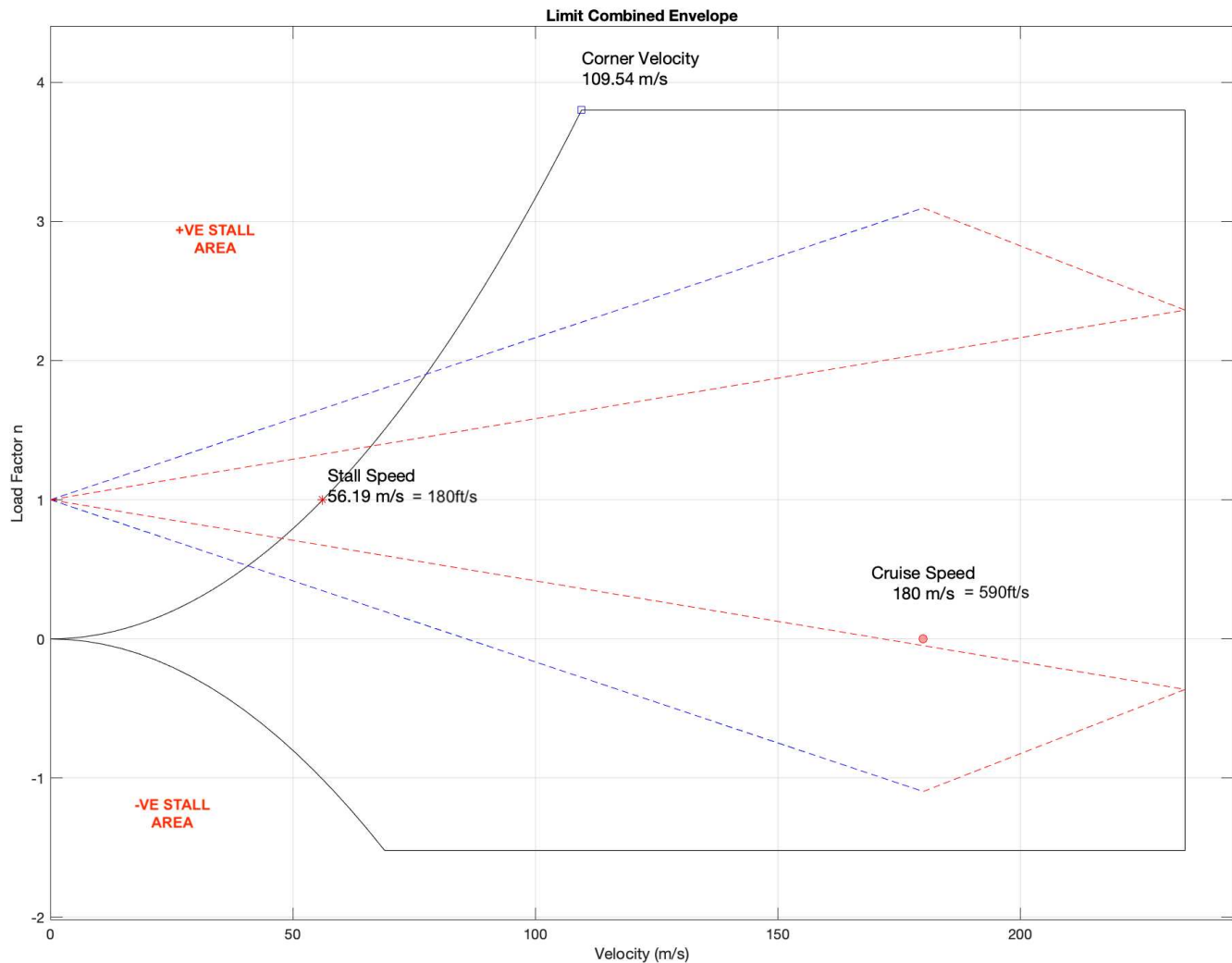


**Figure 3.3 – V-n diagram)**

**Table 3.2 – Optimal Plane Configuration**

Category	Notation	Unit	$\pm\%$ error
Crew Weight	$w_{crew}$	660 lb	$\pm 2\%$
<i>Passenger Payload</i>	$w_{pass}$	12000 lb	$\pm 3\%$
Fuel Weight	$w_{fuel}$	13941 lb	$\pm 3\%$
Battery Weight	$w_{bat}$	lb	$\pm 1\%$
Empty Weight	$w_e$	35723 lb	$\pm 3\%$
Max Gross Takeoff	$w_0$	68000 lb	$\pm 2\%$
Wing Loading	$\frac{w_0}{S}$	$86 \frac{lb}{ft^2}$	$\pm 4\%$
Aspect Ratio	$AR$	12	
Wing Span	$b$	97 ft	$\pm 5\%$
Thrust to Weight	$\frac{T}{w_0}$	0.18	$\pm 1\%$

## 4 Aerodynamics

### 4.1 Airfoil Selection

The airfoil selected for the proposed design depends upon the cruising speed, which in turn is related to the powerplant chosen. The target  $V_{cruise}$  is 350kts ( $Mach = 0.53$ ) for this project. Sweepback is unnecessary in this speed range so aspect ratios can be high ( $\geq 10$ ).

From Raymer's Equation 4.5 we get our  $Cl_{design}$  as:

$$Cl_{design} = \frac{1}{q} * \frac{W}{S} \approx 0.2 \quad (4.1)$$

Additionally from Raymer[8] Figure 5.3 our maximum lift coefficient for a single slotted flap is about  $CL_{max} = 2.1$ . Therefore, the  $Cl_{design} = 0.2$  multiplied by 10 tells us our airfoil number. The third digit starts with 2 and the last couple of digit's possible between 15-18% as a the root airfoil. Based on those values We narrowed down the list of airfoils to NACA 6-series and NACA-4 series for this aircraft. The NACA 6-series have smaller leading edge radii than the NACA 4-series and the NACA 5-series airfoils [9]. Keep in mind that due to XFLR limitation these airfoils are selected based on analysis of  $Re = 9 * 10^6$  for XFLR.

**Table 4.1** – Aifoils Considered

44XX	63XXXX	64XXXX
NACA-4415	NACA-63(3)218	NACA-64(2)415

It is recommended that the airfoil selected be chosen both on the value of  $Cl_{max}$  and upon the post stall variation of cl with angle of attack. An abrupt drop in section lift coefficient is to be avoided, and the airfoil with the smallest decrease in  $Cl$  for angles of attack above the stall is highly desirable, even at the expense of a smaller value of  $Cl_{max}$ .

Therefore NACA-63218 is the suggested airfoil section for the main wing because of its favorable stall characteristics.

The maximum thickness of the 4- and 5-digit airfoils is at 30% chord. The position of the maximum thickness of the 63, 64, and 65 series is located progressively aft. The 63 series airfoils might be considered for the turboprop aircraft. It is also possible to investigate those airfoil sections used by the competition (market survey aircraft) to aid in justifying the choice of airfoil.

### 4.2 Main Wing

For turboprops, a simple and efficient wing geometry is preferred [8]. Tapered wing generally have closer efficiency (78-80%) to that an elliptic wing (85%). Main factors that needed consideration were the Lift, Engine height clearance (turboprop) and ease of manufacturing. A typical trape-

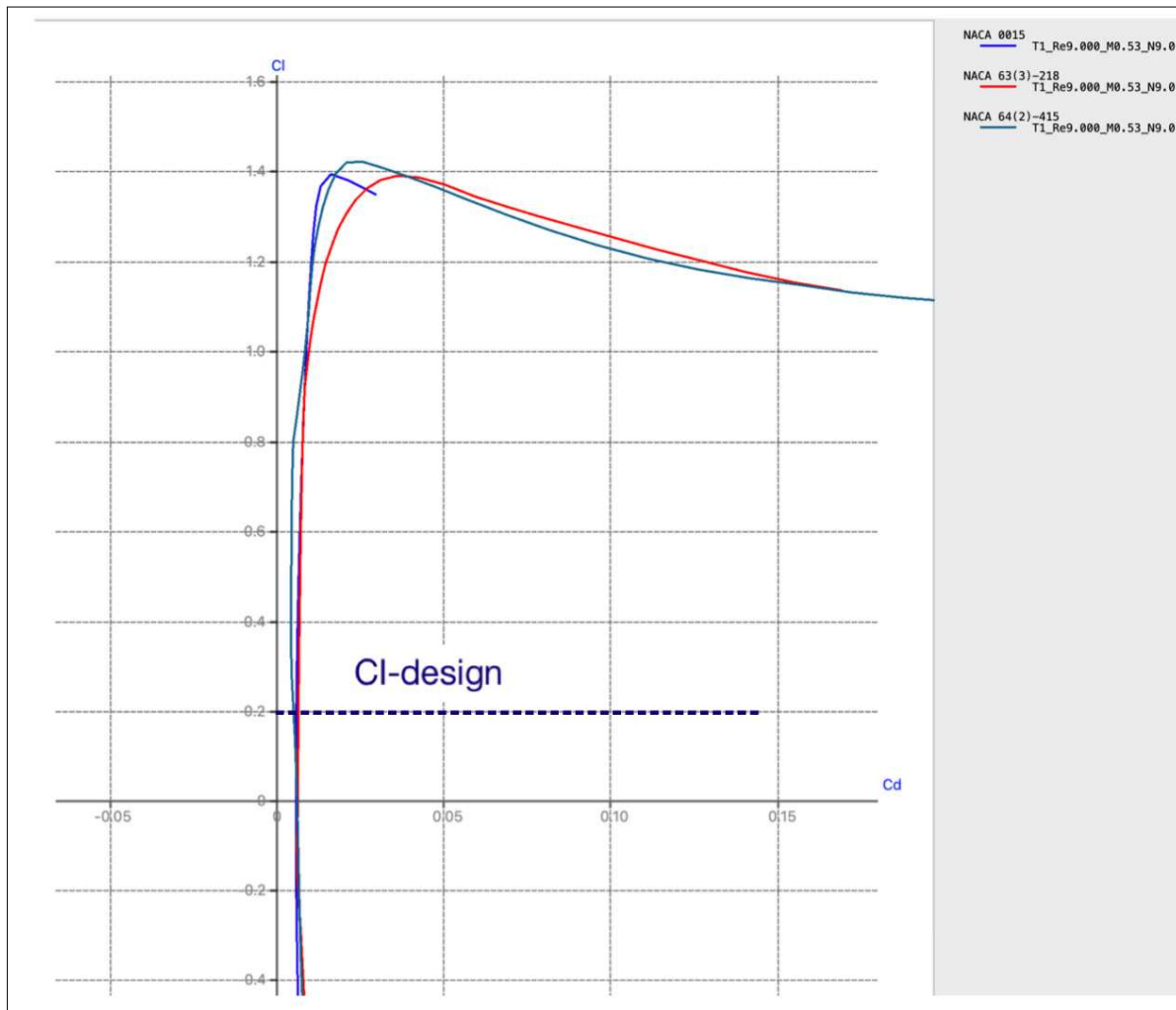


**Figure 4.1 –  $C_l$ . vs.  $C_d$  at design Limit**

Zoidal plan form requires the wing root and tip have different airfoil sections. This is because thicker airfoils at the root are necessary to accommodate the high wing root bending moment. On the other hand the tip airfoil thickness can be reduced for better airfoil performance due to much lower bending moments. Since there is no twist, the amount of lift produced by each wing section will be proportional to the chord length keeping the aircraft stable and steady. Additionally, the wing will have a dihedral angle of  $\Gamma = 4$  to factor in the stability of the aircraft about the roll axis. Table 7.1 shows the summary of our tapered wing dimension.

### 4.3 Flaps and Slats

IMT-22 will utilise a slotted flap. Typically the flap depth  $c_F$  amounts to about 30% of the chord. The slotted flap increases lift by increasing the airfoil camber. Ailerons, elevators and rudders will be slotted flaps for this aircraft. This setting would accommodate the slightly small  $C_l$  values to about  $CL_{max} = 2.1$  hitting that required high lift during landing and takeoff.

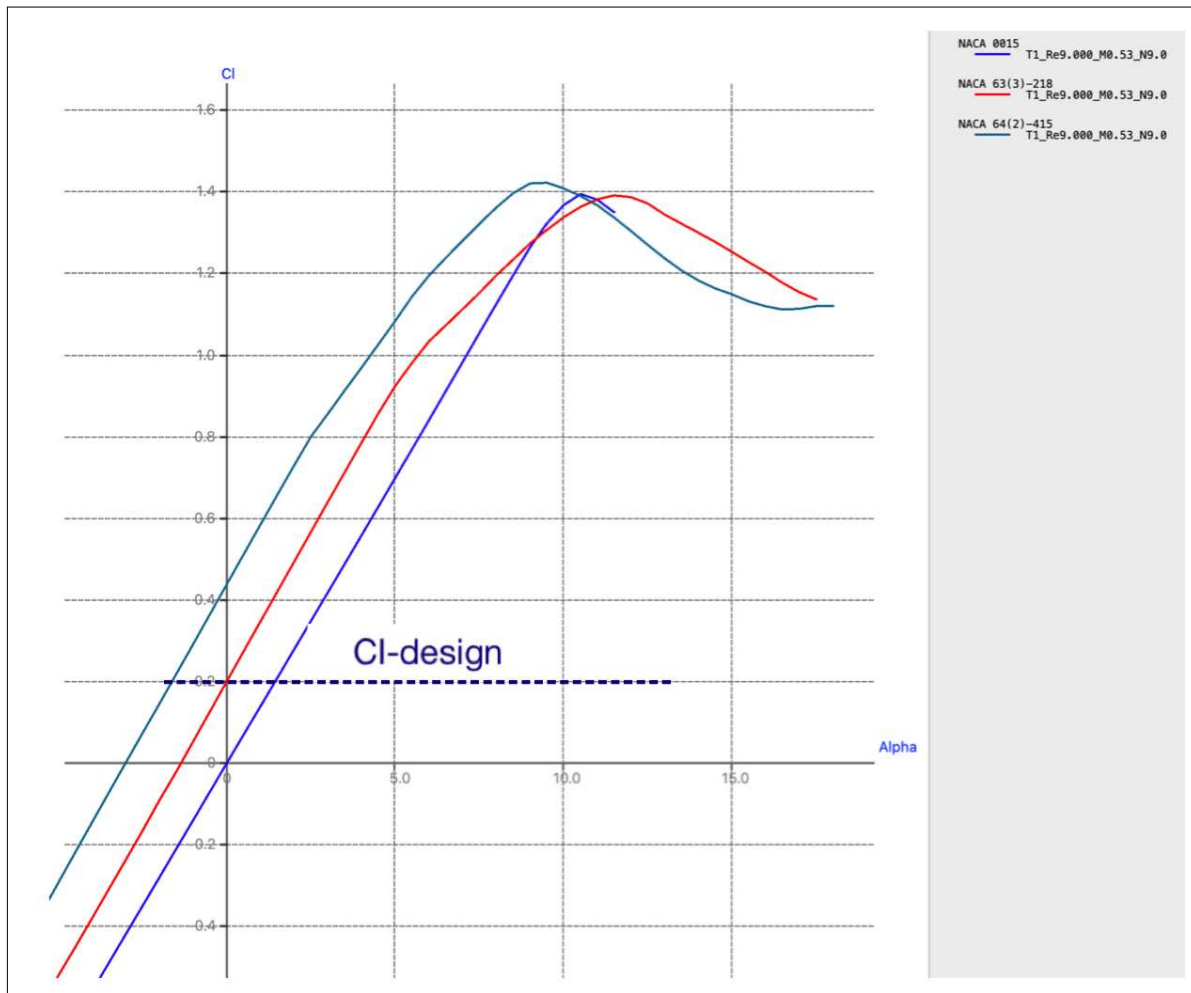


**Figure 4.2 –  $Cl$ . vs Alpha**

**Table 4.2 – Wing Specification**

Parameter	Value	Parameter	Value
Root Airfoil	NACA: 63(3)-218	Aspect Ratio ( $AR$ )	12
Root Airfoil	NACA: 63(3)-215	Taper Ratio ( $\lambda$ )	0.45
Span ( $b$ )	100.2ft	Dihedral Angle ( $\Gamma$ )	4-deg
Root Chord	11.2ft	Sweep Angle ( $\delta$ )	0
Tip Chord	5.04ft	Max $\frac{t}{c}$	24%
Total Area	790ft <sup>2</sup>	$X_{Loc}$	37

## 4.4 Tail Configuration

Four different tail configurations were considered for this aircraft. Stability, Ease of Manufacture and drag. Table 4.3 is a selection matrix that compares each of this based on weights. T-Tail's greatest advantage is keeping the elevators out of the disturbed airflow from the wing and fuselage. This also allows for improved glide ratio.

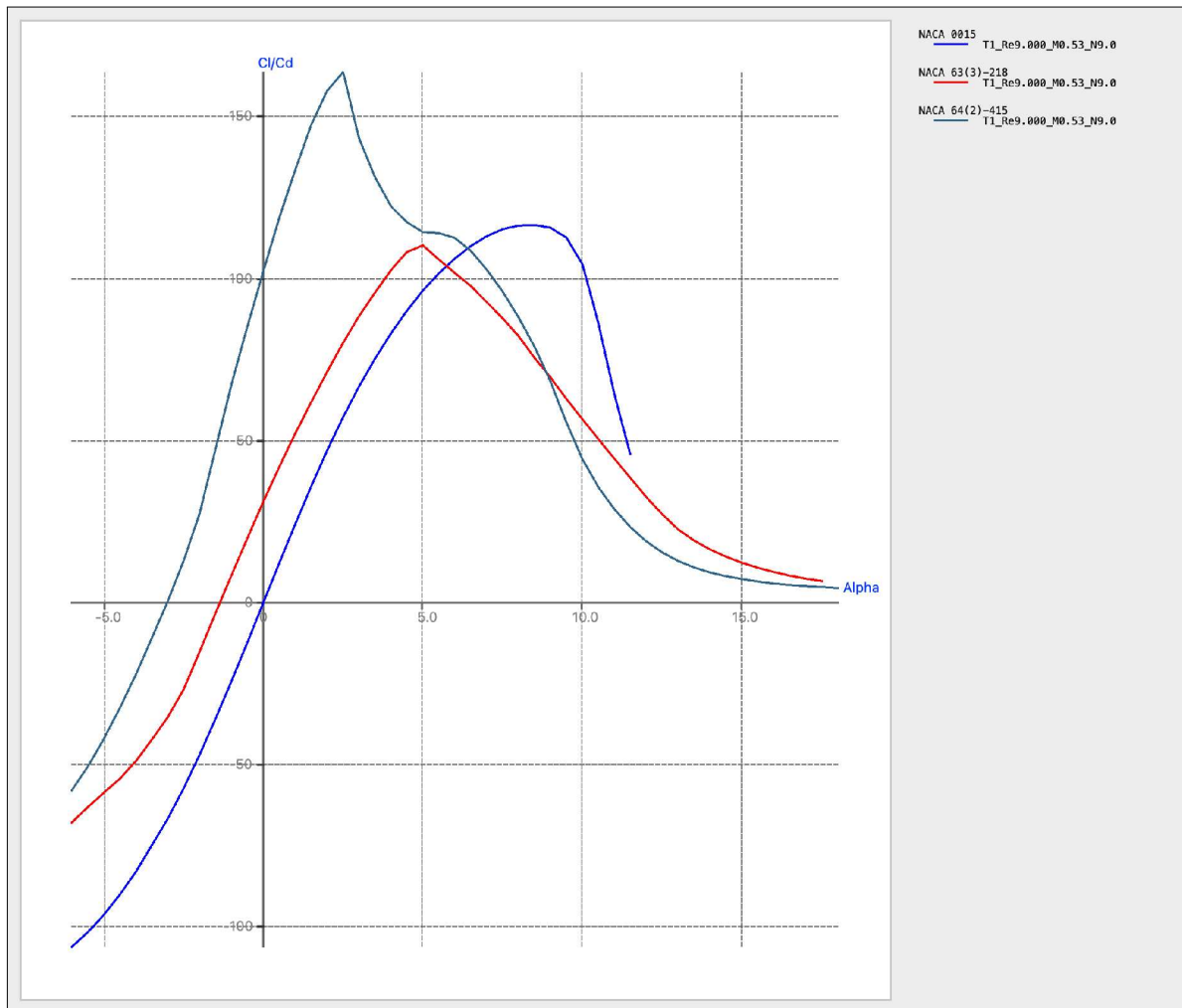


**Figure 4.3 –  $Cl/Cd$  vs.  $\alpha$**

**Table 4.3 – Tail Configuration Matrix**

Criteria	Weight	V-Tail	H-Tail	T-Tail	Conventional
Manufacturing	20	1	3	4	3
Stability	30	1	4	3	2
Drag	50	4	1	2	1
<b>Total</b>	<b>100</b>	<b>250</b>	<b>250</b>	<b>270</b>	<b>170</b>

For both Horizontal tail NACA0012 airfoil has been chosen. For vertical tail NACA0015 airfoil has been chosen.

#### 4.4.1 Horizontal

Summary of the Horizontal Tail:

**Table 4.4 – Horizontal Tail**

Parameter	Value	Parameter	Value
Root Airfoil	NACA-0012	Aspect Ratio ( $AR$ )	5.4
Tip Airfoil	NACA-0012	Taper Ratio ( $\lambda$ )	0.6
Span( $b$ )	26.25ft	Incidence Angle ( $\Gamma$ )	-1.5
Root Chord	6.1ft	Sweep Angle ( $\delta$ )	0
Tip Chord	3.66ft	Max $\frac{t}{c}$	12%
Total Area	127.97ft <sup>2</sup>	$X_{Loc}$	55.8ft

#### 4.4.2 Vertical

Similarly below is a summary of the vertical Tail:

**Table 4.5 – Vertical Tail**

Parameter	Value	Parameter	Value
Root Airfoil	NACA-0015	Aspect Ratio ( $AR$ )	3.9
Tip Airfoil	NACA-0015	Taper Ratio ( $\lambda$ )	0.6
Span( $b$ )	14.76ft	Dihedral Angle ( $\Gamma$ )	0
Root Chord	9.343ft	Sweep Angle ( $\delta$ )	0
Tip Chord	5.7ft	Max $\frac{t}{c}$	15%
Total Area	111.0ft <sup>2</sup>	$X_{Loc}$	56.2ft

## 4.5 Optimization

# 5 Propulsion

## 5.1 Hybrid Engine Configuration

For the hybrid powertrain, there were 2 configurations analyzed to integrate the hydrocarbon and electrical propulsion systems. These options were:

**Series:** In a series system, the engine is connected to a generator rather than being directly connected to the driveshaft. This generator is used to power a single electric motor, with additional power supplied by a main battery. The battery can also be charged directly through the generator. A series system offers distinct efficiency advantages by allowing the turboprop engine to run at its highest efficiency at all times and using electrical motor to augment the power required. The series system is also a simple design that requires little additional development to adapt current engine technology[1]. However, the addition of a generator reduces the efficiency of the system. The series system is shown in 5.1.

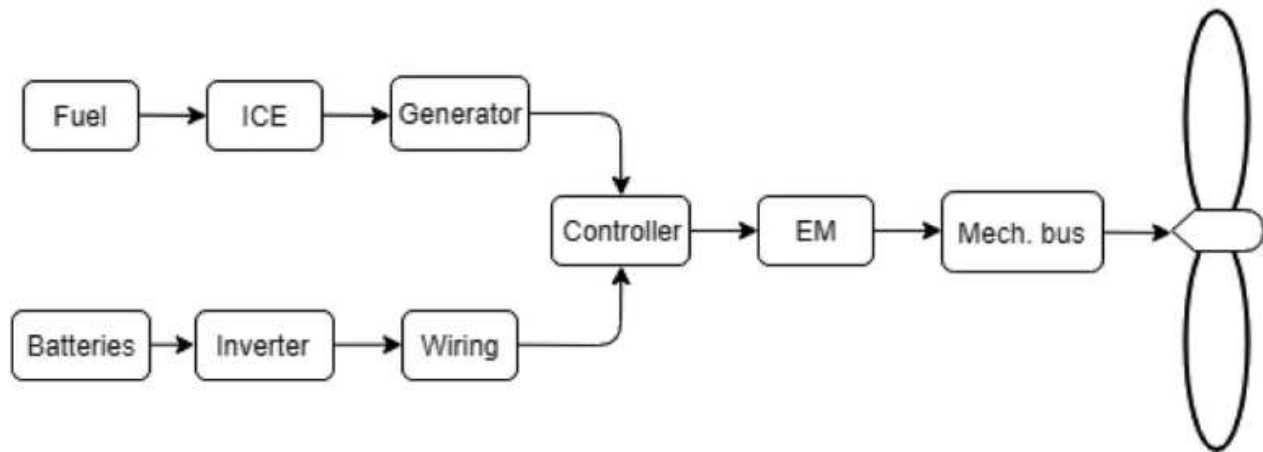


**Figure 5.1 – Series Powertrain**

**Parallel:** A parallel system uses a single gearbox to mate both the electric and turboprop shafts to rotate one shared driveshaft that drives the propeller[1]. The parallel system is safer than the series configuration in the event of a single motor / engine failure, as well as more efficient than the series configuration. Parallel systems are more complex, and louder than series configurations. The parallel system is shown in 5.2.

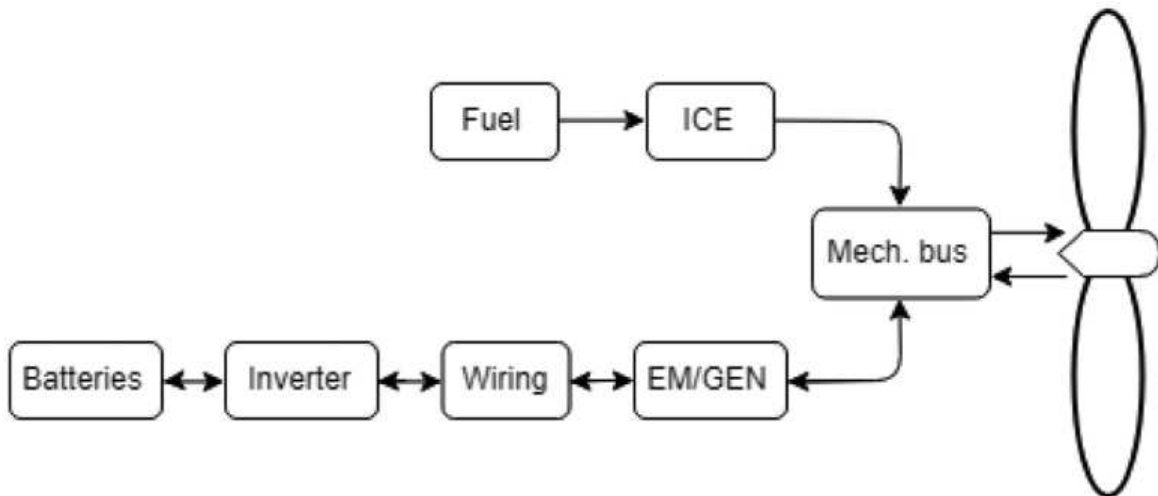


**Figure 5.2 – Parallel Powertrain**

**Distributed:** A distributed system uses a separate hydrocarbon system as well as an electrical system. Distributed hybrid systems are most similar to conventional hydrocarbon aircraft, as the electrical system is completely isolated from the engines. This is the heaviest, but simplest configuration.

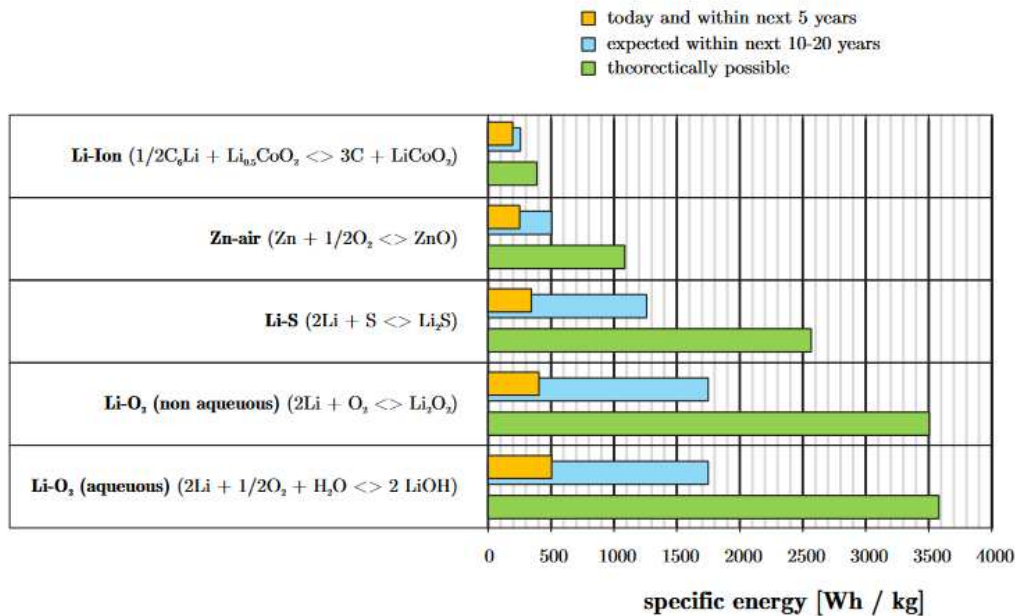
The selection matrix shown below was used to determine the configuration used for the aircraft.

**Table 5.1 – Propulsion Selection Matrix**

Criteria	Weight	Series	Parallel	Distributed
Complexity	20	2	1	3
Efficiency	45	2	3	1
System Weight	35	3	2	1
<b>Total</b>	<b>100</b>	<b>235</b>	<b>225</b>	<b>140</b>

## 5.2 Battery Sizing

To size the battery, the gravimetric energy density of the battery must first be estimated for the production year of 2035. The current energy density of cutting edge Lithium-Ion batteries is 245 kilowatt hours per kilogram. In 2035, using the Hepperle 2012 energy report [4], the energy density of the best option available was pessimistically estimated to be  $1050 \frac{kW\cdot h}{kg}$  using Lithium-Sodium batteries.

**Figure 5.3 – Predicted Energy Density of Battery Types**

The battery was sized by estimating the amount of energy required to power the aircraft for 30 minutes on electric power only. Using Table 5.2 from Raymer, the power to weight for the aircraft was estimated to be  $0.20 \frac{hp}{lb} = 14000 \text{ hp}$ . Using the following equations, the mass of the battery was calculated.

$$M_{batt} = \frac{Pt}{e_{sb}\eta_{prop}} = 6288 \text{ kg} \quad (5.1)$$

For electric aircraft, Brequet's Range equation can be re-derived to be:

$$R = 3.6 \frac{L}{D} \frac{e_{sb}\eta b 2 s \eta_p}{g} \frac{w_b a t}{w} \quad (5.2)$$

Using this equation, the additional range provided by the battery can be estimated. When initially sizing the aircraft, this equation was also used to attempt to find a battery mass fraction (BMF) to see if the mission could be done with electric power alone. The BMF was found to be over 60%, and with any reasonable empty weight fraction, this would not be valid.

From the electric range equation, as electric flight does not result in a loss of mass, the range from electric flight can be optimized by using the electric system as late as possible in the planned trip. As a result, our cruise estimates were broken up into two cruises:

**Normal Cruise:** The first section uses the turboshaft engines to power the generator. The power from the generator is then immediately used to power the electric motors.

**Electric Cruise:** This section uses only the energy stored in the battery to cruise. This section should always be done as late as possible in the mission to optimize efficiency.

With the current version of the aircraft, the electric cruise distance of the aircraft is 212 nmi when done at the end of the normal cruise section.

### 5.3 Efficiencies

The mandatory efficiency requirement is a fuel reduction of 20% over the duration of a 500 nmi mission. All efficiencies used in this section describe the equivalent reduction in fuel used. The sources of efficiency identified were:

**Engine Advancements** Current turboprops use 1970's and 80's engines and have not seen the level of research as turbofan technologies. This can partially be contributed to the monopolization of the turboprop engine segment by Pratt & Whitney, who make 98% of the current civil aviation turboprop engines. However, Pratt and Whitney have developed the 127x series, with an engine in our horsepower class in production by 2025. The 127x series claims a SFC reduction of 18% when compared with the current PW150 series. Approximating another 2% in SFC reduction in the 13 additional years until production, the fuel savings from the usage of updated engines was estimated to be 20%.

Our aircraft would also be a suitable candidate for propfan or open rotor style engines, should the technology ever come to market. With the higher bypass ratio and thrust promised in comparison to turboprop engines, the aircraft is in the correct weight class to benefit the most from this area of research. The additional cabin noise and vibrations would be areas of concern on this new design.

**Regenerative Braking** Much like the similar technology employed in electric vehicles, the rotational inertia of the propeller can be turned back into usable energy via the electric motor. The current estimates of regenerative braking efficiency is 70% energy recapture.

Regenerative braking can be used during taxi and descent phases to minimize energy usage. During descent and landing, the aircraft can utilize a low regenerative strength during the descent glide or propeller windmilling to recapture some of the energy for the next mission. This comes with the added benefit of taxing and descending only under electric power, further reducing the mass fuel fraction required. Additionally, like the 787, regenerative braking is used on the electric braking system. This form of braking is mostly used for weight savings and reliability, but in theory could result in a very small regeneration. The energy recoverable from the descent phase assuming a 5% net energy recovery is shown below:

$$U = mgz = 45000 * 9.8 * 10668 = 4.7GJ = 1306kWH \quad (5.3)$$

$$E_{poten} = U * 0.05 = 59.591kWH \quad (5.4)$$

**Conversion Inefficiencies:** Conversion of the turboshaft energy into electrical energy requires a generator, inverter, and wiring which all require an efficiency loss. The equation for the hybrid efficiency is shown in Equation 5.5.

$$\eta_{hyb} = \eta_{gen}\eta_{invert}\eta_{wiring} = 0.912 \quad (5.5)$$

This efficiency must be applied to all fuel-burning stages of flight, resulting in an efficiency loss of approximately 9%. This may improve before 2035, as significant work is being done to improve inverter efficiency and improving generator integration. Supercooling has been proposed to improve generator efficiency to over 99.99%, but this requires the storage of unstable and complex liquid hydrogen storage unsuitable for an aircraft of this size and needed reliability.

The overall efficiency of the aircraft was measured using the equation below using the efficiencies outlined in this section, as well as accounting for the lack of fuel used during electric cruise, taxi, and descent.

$$\%f_{reduced} = \eta_{desc} + \eta_{taxi} + \eta_{wf} + \eta_{cruise} + \eta_{motor} - \eta_{hyb} = 0.276 \quad (5.6)$$

## 5.4 Integration

Using a series configuration, there are two potential options for electric motor placements and sizes. A "rubber motor" large electric motor can provide the power needed similar to a conventional twin turboprop. A turboshaft engine is placed behind this motor in the nacelle to power the motor and recharge the battery. This configuration has the advantage of simplicity and convention, though it is heavier and more complex than a conventional twin turboprop. The electrical efficiency of such a large motor would also be quite poor. This configuration was chosen to allow for usage of historical data from existing twin turboprops.

The second configuration is a distributed style system, with the leading edge of the wing supporting 20 or more small electric motors[1]. These smaller motors offer better power to weight, efficiency, and thermal characteristics when compared with a single large motor. The large quantity of motors also improves reliability in the event of a motor failure. However, the faster spinning small propellers make this method unsuitable for a 350 knot cruise speed, as the propeller tip exceeds the speed of sound. This distributed system is better suited for high endurance aircraft and low speed applications. There is likely a compromise with 4-8 medium size motors, though this optimization is quite difficult without historical data for similar sized electric aircraft.



**Figure 5.4 – A Conceptual Distributed Electric Regional Aircraft**

## 5.5 Engines

There were two engines of consideration for our power requirement of 6000-7000 ESHP per engine, the Pratt and Whitney PW150 and the Honeywell T-55-GA-715 [7]. The PW150 is the only civil option available, as this T-55 variant is for military applications only. Additionally, there would need to be adjustments to the PW150 to convert to a turboshaft version.

**Table 5.2 – Engine Options**

Engine	ESHp	TSFC	Weight (lbs)
PW150	6200	.43	1521
T-55	6500	0.49	830

As mentioned in the Efficiencies section, the best candidate for the turboprop engines is the PW127x 6000+ hp variant that has not yet been produced [6]. The lowered SFC and weight will greatly improve performance, but the details of this mystery engine are unknown outside of the horsepower range, SFC target, and planned introduction in 2025. This would likely be our engines for the aircraft, or a comparable propfan design. The engines selected for the aircraft were initially sized to be 7050 hp each, for a total ESHP of 14,100 hp total. This estimate was based off of the Raymer value of  $0.20 \frac{hp}{lb}$  for twin turboprop aircraft. The 4-blade propeller was then sized to be:

$$D = K_p P^{1/4} = 1.5(7050^{1/4}) = 9.16\text{ft} \quad (5.7)$$

## 6 Stability & Control

### 6.1 Weight & Balance

In order to obtain accurate stability, we need to accommodate all the component weights to a greater degree. A summary of weights and balances sheet is listed in 6.1 below. Distances are with  $x = 0$  at the leading edge of the wing.

**Table 6.1 – Weights and Balances Sheet**

Category	X <sub>Loc</sub> (ft)	Mass (lbs)
Empty Wing	3.9	5240
Horizontal Tail	57.9	3400
Vertical Tail	56.3	3600
Fuselage	-2.4	7907
Crew Weight	-28	660
Passenger Payload	5.0	12000
Fuel Weight	3.85	13941
Battery Weight	-21.0	13973
Empty Weight	3.01	35723
Max Gross Takeoff	3.29	68343

Passenger CG and Fuel CG were intentionally located close to the quarter chord of the main wing to minimize the change in  $\frac{C_m}{\alpha}$  due to the usage of fuel or low passenger quantities. The engine masses were also placed at the same Z as the CG to align the center of thrust with the CG. The model used for stability analysis is shown in 6.1.

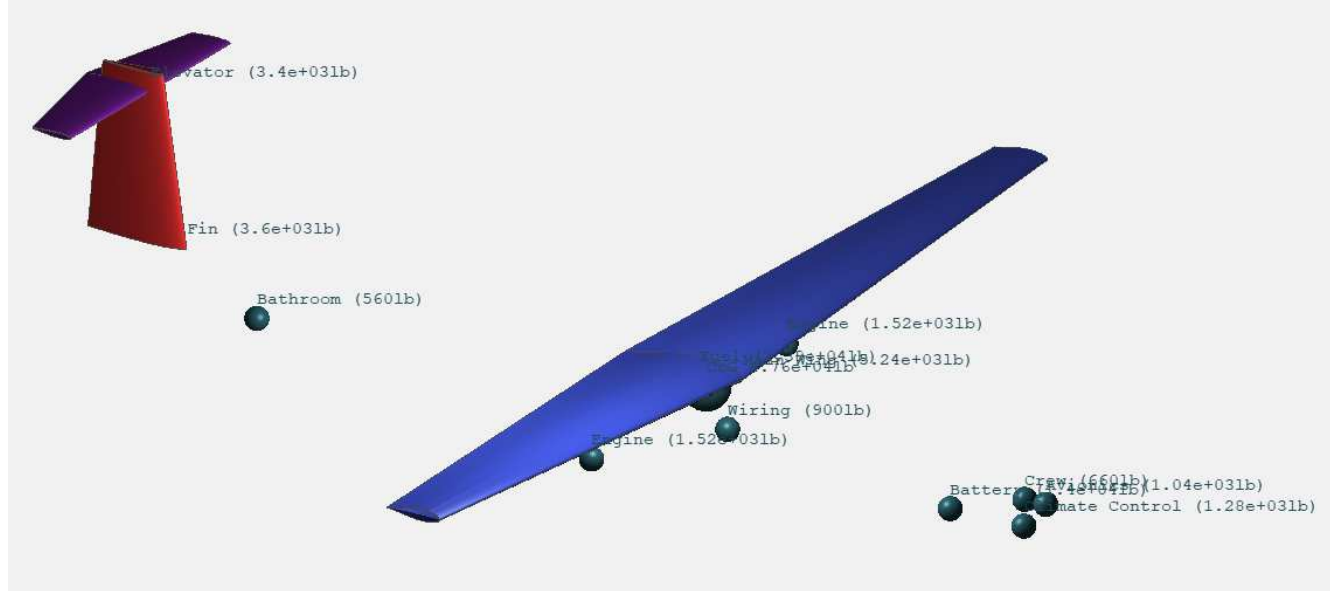


**Figure 6.1 – XFLR Plane with Masses**

## 6.2 Static Margin

The static margin can be found from the equation:

$$SM = \frac{X_{NP} - X_{CG}}{C_{MAC}} * 100 = \frac{6.099 - 2.908}{8.509} * 100 = 37.4\% \quad (6.1)$$

This static margin is quite high, indicating a low level of maneuverability. This is desirable for a civil transport aircraft, but this if the plane is found to be too unresponsive, the angle of incidence of the main wing or elevator can be changed. The elevator incidence for these tests was at -1.5 degrees.

## 6.3 Longitudinal Stability

Preliminary aircraft CG was placed at the quarter chord location of the main wing plus 5 feet. Analysis was then run to determine trim angle by visually confirming a negative slope  $C_m$  vs  $\alpha$  and a positive trim angle between 2.5 - 4 degrees.

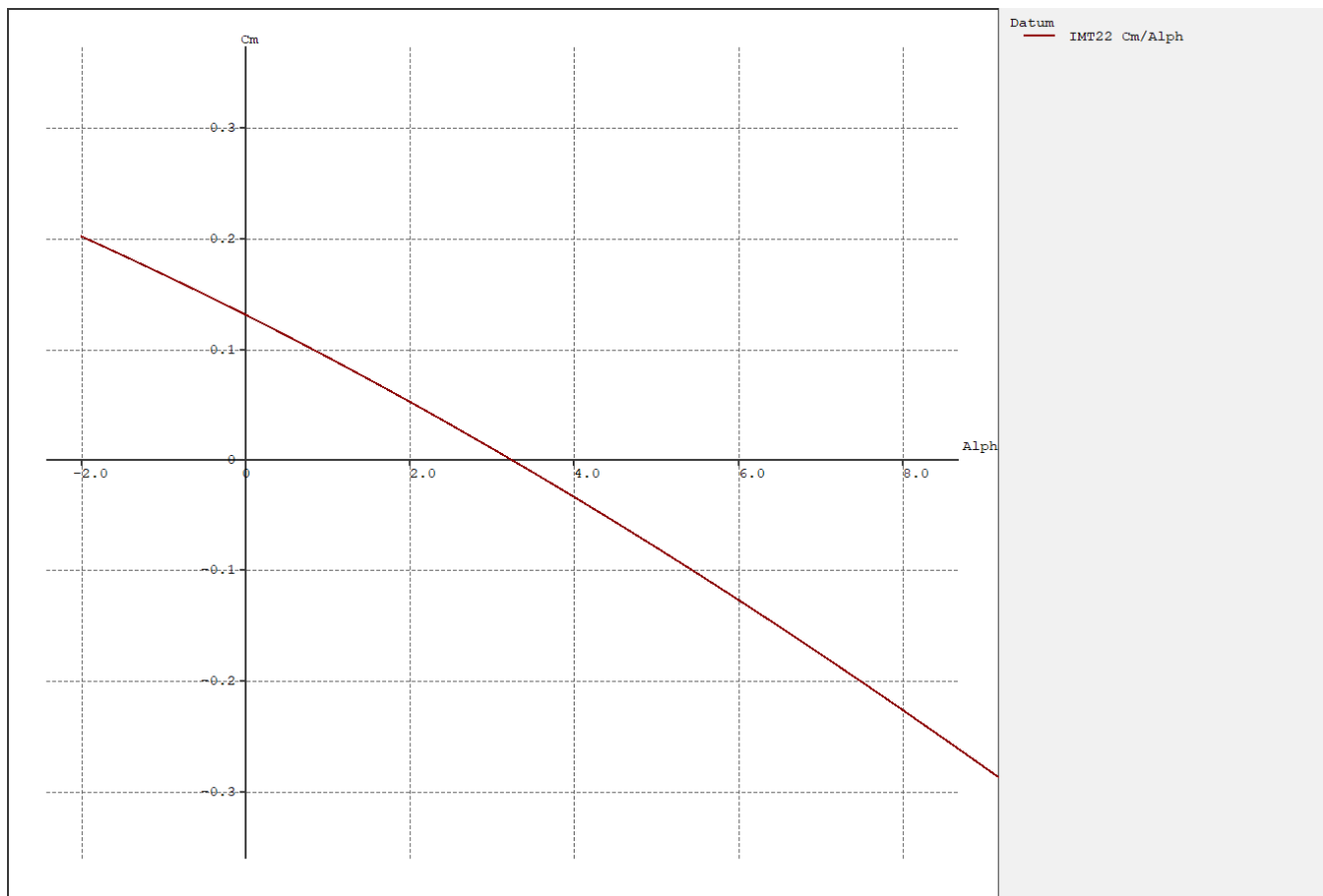


**Figure 6.2 – C<sub>m</sub> vs. Alpha for the Max Takeoff Weight**

The trim angle for the aircraft at maximum takeoff weight was 3.28 degrees.

## 6.4 Lateral Stability

To determine directional stability, a Type 5 analysis can be used to plot C<sub>n</sub> vs Beta and examine the slope. A stable aircraft will have a  $\frac{dC_n}{d\beta} > 0$ , implying a restoring yaw moment.

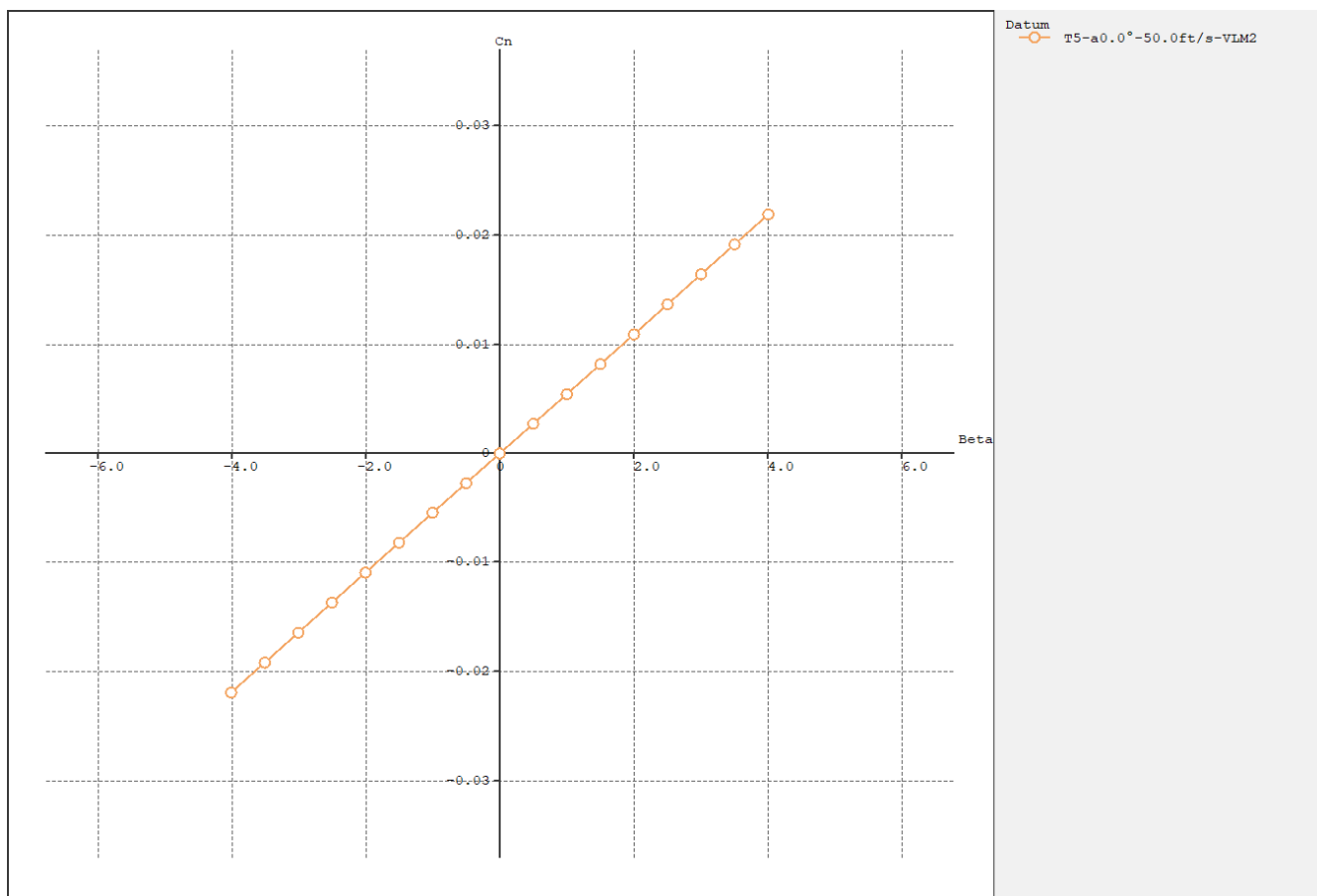


**Figure 6.3 –  $C_n$  vs. Beta for the Max Takeoff Weight**

The slope  $\frac{dC_n}{d\beta}$  was found to be 0.0053, implying the aircraft is directionally stable.

To examine lateral stability, a stability analysis T-7 VLM2 can be used to determine if  $\frac{dC_l}{d\beta}$  would be positive. Unfortunately, due to the Reynold's number limitation this analysis cannot be run for this size and speed of aircraft. The maximum Reynold's number found to function was 9,000,000. However, to run the T-7 analysis, a Reynold's number of 13,000,000 is required for the root airfoil. This technical issue has resulted in an inability to examine lateral stability for now. If the analysis was successfully run, a negative  $\frac{dC_l}{d\beta}$  would imply a stable aircraft. In the future, a scaled version of the aircraft may be used to attempt to run this analysis.

## 6.5 Empty vs Full Weight

During flight, the fuel weight will decrease as it is used, though the CG location can be constant by pumping fuel around. However, in the event of pure electric flight, the plane must still be stable without the mass of the fuel. Similarly, for lower capacity flights or transports, the aircraft must still be stable without passenger weights. To determine the empty stability, the longitudinal stability was examined for a no fuel case, a no passenger case, and a no fuel and no passenger case.

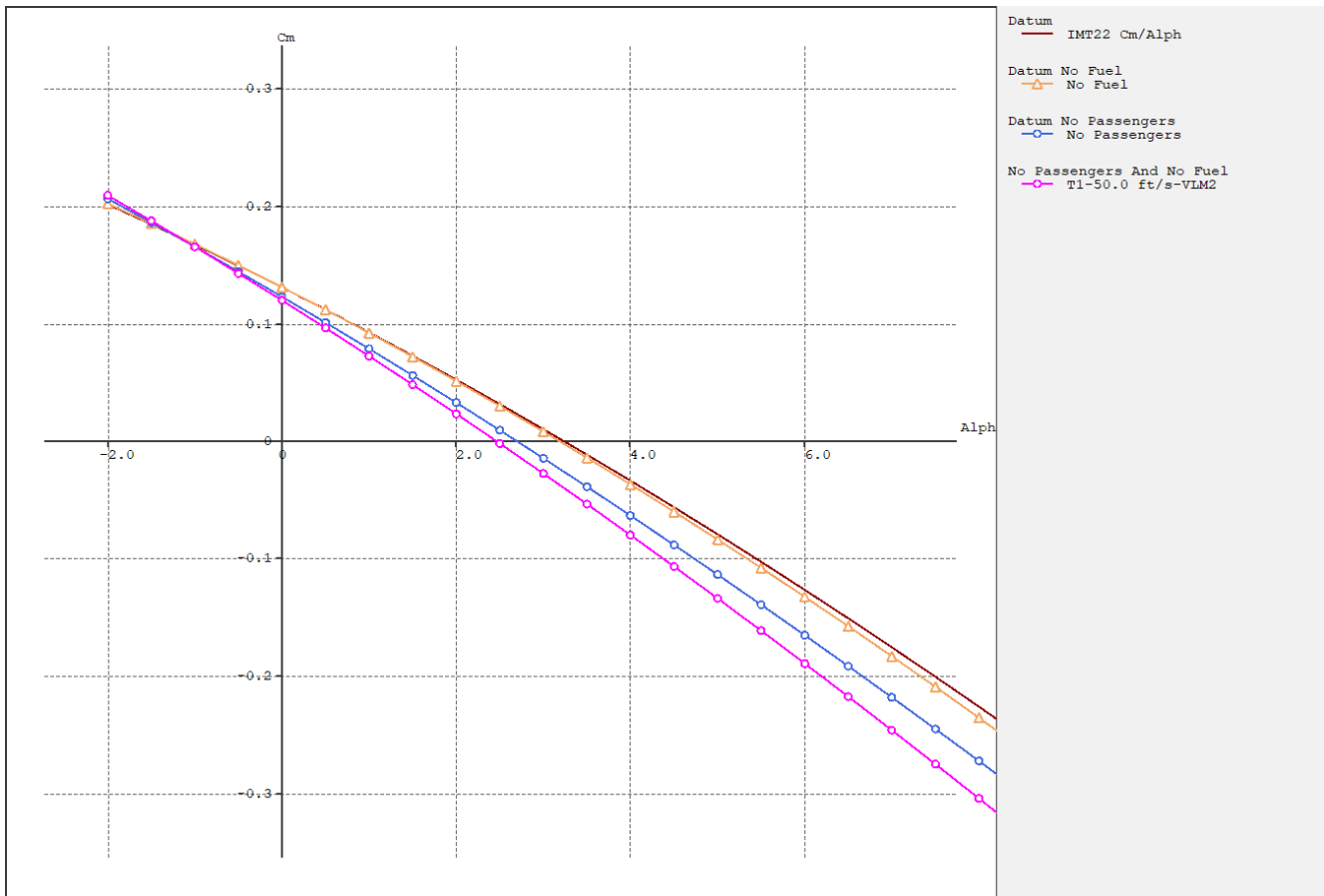


**Figure 6.4 –  $C_m$  vs.  $\alpha$  for Empty Weights**

The trim angles were both lower for the empty cases, but still within acceptable ranges. The "no-fuel" case had a trim angle of 3.18 degrees, the "no-passenger" case had a trim angle of 2.70 degrees, and the "neither" case had a trim angle of 2.46 degrees. There is room for improvement through better organization of passenger seating and cargo, in addition to battery placement.

## 7 Structures

The structure of the airplane is one of the most important parts of an aircraft. It is what withstands all the aerodynamic forces as well as the stresses of the different varying weights on the plane, such as the passengers, wings and fuel. On top of all these, perhaps the most important aspects of the structure of an airplane, is that it makes sure that everyone gets to their destination in one piece by not breaking while in flight.

### 7.1 Material Selection

Materials can make or break an aircraft. Choosing the correct material for your aircraft will either make your plane famous on the news for a crash or not heard about at all because it never went down. With that being said, the material selection used for IMT22 can be seen in the Table 7.1. Table 7.1 was used to compare the properties of materials which allowed us to choose the

best material for each section of the airplane. This data can be found in Matweb.com [5]. After consideration of materials, it was found that using composite materials reduced our initial weight,  $w_0$ , by 14%. This was one of the reasons we chose it. In addition to composite materials being lighter than traditional materials such as Al-6061, they are also better suited for aspects of the aircraft.

**Table 7.1 – Material Selection**

Material	Density (slug/in <sup>3</sup> )	Young's Modulus (ksi)	Yield Strength (psi)	Tensile Strength (psi)	Elongation %
Fiberglass	4.831	10000	439900	439900	4.8
Carbon Fiber	3.394	5200	25000	15000	2
Al-6061	5.237	10000	7000	17000	25
Ti-6Al-4V	8.593	16500	160000	170000	10

## 7.2 Fuselage

The fuselage was designed to have the passengers and flight attendant be in the main section with an overhead luggage section for their carry-on luggage, extra compartments for storage, the lavatory, as well as the food and drink storage the flight attendant will be using. Under the main section is the undercarriage and this runs the length of the fuselage. This section will be used to hold checked in luggage as well as the main battery.

## 7.3 Landing Gear

The landing gear configuration we chose for our turboprop were tricycle landing gear. This is because it is the most common type of landing gear used for turboprop planes. Tricycle landing gear are used with turboprops because they have good ground stability and they allow for a flat cabin floor since our design is for a passenger airplane.

## 7.4 CAD Drawing

Many of the dimensions for the IMT22 came from using measurements and parameters outlined in Rayemer's book [8]. These parameters and measurements led to the design all the way from the fuselage, seating arrangement, passenger and flight attendant chairs to the design of the lavatory. Figures 7.1-7.5 show the CAD model and Figures 7.6-7.7 show CAD Drawings of the IMT22. The figures show the following:

Figure 7.1 shows a three-dimensional view.

Figure 7.2 shows a side view.

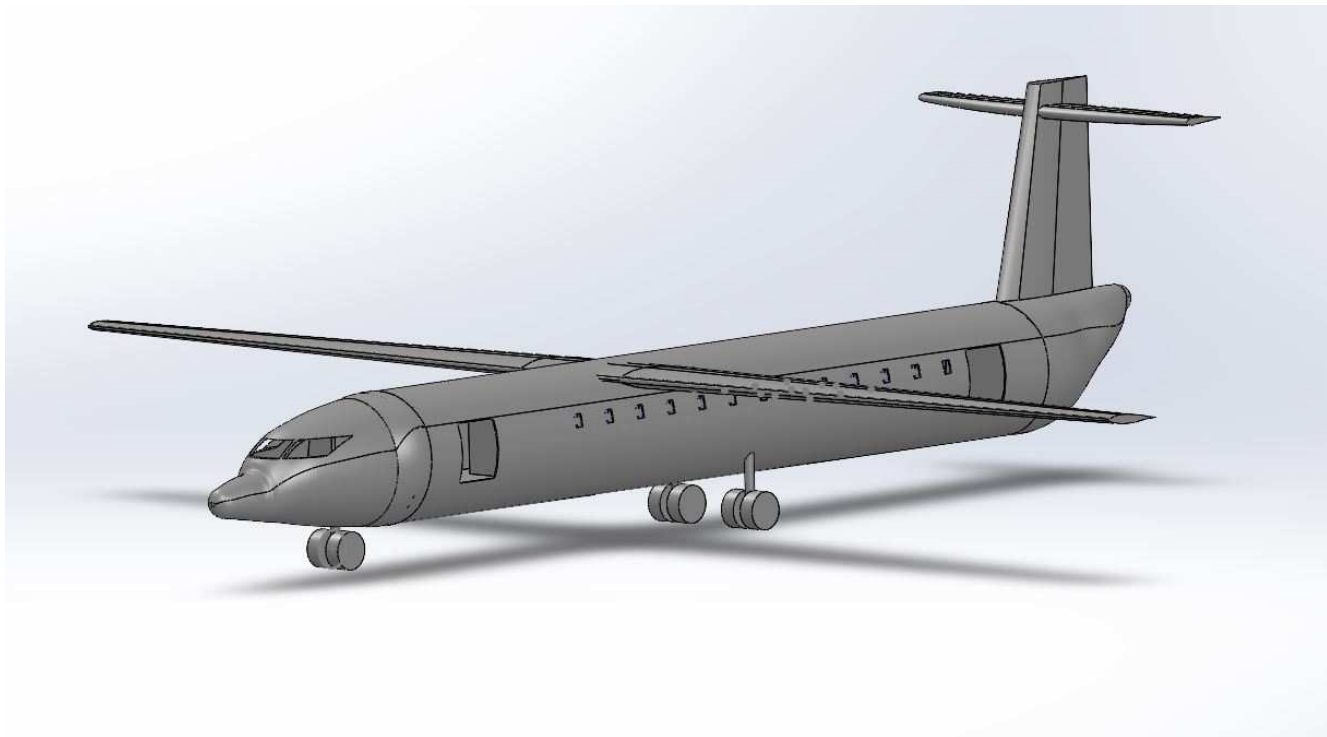
Figure 7.3 shows a front view.

Figure 7.4 shows top view.

Figure 7.5 shows a three-dimensional view with the plane cut right down the middle, the x-z plane, so that the following can be seen: half the passenger's seating arrangement, flight attendant's seat, lavatory (located on back of plane), the cockpit, the emergency exit, as well as the undercarriage.

The IMT22 CAD drawing shows all the dimensions for the following sections of the plane: Wingspan of the Main Wing, Vertical Wing and Horizontal Wing, the length of the Fuselage, as well as the length from leading edge of the Horizontal Wing to the leading edge of the Main Wing.

The IMTSEATS22 CAD drawing describes the layout and inner dimensions of the seats for the passengers as well as the aisle length.



**Figure 7.1** – Three-Dimensional View of aircraft

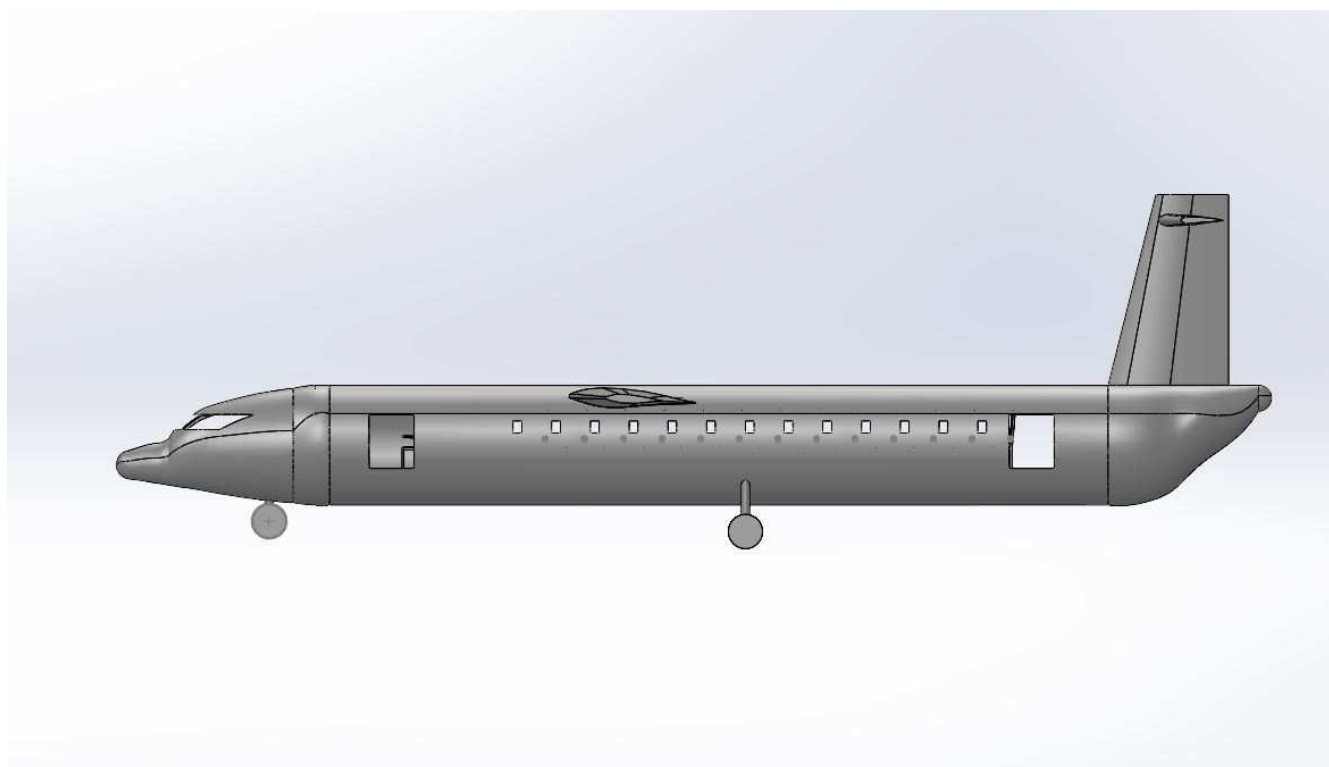


**Figure 7.2** – Side view of CAD Model

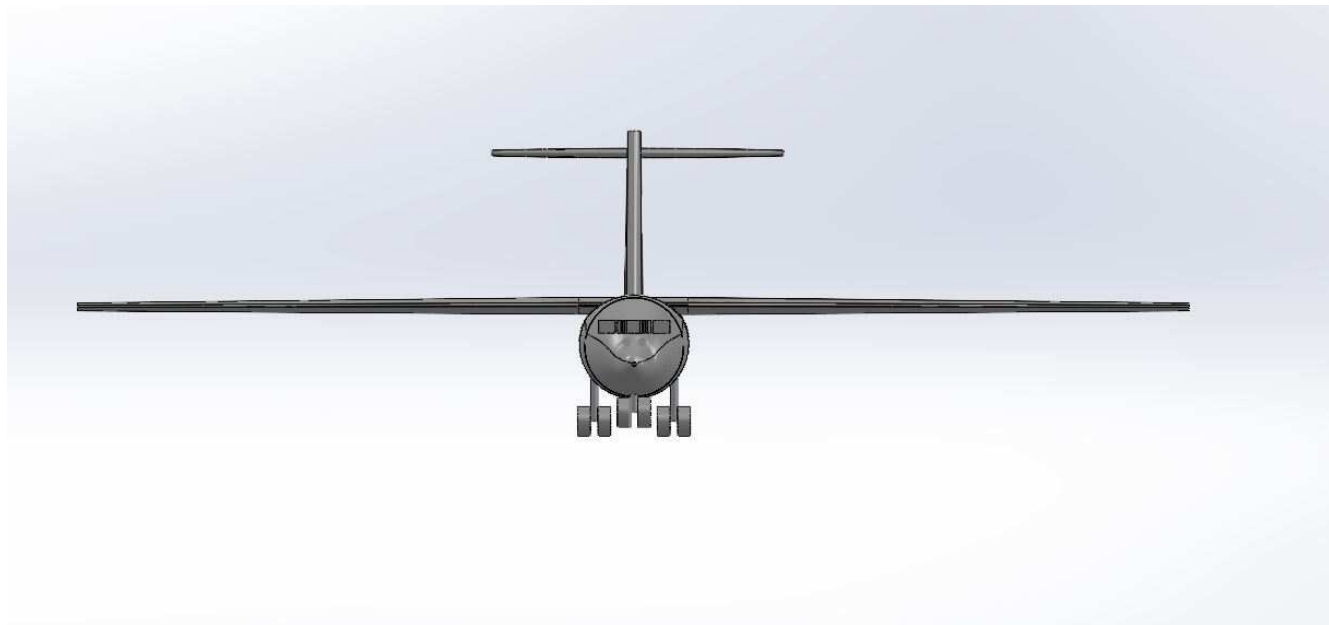


**Figure 7.3** – Front view of CAD Model

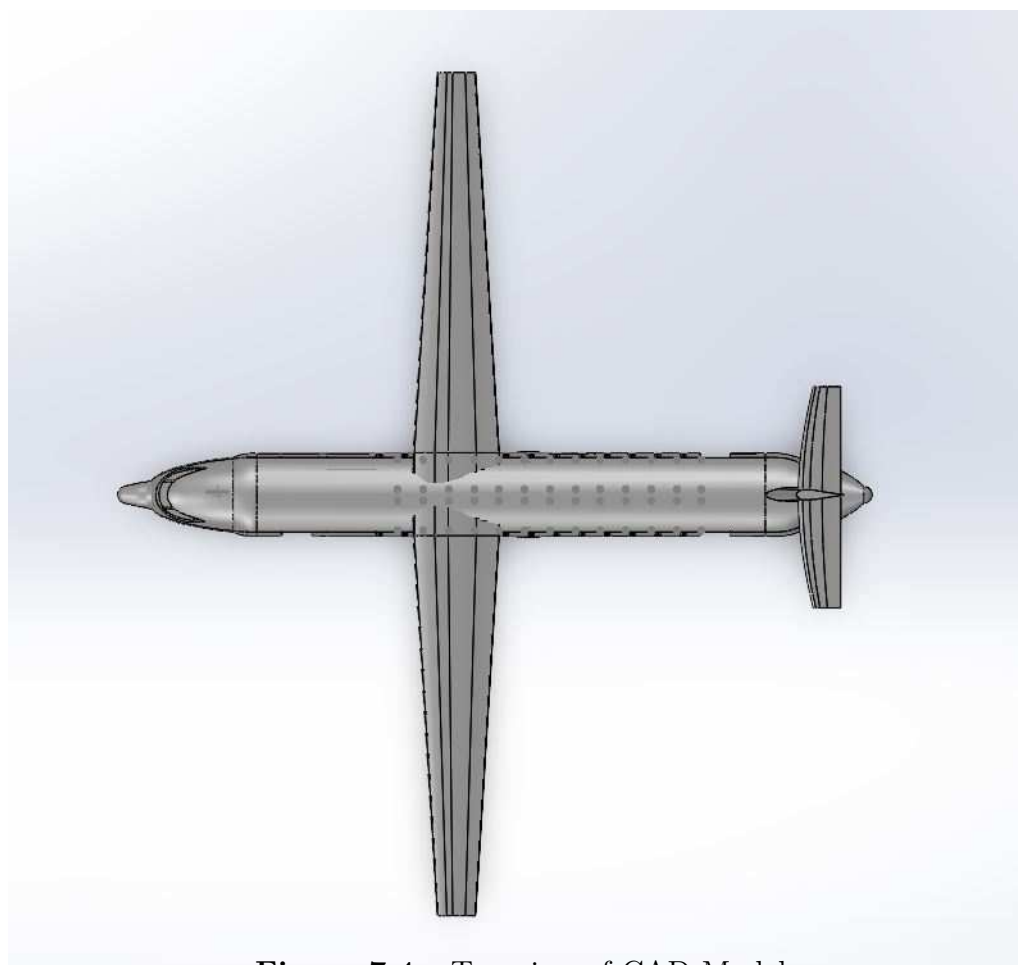


**Figure 7.4** – Top view of CAD Model

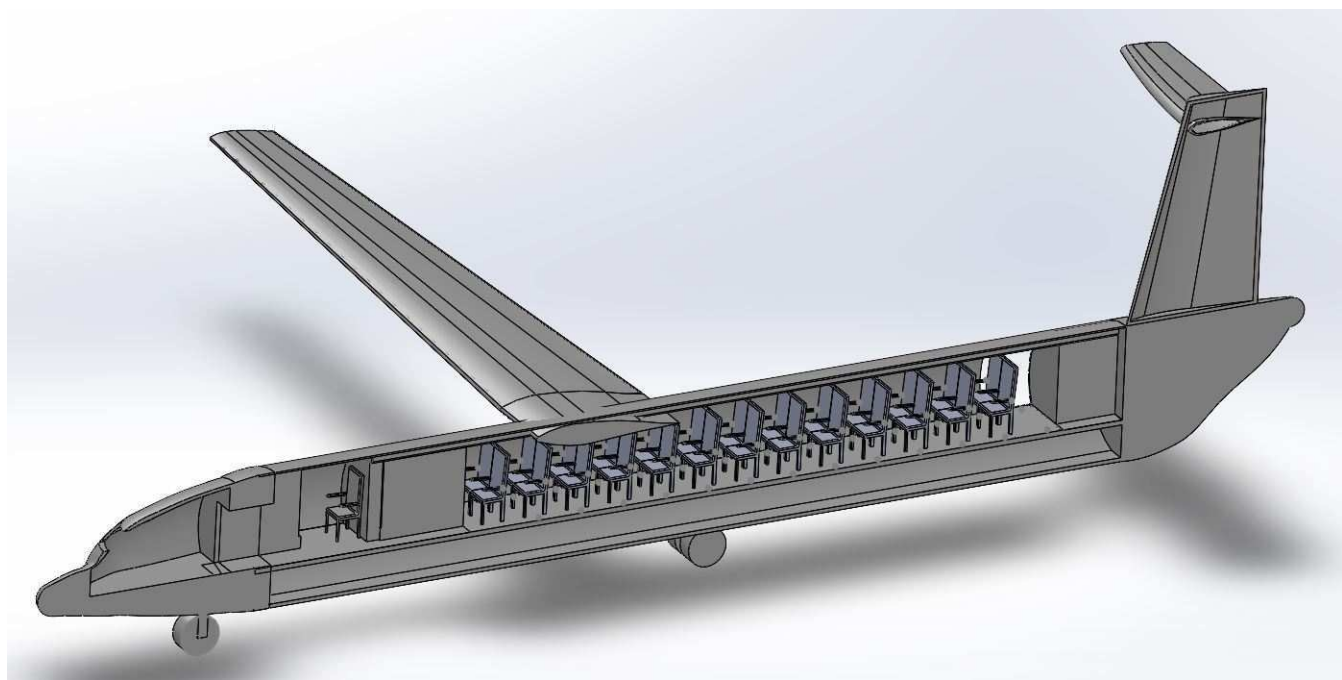
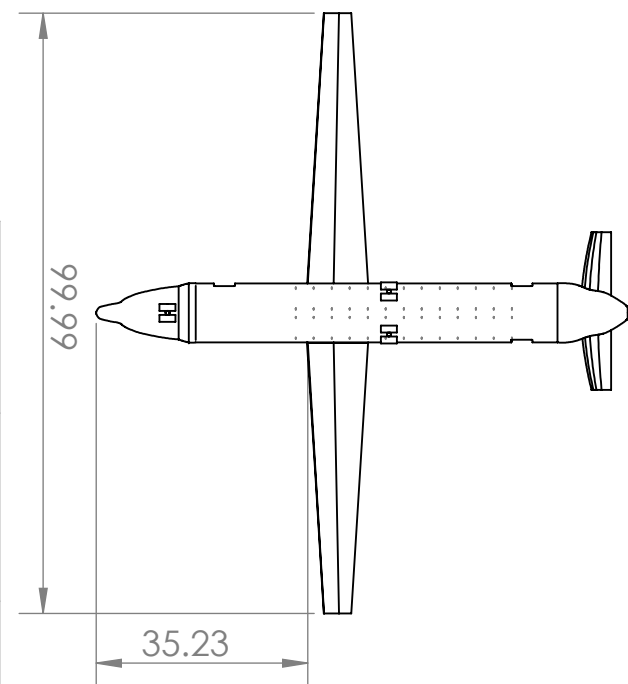
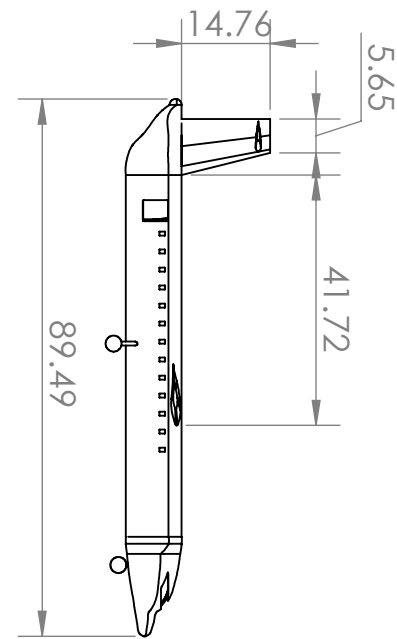
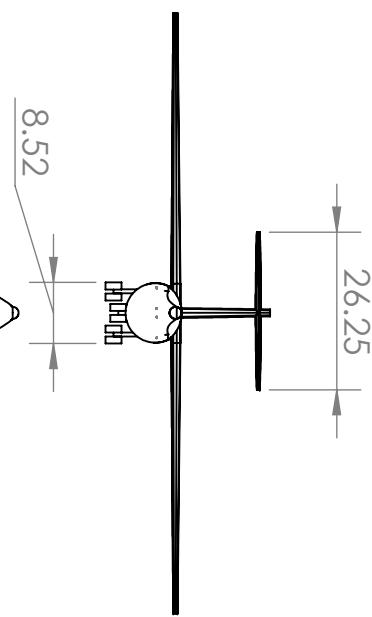


**Figure 7.5** – Three-Dimensional view with cut in half along x-z plane

2

B



A

UNLESS OTHERWISE SPECIFIED:			
DRAWN	NAME	DATE	TITLE:
DIMENSIONS ARE IN INCHES			
TOLERANCES:			
FRACTIONAL: ±			
ANGULAR: MACH: ±			
BEND: ±			
TWO PLACE DECIMAL: ±			
THREE PLACE DECIMAL: ±			
INTERPRET GEOMETRIC			
TOLERANCING PER:			
MATERIAL			
COMMENTS:			
SIZE	DWG. NO.	REV	
<b>A</b>	<b>IMT22</b>		
SCALE: 1:38	WEIGHT:	SHEET 1 OF 1	

**PROPRIETARY AND CONFIDENTIAL**

THE INFORMATION CONTAINED IN THIS DRAWING IS THE SOLE PROPERTY OF <INSERT COMPANY NAME HERE>. ANY REPRODUCTION IN PART OR AS A WHOLE WITHOUT THE WRITTEN PERMISSION OF <INSERT COMPANY NAME HERE> IS PROHIBITED.

1

A

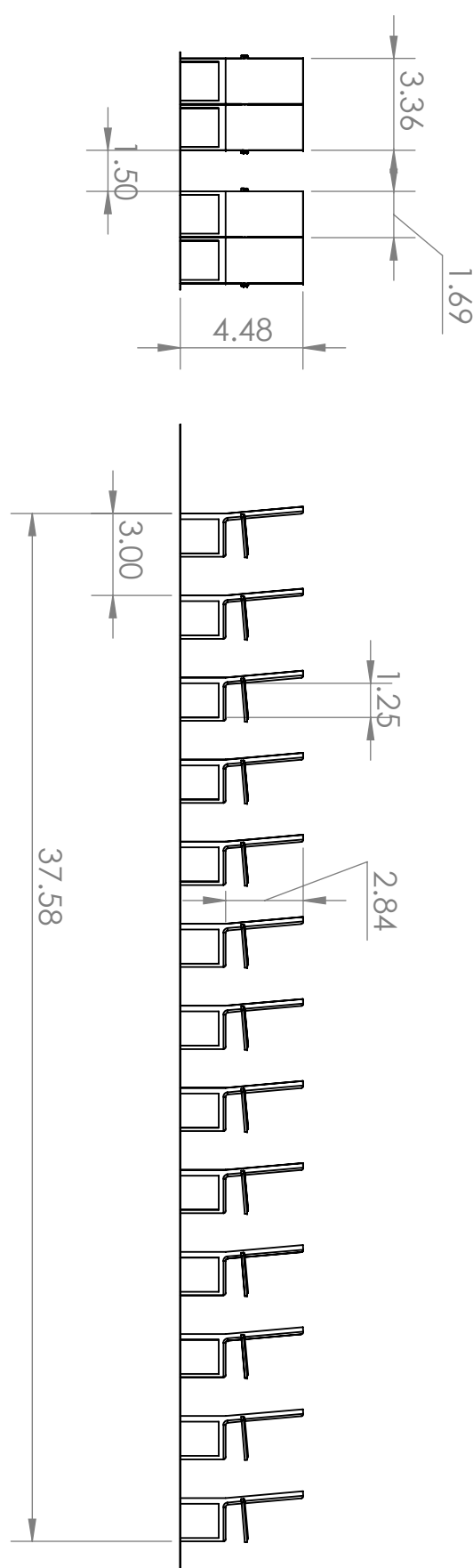
B

2

1

B

B



A

A

# MORBIN SEATS

UNLESS OTHERWISE SPECIFIED: DIMENSIONS ARE IN INCHES TOLERANCES: FRACTIONAL: ± ANGULAR: MACH: ± TWO PLACE DECIMAL: ± THREE PLACE DECIMAL: ± INTERPRET GEOMETRIC TOLERANCING PER: MATERIAL			DRAWN	NAME	DATE
TITLE:					
<b>A</b> IMT SEATS22					
SCALE: 1:75	DWG. NO.		REV		
WEIGHT:				SHEET 1 OF 1	
NEXT ASSY	USED ON	FINISH			
APPLICATION		DO NOT SCALE DRAWING			

## 8 Cost Analysis

The ability of turboprops to operate with a lower carbon footprint is highly exceptional. Still, according to ICCT research [3] these turboprops are an old technology, and their cost were certainly unmatched to today's standard. Which makes it very difficult to adjust the cost to today's standard. Therefore the DAPCA-IV model from Raymer [8] won't be highly accurate unless adjusted for yearly index. For this reason some of the values for the model have been adjusted to reflect the cost estimation for IMT-22 aircraft.

### 8.1 2022 Adjustments

One of the factors that will be adjusted are the wrap rates. We'll be using the 2021 wrap rate factor for the 2012 values listed in Raymer's book. This factor is shown in Equation 8.1 from CAVU financial solutions [2].

$$W_{rate} Fudge = (1 + Fringe) * (1 + Overhead) * (1 + GA) = 1.11 \quad (8.1)$$

Another adjustment to be accounted for is the design and fabrication section of the aircraft. Since most of the IMT-22 structure will be made from composite (CFPR), a fudge factor of 1.2 will be used to adjust the DAPCA-IV hours.

Additionally DAPCA tends to over-predict commercial aircraft costs. Instead Raymer advised those can be factored by (0.9-0.25) fudge. So a 0.7 fudge factor is a safe assumption to balance out the offset.

### 8.2 R&D Cost

The research and development costs are displayed in 8.1. The Avionics accounts for an adjustment of \$10,000 per pound. Additionally the IMT-22 will be equipped with two PW150 engines valued at \$1,300,000 each in present day. Early guesstimates is that about 15 planes to be produced in 5 years.

### 8.3 Operation & Maintenance

To determine maintenance and operations cost, we need several other costs. For commercial aircraft (which fly many more hours per year), the fuel totals about 38% of OM costs, the crew salaries about 24%, and the maintenance about 25%. The depreciation of the aircraft purchase price is about 12% of total OM costs, and the insurance is the remaining 1%. Using a script listed in the appendix we get those values listed in the Table below. A 6\$ per gallon fuel cost will be used to estimate the total fuel cost per year.

**Table 8.1 – Research and Development Cost**

Category	USD
Engineering	\$85,128,938
Tooling	\$36,791,539
Manufacturing	\$6,699,569,760
Quality Control	\$6,380,436
Development Support	\$16,397,164
Flight Test Cost	\$37,378,72
Material Manufacturing Cost	\$883,859,52
Flight Test Control	\$14,837,075
Total Engine Cost (15x2)	\$37,000,000
Avionics	\$109,000,000

**Table 8.2 – Operational & Maintenance Cost**

Category	USD
Fuel cost per year	\$167,076,000
O&M Total	\$439,673,684
Crew	\$105,521,684
Maintenance Cost	\$109,918,421
Depreciation Cost	\$52,760,842
Insurance Cost	43,967,368
Landing Fee	\$87,934,736

## 8.4 Pricing and Revenue

Based on a historical data planes like (ATR-600, the ITM-22 would sell at starting price of 12,000,000 with a 12% profit margin in present day. Compared to a total cost per plane (R&D and O&M) that is about 4,440,612,777, it's break even point is after selling 37 planes.

## 9 Conclusion

### 9.1 Efficiency Merit

As discussed in the Propulsion section, the efficiency target was met and exceeded by 7%. The aircraft is ICAO class C compliant, can carry 54 passengers with luggage including crew, and takes off in under 4500 ft. The plane also exceeds the minimum cruise speed of 275 knots with a cruise speed of 350 knots, in addition to an additional 200 nautical miles of range over the required 1000.

### 9.2 Conclusion

The IMT22 is a regional turboprop hybrid boasting a 1200 nautical mile range, 52 passenger capacity, and 12660 pounds of passengers or cargo, all while reducing fuel usage by 27% when compared with current turboprop competitors. Further efficiency gains may be found in future analysis through improved battery energy density, advanced composite techniques, and the addition of winglets to maximize the efficiency of the aircraft.

## 10 Appendix

### 10.1 Codes and Scripts

#### 10.1.1 Plane Class and Equations

```

P_Wmetric = 8 #KW/kg, 2035
P_W_motor = P_Wmetric * 1.34102 /2.2046
def motorWeights(P_W_motor,hp_req):
    return hp_req / P_W_motor
Tfactor = [motorWeights(P_W_motor,21200)-motorWeights(P_W_motor,28000),0,motorWeights(P_W_
#print(Tfactor)

class Plane:
    def __init__(self, number, T_W, W_S,L_D,SFC,n_hyb,Tfactor):
        self.number = number
        self.T_W = T_W
        self.W_S = W_S
        self.S = 833.35
        self.L_D = L_D
        self.SFC = SFC
        self.n_hyb = n_hyb
        self.w0 = W_S * self.S + Tfactor

    def set_w0(self,w0):
        self.w0 = w0
    def get_w0(self):
        return self.w0
    def get_W_S(self):
        return self.W_S

    def __str__(self):
        return ("Plane " + str(self.number) +", w0 = " + str(self.w0) + ", T_W = " + str(self.T_W)
               ", W_S = " + str(self.w0/self.S) + ", T0_dist = " + str(self.T0distance()))

    def wf_w0(self):
        KTAS = 350
        wTO = 1
        wClimb = .985

```

```
wCruise1 = Cruise_wFrac(1000-239.2,self.SFC,KTAS,self.L_D)
rangeElec = Range_electric(15,1050,.912,.80,6291,68343*wClimb*wCruise1) * 0.539957
wLoit1 = End_wFrac(0.75,self.SFC,self.L_D*.866) #45 min
wCruise2 = Cruise_wFrac(200,self.SFC,KTAS,self.L_D)
wLoit2 = End_wFrac(0.33333,self.SFC,self.L_D*.866)
wLand = 1
return 1.06 * (1- (wT0*wClimb*wCruise1*wLoit1*wLand*wCruise2*wLoit2)*self.n_hyb)

def we_w0(self):
    if self.w0:
        return 0.912*self.w0**-0.05
    else:
        return "Still need w0!"

def Vstall(self): #USE IMPERIAL, returns ft/s
    return np.sqrt((2*self.w0)/(0.00238*self.S*2.2))
def Vapproach(self):
    return self.Vstall() * 1.3

def T0distance(self):
    denSL = 0.00238
    vStall = self.Vstall()
    mu_r = 0.025
    K = 0.2
    Cl_max = 2.2
    C_d = 0.02
    v_lof = 1.1 * vStall
    v_avg = 0.707 * v_lof
    Cl_opt = mu_r / 2*K
    D_avg = C_d + 2*K*Cl_opt**2
    q_avg = (1/2) * denSL * v_avg**2
    a_avg = (32.2/self.w0) * ((self.T_W*self.w0)-(D_avg*q_avg*self.S)-mu_r*(self.w0-(q_avg
    return ((v_lof**2)/(2*a_avg))
```

### 10.1.2 Script for Trade Study

```

import numpy as np
import matplotlib.pyplot as plt

#Trade Study: W/S +- 10 and T/W +- 0.05; Constraints: T0_dist < 4500
delta_t_w = [-0.05,0,0.05]
delta_W_S = [-10,0,10]
L_D = 15
SFC = 0.3818
n_hyb = 0.910425
S = 833.35
W_S = 82.01
T_W = 0.205

planes = []
for i in range(len(delta_W_S)):
    for j in range(len(delta_t_w)):
        planes.append(Plane(i*3+j+1,T_W + delta_t_w[j],W_S + delta_W_S[i],L_D,SFC,n_hyb,Tfactor))
Neg_T_W = planes[::3]
Neut_T_W = planes[1::3]
Pos_T_W = planes[2::3]
for i in Neg_T_W:
    print(i.get_w0(),i.T0distance(),(i.Vapproach()*0.592484))
    for i in Neut_T_W:
        print(i.get_w0(),i.T0distance(),(i.Vapproach()*0.592484))
    for i in Pos_T_W:
        print(i.get_w0(),i.T0distance(),(i.Vapproach()*0.592484))

```

5.1	Propulsion Selection Matrix . . . . .	15
5.2	Engine Options . . . . .	19
6.1	Weights and Balances Sheet . . . . .	19
7.1	Material Selection . . . . .	24
8.1	Research and Development Cost . . . . .	31
8.2	Operational & Maintenance Cost . . . . .	31

## References

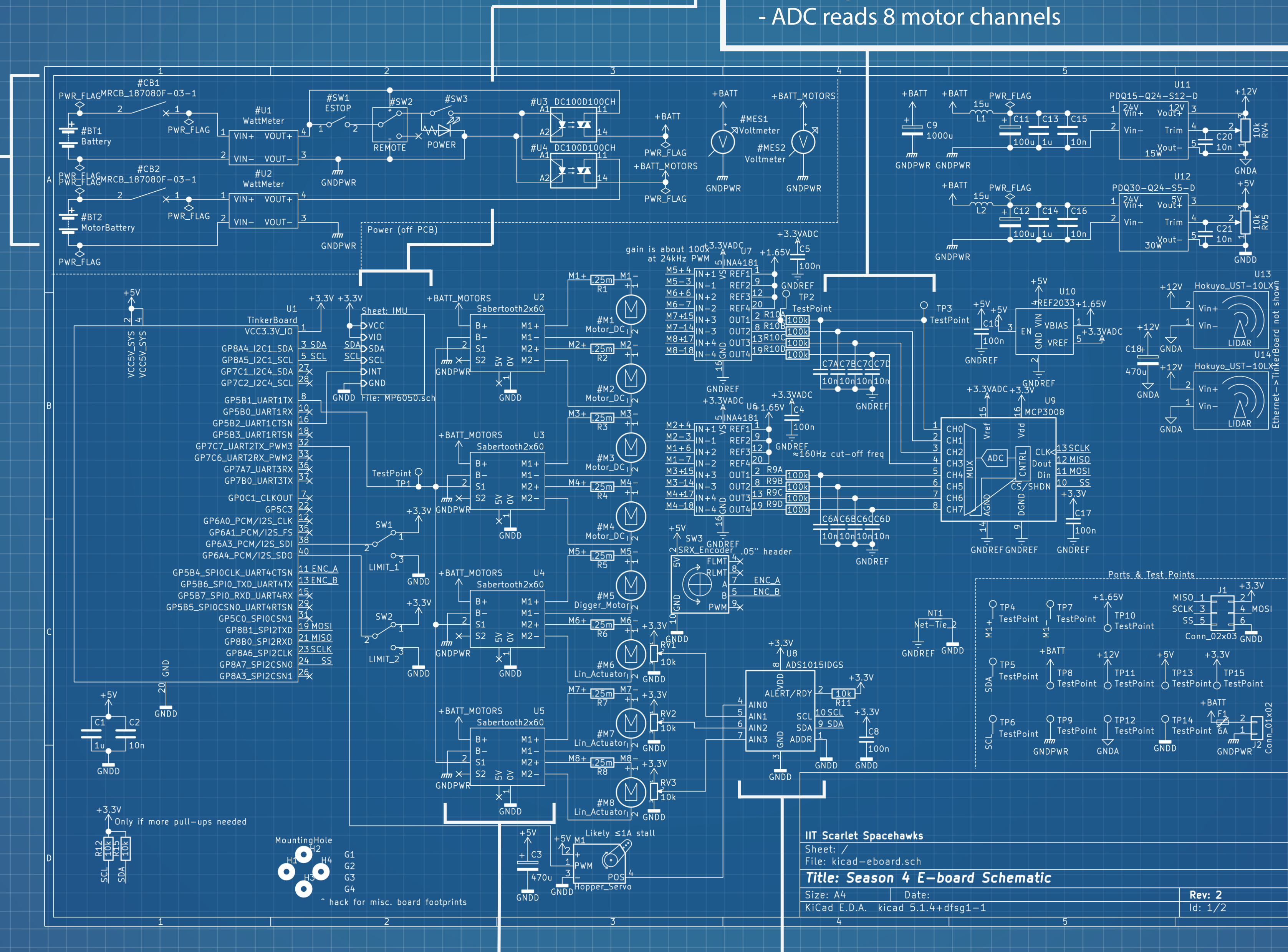
- [1] Guillem Moreno Bravo, Nurgeldy Praliyev, and Árpád Veress. “Performance analysis of hybrid electric and distributed propulsion system applied on a light aircraft”. In: *Energy* 214 (2021), p. 118823. ISSN: 0360-5442. DOI: <https://doi.org/10.1016/j.energy.2020.118823>. URL: <https://www.sciencedirect.com/science/article/pii/S0360544220319307>.
- [2] Cavu Cost Financial Solutions. Sept. 2022. URL: <https://cavuadvisors.com/about-us/>.
- [3] Embraer. *Why Embraer Plans To Double Its Turboprop Sales Estimation*. 2021. URL: <https://simpleflying.com/embraer-turboprop-sales-estimation/> (visited on 10/16/2022).
- [4] Martin Hepperle. “Electric Flight - Potential and Limitations”. In: (Oct. 2012).
- [5] MatWeb. *MatWeb Material Property Data*. 2022. URL: <https://www.matweb.com/> (visited on 10/19/2022).
- [6] Pratt and Whitney. *Pratt Whitney Canada Announces Certification of PW127XT-M Regional Turboprop Engine*. 2021. URL: <https://newsroom.prattwhitney.com/2022-08-26-Pratt-Whitney-Canada-Announces-Certification-of-PW127XT-M-Regional-Turboprop-Engine> (visited on 10/16/2022).
- [7] Pratt and Whitney. *PW100/PW150 Series*. 2021. URL: <https://www.pwc.ca/en/products-and-services/products/regional-aviation-engines/pw100-150> (visited on 10/16/2022).
- [8] Daniel Raymer. “Aircraft Design: A Conceptual Approach, Sixth Edition”. In: *Aircraft Design: A Conceptual Approach, Sixth Edition* (2018). DOI: 10.2514/4.104909.
- [9] Pasquale M Sforza. *Commercial Airplane Design Principles - 7.1 Introduction - Knovel*. 2014, p. 598. ISBN: 9780124199538.

# PROJECT THREE

## Power Electronics

- Twin 3S LiPo batteries
- Resettable circuit breakers to prevent overcurrent
- Watt meters to measure energy usage for competition
- Switches: emergency stop, remote E-stop, ordinary power switch
- Solid-state relays (SSRs) to toggle power to the robot based on switches

High current to stalled motors caused brownouts. A second battery prevented voltage sags to microelectronics.



## Motor Control

- Sabertooth 2x60 motor controllers
- 60A/motor continuous
- One-way serial comms
- Software closed-loop control

Unfortunately, Sabertooths return no information about motor output or power consumption. For closed-loop control, we added linear actuator position tracking, current sensing, and an encoder on the most critical motor.

## Inertial Measurement Unit (IMU)

- Reports velocity and position in space
- Communicates via I2C
- Option to use MPU-6050 directly or use breakout board

## Current Sensing

- Detect motor stalls, disconnects, performance
- Current sense amplifiers across 0.25mΩ shunts
- Filtering to remove 24kHz PWM
- ADC reads 8 motor channels

IIT Scarlet Spacehawks  
Sheet: /  
File: kicad-eboard.sch  
Title: Season 4 E-board Schematic  
Size: A4 | Date:  
KiCad E.D.A. kicad 5.1.4+dfsg1-1 | Rev: 2  
Id: 1/2

## Potentiometer ADC

- Three linear actuators, four-wire servo
- Raspberry Pi can't read analog inputs
- I2C ADC measures these voltages

**Team Lead:** Andrea de Fonseca  
Jiyeoun Jang  
Anil Kumar  
Jordan Lauer

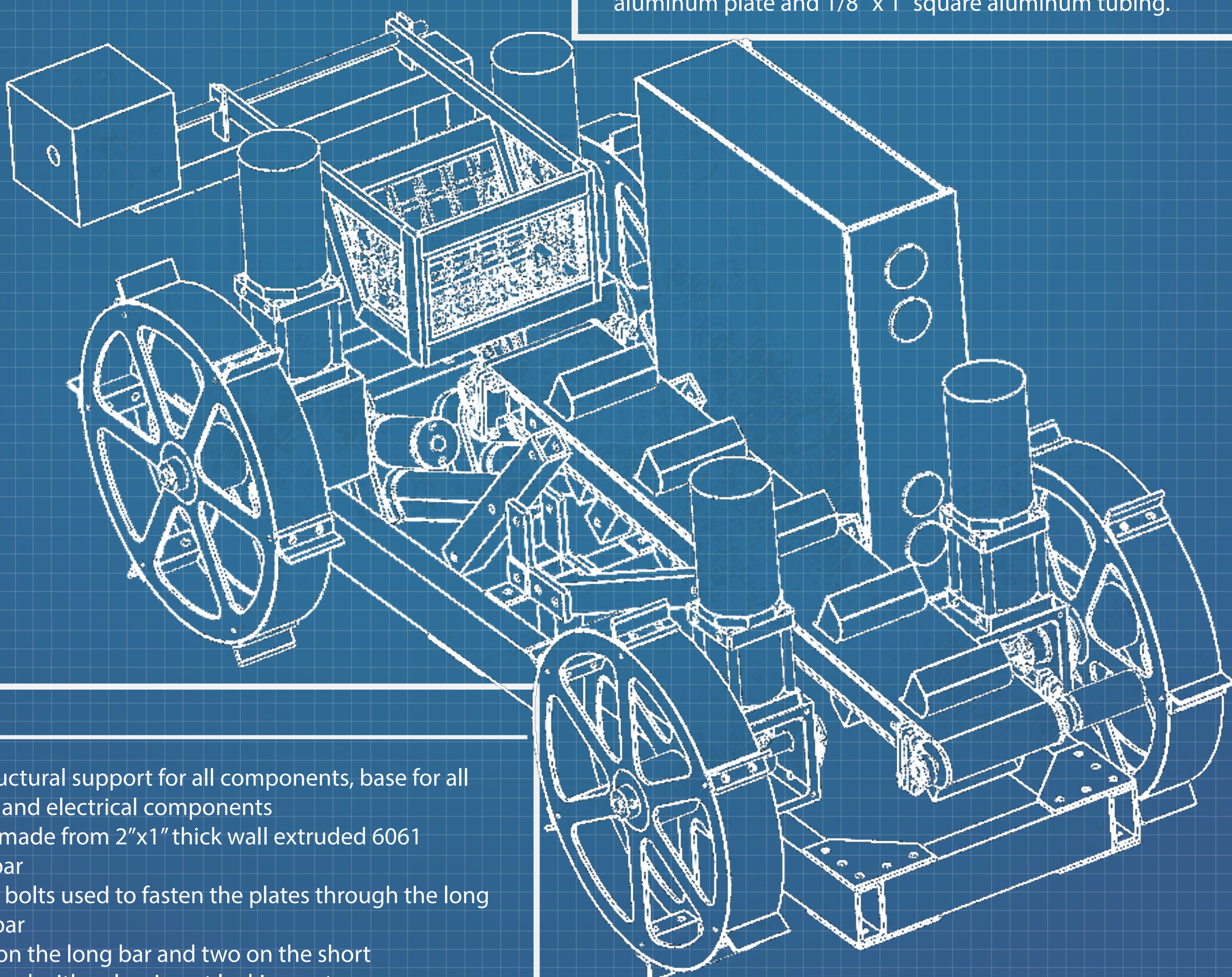
# Mechanical

## Hopper

- 6" linear actuator to raise and lower depending on the location of the trench digger at any given time
- Allows for the easy deposit of regolith into the competition collection bin.
- Designed bending arm to allow actuator to pull hopper down even further, getting it closer to trench digger and creating an easier angle for regolith collection
- Beams are made of 1/4" x 3/4" aluminum with a 23-gauge wire with 1/4" square mesh opening that allows any BP-1 to be released and regolith to remain

## Trench Digger

- Belt and frame: Belt and frame from 2019 rover were reused, length reduced by 3cm to allow clearance between chassis and belt buckets.
- Rollers and mounting assemblies: Rollers and mounting assemblies from 2019 rover were reused. The BAG motor by VEX Robotics with a 1:50 planetary gearbox and encoder was utilized.
- Buckets: Designed with a height relative to belt of about 4cm, assuming a regolith average diameter of 2cm. Width of buckets set to match trench diggers. Also designed with slits on sides so BP-1 dust could be deflected as we dig.
- Linear actuators: Two-linkage linear actuator system allows constraint of diggers movement and get depth required for regolith extraction. Custom-fabricated mounting brackets designed for belt's supporting linkages. To simplify fabrication, bracket redesigned as an assembly of several pieces of 1/8" aluminum plate and 1/8" x 1" square aluminum tubing.



## Chassis

- Provides structural support for all components, base for all mechanical and electrical components
- Main frame made from 2"x1" thick wall extruded 6061 aluminum bar
- 1/4" diameter bolts used to fasten the plates through the long side of the bar
- Three bolts on the long bar and two on the short
- Bolts tightened with nylon-insert locking nuts
- All mounted features used this mounting system
- Use of thick wall aluminum allowed fasteners to be tightened heavily without deforming the material

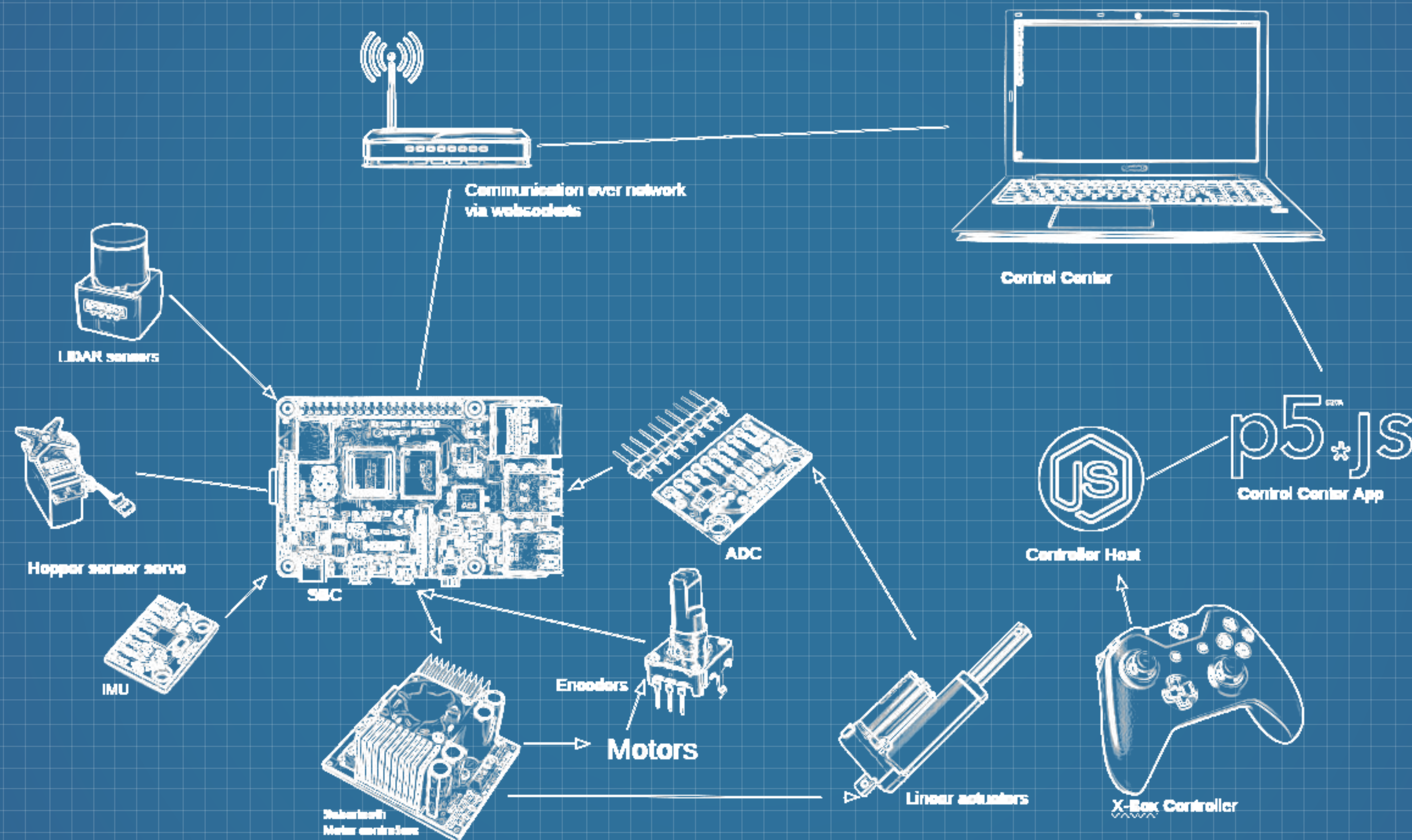
**Team Lead:**

Cameron Haley  
Eyob Ghebrejesus  
Peter Kwiecinski

# Programming

## Software

- Frontend
- Xbox controller host
- Robot main program
- Motors module
- IMU module
- Vision module
- Kalman Filter Module



# Scoops

**Systems Engineer:**

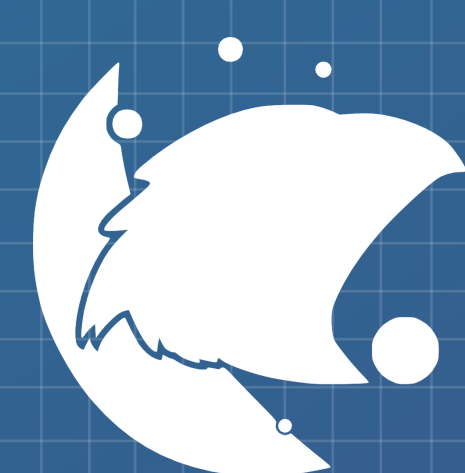
Kristin Petersen

**Outreach Coordinator:**

Daberechi Onyeacholem

**Faculty Advisor:**

Dr. Mahesh Krishnamurthy



NASA

# PROJECT FOUR

# HYBRID-TURBOPROP AIRCRAFT PERFORMANCE & SIMULINK

---

## Team Structure

<sup>1</sup>Eyob Ghebreiesus <sup>2</sup>James Szewczyk <sup>3</sup>Marek Jelen <sup>4</sup>Matt Tobin

<sup>1</sup> M.Eng. Aerospace Engineering. Aerodynamics Lead. Deputy for Stability Control.

<sup>2</sup> B.Sc. Aerospace Engineering. Propulsion Lead, Deputy for Structures

<sup>3</sup> M.Eng. Aerospace Engineering. Stability Control Lead, Deputy for Aerodynamics

<sup>4</sup> M.Sc. Aerospace. Structures Lead, Deputy for Propulsion.

Homepage: *Project Morbius*

Created on *October 25<sup>th</sup>, 2022*

Published on *December 1<sup>st</sup>, 2022*

Copyright © 2022

All rights reserved. This Lab report or any portion thereof may not be reproduced or used in any manner whatsoever without the express written permission of the publisher except for the use of referencing for educational purposes.

The above copyright notice and this permission notice shall be included in all copies or substantial portions of the document.

Produced via LaTeX, Inc U.S.A.

MIT License for the GitHub Project, 2022

[github.com/eyobghiday/project-morbius](https://github.com/eyobghiday/project-morbius)

Department of Mechanical, Materials and Aerospace Engineering

ILLINOIS INSTITUTE OF TECHNOLOGY

# Contents

<b>1</b>	<b>Introduction</b>	<b>1</b>
1.1	Project Summary . . . . .	1
1.2	XFLR5 Data and Values . . . . .	1
<b>2</b>	<b>Coefficient Increment Graphs</b>	<b>2</b>
<b>3</b>	<b>Simulink Control Blocks</b>	<b>6</b>
<b>4</b>	<b>Glide Performance</b>	<b>8</b>
<b>5</b>	<b>Takeoff and Climb Performance</b>	<b>9</b>
<b>6</b>	<b>Holding Performance</b>	<b>10</b>
<b>7</b>	<b>Landing Performance</b>	<b>12</b>
<b>8</b>	<b>Risk Analysis</b>	<b>14</b>
8.1	Risk Control and Assessment . . . . .	15
<b>9</b>	<b>Conclusion</b>	<b>15</b>
<b>10</b>	<b>Appendix</b>	<b>16</b>
10.1	Matlab Script for generating coefficients . . . . .	16
10.2	Matlab Script for Plotting Graphs . . . . .	21
<b>References</b>		<b>23</b>

# List of Tables

1.1	Team Organization Chart . . . . .	1
1.2	XFLR5 Values . . . . .	2
8.1	Risk Definitions . . . . .	14
8.2	IMT-22 Anticipated Qualitative Risk Grading . . . . .	14
8.3	IMT-22 Risk Assessment . . . . .	15

# List of Figures

2.1	Airplane Datum at Trim Conditions . . . . .	3
2.2	dCn, dCy, dCl of Beta(Side Slip) . . . . .	4
2.3	( $C_L$ , $C_M$ , $C_D$ ) of Elevator deflection . . . . .	4
2.4	dCn, dCy, dCl of Rudder . . . . .	5
2.5	dCn, dCy, dCl of Aileron . . . . .	5
3.1	Full Simulink Model . . . . .	6
3.2	Angle Of Attack Holding Block . . . . .	6
3.3	Phugoid Damping Block . . . . .	7
3.4	Throttle Control Block . . . . .	7
3.5	Roll Angle Holding Block . . . . .	7
4.1	Glide Trajectory. (X,Z) Plane . . . . .	8
5.1	Take off and Climb. (X,Z) Plane . . . . .	9
5.2	Thrust vs X-distance for Takeoff and Climb . . . . .	10
5.3	Elevator Deflection vs X-distance for Takeoff and Climb . . . . .	10
6.1	Hold Top View. (X,Y) Plane . . . . .	11
6.2	Hold Side View. (X,Z) Altitude Plane . . . . .	11
7.1	Landing Top View. (X,Y) Plane . . . . .	12
7.2	Landing Side View. (X,Z) Altitude Plane . . . . .	13
7.3	Landing Roll Angles . . . . .	13

## Abbreviations and Symbols

$\alpha$	Aircraft angle of attack [deg]	NiCd	Nickel-cadmium
AIAA	American Institute of Aeronautics and Astronautics	$S_{wet}$	Wetted area
$AR$	Aspect ratio [-]	$TE$	Trailing Edge
$b$	Wingspan [in, ft]	$\theta$	Theta
$c$	Wing chord [in]	$\frac{T}{W}$	Thrust-to-weight ratio [-]
$C_d, C_D$	Drag coefficient (2D, 3D) [-]	UAV	Unmanned aerial vehicle
$C_{D0}$	Zero-lift drag coefficient	$\frac{W}{S}$	Wing loading [-]
$C_f$	Skin friction coefficient	$W_S$	Sensor pod weight [oz., lbf.]
$C_{HT}$	Horizontal tail coefficient [-]	$v$	Velocity [ft/s]
$C_l, C_L$	Lift coefficient (2D, 3D) [-]	$Wh$	Watt-hours
$C_{L\max}$	Maximum lift coefficient [-]		
$C_m, C_M$	Moment coefficient (2D, 3D) [-]		
$C_{VT}$	Vertical tail coefficient [-]		
CA	Cyanoacrylate adhesive		
CAD	Computational Aided Design		
CFD	Computational fluid dynamics		
CG	Center of gravity [in]		
CNC	Computer numerical controlled		
$D$	Drag		
$e$	Oswald efficiency		
ESC	Electronic speed controller		
FEA	Finite element analysis		
$g$	acceleration of gravity		
IC	Integrated Circuit		
IIT	Illinois Institute of Technology		
$LE$	Leading Edge		
LED	Light Emitting Diode		
$L$	Lift		
$\frac{L}{D}$	Lift-to-drag ratio [-]		

# 1 Introduction

The team is made of four members in total and their roles are shown in Table 1.1. Each role has a lead and a deputy that represent their significance and the tasks delegated.

**Table 1.1 – Team Organization Chart**

Section	Lead	Deputy
XFLR5 Coefficients	Eyob Ghebreiesus	James Szewczyk
Climb Performance	James Szewczyk	Eyob Ghebreiesus
Glide Trajectory	Matthew Tobin	James Szewczyk
Landing Performance	James Szewczyk	Eyob Ghebreiesus
Hold Performance	Eyob Ghebreiesus	James Szewczyk
Presentation Slides	Matthew Tobin	Marek Jelen
LaTeX Report	Eyob Ghebreiesus	Matt Tobin, James Szewczyk

## 1.1 Project Summary

With the conceptual design of the It's Morbin Time 2022 (IMT-22) aircraft being completed, control system modelling could begin. To test this, a MATLAB Simulink model was made to control a variety of maneuvers that an aircraft would complete during a standard transportation mission. To be able to run the analysis for IMT-22, Simulink required the datum and aircraft's aerodynamic coefficients increment matrices, in addition to the aircraft's weight, center of gravity and center of pressure. These values were found from the XFLR5 model made for the aircraft in the conceptual design phase.

This report begins with discussing the values used in the XFLR5 model to compute the aerodynamic coefficients, which were needed to run the Simulink model. The report then moves on to discuss the different maneuvers the aircraft will be completing. First, the glide performance is shown to demonstrate how the aircraft will fly in the case of all engines out and the control surfaces at trimmed conditions. The aircraft's glide path can be seen and its Lift-to-Drag ratio is computed. The second maneuver is the takeoff and climb performance. The aircraft's climb rate and leveling flight variation is obtained. The third maneuver evaluated the holding pattern performance. This showed the aircraft's ability to fly a standard holding pattern with minimal altitude change. The final maneuver demonstrates exiting the pattern and preparation for landing.

## 1.2 XFLR5 Data and Values

The first step before creating the Simulink model is to generate the coefficient blocks of a variety deflections and roll angles, as well as getting the values required for the MATLAB Simulink. Table 1.2 shows the numbers and values needed for Simulink. Simulink's linear interpolation was used for values not discretely calculated in the XFLR simulations.

**Table 1.2 – XFLR5 Values**

Parameter	Value	Unit
Initial Mass	27016	kg
$[X_{cog}, Y_{cog}, Z_{cog}]$	$[-0.886, 0, -0.631]$	m
$X_{np}$	-1.862	m
<i>Density</i>	1.225	$\frac{kg}{m^3}$
<i>Cruise Speed</i>	180	$\frac{m}{s}$
<i>MAC</i>	2.59	m
<i>Span</i>	30.54	m
<i>Ref Area</i>	75.59	$m^2$

Also from XFLR, the inertia matrix used for the model of the IMT-22 is:

$$\begin{bmatrix} I_{xx} & I_{xy} & I_{xz} \\ I_{yx} & I_{yy} & I_{yz} \\ I_{zx} & I_{zy} & I_{zz} \end{bmatrix} = \begin{bmatrix} 229042 & 0 & 264144 \\ 0 & 1444714 & 0 \\ 264144 & 0 & 1531691 \end{bmatrix} \left[ \begin{array}{l} kg \cdot m^2 \\ kg \cdot m^2 \\ kg \cdot m^2 \end{array} \right]$$

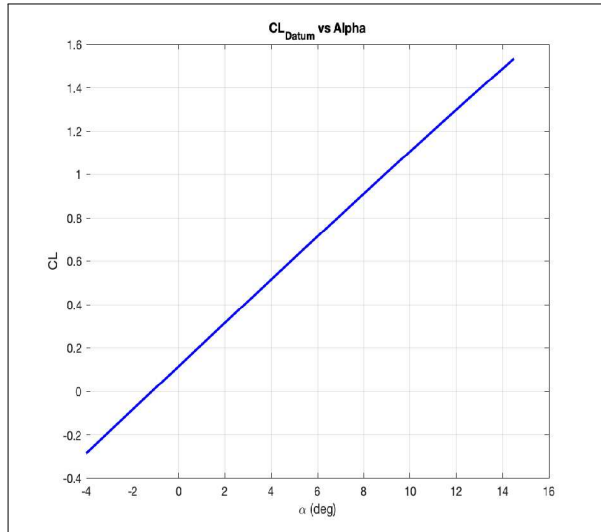
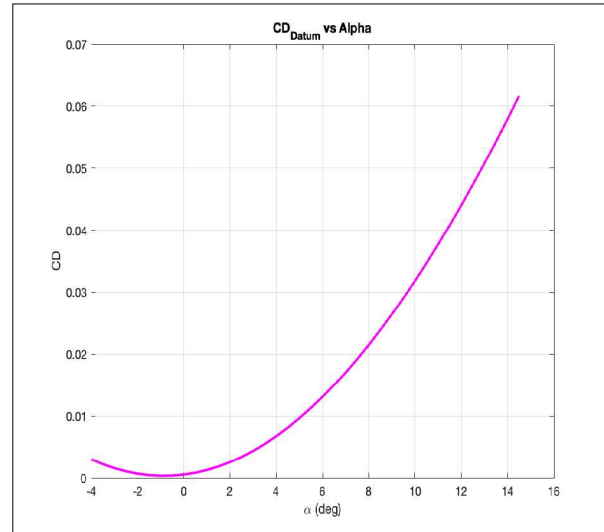
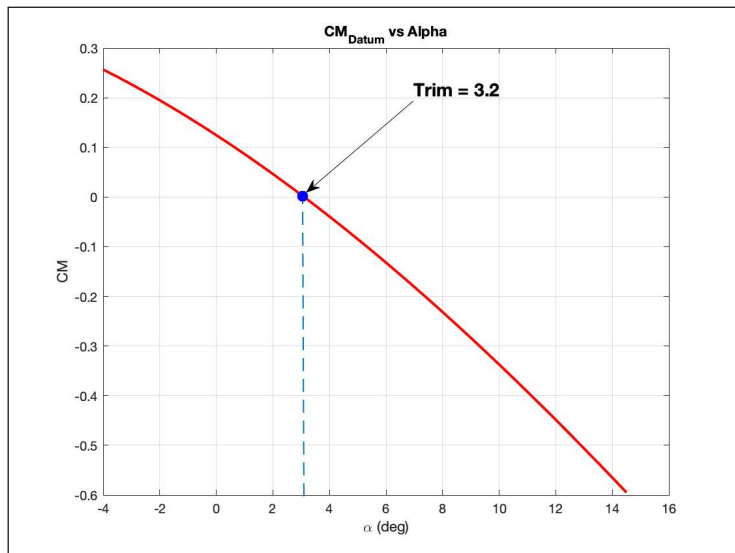
## 2 Coefficient Increment Graphs

Before flight simulation was able to be ran in the Simulink model, it is necessary to create matrices of both the datum and increment matrices for each of the surface deflections for the aerodynamic coefficients. The datum is a simulation of the aircraft in level flight at cruise with no control surface deflections. To begin with Figure 2.1a, 2.1b and 2.1c show the  $C_L$ ,  $C_D$ ,  $C_M$  graphs from the XFLR5. Notice the trim angle 3.2 deg shown in Figure 2.1. These values are plotted as a function of angle of attack. The lift, drag and moment coefficients for the datum and elevator deflection are found in Figure 2.3 respectively. The roll, pitch, and yaw deflection coefficients for beta, rudder, and aileron are found in Figures 2.2, 2.4, and 2.5, respectively. The Matlab script used to generate those plots can be found in the appendix (10) section.

For the datum value, it can be seen that  $C_D$  increases as angle of attack increases and for low angle of attack the value approaches zero. At high angles of attack,  $C_D$  increases with positive elevator deflection and vice versa. For the coefficient of lift,  $C_L$ , it increases with increasing angle of attack as well as positive elevator deflection since the elevator produces more lift. Since the aircraft is longitudinally stable, the moment coefficient,  $C_M$ , decreases with increasing angle of attack and the trim occurs at an angle of attack of 3.2 degrees.

The coefficients of roll, yaw, and pitch are  $C_I$ ,  $C_Y$ , and  $C_n$ , respectively. These values are dependent on the side slip angle and aileron and rudder deflection. Positive side slip results in a negative  $C_I$ , which is needed for the aircraft's lateral stability. Also, having positive aileron deflection rolls the aircraft to the right, thus the increment for  $C_I$  from aileron deflection is positive. For  $C_Y$ , having

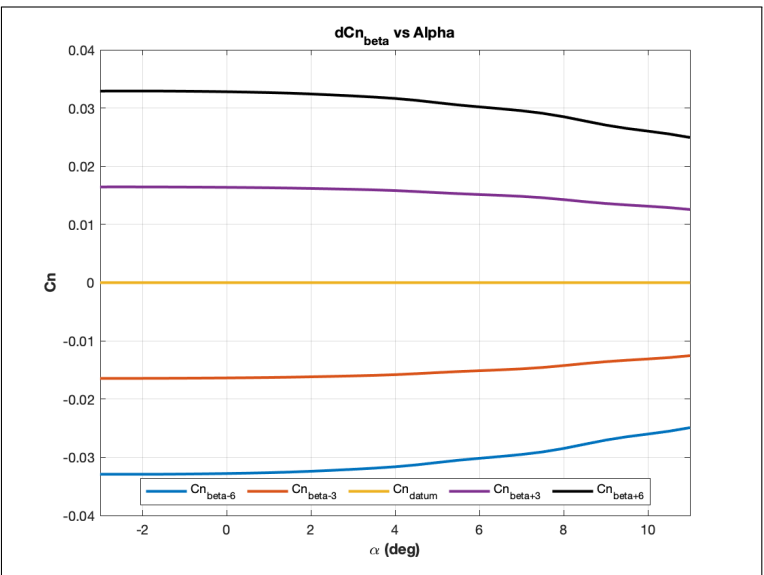
a positive side slip causes the aircraft to return to the trimmed condition, if it has drifted away. For  $C_n$ , it will be positive when the side slip is positive and having a positive rudder deflection will result in a negative  $C_Y$ .

(a)  $C_L$  Datum(b)  $C_D$  Datum.(c)  $C_M$  Datum showing Trim

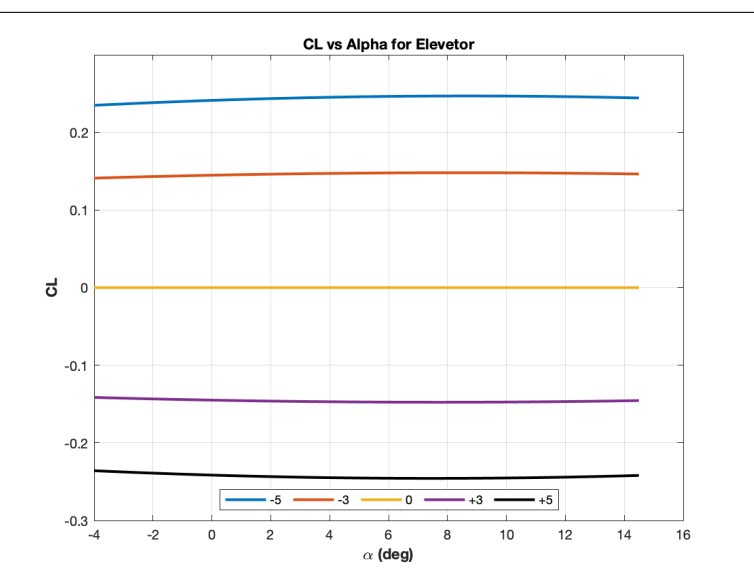
Control Surface	Deflection Angle
Elevator	1
Rudder	0
Aileron	0
Flaps	0
Slats	0
Trim Angle	3.2

(d) Table of Deflection

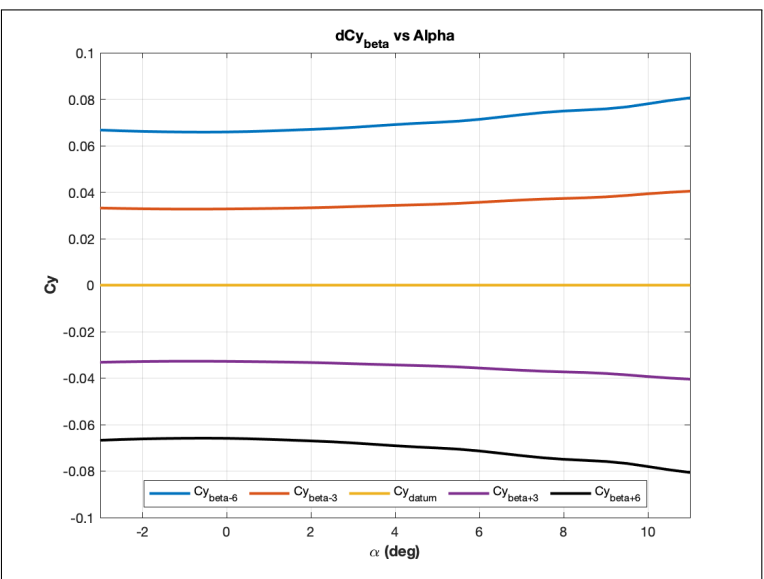
**Figure 2.1** – Airplane Datum at Trim Conditions



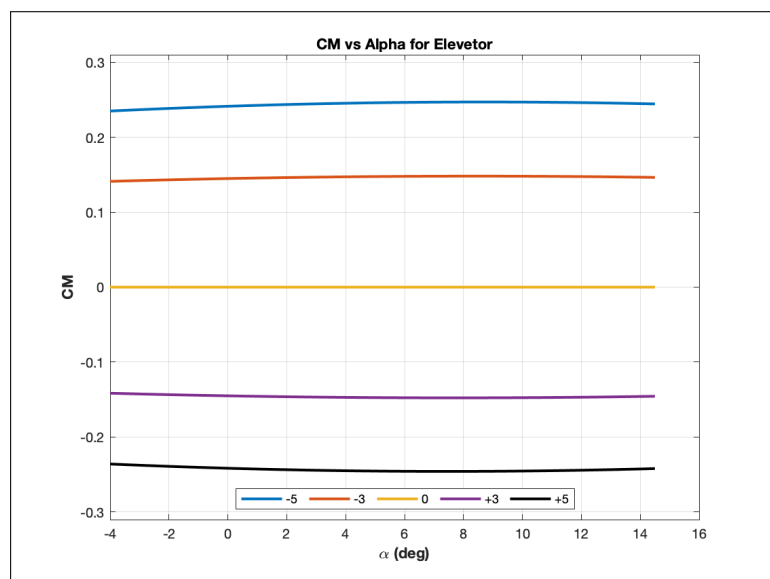
(a) dC<sub>n</sub> Beta



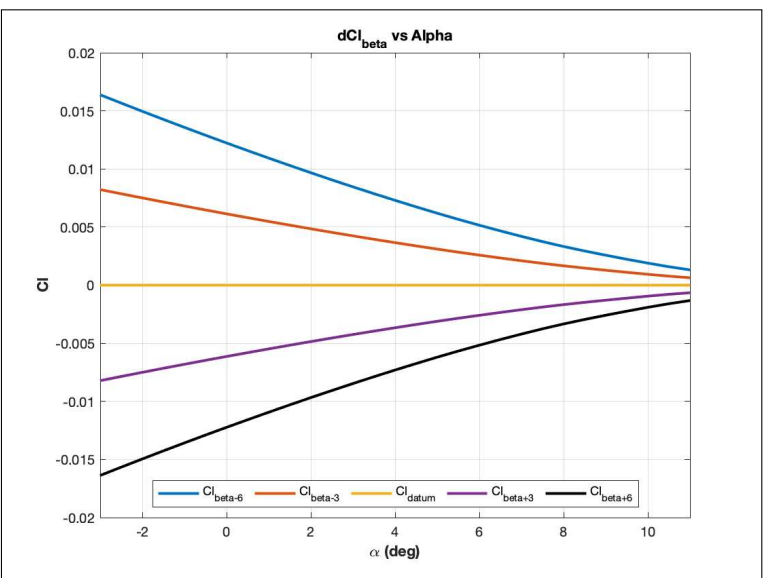
(a) C<sub>L</sub>



(b) dC<sub>y</sub> Beta

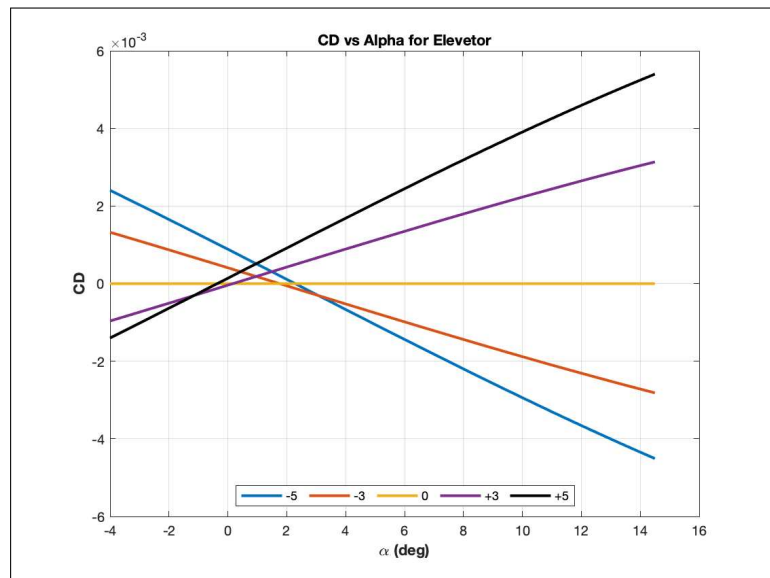


(b) C<sub>M</sub>



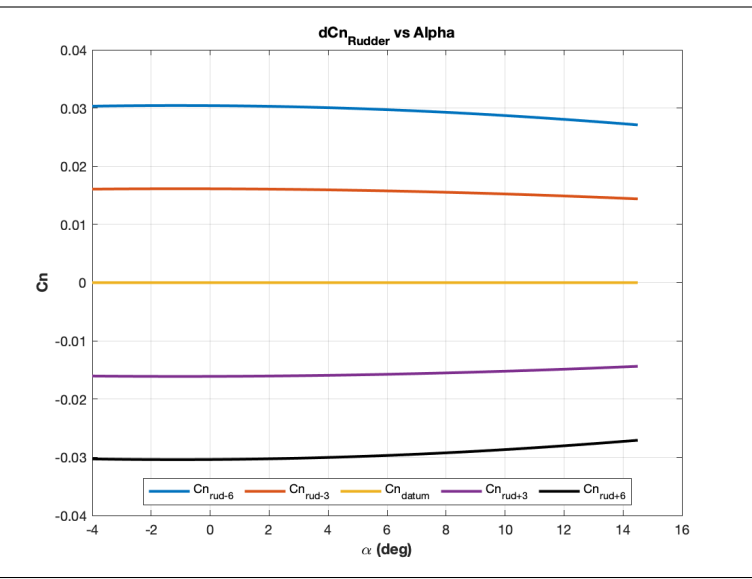
(c) dC<sub>l</sub> Beta

Figure 2.2 – dC<sub>n</sub>, dC<sub>y</sub>, dC<sub>l</sub> of Beta(Side Slip)

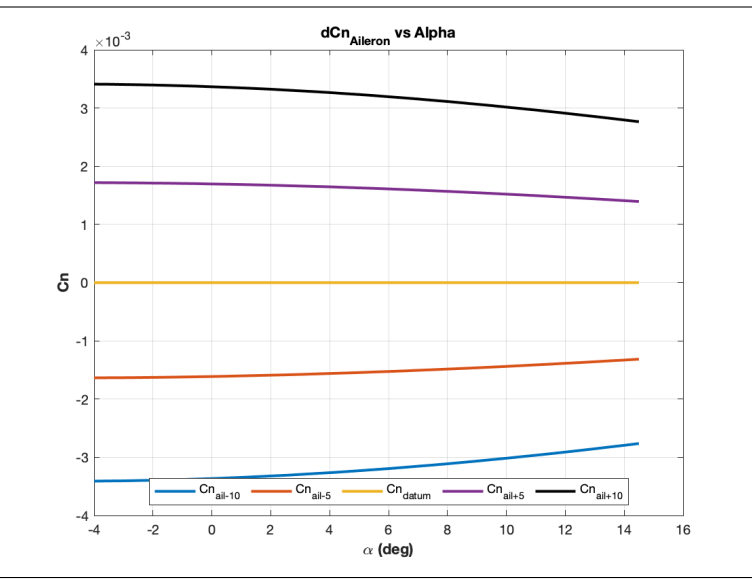


(c) C<sub>D</sub>

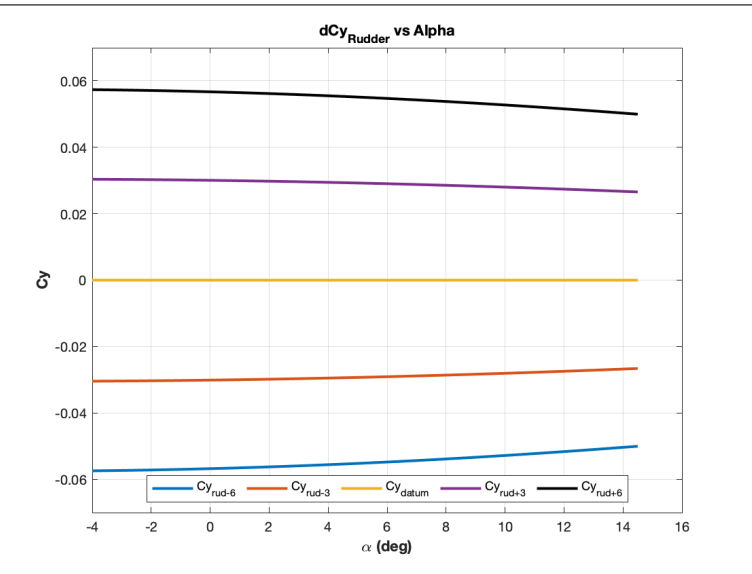
Figure 2.3 – (C<sub>L</sub>, C<sub>M</sub>, C<sub>D</sub>) of Elevator deflection



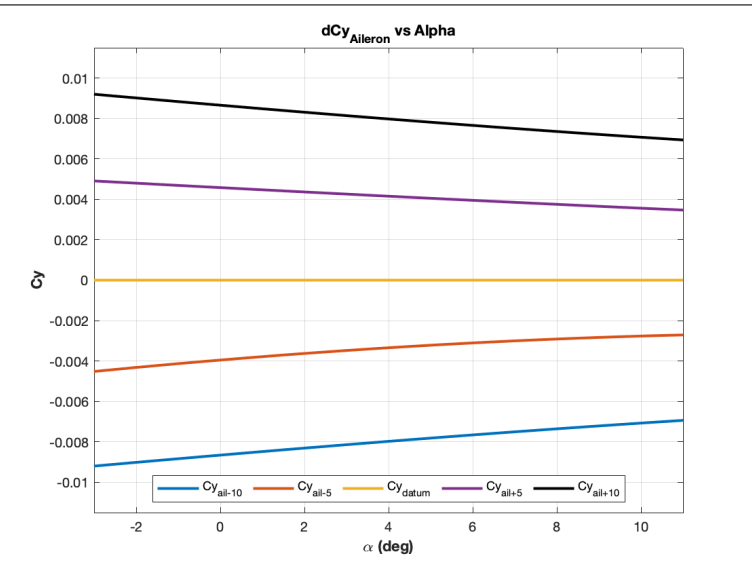
(a) dCn Rudder



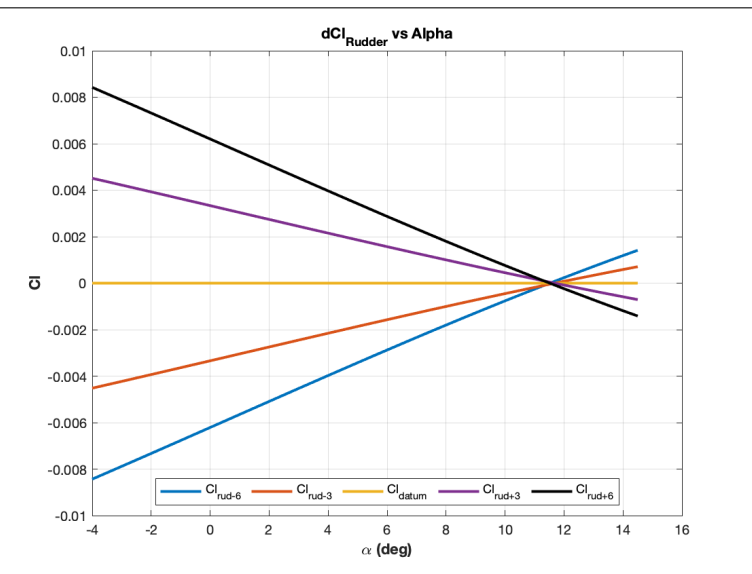
(a) dCn Aileron



(b) dCy Rudder

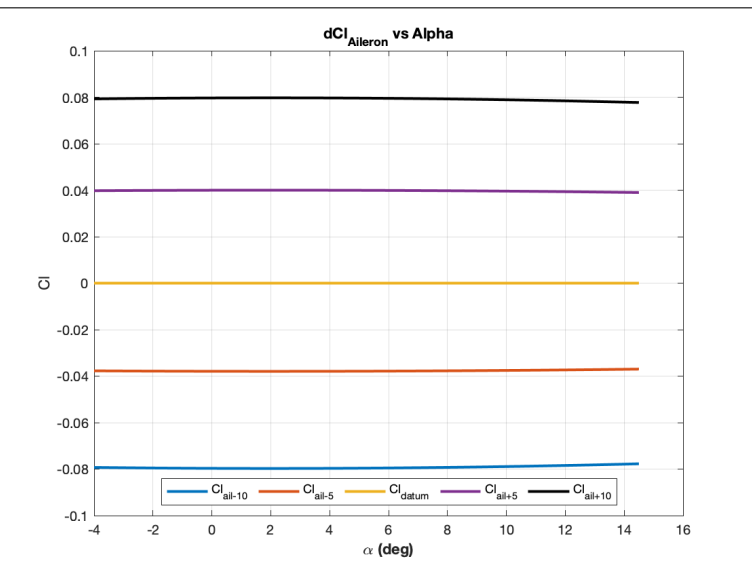


(b) dCy Aileron



(c) dCl Rudder

Figure 2.4 – dCn, dCy, dCl of Rudder



(c) dCl Aileron

Figure 2.5 – dCn, dCy, dCl of Aileron

### 3 Simulink Control Blocks

The full Simulink 6 degree of freedom (6DOF) model is shown in Figure 3.1 for the six-degree of freedom configuration. Not all blocks were utilized for the glide and climb tests, and a 3 degree of freedom model was used in these two tests to simplify and improve runtime.

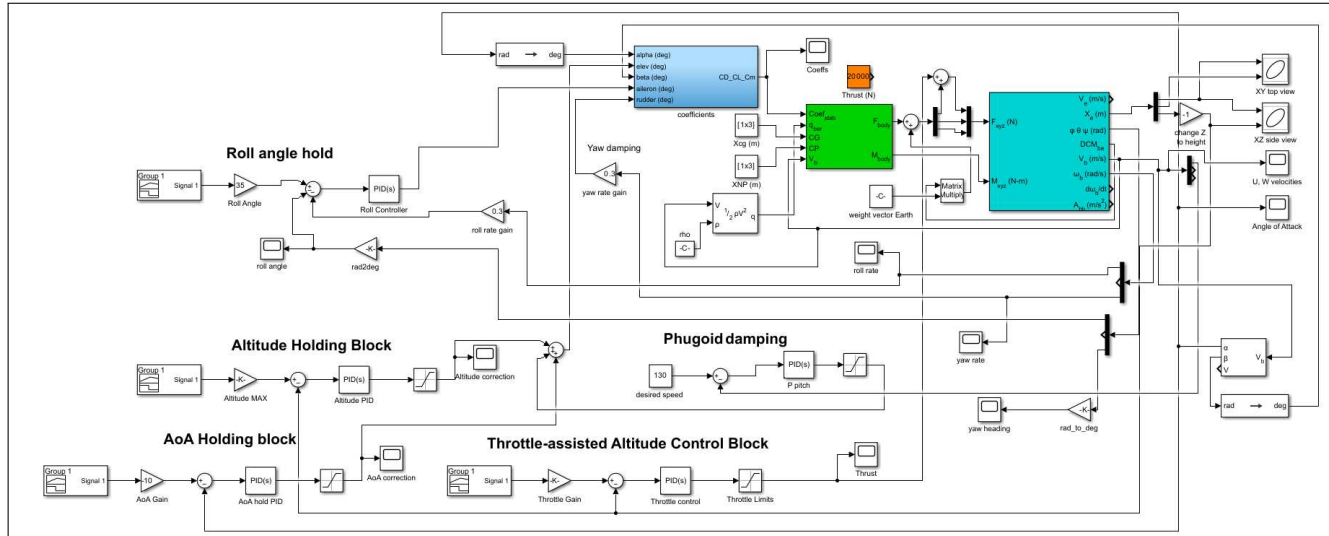


**Figure 3.1 – Full Simulink Model**

Each block of the control system is further zoomed in below, as well as a description of the feedback source and output signal destination. Deflection of the elevator was limited to  $\pm 20$  degrees. The throttle range in Figure 3.4 was limited to a range of 0 to 30,000 kilonewtons.

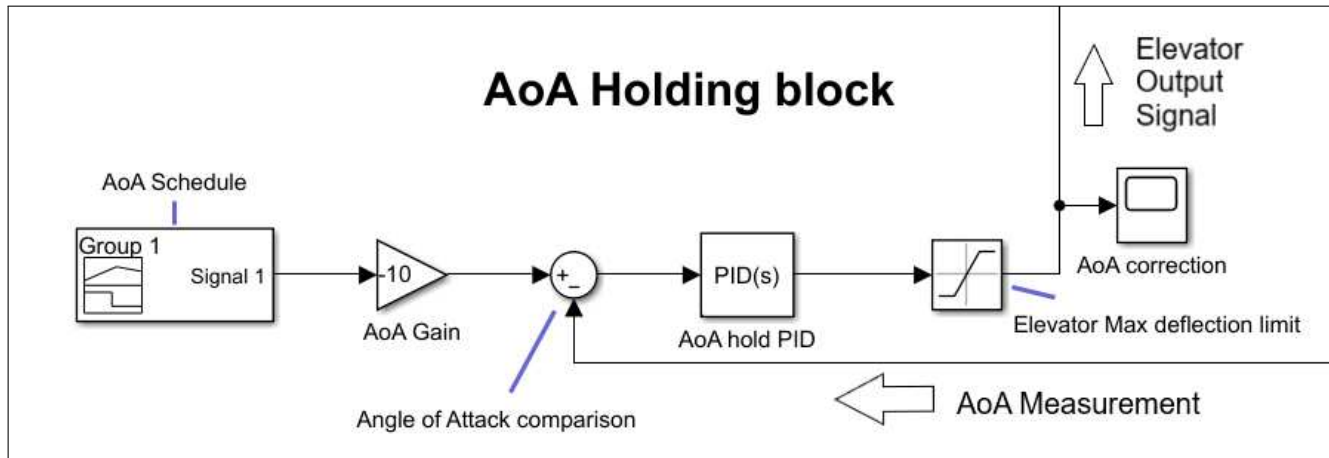


**Figure 3.2 – Angle Of Attack Holding Block**

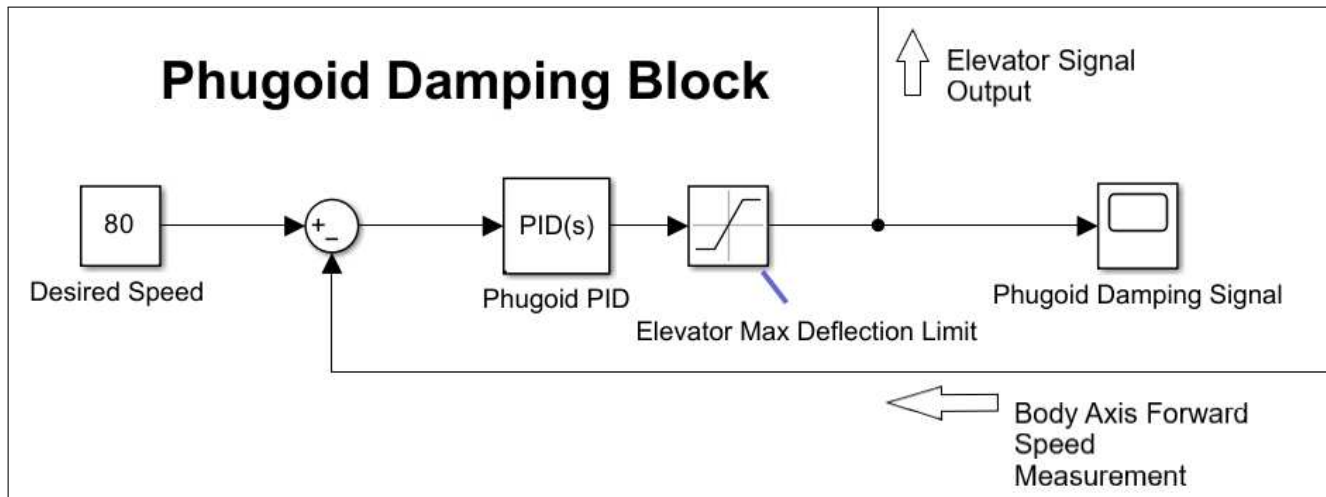


**Figure 3.3 – Phugoid Damping Block**

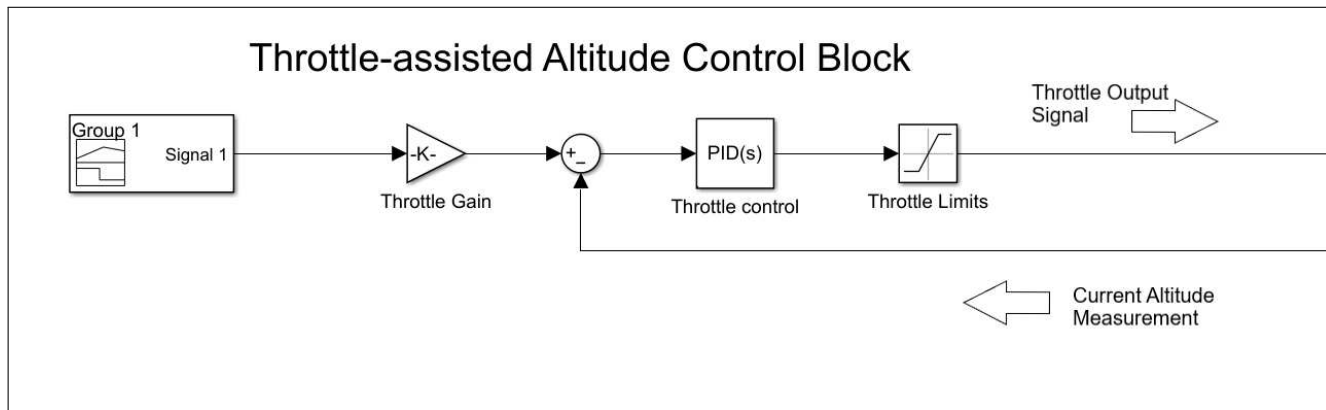


**Figure 3.4 – Throttle Control Block**

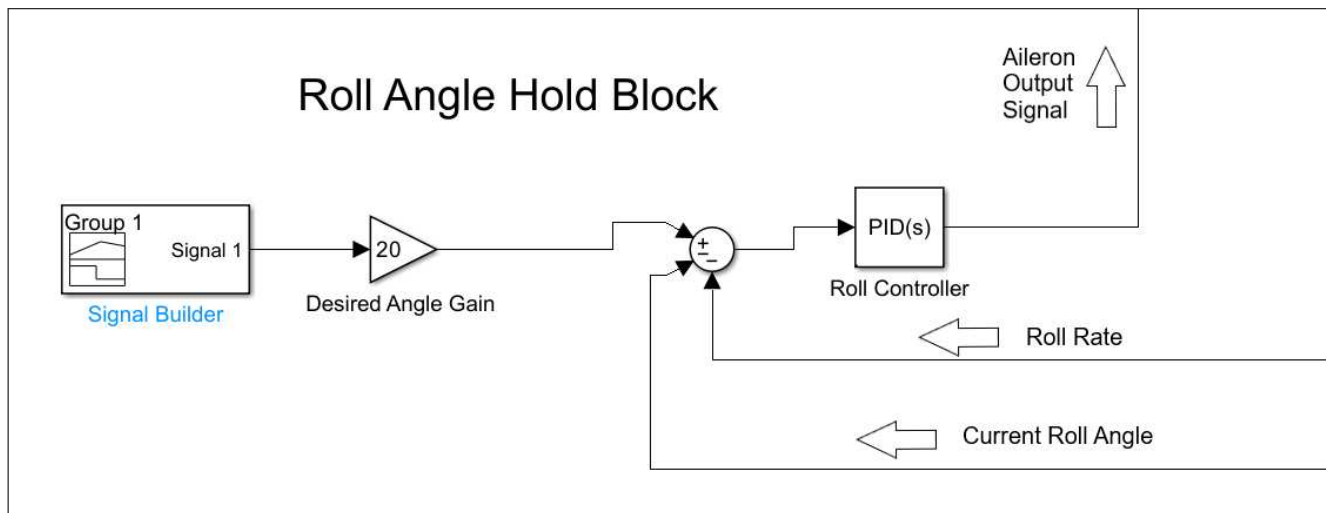


**Figure 3.5 – Roll Angle Holding Block**

PID Controllers were used in the blocks shown to control the aircraft during flight. The initial gains for the controllers were estimated using the Ziegler–Nichols method [8], with further adjustment

to reduce overshoot and attempt to improve settling time. I gain was not used in the throttle control due to the large instability and satisfactory performance of a PD system. Over damping was used in the altitude control systems to allow for a smooth transition to the desired altitude with no overshoot.

## 4 Glide Performance

The glide trajectory was found by releasing the aircraft from an altitude of 3,000 ft at its cruise speed of 180 knots with no thrust. The aircraft was trimmed and an elevator deflection of -3.23 degrees was used to damp the phugoid motion. The ailerons and rudder deflection angles were set at zero degrees as well. Figure 3.1 shows the X-Z trajectory of the glide. The aircraft lost an altitude of 3,000 ft and traveled a distance of 160,000 ft or (a glide of 32 miles) before it hit the ground. The calculated lift-to-drag ratio ( $L/D$ ) of 30.1 is high for an airplane of this size, but given the higher aspect ratio and limitation of drag calculation, the actual  $L/D$  is likely lower.

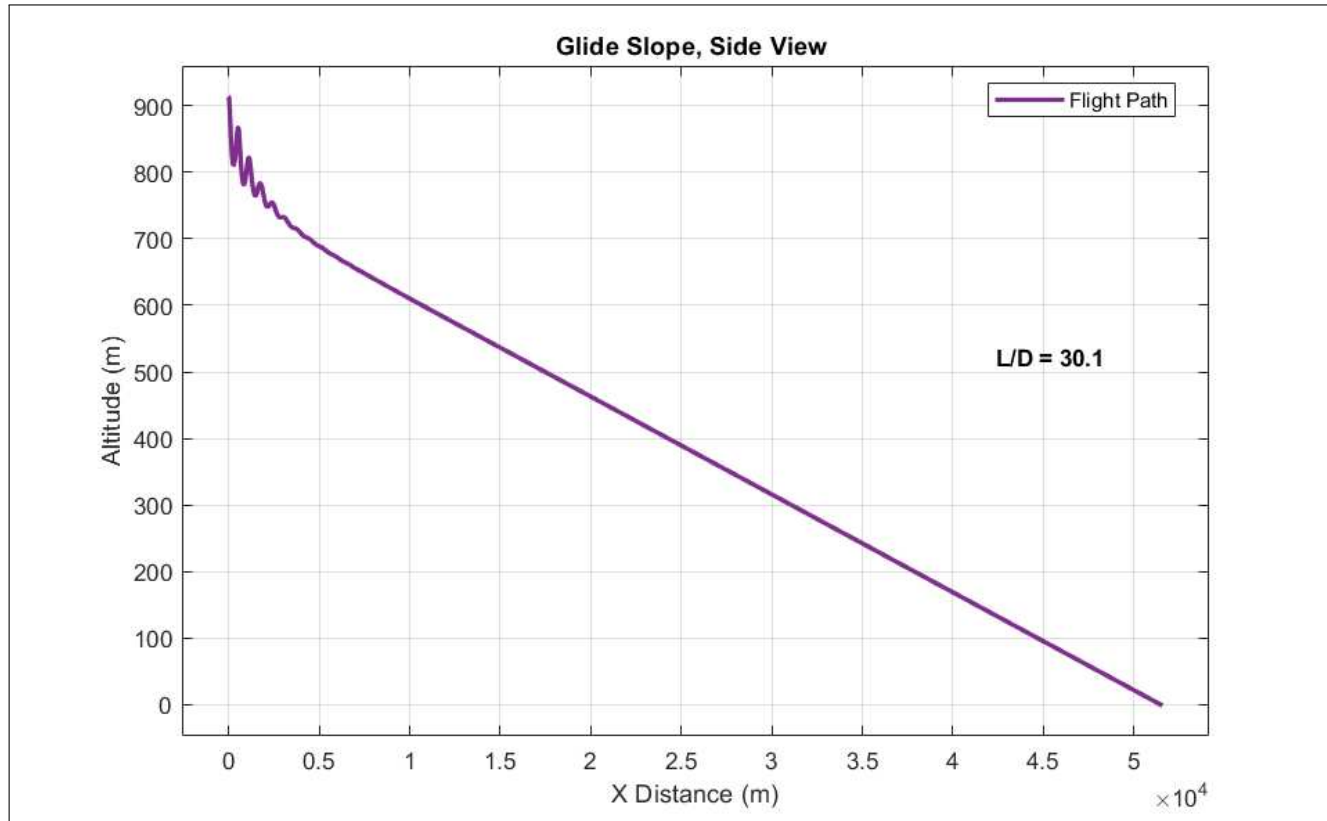


**Figure 4.1 – Glide Trajectory. (X,Z) Plane**

## 5 Takeoff and Climb Performance

For takeoff and climb, the aircraft must begin at rest at ground level, and climb to an altitude of 2500 feet above ground level (762 meters) with a climb rate greater than 600 feet per minute. The aircraft must then maintain level flight for 10 seconds afterward.

Maximum thrust was used for takeoff and climb, and reduced for cruising conditions. The maximum angle of attack experienced by the aircraft was 8 degrees shortly after takeoff, with a takeoff distance of 2378 ft (725 m) using Yechout [7] average acceleration method to find takeoff distance and time. At no point during climb did velocity drop below stall speed. Level flight was attained, with a small drop in altitude of .25 meters in the 10 seconds after leveling out.

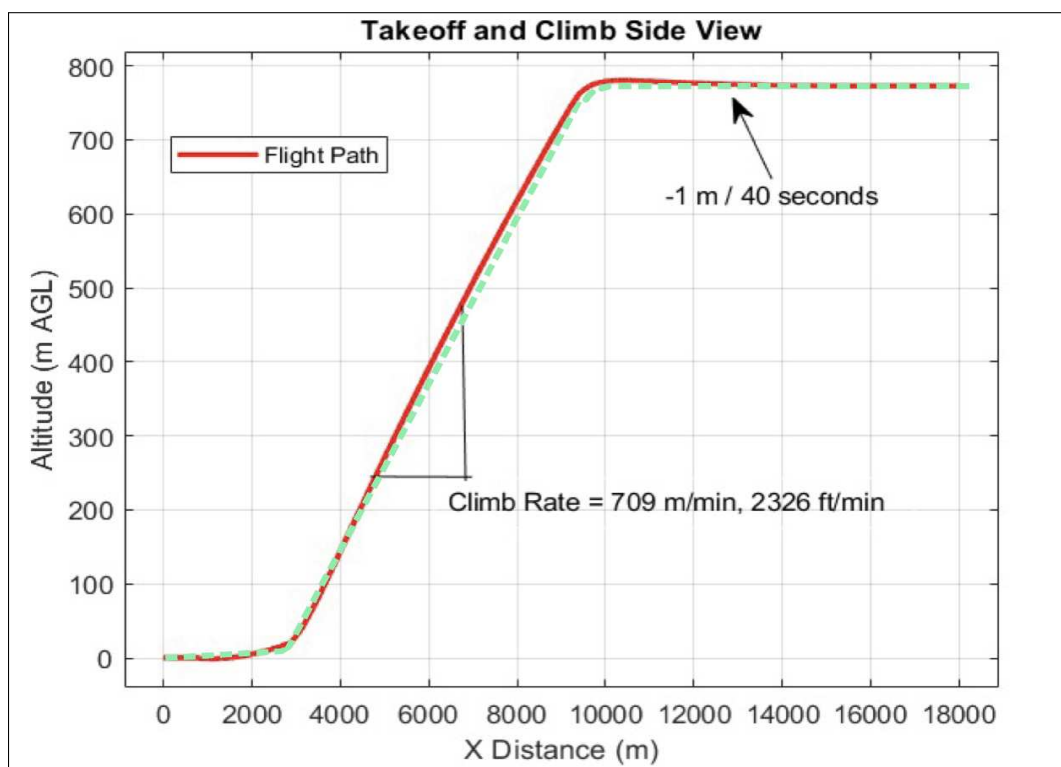


**Figure 5.1** – Take off and Climb. (X,Z) Plane

The climb rate of the aircraft was 2326 feet (709 meters) per minute. This is well above the 600 ft/min requirement, but is concerning. Investigation of the velocities indicate the craft was still accelerating during climb, up to a final velocity of 230 m/s. This excess velocity is the result of using maximum thrust for climb. Additionally, this may be caused by a failure to model viscous effects, compressibility effects, and stall prediction in this simulation. As a result of the high speed, elevator control is the dominant control method during the simulation. Further iteration would seek to more accurately model this climb prediction with a reduced throttle profile, better modelling of aerodynamic effects, and a plane speed control method.

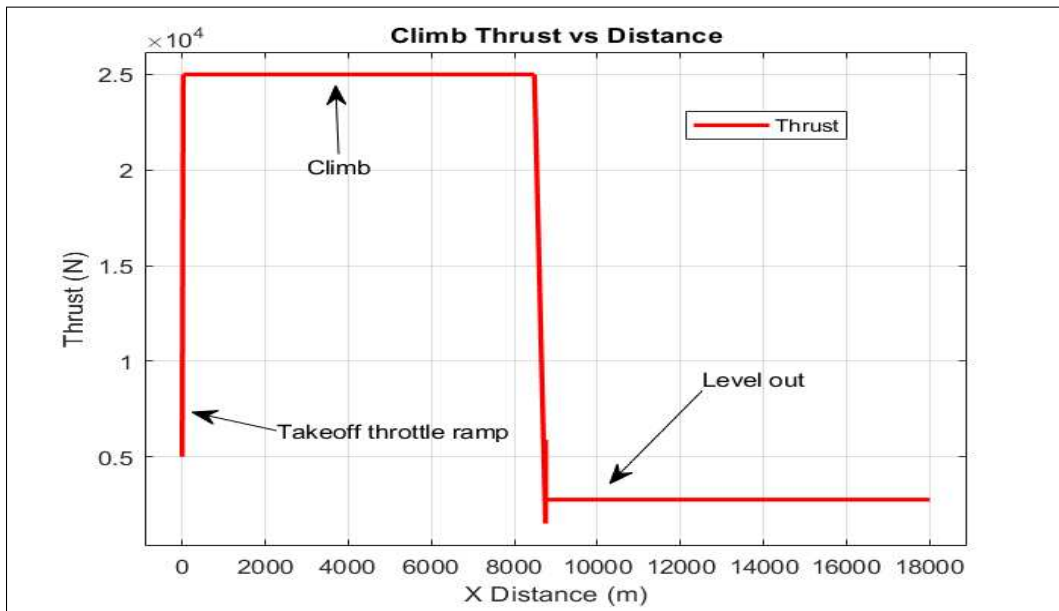


**Figure 5.2 – Thrust vs X-distance for Takeoff and Climb**

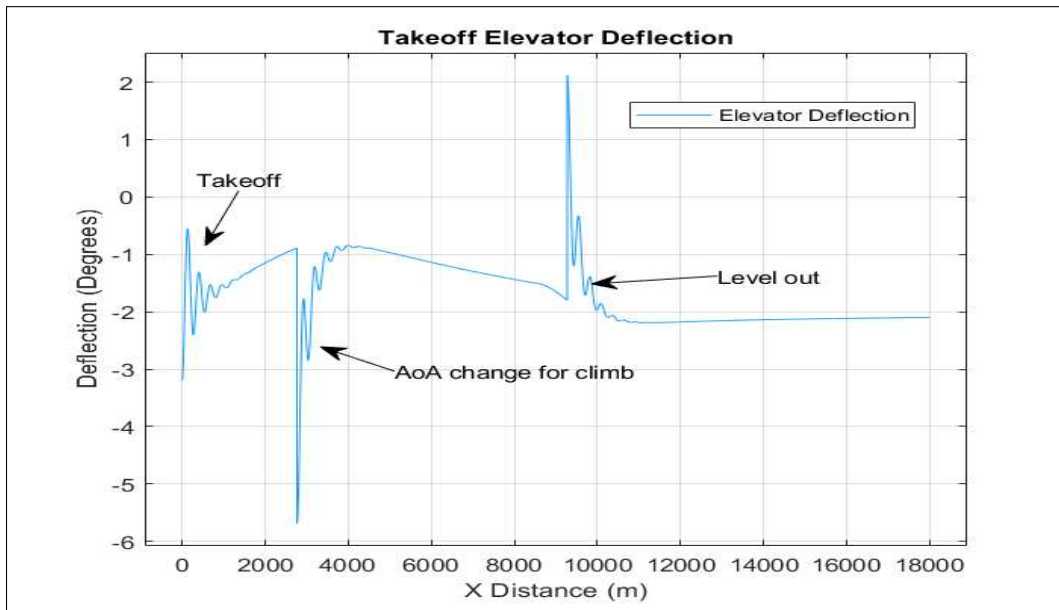


**Figure 5.3 – Elevator Deflection vs X-distance for Takeoff and Climb**

## 6 Holding Performance

The airplane is required to enter a holding pattern. The airplane uses a direct entry at 5,000 m (16,404 ft) above ground level (AGL) at a speed of approximately 253 kts (130 m/s). After flying for 1 minute, the plane makes a left turn at 3 deg/sec for 1 minute so that it is flying at 180 degrees from the original heading. The plane flies on this heading for 1 minute, then begins another 3 deg/sec left turn for 1 minute. The plane then is back on the inbound leg to the holding fix.

The results of the desired and actual (x,y) trajectory is shown in Figure 6.1. The bank angle used was 25 degrees. After damping the phugoid motion during the entry, the height of the aircraft during the pattern varies by approximately  $\pm 12$  meters (40 ft) see Figure 6.2. The distance between the inbound and outbound leg is approximately 6.32 miles. This can be reduced by increasing the bank angle and / or lowering the speed of the aircraft.

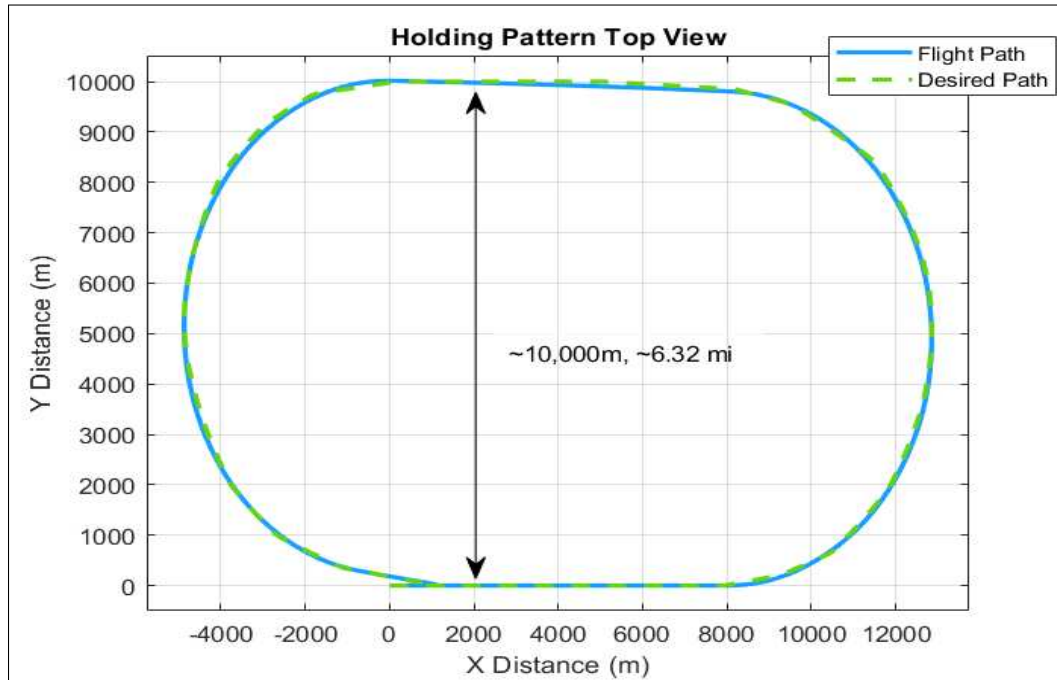


**Figure 6.1 – Hold Top View. (X,Y) Plane**

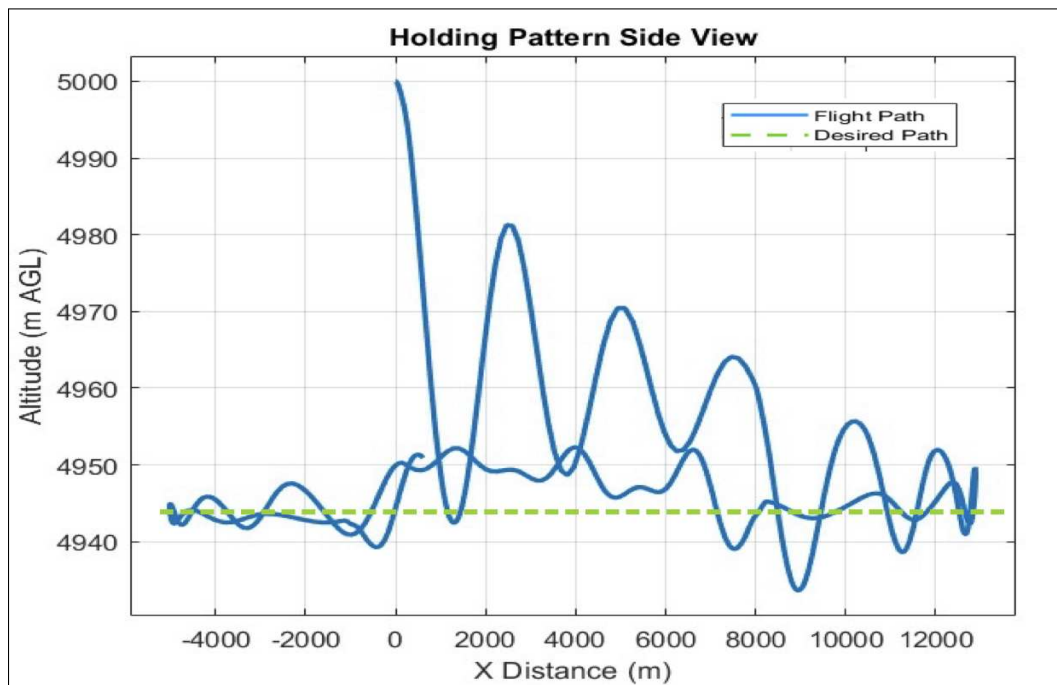


**Figure 6.2 – Hold Side View. (X,Z) Altitude Plane**

## 7 Landing Performance

For the first 25 seconds, the airplane enters the downwind leg of a left-hand landing pattern at 45 deg and an altitude of 1000 ft (305 m) AGL at a speed of 80 m/s (155 knots). The airplane then makes a 45 deg right turn to fly the downwind leg. It was then slowed down to an approach speed of 60 m/s (116.6 knots) in order to descend to 600 ft AGL on the downwind leg. Figure 7.1 shows the commanded and actual top view (x,y) flight trajectory. The airplane then makes a 90 deg left turn to fly the base leg. The airplane makes another left turn, which is aligned with the runway for its final approach maintaining its altitude and speed during the turn.

Figure 7.2 is the actual altitude trajectory (x,z) plot in comparison with the desired altitude trajectory. The distance between the downwind leg final landing is approximately 8 miles. This distance can be shortened via pilot control, and the long distance is a symptom of the overdamped altitude control, implemented to prevent ground strikes [7]. Figure 7.3 shows the roll angles commanded during landing. The targeted bank angle was 35 degrees. Thrust was varied during landing with a signal builder and PD controller to reduce thrust for landing after executing the turns. Thrust on final approach was reduced to zero for landing.

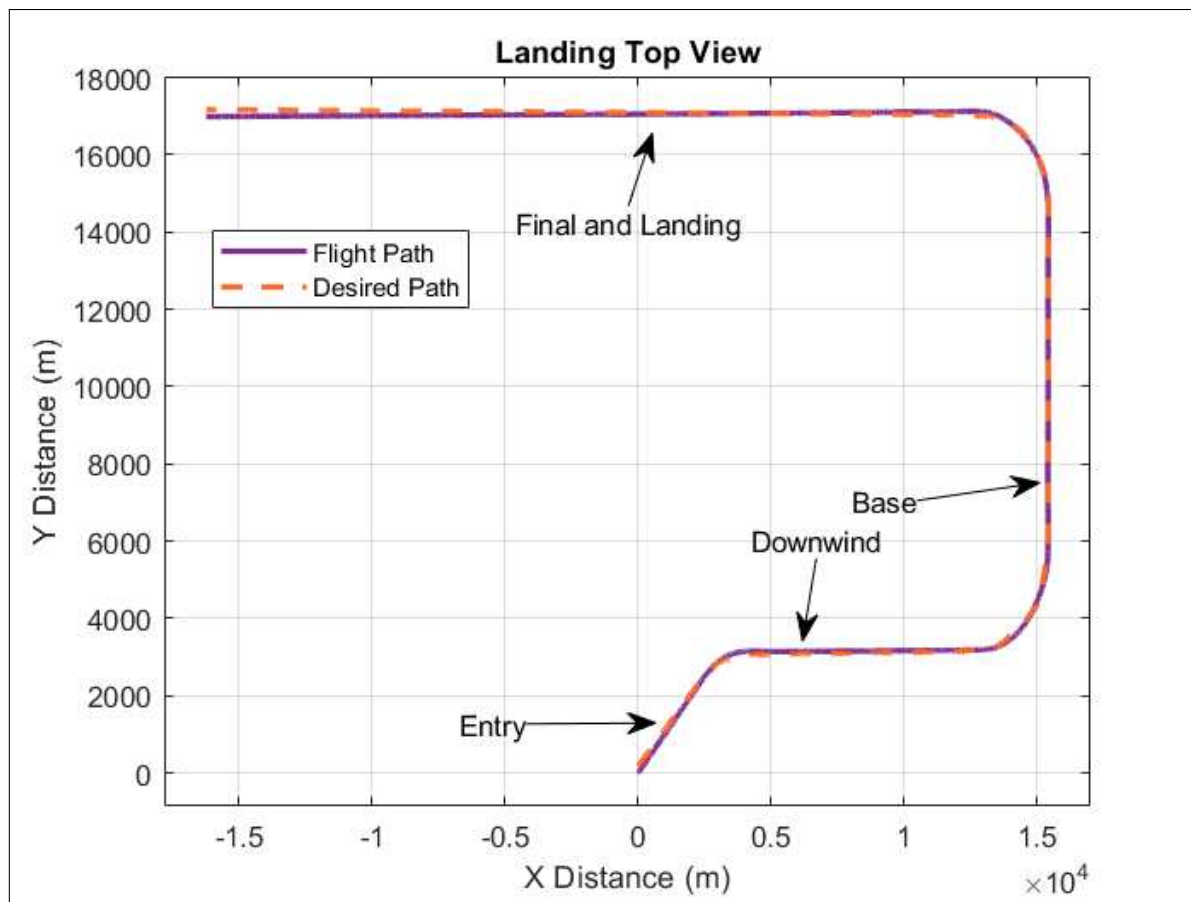


**Figure 7.1 – Landing Top View. (X,Y) Plane**

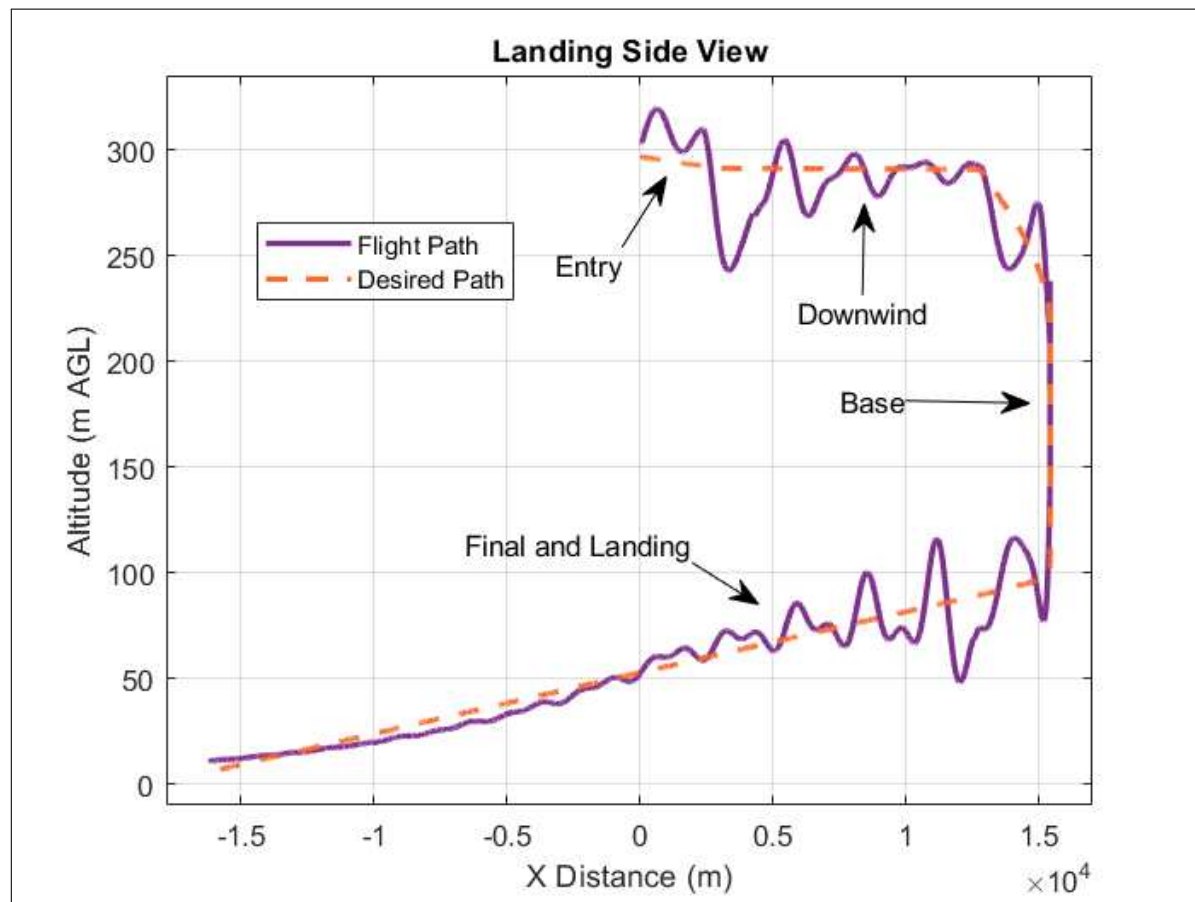


**Figure 7.2 – Landing Side View. (X,Z) Altitude Plane**

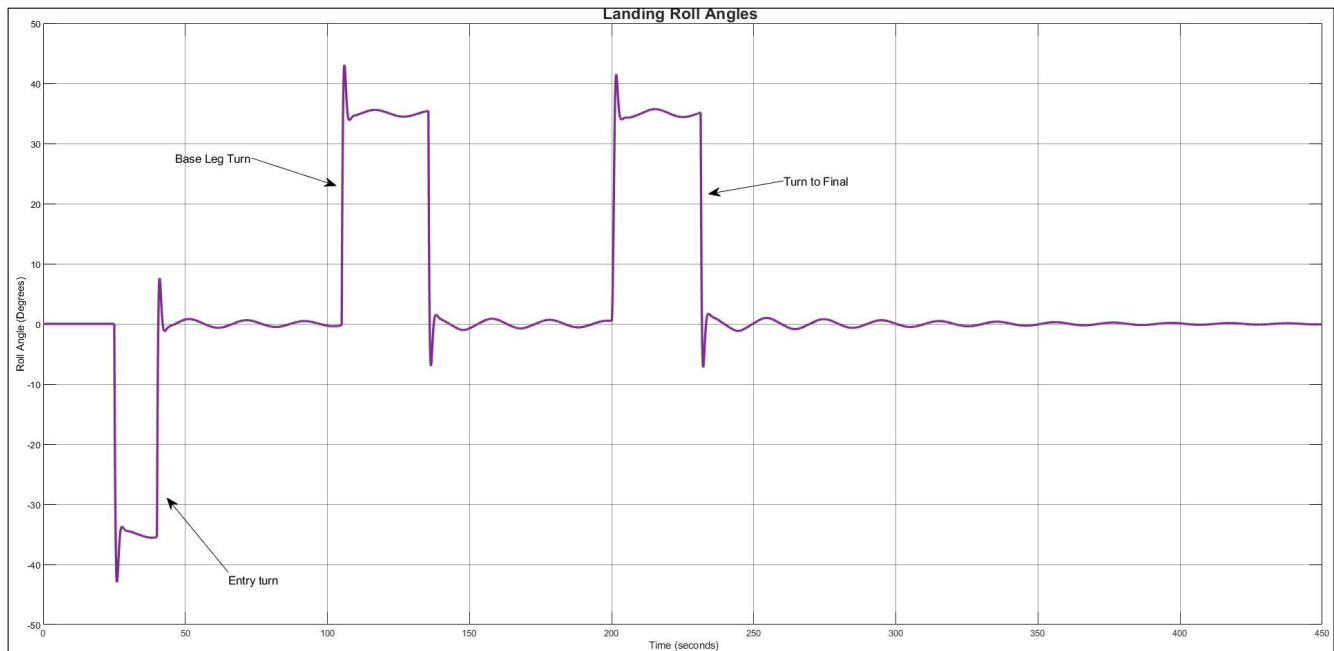


**Figure 7.3 – Landing Roll Angles**

## 8 Risk Analysis

The success of this project depends on meeting the performance metrics and thereby achieving the goals mentioned in the mission statement. Risk assessment assures the stakeholders, engineers and customers whether the plane is on track to be safe, hazard free, secure, and feasible for commercial use. It is impossible to avoid risks completely. However they can be prevented and mitigated ahead of time via risk analysis. In the time frame of product development, engineers usually have a way of anticipating the risks and accepting the technological risks encountered to a certain degree [6].

The team has provided a risk assessment definition in Table 8.1 based on the resources provided by Department of Defense [1], NASA Safety Measure [4], and United States Air force [3]. These sources provide the basic guideline to help assessing the risks and provide some mitigation mechanisms. They are divided in to two sections: Probability and Severity. Probability is the likelihood of risk to occur, while severity is the effect of the risk. To determine the risk assessments a color grading scale is provided in Table 8.2. Since this plane is a model only (no actual testing), the risks are mostly catered to the overall qualitative risk control. The risks anticipated column are color graded based on probability of that hazard occurring. Red colored risks will hinder all types of operation and may lead to complete failure of the mission. Light yellow/green are less likely to occur and thus may be accepted depending on the safety assessment. The values are assigned based on that specific risk severity.(i.e. 1 is catastrophic while 4 is negligible).

**Table 8.1 – Risk Definitions**

Risk Probability	Description
Frequent (A)	Often occurs, and is consistent threat to mission.
Probable (B)	Will occur several times in the life of an item
Occasional (C)	Likely to occur in the life span.
Remote (D)	Unlikely but Possible.
Improbable (E)	Highly unlikely to occur.
Eliminated (F)	Incapable of occurrence.
Risk Severity	Description
Catastrophic (1)	Could result in complete mission failure. death, irreversible impact.
Critical (2)	Results in partial disability, injuries, environmental impact, or monetary loss.
Marginal (3)	Injury or occupational illness for one or more lost work, moderate env-impact.
Negligible (4)	Injury or occupational illness not resulting in a lost work, minimal env-impact.

**Table 8.2 – IMT-22 Anticipated Qualitative Risk Grading**

Risk Probability	Risk Severity			
	Catastrophic (1)	Major (2)	Minor (3)	Negligible (4)
Frequent (A)	A1	A2	A3	A4
Probable (B)	B1	B2	B3	B4
Improbable (E)	E1	E2	E3	E4

## 8.1 Risk Control and Assessment

The IMT-22 airplane is designed by taking the main anticipated risks into account. The components are designed and selected in a manner they can mitigate and avoid the potential risks listed in Table 8.3. The risks are divided into three sections. The Pre-flight (conceptual design, modeling and testing) phase, Post-flight phase (after landing), and In-flight phase (operation and performance). For a potential risk hazard, mitigation solutions were incorporated based on FAA Part 25 [2] and NTSB Safety Measures [5]. Although there are no perfect solutions, mitigation measures seek to lessen the impact of foreseen risks should they arise.

**Table 8.3 – IMT-22 Risk Assessment**

Hazard	Assessment	Risk	Mitigation
<b>Pre Flight (testing, maintenance, simulation)</b>			
Operational Cost	B2	Delayed project timeline	Clarified method on fund acquisition & allocation
System Design (Manufacturing Delays)	A4	Hinder project timeline, and delivery	Controlled and designated resource - allocation. Supply chain reorganization.
Faulty component	B1	Fatal crash, death, serious environmental impact	Pre-certification testing, and routine maintenance
Technological Limitation	B4	Does not meet the 2035 entry	Active research and development, modular design
<b>In Flight (live operation and performance)</b>			
Electrical, Fuel, or Hydraulic issue	B1	May cause fatal crash or hull loss	Redundant systems, proper insulation and compartmentalizing
Thermal (Fire) Issues	B3	Engine, Electrical, Mechanical	Double wall bumpers, electrical insulation and gaps, battery fire-suppression system.
Foreign Airplanes	E1	Mid air collision, causing fatal crash	Active tracking of other airplanes, instrumentation
<b>Descend Flight (landing, taxi)</b>			
Possible Engine Failure	B1	Crash landing, Environmental damage, Fire	Fully battery power for 30 minutes Single engine capability with glide up to 32 miles.
Vibrational Wear	B3	Structural and payload damage	Incorporate force damping measures, distribute static loads, preventative maintenance.
Control Burnout	B4	Minor effects on landing performance	Provide engineered stall warning Pilot stick shake feedback Proper signs and warning alerts.

## 9 Conclusion

As shown on the Simulink and performance simulations, the IMT-22 achieves all the desired results. The aircraft can glide up to 32 miles, climb up to a rate of 709 ft/minute at 70% max thrust and can land with one or no engine. The fuel efficiency target was met and exceeded by 7%. The aircraft is also ICAO class C compliant and FAA Part 125 B and C certified. It can carry 54 passengers with luggage including crew, and takes off in under 2500 ft which is 2000 ft less than the required. The plane also exceeds the minimum cruise speed of 275 knots with a cruise speed of 350 knots (180 m/s), in addition to an additional 200 nautical miles of range over the required 1000 nautical miles.

Overall, the IMT-22 is a regional turboprop hybrid with an estimated 1200 nautical mile range, 52 passenger capacity, and 12660 pounds of passengers or cargo, all while reducing fuel usage by 27% when compared with current turboprop competitors. It is also reasonably priced and is expected to enter commercial service by 2035. Further efficiency gains may be found in future analysis through improved battery energy density, advanced composite techniques, and the addition of winglets to maximize the efficiency of the aircraft.

## 10 Appendix

### 10.1 Matlab Script for generating coefficients

```
%%%%% Eyob Modded Lab-12 on 11_20 %%%%%%
% Read 5 XFLR5 data files for the crater_maker design

Datum = csvread('Datum.csv',7,0,[7 0 44 12]);
%Elevator increment data
Data_en3 = csvread('Datum-3.csv',7,0,[7 0 44 12]);
Data_en5 = csvread('Datum-5.csv',7,0,[7 0 44 12]);
Data_ep3 = csvread('Datum+3.csv',7,0,[7 0 44 12]);
Data_ep5 = csvread('Datum+5.csv',7,0,[7 0 44 12]);
%Rudder Increment data
Data_rn5 = csvread('Datum_Fin-5.csv',7,0,[7 0 44 12]);
Data_rn10 = csvread('Datum_Fin-10.csv',7,0,[7 0 44 12]);
Data_rp5 = csvread('Datum_Fin+5.csv',7,0,[7 0 44 12]);
Data_rp10 = csvread('Datum_Fin+10.csv',7,0,[7 0 44 12]);
%Aileron Increment data
Data_an5 = csvread('DatumAil-5.csv',7,0,[7 0 44 12]);
Data_an10 = csvread('DatumAil-10.csv',7,0,[7 0 44 12]);
Data_ap5 = csvread('DatumAil+5.csv',7,0,[7 0 44 12]);
Data_ap10 = csvread('DatumAil+10.csv',7,0,[7 0 44 12]);
%Beta Increment data
Data_bp3 = csvread('Datum_Beta+3.csv',7,0,[7 0 44 12]);
Data_bn3 = csvread('Datum_Beta-3.csv',7,0,[7 0 44 12]);
Data_bp6 = csvread('Datum_Beta+6.csv',7,0,[7 0 44 12]);
Data_bn6 = csvread('Datum_Beta-6.csv',7,0,[7 0 44 12]);

% datum values
alpha = Datum(:,1); % read angles of attack
% alpha = alpha(1:48);
CL_datum = Datum(:,3);
% CL_datum1 = CL_datum(1:38);
CD_datum = Datum(:,6);
% CD_datum1 = CD_datum(1:38);
Cm_datum = Datum(:,9);
% Cm_datum1 = Cm_datum(1:38);
```

```
% Create side force increment vectors for beta
dCY_bn6 = Data_bn6(:,7) - CY_datum(1:38);
dCY_bn3 = Data_bn3(:,7) - CY_datum(1:38);
dCY_b0 = CY_datum - CY_datum; %Should be all zeros
dCY_bp3 = Data_bp3(:,7) - CY_datum(1:38);
dCY_bp6 = Data_bp6(:,7) - CY_datum(1:38);

% Create roll moment increment vectors for beta
dCl_bn6 = Data_bn6(:,8) - Cl_datum(1:38);
dCl_bn3 = Data_bn3(:,8) - Cl_datum(1:38);
dCl_b0 = Cl_datum - Cl_datum; %Should be all zeros
dCl_bp3 = Data_bp3(:,8) - Cl_datum(1:38);
dCl_bp6 = Data_bp6(:,8) - Cl_datum(1:38);

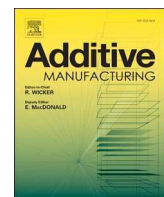
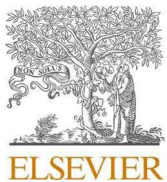
% Create yaw moment increment vectors for beta
dCn_bn6 = Data_bn6(:,10) - Cn_datum(1:38);
dCn_bn3 = Data_bn3(:,10) - Cn_datum(1:38);
dCn_b0 = Cn_datum - Cn_datum; %Should be all zeros
dCn_bp3 = Data_bp3(:,10) - Cn_datum(1:38);
dCn_bp6 = Data_bp6(:,10) - Cn_datum(1:38);

% Sideslip angle increment vector
dbeta = [-6, -3, 0, 3, 6];

% Combine vectors into single array for each variable
dCY_beta_alpha = [dCY_bn6(1:38), dCY_bn3(1:38), dCY_b0(1:38), dCY_bp3(1:38), dCY_bp6(1:38)]
dCl_beta_alpha = [dCl_bn6(1:38), dCl_bn3(1:38), dCl_b0(1:38), dCl_bp3(1:38), dCl_bp6(1:38)]
dCn_beta_alpha = [dCn_bn6(1:38), dCn_bn3(1:38), dCn_b0(1:38), dCn_bp3(1:38), dCn_bp6(1:38)]

% Save to a .mat file
save('dCY_beta_alpha.mat', 'dCY_beta_alpha')
save('dCl_beta_alpha.mat', 'dCl_beta_alpha')
save('dCn_beta_alpha.mat', 'dCn_beta_alpha')
```

# PROJECT FIVE



## Laser-beam powder bed fusion of cost-effective non-spherical hydride-dehydride Ti-6Al-4V alloy



Mohammadreza Asherloo<sup>a</sup>, Ziheng Wu<sup>b</sup>, Melody H. Delpazir<sup>a</sup>, Eyob Ghebreiesus<sup>a</sup>, Sara Fryzlewicz<sup>c</sup>, Runbo Jiang<sup>b</sup>, Benjamin Gould<sup>d</sup>, Mike Heim<sup>e</sup>, Dave Nelson<sup>e</sup>, Mike Marucci<sup>f</sup>, Muktesh Paliwal<sup>f</sup>, Anthony D. Rollett<sup>b</sup>, Amir Mostafaei<sup>a,\*</sup>

<sup>a</sup> Department of Mechanical, Materials and Aerospace Engineering, Illinois Institute of Technology, 10W 32nd Street, Chicago, IL 60616, USA

<sup>b</sup> Department of Materials Science and Engineering, Carnegie Mellon University, Pittsburgh, PA 15213, USA

<sup>c</sup> Department of Computer Science, Illinois Institute of Technology, 10 W 31st Street, Chicago, IL 60616, USA

<sup>d</sup> Applied Materials Division, Argonne National Laboratory, Lemont, IL 60439, USA

<sup>e</sup> Nel Pretech Corporation, 8420 183rd Place, Tinley Park, IL 60487, USA

<sup>f</sup> Kymera International - Reading Alloys, Robesonia, PA 19551, USA

### ARTICLE INFO

#### Keywords:

Additive manufacturing

Process map

Build rate

Porosity

Synchrotron-based dynamic x-ray radiography

### ABSTRACT

Hydride-dehydride (HDH) Ti-6Al-4V powders with non-spherical particle morphology are typically not used in laser-beam powder bed fusion (LB-PBF). Here, HDH powders with two size distributions of 50–120 µm (fine) and 75–175 µm (coarse) are compared for flowability, packing density, and resultant density of the LB-PBF manufactured parts. It is shown that a suitable laser power-velocity-hatch spacing combination can result in part production with a relative density of > 99.5% in LB-PBF of HDH Ti-6Al-4V powder. Size, morphology, and spatial distribution of pores are analyzed in 2D. The boundaries of the lack-of-fusion and keyhole porosity formation regimes are assessed and results showed parts with a relative density of > 99.5% could be LPBF processed at a build rate of 1.5–2 times of the nominal production rates in LPBF machines. The synchrotron x-ray high-speed imaging reveals the laser-powder interaction and potential porosity formation mechanism associated with HDH powder. It is found that lower powder packing density of coarse powder and high keyhole fluctuation result in higher fractions of porosity within builds during the LB-PBF process.

### 1. Introduction

In powder-based metal additive manufacturing (AM), both the feedstock and the 3D-printing processes considerably affect the part integrity and cost of the manufactured components. Spherical powders have been extensively used in LB-PBF machines, and there have been various concerns related to powder (i.e., entrapped gas), processing defects (e.g., pores, spatter, roughness), part quality, and performance. Also, the production of fine powder is expensive which reduces their competitiveness and limits their commercial scale-up. Compared to conventional atomized pre-alloyed powder with spherical morphologies, the direct synthesis of non-spherically shaped powder via chemical and mechanical milling methods results in pore-free particles that are more economically efficient [1–3].

Ti-6Al-4V is one of the most popular alloys in metal AM primarily due to its wide application, e.g., aerospace components and orthopedic

implants [4]. Gas atomization (GA) is the primary powder manufacturing process that supplies powder for the metal AM industry [5]. The standard procedure is extremely energy-intensive and relatively expensive. Therefore, alternative powder production methods are required, which would be cost-effective for being used in metal additive manufacturing. In recent years, many technologies for the production of low-cost Ti-powder have become commercialized [6,7]. The hydride-dehydride (HDH) process is an alternative way to produce Ti-6Al-4V powder by using the brittle nature of titanium hydride. This process has the potential to be much greener and has a significantly lower eco-impact. Compared with GA powder, a lower production cost is the primary advantage that comes with HDH powder; depending on the powder size distribution, the powder cost can be reduced by more than 30% [8,9]. Additionally, it is possible to eliminate the presence of entrapped gas porosity, which can be inherited by as-built AM components and affect the resulting mechanical performance [5,10]. The HDH

\* Corresponding author.

E-mail address: [mostafaei@iit.edu](mailto:mostafaei@iit.edu) (A. Mostafaei).

powder with non-spherical particle morphology and larger powder size would decrease spattered particles due to the mechanical interlocking characteristics and higher weight compared to gas atomized powder with PSD of  $< 50 \mu\text{m}$  [11].

Replacing GA with HDH powder in AM can be challenging and requires a substantial amount of research to understand the physics of laser-powder interaction, melt pool dynamics, and possible defect formation mechanisms [12]. These challenges are primarily caused by the non-spherical powder morphology. Size control is more difficult with HDH powder owing to its non-spherical morphology; for instance, an elongated particle can pass through a finer sieve with its smallest dimension during the screening process resulting in a powder batch with larger size distribution. This will also affect the packing density in the powder bed of HDH powder. Recently, studies have been conducted to use non-spherical powder in the PBF AM processes. Medina [13] studied the effect of blending HDH titanium powder with spherical one in order to reduce the cost of part production and was able to increase the density of the parts using the double melting in electron beam AM. Li et al. [14] reported on the use of another type of non-spherical powder, i.e., water atomized (WA) powder in LB-PBF. They concluded that GA 316 L stainless steel powders yield higher density parts because of lower oxygen content and higher packing density compared to WA. Rogalsky et al. [9] investigated the use of non-spherical WA iron powder in LB-PBF and showed that the poor packing density of this type of powder results in lower laser adsorption and final part density, however, by using a powder layer thickness of 60  $\mu\text{m}$  compared to 40  $\mu\text{m}$ , the impact of packing density on final parts was insignificant. Varela et al. [15] investigated LB-PBF of non-spherical HDH Ti-6Al-4V powder (mono-modal particle size distribution with  $D_{10}$ ,  $D_{50}$ , and  $D_{90}$  of 54.9, 72.7, and 88.9  $\mu\text{m}$ ) and were able to manufacture parts with a relative density of 98.9% (using layer thickness of 30  $\mu\text{m}$ , and the optimum process parameter is missing).

There are both fundamental and industrial reasons for understanding how the powder characteristics of the HDH powders (due to differences in powder packing density and powder flowability as compared to spherical particles) may affect the characteristics of thermal profile, microstructure, and defect content as well as cost and speed of production. Here, we choose to use LB-PBF on HDH Ti-6Al-4V powders. The

feedstock powder is analyzed to understand how morphology and particle size distribution affect the AM process. Additionally, LB-PBF parameters such as laser power, scan speed, and hatch spacing are optimized to determine a process window with a relative density of  $> 99.5\%$  in as-built parts. Density measurements, including Archimedes and segmented 2D optical micrographs, are performed. Synchrotron-based dynamic x-ray radiography visualizes laser-powder interaction and potential porosity formation mechanisms associated with HDH powder. Selected samples are further evaluated for microstructure, phase formation, and porosity.

## 2. Experimental procedures

### 2.1. Feedstock powder

Ti-6Al-4V feedstock powder with two different mean sizes and particle size distributions (PSD) were supplied by Kymera International - Reading Alloys. Fig. 1 showed that both powders had non-spherical morphology characterized by scanning electron microscopy (JEOL 5900LV), and, based on the manufacturer's specification, the particle size distributions were in the range 50–120  $\mu\text{m}$  for the fine powder (Fig. 1a,b) and 75–175  $\mu\text{m}$  for the coarse powder (Fig. 1c,d). The chemical compositions of the feedstock powders provided by the manufacturer are given in.

Table 1 and compared to the nominal Ti-6Al-4V alloy. To acquire the mean size and PSD, a total of  $\sim 1100$  HDH powder particles were imaged (using an FEI Aspex Express SEM microscope) to ensure adequate powder statistics, and results are illustrated in Fig. 1e. The coarse powder showed monomodal size distribution with powder size of  $d_{10} = 83 \mu\text{m}$ ,  $d_{50} = 109 \mu\text{m}$ , and  $d_{90} = 142 \mu\text{m}$  with a mean size of 112  $\mu\text{m}$  and average circularity of 0.46, whereas the fine powder showed a bimodal size distribution with powder size of  $d_{10} = 28 \mu\text{m}$ ,  $d_{50} = 82 \mu\text{m}$  and  $d_{90} = 103 \mu\text{m}$  with a mean size of 76  $\mu\text{m}$  and average circularity of 0.68. The flowability of HDH powders was characterized with a Freeman FT4 rheometer; more specifically, the powder-specific energy (SE) and the bulk flow energy (BFE) were measured.

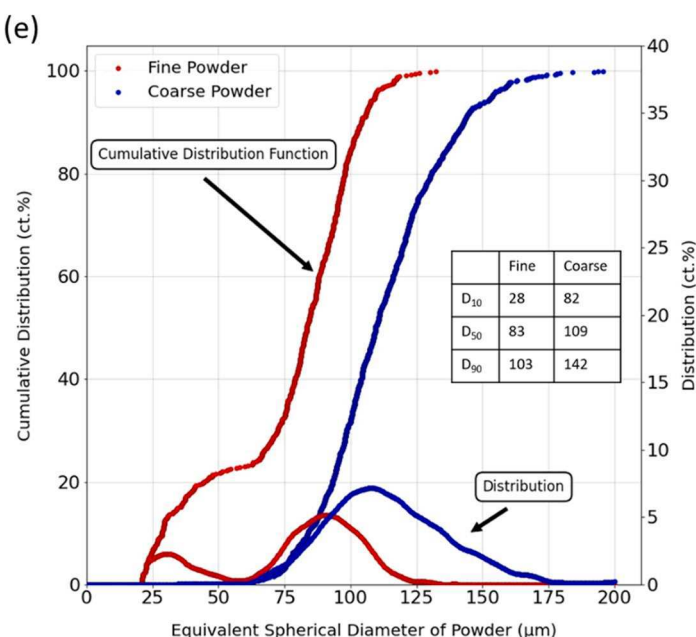
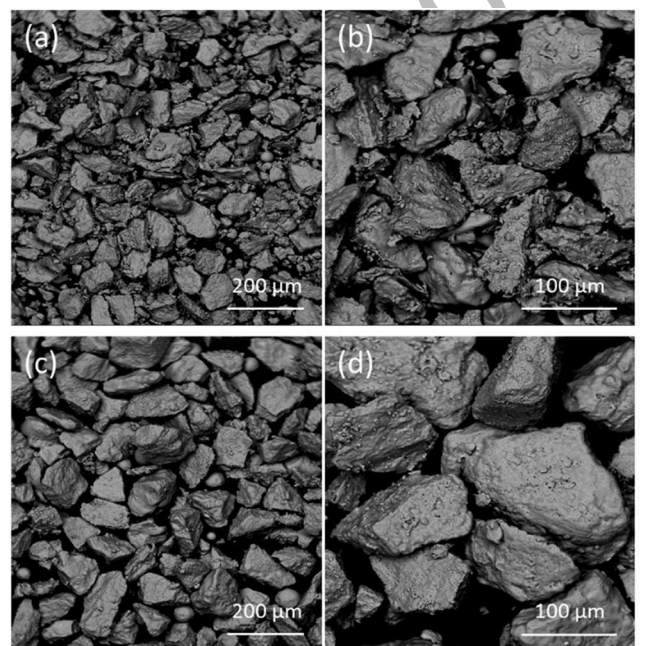


Fig. 1. SEM micrographs of the HDH Ti-6Al-4V powders at two magnifications; (a,b) fine powder and (c,d) coarse powder. (e) Particle size distribution measured via SEM image analysis and ImageJ software.

**Table 1**

Nominal chemical composition of Ti-6Al-4V alloy and the feedstock HDH Ti-6Al-4V powder provided by the manufacturer [wt%].

ASTM B 348[16]	Ti	Al	V	Fe	C	H	N	O
	Bal.	5.5–6.75	3.5–4.5	< 0.40	< 0.08	< 0.015	< 0.05	< 0.20
Fine powder	Bal.	6.08	3.88	0.19	0.02	0.005	0.02	0.17
Coarse powder	Bal.	6.02	3.92	0.22	0.03	0.006	0.02	0.17

## 2.2. Laser-beam powder bed fusion

To develop a processing map for the HDH Ti-6Al-4 V powder with the two size distributions, different combinations of laser power (P), scan speed (or velocity, V), and hatch spacing (H) were selected (see Fig. 2a). Fifty-three combinations of P-V-H were chosen to manufacture coupons of  $15 \times 10 \times 10$  mm<sup>3</sup> using an EOS M290 machine from the fine and coarse HDH Ti-6Al-4 V powders. The layer thickness was constant at 60  $\mu\text{m}$  (see ref. [17] for the reason of thickness selection). For each combination, two samples were LB-PBF processed to evaluate the printability of HDH powders. Fig. 2b shows the layout of all as-built coupons fabricated on the base plate, and parts were removed using wire electrical discharge machining (GF Machining Solutions AC Progress VP3 Wire EDM Machine).

## 2.3. Characterizations of as-build coupons

The relative density of the as-built coupons was measured using the Archimedes method to evaluate the density of the replicated coupons, and it was found that the standard deviation (std) was between 0.002 and 0.5. Smaller std values were attained for samples with relative densities of > 99.9%. As-built samples were cross-sectioned parallel to the build direction using an EDM machine (Mitsubishi FX10k Wire EDM Machine) and mounted by fast cure acrylic powder resin and hardener (MetLab) for metallographic observations. Then, mounted samples were ground using sandpapers up to 800 grit sizes and polished using 3  $\mu\text{m}$  diamond solution, 1  $\mu\text{m}$ , and 0.05  $\mu\text{m}$  alumina solution, then, samples were etched using Kroll's reagent. A Nikon Eclipse MA200 optical microscope was utilized to analyze the porosity. Optical images were taken from the entire vertical cross-section of sample surfaces at a magnification of 50  $\times$  with a resolution of 1280  $\times$  960 pixels and then were stitched, converted to binary with the suitable threshold, and analyzed using ImageJ software [18] to determine the percentage and size distribution of pores. The Vickers microhardness was measured on the vertical cross-section of the LB-PBF Ti-6Al-4V parts (fine powder) using a Buehler Micromet 2 machine with a load of 500 g and a dwell time of 15 s. Ten indentations were conducted on each sample, and the average number was reported.

## 2.4. High-speed synchrotron x-ray imaging

The dynamic x-ray radiography (DXR) experiments were performed at the 32-ID-B beamline of the Advanced Photon Source at Argonne National Lab. To replicate the laser melting conditions of the LB-PBF process, a miniature single-bead powder bed was set up in an argon (1 atm) chamber where a ytterbium fiber laser with a wavelength of 1070 nm, maximum output power of 540 W, and spot size of 71.5  $\mu\text{m}$  scans from the top. The powder bed consists of a powder layer ( $\sim 200 \mu\text{m}$ ) and a thin slab (1 mm thickness  $\times$  2.89 mm height) of Ti-6Al-4V substrate. The powder layer was placed on the top surface of the substrate which was sandwiched by two glassy carbon plates (1 mm thickness  $\times$  3 mm height). Polychromatic x-rays with the first harmonic energy of 24.4 keV were used to illuminate the powder bed. The transmitted x-rays were converted into visible light by a LuAG:Ce scintillator and later captured by a Photron FastCam SA-Z high-speed camera at a frame rate of 25,000 Hz.

## 2.5. Powder packing analysis

The powder packing analysis utilized the 2D vertical cross-sections of the powder computed tomography (CT) shown in Fig. 3a as the input. The CT dataset was acquired in a Zeiss Metrotom 800 system using x-rays with 85 kV and 47 mA resulting in a spatial resolution of 5.4  $\mu\text{m}/\text{pixel}$ . The powder specimen was contained in a Kapton tube with an inner diameter of approximately 3.49 mm. Fig. 3b shows an example of a synthetic powder bed image consisting of a 120  $\mu\text{m}$  powder layer, which was extracted from the powder tomography, and a solid substrate, which was assumed to be fully dense and possessed a smooth top surface. The selection of the 120  $\mu\text{m}$  powder layer thickness was based on the 60  $\mu\text{m}$  layer thickness used in the actual LB-PBF fabrication. As discussed in many studies [19,20] the powder layer thickness converges to a value, which can be approximated by  $(\frac{\text{layer thickness}}{\text{powder packing fraction}})$ , after the first ten layers of deposition. Semi-circular melt pools with various depths, from 43.2  $\mu\text{m}$  to 411.2  $\mu\text{m}$  with an increment of 21.6  $\mu\text{m}$ , were overlaid on the powder bed image where only the overlapping area was used in the packing fraction calculation, i.e., the ratio between the black solid pixel and the white empty pixel, as shown in Fig. 3b. Once the

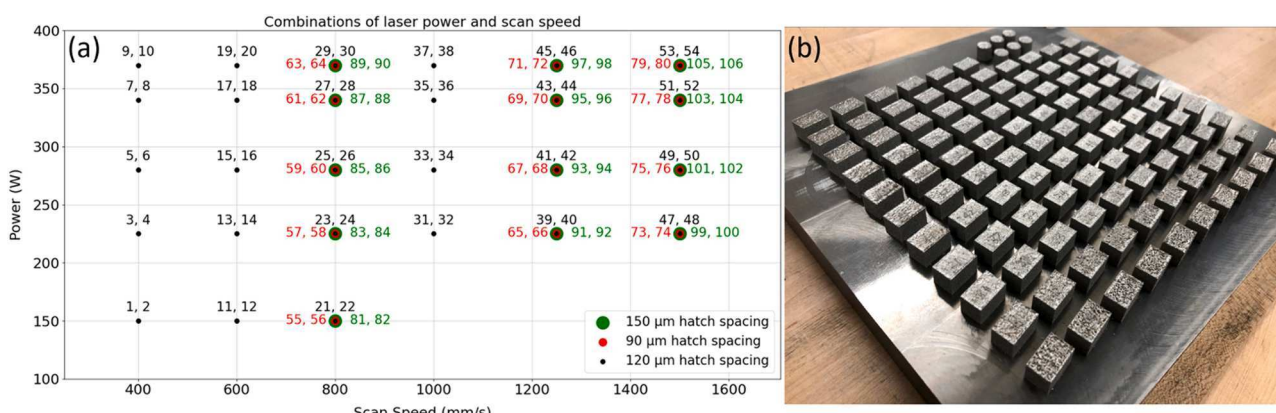


**Fig. 2.** (a) An overview indicating process parameter combinations associated with sample numbers in which two coupons were LB-PBF processed for each P-V-H combination. (b) Photograph of the LB-PBF processed HDH Ti-6Al-4 V parts to optimize process parameters of laser power, scan speed, and hatch spacing using the HDH powders.

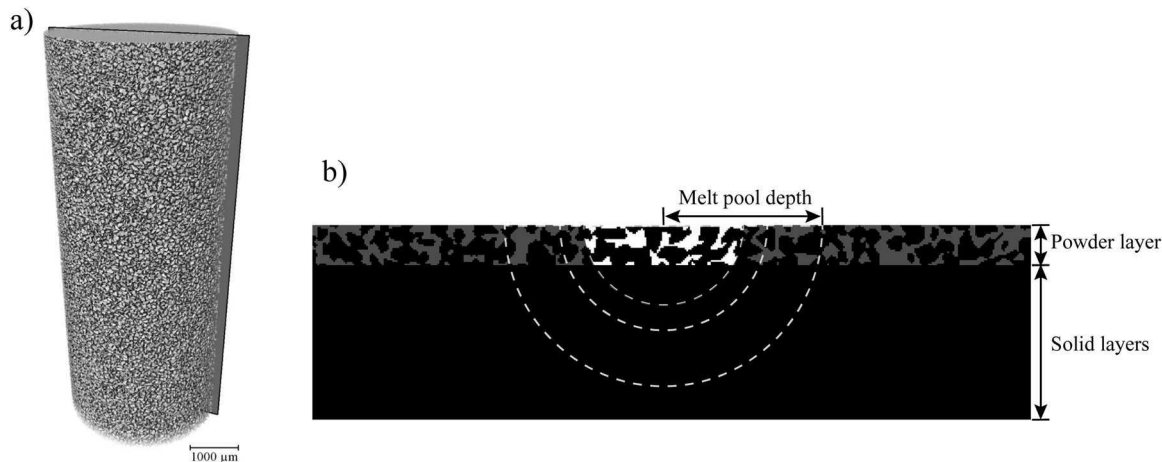


**Fig. 3.** CT of the fine HDH powder with a cross-sectional plane demonstrating how the powder images were extracted in (a) and (b) an example synthetic powder bed image with semi-circular melt pools showing how the powder packing fraction was calculated.

packing calculations at all melt pool sizes were completed, the model repeats the same process on a new powder bed image. A total of 660 images were used in this study.

### 3. Results and discussion

#### 3.1. Powder flowability

Flowability is an important indicator of powder's spreadability and printability, which is essential to the quality of powder bed in additive manufacturing. With the irregular shape, HDH powder is expected to have lower flowability than GA powder owing to powder interlocking during spreading. It is shown in [8] that the GA powder had BFE and SE values of 365 mJ and 2.32 mJ/g, respectively, whereas for the HDH powder, they were 319 mJ and 2.40 mJ/g in coarse powder and 341 mJ and 2.7 mJ/g in fine powder, respectively. Surprisingly, the used HDH powders with the powder size distributions of 50–120 μm and 75–175 μm had even better flowability than GA powder with a powder size distribution of 20–63 μm. This better powder flow of the HDH powder is most likely because coarse powders are known to flow better than fine ones. The good flowability enables us to spread and form a

high-quality HDH powder bed during LB-PBF to fabricate nearly fully dense components.

#### 3.2. Powder packing analysis using powder tomography

Average packing fraction is the popular metric for quantifying powder packing; however, it overlooks the importance of local packing since pore formation is also a local event during laser melting. As proposed in our previous study [17], the local low-density packing spots could be the reason for the formation of pores akin to lack-of-fusion. They could result in depressions on the top surface of a melt track which later cause variation of layer thickness at the subsequent deposition and induce pore formation. The packing analysis was motivated by studies [21,22] from the geomechanics community where the concept of local packing was used to quantify the packing of porous media. The goal was to show if the powder size distribution and morphology could influence the local packing condition by comparing the fine HDH powder against the coarse HDH powder and the standard gas atomized powder reported in our previous study [17]. Although the powder specimen in a Kapton tube may not perfectly replicate an actual powder bed, the results do provide information about the relative

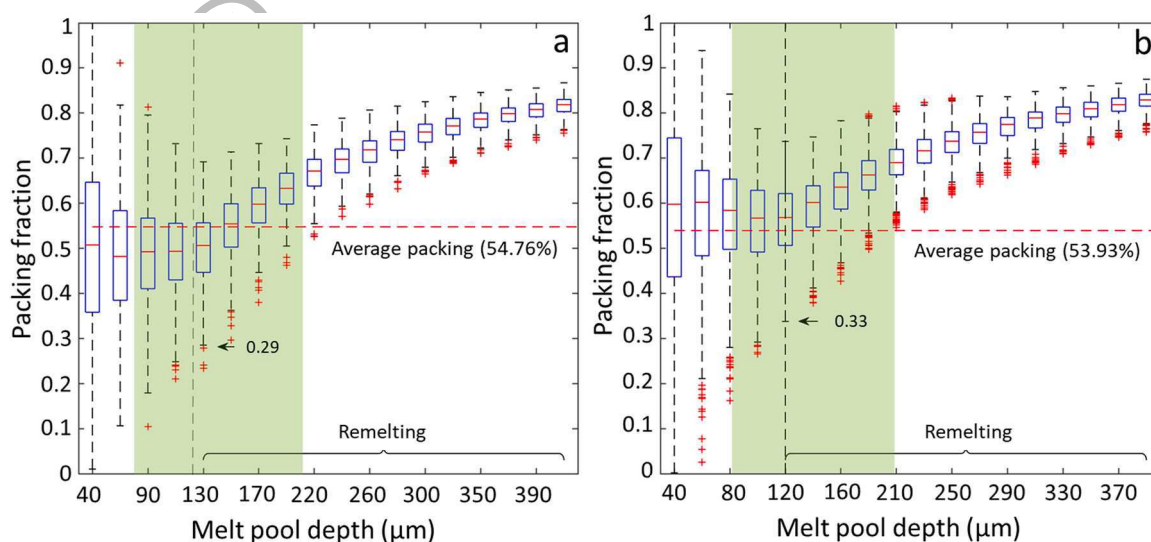


**Fig. 4.** Powder packing fractions at various melt pool sizes in a) a fine HDH Ti-6Al-4V powder specimen and b) a coarse HDH Ti-6Al-4V powder specimen (reprinted from [17]). Note that the average packing was calculated using only the powder μXCT images; thus, there is a difference between the median of packing at a specific melt pool depth and the average packing, especially when remelting occurred.

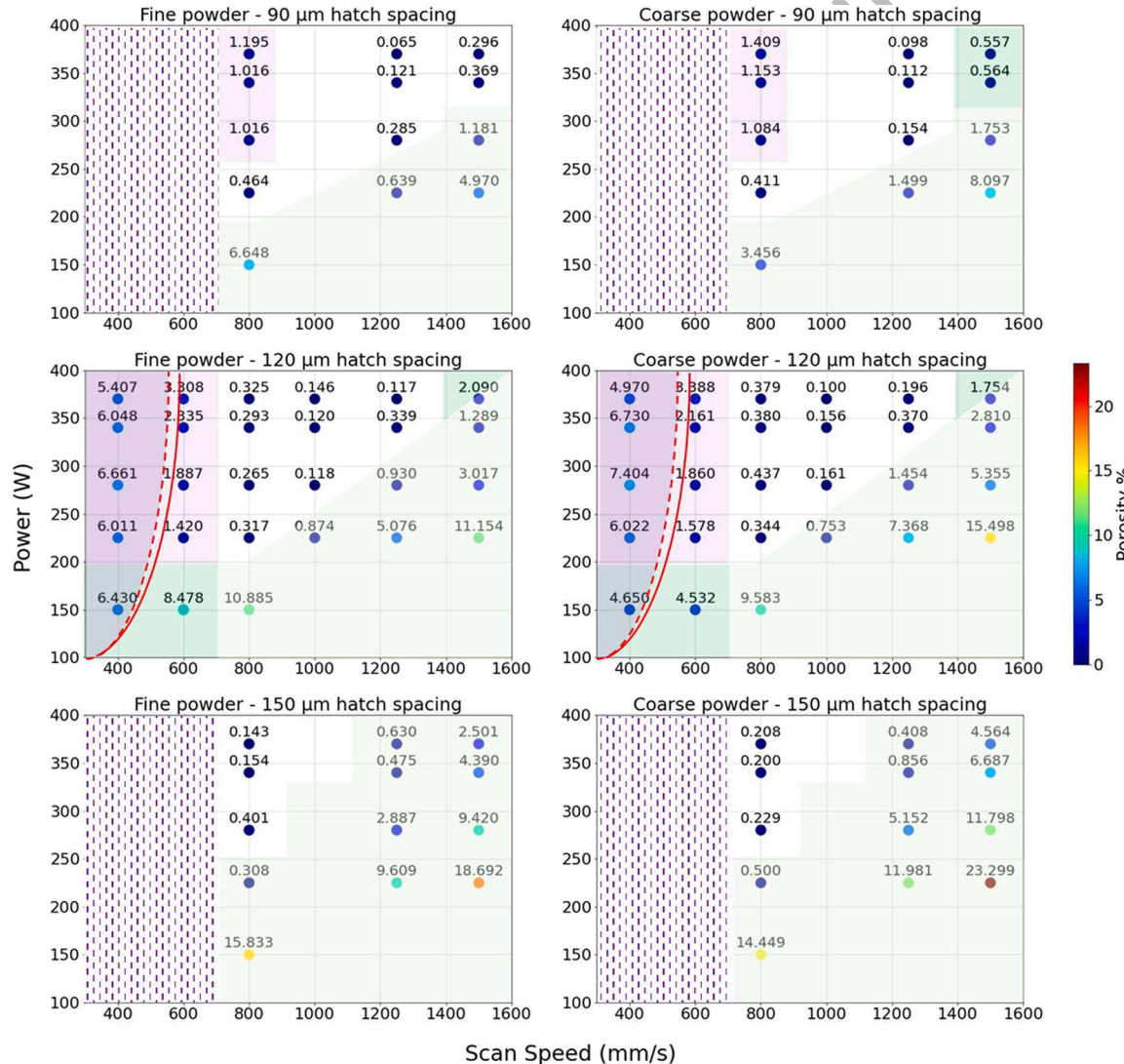
packing of different powders.

Fig. 4 summarizes the packing for each melt pool size into a single box-and-whisker plot highlighting the median, the 25th and 75th percentiles, and the minimum and maximum without considering the outliers. A smaller melt pool is more sensitive to the packing condition as suggested by the larger packing variation since the gas pockets between particles can easily dominate the area fraction of a melt pool when no solid substrate is re-melted. As the melt pool size increases, the variation of packing fraction significantly decreases as more remelting occurs with a bigger melt pool. Since the solid substrate was set to be fully dense, remelting also shifted the medians upward and away from the average packing fraction at larger melt pool depths as shown in Fig. 4. This observation aligns well with our optimization strategy in the fabrication which is to promote pore escape by increasing energy density. The average packing is 54.76% in the fine HDH powder specimen which is similar to the 53.93% and 58.02% average packing in the coarse HDH powder and the standard gas atomized powder [17], respectively. However, when only focusing on the common size range of LB-PBF melt pools (highlighted in green in Fig. 4), the fine HDH powder specimen obviously possessed many low packing density spots with as low as 20%

packing fraction. By contrast, the standard powder maintains a minimum packing of 50% for the same melt pool size [17]. Furthermore, the difference in powder packing density between the coarse and fine HDH powders was insignificant. Similarly, the porosity results discussed in the later section also show that limited options of laser power and speed combination are available for fabricating components with > 99.9% density when using the fine HDH powder. That said, in addition to size distribution, powder morphology is another important factor affecting packing. Yet, further optimization is possible if more fine powder is added to reduce local packing variation by filling interparticle air pockets.

### 3.3. Density measurements and porosity analysis of LB-PBF processed HDH Ti-6Al-4V

The relative densities of LB-PBF processed HDH Ti-6Al-4V from both fine and coarse powders were measured based on image analysis on the cross-section of as-build coupons, and results were shown in Fig. 5. The process map was optimized by means of adjusting the laser power, scan speed, and hatch spacing in the range of 150–370 W, 400–1500 mm/s,



**Fig. 5.** Porosity percentage of the LB-PBF processed HDH Ti-6Al-4V powder using different combinations of printing parameters of laser power, scan speed, and hatch spacing. The purple region indicates keyhole porosity, and the green regions denote lack of fusion porosity areas. The process window (white area) is defined as the area with a relative density > 99.5%. In the middle row, the curved lines indicate the boundary between the keyhole porosity regime on the left and the stable melting regime on the right (consisting of a stable keyhole, transition, and conduction regimes). The Red dashed line shows the boundary for the bare plate and the red solid line shows the boundary when the powder is deposited on the plate [30].

and 90–150  $\mu\text{m}$ , respectively. In critical components for aerospace application, full density, defect-free AM parts are needed (e.g., a relative density of  $\geq 99.9\%$ ) [23]; while in our study, we consider a relative density of  $> 99.5\%$  as part of the process map, and further tuning of process parameters can be applied to expand the process window such that higher densities can be attained. Fig. 5 illustrated three main regions of (1) green – parts with lack of fusion porosity (LoF), (2) purple – parts with keyhole porosity, and (3) white – parts with a relative density of  $> 99.5\%$ .

Typically, large, irregularly shaped pores are categorized as LoF porosity, which is severely detrimental to ductility and fatigue resistance [24], and they often contain unmelted powder particles. LoF defects form in the LB-PBF processed parts due to inadequate melt pool overlap [25] as well as powder characteristics (i.e., here, non-spherical powder of HDH Ti-6Al-4 V), laser beam fluctuations, and gas flow, leading to imperfect powder bed melt formation [25–28]. On the P-V map, LoF porosity occupies the low laser power and high scan speed regions. In past years, energy density has been used as a measure to predict the relative density of AM parts; however, it is possible for similar energy densities to result in different final densities (varying by as much as 60%) [29].

Tang et al. [25] developed a simple geometric model to predict the boundary of the LoF porosity for Ti-6Al-4 V, called LoF index, as follow:

$$\left(\frac{H}{W}\right)^2 + \left(\frac{L}{D}\right)^2 \leq 1 \quad (1)$$

where  $H$  is the hatch spacing,  $W$  is the melt pool width,  $L$  is the layer thickness, and  $D$  is the melt pool depth. This model assumes that a melt pool with semi-circle geometry forms such that melt pool width ( $W$ ) is twice the melt pool depth ( $D$ ), i.e.,  $W = 2D$ . Therefore, we can differentiate the Rosenthal equation [31] and approximately calculate the melt pool depth as follow:

$$D = \sqrt{\frac{2Q\varepsilon}{\pi e\rho C_p V(T_m - T_0)}} \quad (2)$$

where  $Q$  is the laser power,  $\varepsilon$  is the absorptivity of Ti-6Al-4 V alloy,  $e$  is the base of natural logarithms,  $\rho$  is the density of the bulk Ti-6Al-4 V alloy,  $C_p$  is the specific heat capacity of the bulk Ti-6Al-4 V,  $V$  is the scan speed,  $T_m$  is the melting temperature, and  $T_0$  is the pre-heat temperature such that  $(T_m - T_0)$  (see Table 2).

The melt pool depth and melt pool width were estimated using Eq. (2), and results were shown in Fig. 6. The LoF boundary was determined based on Eq. (1), and values higher than 1 were considered improper P-V-H combinations resulting in large, irregular pores, in agreement with 2D micrograph analyses on the cross-section of the as-build specimens (green areas in Fig. 5). Two regions in Fig. 6 are (1) values higher than 1 in which LoF porosity is expected and (2) values much less than 1 in which the geometric model predicts the reduced occurrence of LoF porosity. In other words, it can be assumed that the content of irregular defects decreases when the LoF index values decrease. For instance, samples #99 (fine powder) and #100 (coarse powder) had an LoF index of about 2.05 which was over 100% higher than 1; therefore, it was assumed that most pores were LoF porosity due to a consequence of insufficient melt pool overlap. Green dash lines in Fig. 6 represent a

nominal build rate of 4.5  $\text{mm}^3/\text{s}$  derived from nominal printing parameters (see Table 3) provided by the EOS M290 manufacturer to obtain an optimum relative density of 99.5%.

One may use  $\frac{H}{W}$  and  $\frac{L}{D}$  ratios to characterize melt pool overlap. When  $\frac{L}{D}$  ratio is less than 1, sufficient vertical overlap is achieved and LoF is lowered. Also, lateral overlap or  $\frac{H}{W}$  should remain below 1 to minimize sensitivity to process settings [25]. Those P-V-H combinations with reduced  $\frac{H}{W}$  and  $\frac{L}{D}$  ratios indicated sufficient melt pool overlap and lowered chance of LoF porosity. As an example, specimens #71 (P: 370 W, V: 1250 mm/s, and H: 90  $\mu\text{m}$  with a relative density of 99.935%) and #72 (P: 370 W, V: 1250 mm/s, and H: 90  $\mu\text{m}$  with a relative density of 99.902%) had an LoF index of 0.634 and  $\frac{H}{W}$  and  $\frac{L}{D}$  ratios of 0.478 and 0.637, respectively. In the P-V maps with the hatch spacing of 120  $\mu\text{m}$  (in both fine and coarse powders), there were three combinations of 150 W & 400 mm/s (Samples #1 and #2), 150 W & 600 mm/s (Samples #11 and #12), and 370 W & 1500 mm/s (Samples #53 and #54) with LoF index of 0.641, 0.961, 0.974, respectively, in which LoF porosity was seen on micrographs (see Fig. 7). This could be attributed to the low powder packing density of HDH powder and low laser power of 150 W (leading to the formation of a shallow melt pool) or capillary instability of the melt pool due to high laser power and high scan speed.

In addition to irregular pores, spherical keyhole porosity may be generated in the LB-PBF process powder during keyhole printing mode [30,33]. Formation of this defect usually occurs at low scan speed and high laser power. At a high laser power, the laser drills deeper into the base plate forming a "J" shaped melt pool (elongated melt pool) with a vapor cavity in the center. In other words, keyholes with a high depth-to-width ratio show a strong tendency for pinching off the tip of the keyhole. Recently, Zhao et al. [30] revealed that the boundary between the keyhole porosity and stable melting regimes in the P-V process map of spherical Ti-6Al-4 V powder has a non-linear relationship with laser power and scan speed, as indicated by two curved lines in Fig. 5. It is worth noting that the keyhole porosity (shape and size) is affected by keyhole depth during keyhole printing mode. The determined unstable keyhole porosity regime (left side of the red dashed line) resulted in a large keyhole pore formation. For instance, at a constant scan speed of 400 mm/s, it was seen when the laser power increased from 150 W (Sample #1) to 370 W (Sample #9), variation in porosity percentage was minimal but microscopy observation and pore analysis revealed evolution in pore morphology and size distribution (see Fig. 7 and Fig. 8). In fact, LoF pores were dominant defect in the microstructure when low laser power of 150 W was applied then by increasing it to 225 W, a transition from the conduction to keyhole mode resulted in the formation of round keyhole pores (due to entering to the unstable regime at low scan speed of 400 mm/s and gas bubble entrapment inside the melt pool occurred). The right side of the boundary (see the red curved line in Fig. 5) (stable melting regime) consists of stable keyhole, transition, and conduction regimes. In another situation in which the power was constant (e.g., 340 W), keyhole pores appeared in the microstructure (due to unstable key mode printing) when the scan speed was  $\leq 600$  mm/s; while a transition between non-stable to stable keyhole mode (e.g., at laser scan speed of  $> 600$  mm/s) resulted in the formation of minimal spherical pores in the process window with less than 0.5% pores in the microstructure. As the scan speed was set at 1500 mm/s, a transition from keyhole to conduction mode led to the formation of LoF pores.

In Fig. 5 and for the hatch spacing of 120  $\mu\text{m}$ , the area between the dashed and solid lines indicated the difference between presence and absence of powder during the laser melting process, the deposition of powder expanded the keyhole porosity regime to higher scan velocities at a constant power; nevertheless, the expansion seemed inadequate to explain remnant porosities in the LB-PBF processed HDH Ti-6Al-4 V powder. Thus, the proposed keyholing boundary (at the presence of metal powder) in [30] would be shifted to the right side when non-spherical powder is used, perhaps because of stronger interruptions

**Table 2**  
Physical properties of Ti-6Al-4V alloy [4,32].

Physical Property	Sign	Value
Absorptivity	$\varepsilon$	0.48
Bulk density [ $\text{kg}/\text{m}^3$ ]	$\rho$	4430
Specific heat capacity [ $\text{J}/\text{kg.K}$ ]	$C_p$	526
Melting temperature [ $\text{K}$ ]	$T_m$	1660
Thermal conductivity [ $\text{W}/\text{m.K}$ ]	$k$	6.7
Thermal diffusivity [ $\text{m}^2/\text{s}$ ]	$\alpha$	$2.87 \times 10^{-6}$

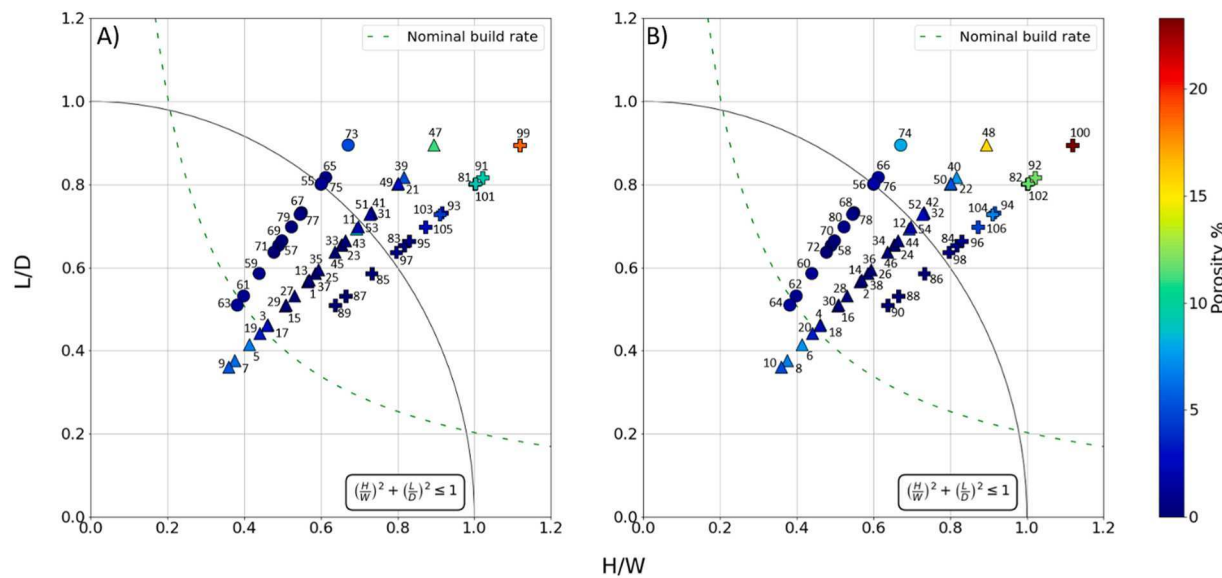


**Fig. 6.** Processing map of hatch spacing and layer thickness relative to melt-pool dimensions of melt pool depth and width of samples fabricated using A) fine and B) coarse powder; conditions within the circular arc would avoid irregular lack-of-fusion porosity (LoF index) which means melt pool overlap and overlap depth must obey geometric criterion.

**Table 3**

Summary of process parameters, build rate, and energy density of selected samples with a relative density of > 99.8%. Nominal process parameters for LB-PBF of spherical Ti-6Al-4V were provided by the EOS M290 machine manufacturer. Note: The spherical powder used in the EOS M290 machine had  $d_{50} = 39 \mu\text{m}$ , while HDH powder had a significantly higher median size, i.e.,  $d_{50} = 82 \mu\text{m}$  and  $d_{50} = 109 \mu\text{m}$  for fine and coarse powders, respectively.

Samples No.	P (W)	V (mm/s)	H (μm)	L (mm)	Build Rate (mm <sup>3</sup> /s)	Energy Density (J/mm <sup>3</sup> )	Relative Density (%)
27	340	800	120	60	5.67	59	99.707
28	340	800	120	60	5.67	59	99.620
37	370	1000	120	60	7.2	51.4	99.854
38	370	1000	120	60	7.2	51.4	99.900
45	370	1250	120	60	9	41.1	99.883
46	370	1250	120	60	9	41.1	99.804
71	370	1250	90	60	6.75	54.8	99.935
72	370	1250	90	60	6.75	54.8	99.902
83	225	800	150	60	7.2	31.3	99.692
84	225	800	150	60	7.2	31.3	99.500
89	370	800	150	60	7.2	51.4	99.857
90	370	800	150	60	7.2	51.4	99.792
Nominal	340	1250	120	30	4.5	75.5	99.548

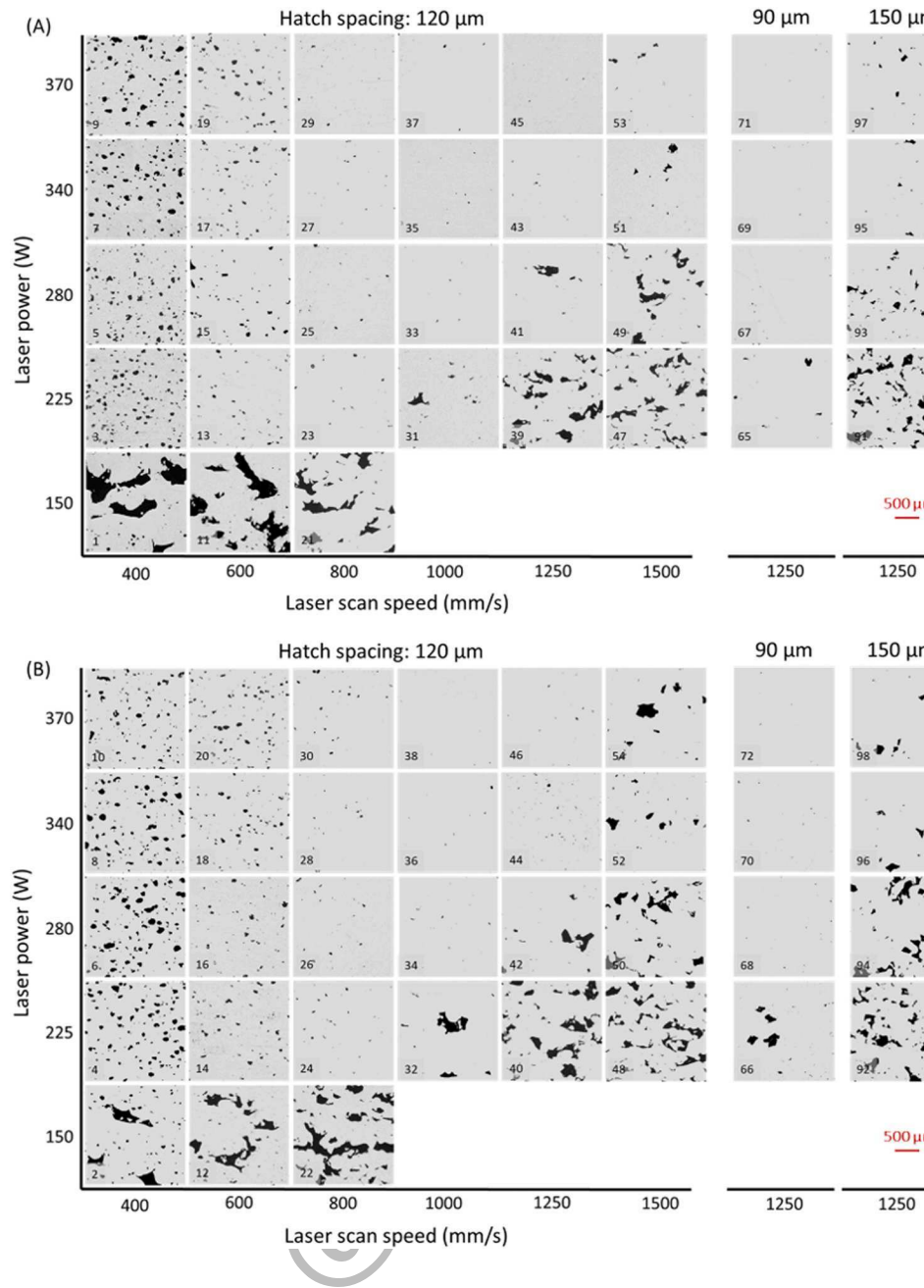
of the laser beam by the non-spherical powder surfaces. This matter can be evaluated by synchrotron x-ray high-speed imaging in which the laser-powder interactions can be visualized in-situ. Finally,  $P$ - $V$ - $H$  combinations indicated that, when the hatch spacing decreased from 120  $\mu\text{m}$  to 90  $\mu\text{m}$ , the process window expanded slightly, however, increasing the hatch spacing from 120  $\mu\text{m}$  to 150  $\mu\text{m}$  resulted in a smaller process window that was shifted to slower scan speeds.

Fig. 8 shows cumulative pore size distributions on a probability scale (Fig. 8a,b) and normalized pore size distributions from the 2D micrographs (Fig. 8c,d). Data was collected from the cross-sectional optical micrographs of the specimens shown in Figure S1. By comparing pore distributions of sample #45 ( $H: 120 \mu\text{m}$  and density of 99.883%) with sample #71 ( $H: 90 \mu\text{m}$  and density of 99.935%), along with increasing hatch spacing from 90 to 120  $\mu\text{m}$ , the size distribution of porosities is significantly changed such that the porosity size distribution is broader in sample #45 compared to sample #71. Additionally, the maximum size of pores in sample #45 is higher than sample #71 by about 50  $\mu\text{m}$ .

(see Figs. 7 and 8c). This difference in pore size distribution can be explained by the difference in melt pool lateral overlap ( $\frac{H}{W}$ ) of these two fabricated parts (see Fig. 6). Sample #71 with  $\frac{H}{W}$  of 0.477 has higher melt pool lateral overlap than sample #45 with  $\frac{H}{W}$  of 0.637. This higher lateral overlap resulted in better remelting of the previously solidified melt pool, thus, removing the majority of bigger porosities [25]. The explained point was observed during comparison of samples #1, #2 ( $P: 150 \text{ W}, V: 400 \text{ mm/s}, H: 120 \mu\text{m}, \frac{H}{W}: 0.566$ ), #21 and #22 ( $P: 150 \text{ W}, V: 800 \text{ mm/s}, H: 120 \mu\text{m}, \frac{H}{W}: 0.8$ ) with samples #9, #10 ( $P: 370 \text{ W}, V: 400 \text{ mm/s}, H: 120 \mu\text{m}, \frac{H}{W}: 0.36$ ), #89 and #90 ( $P: 370 \text{ W}, V: 800 \text{ mm/s}, H: 150 \mu\text{m}, \frac{H}{W}: 0.637$ ), respectively (see Fig. 6).

By comparing sample #1 ( $P: 150 \text{ W}$  and  $V: 400 \text{ mm/s}$ ) and sample #21 ( $P: 150 \text{ W}$  and  $V: 800 \text{ mm/s}$ ), it was seen that (i) porosity characteristics moved from below LoF criterion to over LoF criterion (see Fig. 6a) and porosities were transformed from keyhole mode to LoF along with an increase in total porosity percentage by about 4.4%, (ii) probability of having porosities with an effective diameter of  $< 25 \mu\text{m}$  increased, however, probability of having porosities with an effective diameter of  $> 25 \mu\text{m}$  decreased (Fig. 8a), and (iii) maximum size of porosity decreased by 120  $\mu\text{m}$  from 620  $\mu\text{m}$  to 500  $\mu\text{m}$  (Fig. 8c). Furthermore, Fig. 7 also confirmed that there were many small keyhole pores and a small number of large LoF pores in sample #1, which could be related to the lower packing density and larger packing variation of non-spherical powder compared to standard gas atomized powder. On the other hand, sample #21 showed fewer keyhole pores and more LoF pores than sample #1, which confirmed (i) and (ii).

To investigate the effect of laser power on porosity evolution, samples #2 ( $P: 150 \text{ W}$ ) and #10 ( $P: 370 \text{ W}$ ) with the same scan speed of 400 mm/s were selected. Sample #2 showed a density of 95.35% and sample #10 had a density of 95.03%, which is not so much different. Both samples show similar porosity size probability distribution, but sample #2 had the maximum porosity effective diameter of 431  $\mu\text{m}$ , while, sample #10 had the maximum porosity effective diameter of 185  $\mu\text{m}$  (see Fig. 7B and Fig. 8b,d). With increasing laser power from 150 W to 370 W, the total number of porosities decreased from 66 to 44 per  $\text{mm}^2$  and porosities became substantially smaller without any significant changes in the total density of parts. Therefore, probability plots for the distribution of porosity and distribution of the residual pores vs. effective diameter provided valuable information on the porosity



**Fig. 7.** Optical micrographs taken from cross-section of the LB-PBF processed HDH Ti-6Al-4V (A) fine and (B) coarse feedstock using different laser power-scan speed-hatch spacing combinations. Numbers represent sample numbers and odd numbers in “A” represent LB-PBF of fine powder and even numbers in “B” represent LB-PBF of coarse powder. Irregular coarse pores are known as lack-of-fusion porosity, which can be interconnected, while fine isolated pores are known as keyhole pores. In some cases, fine circular pores in 2D micrographs might be evolved due to improper powder pack density of the HDH powder.

characteristics such as size, number, and distribution as a function of laser power, scan speed, and hatch spacing. We found that (i) higher scan speed and higher laser power further reduce the porosity population, (ii) reducing hatch spacing further improves the part density, (iii) pores smaller than 30  $\mu\text{m}$  dominates the porosity population if the parameter is within the process map, (iv) high scan speed and low laser power lead to the LoF pore formation in which large and interconnected pores dominate the pore volume, and (v) the LoF pores align along the scanning direction.

#### 3.4. Energy density vs. density of LB-PBF processed HDH Ti-6Al-4V

The relative density of samples against energy density was shown in Fig. 9. The volumetric energy density (as opposed to linear energy density) is a parameter used to describe the average input energy on material per volume [34] as follow:

$$E = \frac{P}{V.H.L} \quad (3)$$

where  $P$  is laser power (J),  $V$  is laser scan speed (mm/s),  $H$  is hatch spacing (mm), and  $L$  is layer thickness (mm). As shown in Fig. 9a, there is a general trend of achieving higher densities of > 99.5% with some outliers that can be explained by the individual effects of printing parameters. When laser power and scan speed are doubled, the energy density would remain constant at constant hatch spacing and layer thickness. However, changes in laser power and scan speed directly affect melt pool geometry and the ability of the laser to melt the powder throughout the volume. Thus, the final density of parts would be affected.

Fig. 9b showed the effect of melt pool geometry on porosity difference between parts manufactured using the same printing parameters but different powders (fine and coarse) with respect to the parameters used for the printing, which were shown as energy density (Eq. 3). Melt

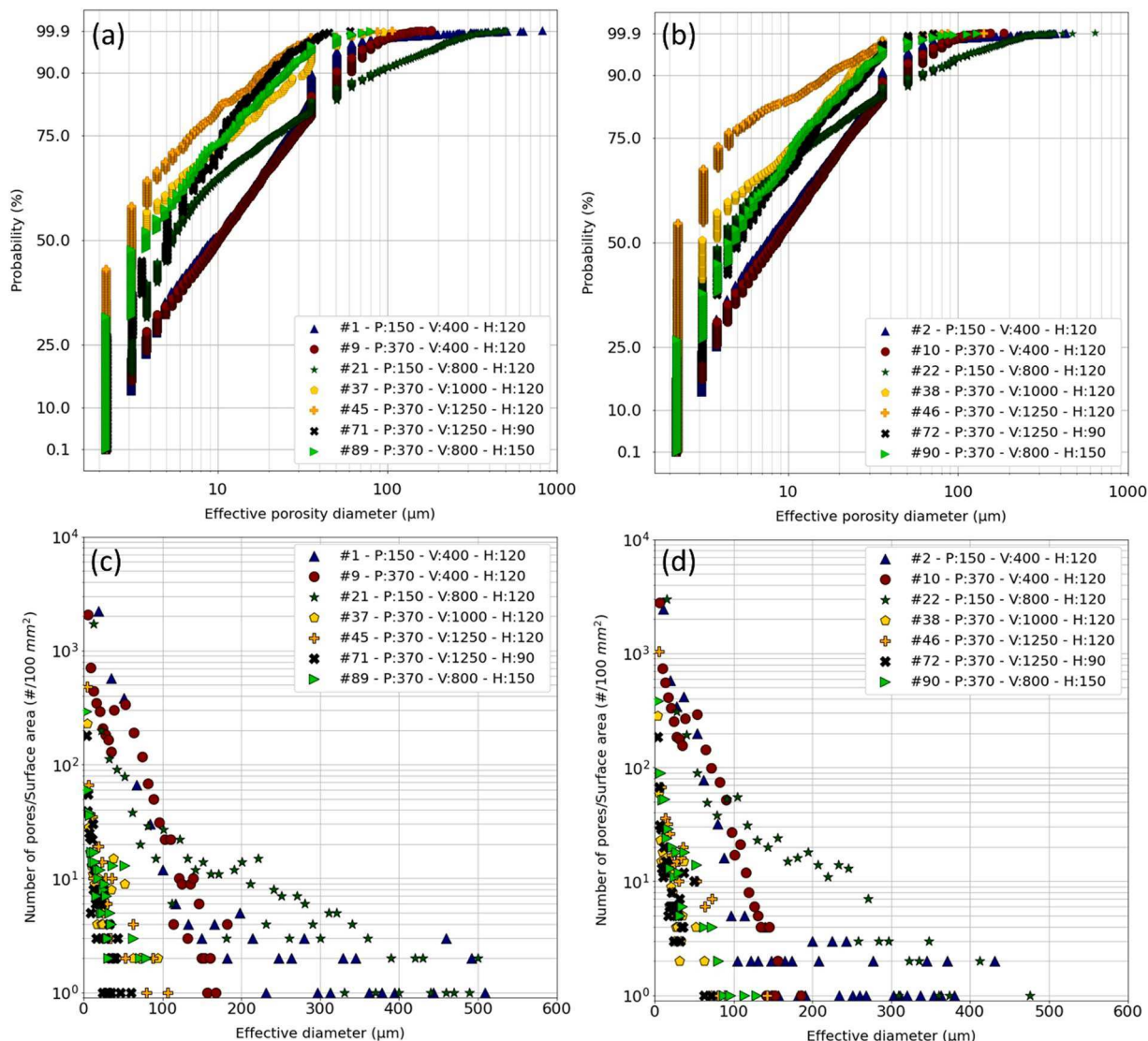


**Fig. 8.** A comparison of probability plots indicating the cumulative porosity size distributions of the LB-PBF processed (a) fine and (b) coarse HDH Ti-6Al-4V powders. Distribution of the residual pores vs. effective diameter on the entire cross-section for the LB-PBF processed (c) fine and d) coarse HDH Ti-6Al-4V powders.

pool geometry is shown by the ratio of  $\frac{L}{W}$  derived from the Rosenthal equation and described as follows [31]:

$$\frac{L}{W} = \sqrt{\frac{\varepsilon e Q V}{32\pi k \alpha (T_m - T_0)}} \quad (4)$$

where  $L$  is melt pool length,  $W$  is melt pool width,  $Q$  is laser power,  $V$  is laser scan speed,  $e$  is the base of the natural logarithm,  $\varepsilon$  is laser absorptivity of Ti-6Al-4 V alloy,  $k$  is the thermal conductivity of Ti-6Al-4 V,  $\alpha$  is the thermal diffusivity of Ti-6Al-4 V,  $T_m$  is the melting temperature, and  $T_0$  is the pre-heat temperature such that  $(T_m - T_0)$  (see Table 2).

The general trend showed higher sensitivity to powder feedstock as the energy density is below  $40 \text{ J/mm}^3$ . It was seen that with decreasing energy density, porosity difference tends to increase. On the other hand, for  $\frac{L}{W}$  of lower than 10, the fine powder shows more porosity content than the coarse powder, and this difference decreases by increasing the  $\frac{L}{W}$  up to 10. By increasing  $\frac{L}{W}$  up to 12, the porosity content in coarse powder increases, and for  $\frac{L}{W}$  of higher than 12, the porosity difference tends to decrease (see Fig. 9b). These variations in porosity content can occur due to the more severe shadowing (see Section 3.7) effect in coarse powder. When the laser scan speed is larger (e.g., L/W ratio higher than

10), laser moves on the particles faster and the shadowing effect prevents full remelting of the previous layers because of high keyhole depth fluctuations, thus, a higher amount of porosity will prevail. On the other hand, when the powder size is smaller (i.e., using fine HDH powder), the shadowing effect will be of less importance; however, smaller powder size resulted in a higher number of powder particles in the same volume which led to a less remelting rate of the previously deposited layer using low laser power and scan speed (e.g., L/W ratio lower than 10). The smaller remelting rate caused a higher porosity percentage in the samples manufactured using fine powder. When the energy density is above  $40 \text{ J/mm}^3$ , sensitivity to powder feedstock decreases. This suggests that the shape of the melt pool (e.g., depth and width) may play an essential role in how easily pores escape from the melt pool. Although powder packing density of both fine and coarse powder is about 54%, fine powder showed more low packing spots compared to coarse powder (see Fig. 4) which can lead to void formation during the powder spreading. This would impact melt pool formation when the energy density is  $< 40 \text{ J/mm}^3$ . Since powder packing density of the irregularly shaped powder is lower than the spherical ones (54% compared with 58%), it is thought that the energy density higher than  $40 \text{ J/mm}^3$  will generate a sufficiently deeper melt pool (in transition or stable keyhole mode printing) compared to the conduction mode printing with a shallower

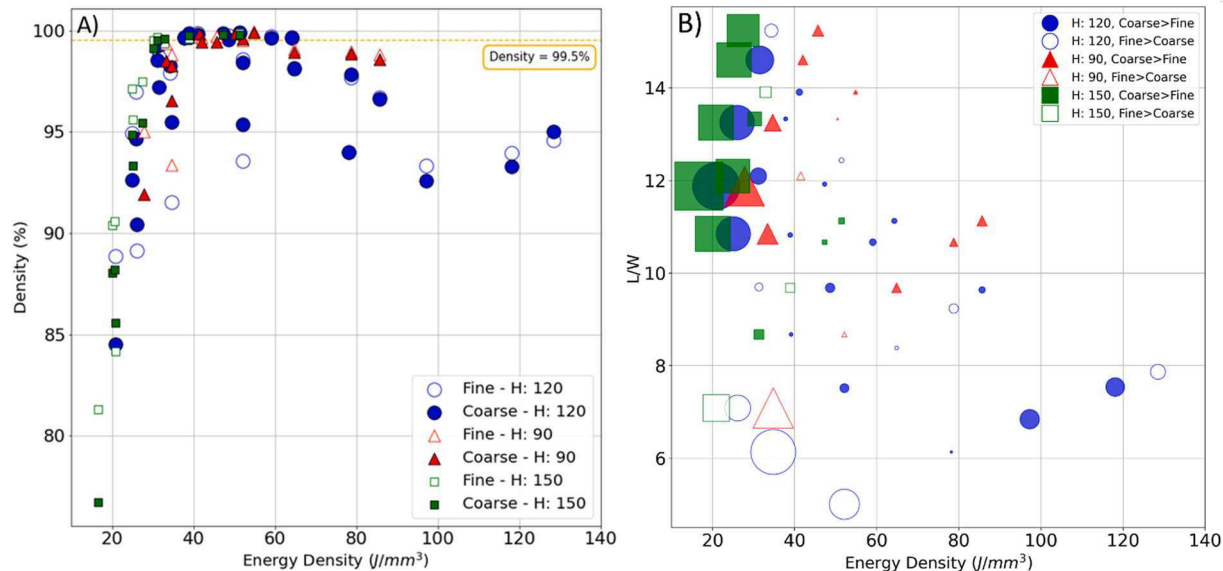


**Fig. 9.** (A) Relative density of LB-PBF HDH Ti-6Al-4V parts fabricated with the corresponding energy density and (B) the relationship between melt pool geometry (y-axis), energy density (x-axis), and the porosity difference between samples printed with fine and coarse powders (size of points). The orange dashed line in (A) denotes the density of 99.5% threshold to find the proper energy density for printing parts. Solid shapes in (B) denote the higher porosity percentage of samples manufactured using coarse powder and hollow shapes denote the higher porosity percentage of samples manufactured using fine powder. Size of the shapes in (B) shows the magnitude of porosity content difference between coarse and fine powder.

melt pool, and therefore may facilitate pore escape.

### 3.5. Build rate vs. density of LB-PBF processed HDH Ti-6Al-4V

In metal AM, quantitative prediction of near fully dense part production as a function of the build rate is crucial, specifically when non-standard powders are developed in powder bed AM machines. The proposed geometric model by Tang et al. [25] was developed with a particular aim to enhance the build rate. The following Eq. (5) can be used to calculate the build rate:

$$\text{Build rate} = V \cdot H \cdot L \quad (5)$$

where  $V$  is the laser scan speed,  $H$  is the hatch spacing, and  $L$  is the layer

thickness. In this study, the layer thickness was fixed at  $60\ \mu m$ , while both scan speed and hatch spacing were varied to improve build rate at which the density of  $> 99.5\%$  was achievable, and the results of build rate ratio vs. density are shown in Fig. 10. To maximize the build rate, a high scan speed is preferred, and a high laser power is required to enhance the melt pool depth and the remelting fraction of the previously deposited layer, while the  $P$ - $V$  combination should be optimized to avoid balling. Further, the analytical Rosenthal equation for the melt-pool size (see Eq. (2)) is proportional to the root square of  $P/V$ , thus, increasing the melt pool size at a constant power can be achieved by reducing scan speed. This will reduce the build rate, and if  $V$  is below a certain speed (see the red dash line in Fig. 5), keyholing porosity occurs.

One practical implication in Fig. 10 is that in many cases, there is

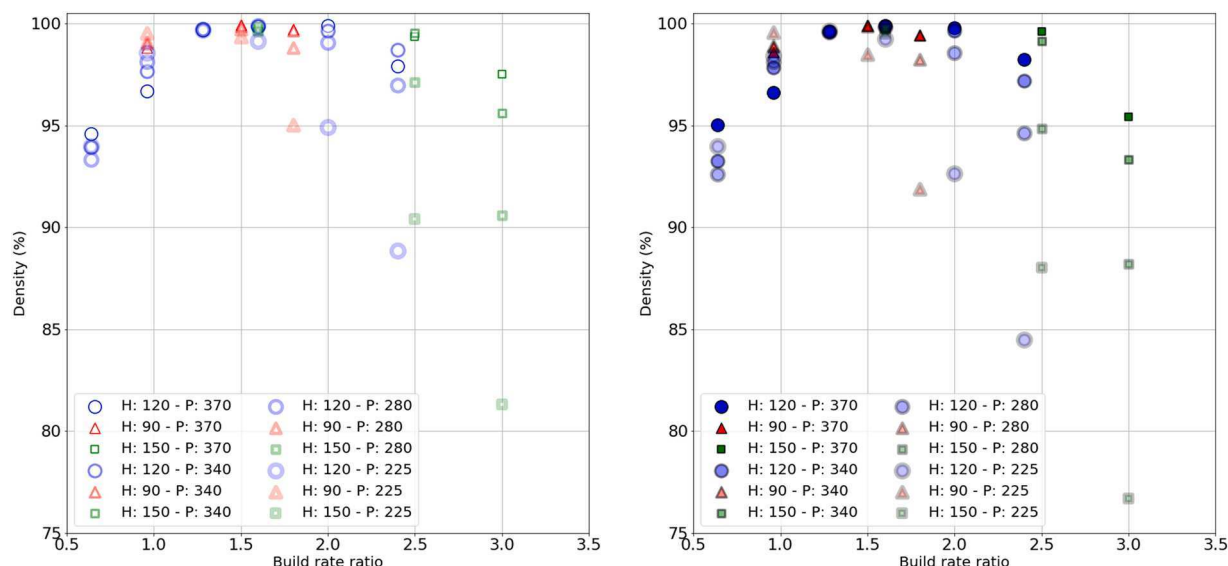


**Fig. 10.** Density variation based on varying LB-PBF process parameters of the fabricated parts from HDH Ti-6Al-4V (left) fine and (right) coarse powders. The build rate ratio is the rate compared to the standard condition (power of 340 W, scan speed of 1250 mm/s, hatch spacing of 120  $\mu m$ , and layer thickness of 30  $\mu m$ ). Build rate increases as the scan speed increases from 400 mm/s to 1500 mm/s.

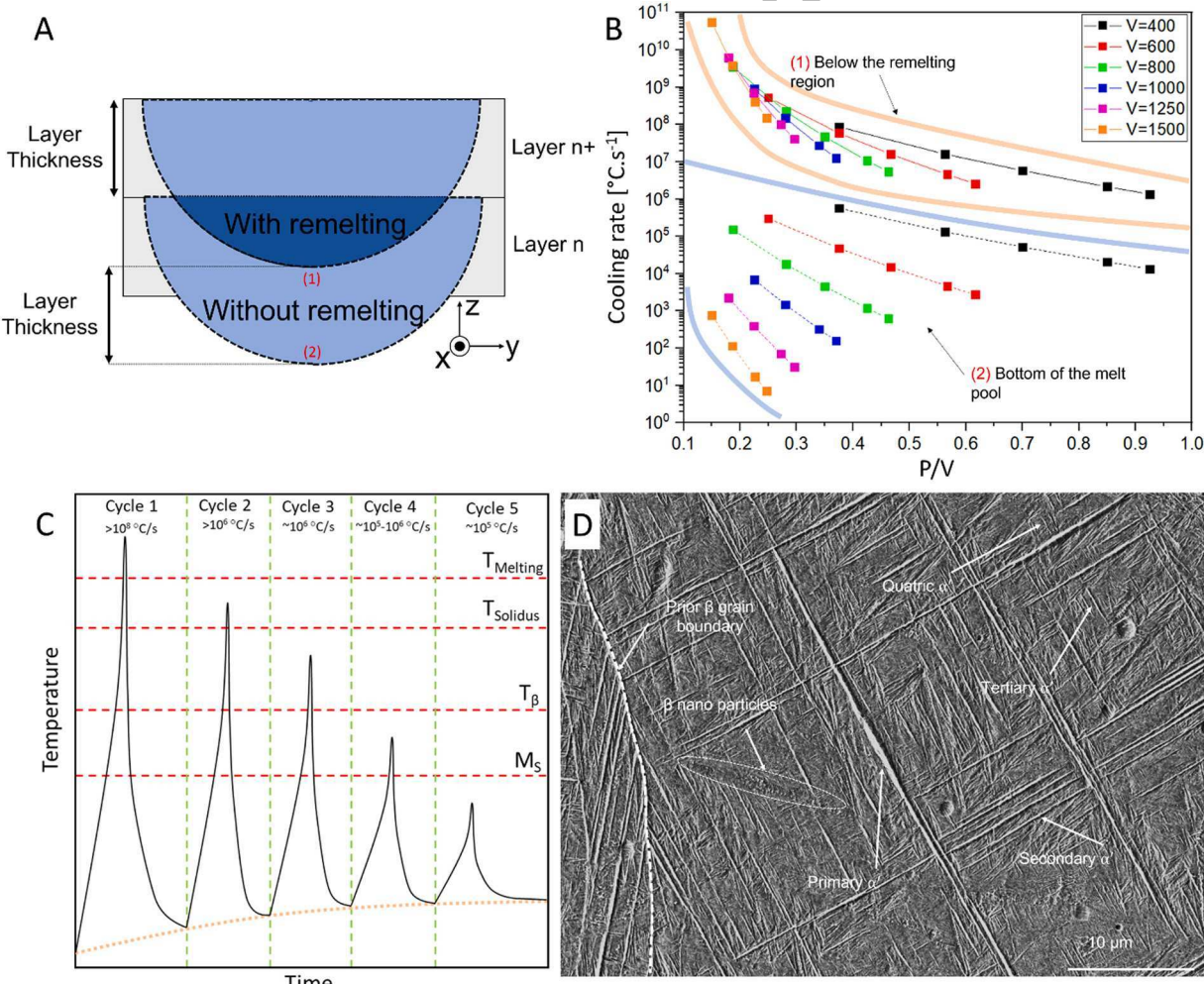
minority of lamellar ( $\alpha + \beta$ ).

Figure S2 illustrated SEM micrographs showing the dominance of the martensitic microstructure in the samples. By comparing samples #37 ( $E = 51 \text{ J/mm}^3, H = 120 \mu\text{m}, V = 1000 \text{ mm/s}$ ) and #89 ( $E = 51 \text{ J/mm}^3, H = 150 \mu\text{m}$  and  $V = 800 \text{ mm/s}$ ), it was seen that samples printed with the same energy density showed different  $\alpha'$  lath widths. Samples with smaller hatch spacings have more laser passes on the surface which leads to more high-temperature heating cycles. In other words, more heating cycles decrease the peak temperature. Lower peak temperature than martensitic start transformation temperature ( $M_s$ ) results in coarsening of the existing martensitic features instead of decomposition of martensite because of insufficient dwell time and relatively lower peak temperature [42]. This point was also confirmed by comparing samples #45 ( $H = 120 \mu\text{m}$ ) and #71 ( $H = 90 \mu\text{m}$ ), in which larger martensite features were seen in sample #71. A similar trend was observed in the samples manufactured using the coarse powder. It appears that energy density can affect microstructure by changing the heat input and thermal history of the part, however, energy density is not a perfect criterion to produce the best final parts. For example, by doubling both laser power and scan speed the energy density will remain the same but the final part properties can be different. Prashanth et al. [29] reported different tensile properties of Al-12Si parts manufactured using the same energy density. They showed that the tensile properties of the parts are dependent on laser power, rather than energy density. Xu et al. [41] also

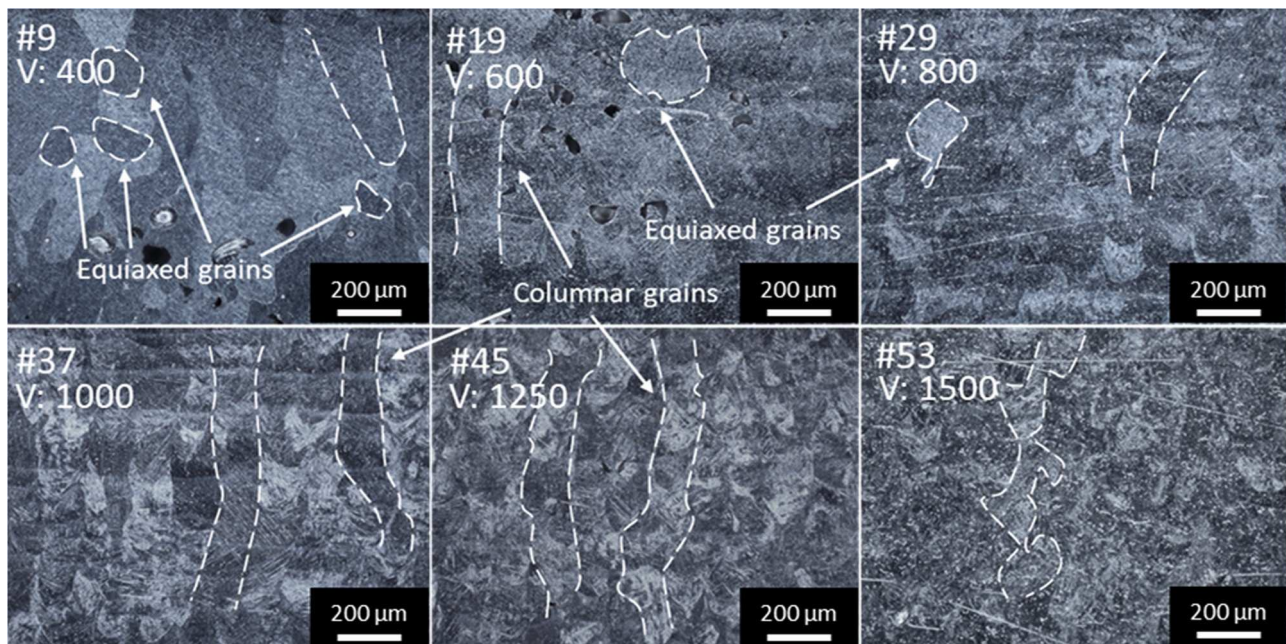
observed when a constant energy density was applied on LB-PBF of Ti-6Al-4 V using different combinations of laser power, scan speed, layer thickness, and FOD constant energy density, the final microstructure varied from fully acicular  $\alpha'$  martensite to mixed acicular  $\alpha'$  martensite and lamellar ( $\alpha + \beta$ ) which indicates that energy density is not a good criterion to rely on. In other words, tuning the LB-PBF processing variables would lead to substantial variations in the constituent phases, owing to the changed thermal profiles.

Fig. 12d Showed different microstructural features present in the LB-PBF Ti-6Al-4V parts. As mentioned before, martensite is the dominant phase in the as-build parts due to the high cooling rate of the LB-PBF process. Along with martensitic features, prior beta grain boundaries are visible. During the solidification process, all liquid phase inside the melt pool transforms to  $\beta$  phase, known as the prior beta phase, and this prior  $\beta$  phase then transforms directly to  $\alpha'$  martensite because of a high cooling rate. Since the martensite finish temperature ( $M_f$ ) is below room temperature [37], a small amount of  $\beta$  phase remains between the  $\alpha'$  needles in the form of  $\beta$  nano particles, as reported by Oh et al. [43] and Y. Xu [44].

The amount of  $\beta$  nano particles is correlated with the cooling rate of the LB-PBF process which is affected by processing parameters. The cooling rate can be estimated using the following equation [45].



**Fig. 12.** A) schematic of two consecutive layers showing the regions with and without remelting and B) Calculated cooling rates against P/V ratio. The region between orange curves shows the cooling rates just below the remelting region and the region between blue curves shows the cooling rates at the bottom of the melt pool. C) schematic representation of thermal cycles in the part because of laser passing on the surface and the corresponding estimated cooling rates and D) SEM micrograph of sample #37 showing different types of martensite features produced based on the heating cycles,  $\beta$  nano particles, and prior  $\beta$  grain boundary.



**Fig. 13.** Optical micrographs of LB-PBF Ti-6Al-4V parts manufactured with laser power of 370 W and different laser scan speed of 400–1500 mm/s as indicated in each micrograph. Micrographs were collected from the near top surface region of the samples.

**Fig. 14d** summarizes the profiles of the melt pool depth as a function of laser melting time. The average keyhole depths are  $261.4 \pm 17.4 \mu\text{m}$  for the gas atomized powder,  $248.2 \pm 14.8 \mu\text{m}$  for the fine HDH powder, and  $247.7 \pm 22.5 \mu\text{m}$  for the coarse HDH powder. Note that the important difference is not the average depths, since it could be affected by the variation of layer thickness, but the standard deviations which reflect the severity of the keyhole fluctuation in the presence of different powders. The keyhole fluctuation is clearly more severe in the coarse HDH powder bed. Surprisingly, the fine HDH powder bed resulted in the mildest fluctuation among the three experiments. **Fig. 14a-c** shows the most intense keyhole fluctuation in all three experiments where porosity formation events were observed more frequently in the coarse HDH powder bed. The larger fluctuation can be attributed to the amplification of the laser shadowing effect in the HDH powder bed as suggested in our previous effort [17]. When the laser is shadowed by a HDH particle, the local cooling is expected to last longer due to the larger particle size. Once the laser path is fully restored, the substrate is often more exposed since the powder layer of the coarse HDH powder possesses lower counts of particles compared with the other powder beds as shown in **Fig. 14a-c**. As the result, both the shrinkage and the expansion of the keyhole are amplified. As shown in **Fig. 14e**, a similar trend was observed in the keyhole width measurements where the standard deviations of width are  $29.0 \mu\text{m}$  for the coarse HDH powder,  $24.2 \mu\text{m}$  for the fine HDH powder, and  $24.1 \mu\text{m}$  for the gas atomized powder. Reducing particle size appeared to be effective to mitigate the violent fluctuation as the fine HDH powder behaved more similarly to the spherical gas atomized powder. It is believed that the smaller particle size of the fine HDH powder bed helped reduce the keyhole fluctuation. The result suggests that it may be feasible to control keyhole behaviors through only altering particle size without eliminating the powder shape irregularity.

Supplementary material related to this article can be found online at doi:10.1016/j.addma.2022.102875.

### 3.8. Vickers microhardness

The microhardness tests were carried out on samples manufactured using fine HDH powder, at a hatch spacing of  $120 \mu\text{m}$ , and various laser power and scan speeds and the results were shown in **Fig. 15**. Increasing laser scan speed while keeping the laser power ( $P = 370 \text{ W}$ ) constant,

causes the hardness to increase up to laser scan speed of  $1250 \text{ mm/s}$  and decrease in hardness by further increase in laser scan speed. This phenomenon can be correlated with the columnar prior  $\beta$  grains morphology as discussed before (see **Fig. 13**). Also, increase in laser power with constant laser scan speed ( $V = 1250 \text{ mm/s}$ ) results in higher hardness due to mainly decrease in porosity content. However, the inverse correlation between the hardness and laser power in the low laser scan speed region ( $V = 400$  or  $600 \text{ mm/s}$ ) was spotted. This can be explained by the fact the increasing laser power in this region results in change in pore formation mechanism at first (from  $P = 150$  to  $P = 225 \text{ W}$ ) and increase in pore size with further increase of laser power. Micro-hardness indent has less probability of contacting larger LoF pores with higher distance between them compared to circular keyhole pores that are more uniformly spread throughout the sample. Results were in agreement of the reported values for LB-PBF Ti-6Al-4V alloy [15,53].

## 4. Conclusions

This study was carried out to show the successful utilization of cost-effective non-spherical HDH Ti-6Al-4V powders in the LB-PBF process to lower the cost of production compared to the use of GA powders. Below are the major findings:

- Despite the possibility of mechanical interlocking between powder particles, HDH powders (both fine and coarse powders with PSD of  $50\text{--}120 \mu\text{m}$  and  $75\text{--}175 \mu\text{m}$ , respectively) showed better flowability compared to GA powders with  $20\text{--}63 \mu\text{m}$  size distribution. This better powder flow of the HDH powder is most easily accounted for by the powder size since coarse powder (e.g., HDH powder with  $D_{50} > 50 \mu\text{m}$ ) is known to flow better than fine ones (e.g., GA powder with  $D_{50} < 35 \mu\text{m}$ ). By using optimized process parameters, samples with a relative density of  $> 99.5\%$  were manufactured.
- The micro-computed tomography analysis showed the overall packing density of the fine and coarse HDH powders was 54.8% and 53.9%, respectively. Similar to the coarse HDH powder, the fine HDH powder also has many low-density packing spots, proven by the Monte Carlo analysis, with 20–40% packing fraction at nominal LB-PBF melt pool sizes.

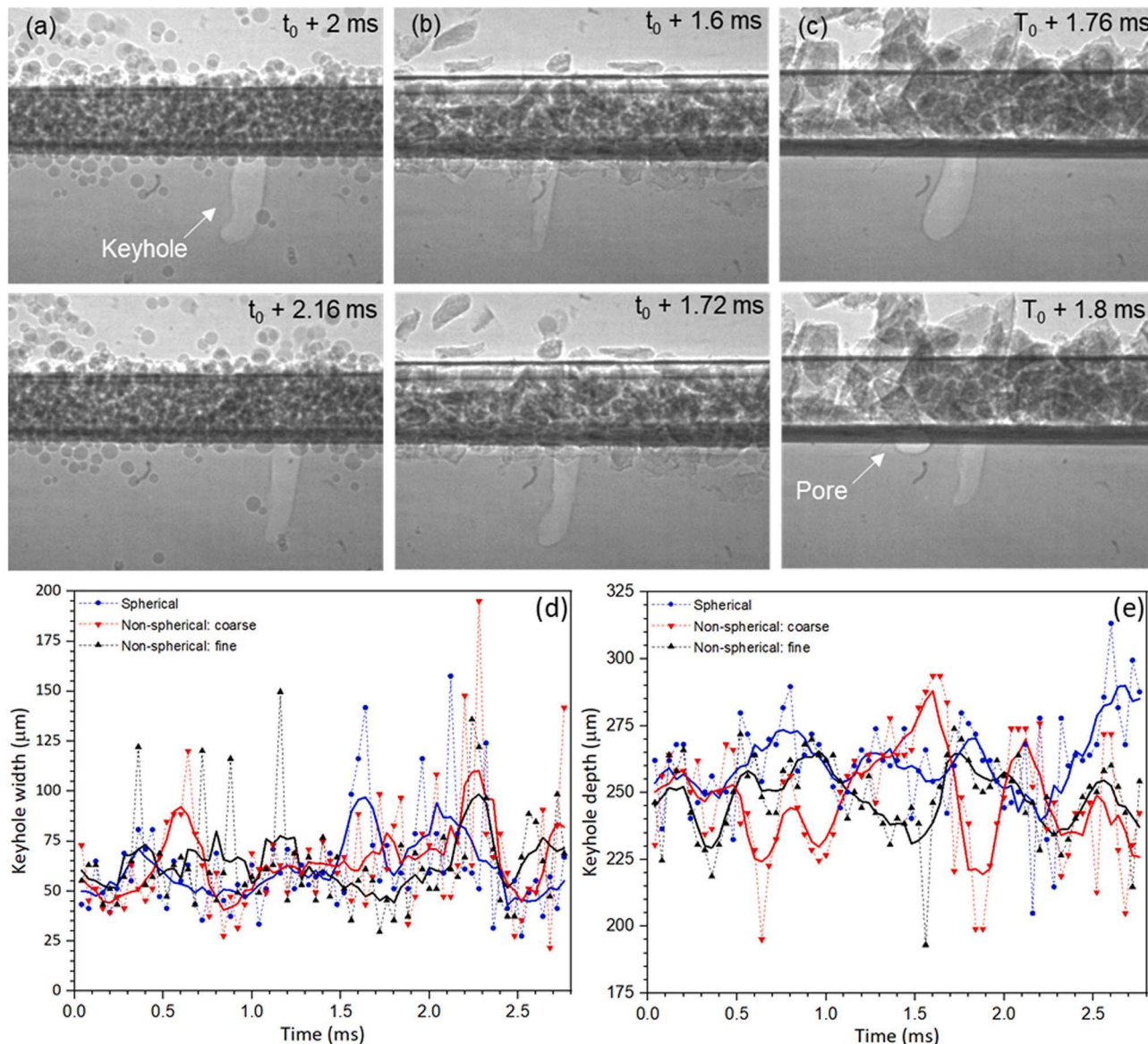


**Fig. 14.** DXR frames collected in the (a) gas atomized, (b) fine HDH powder, and (c) coarse HDH powder added single-bead Ti-6Al-4V experiments at a laser power of 350 W and a scan speed of 700 mm/s showing the fluctuations of keyhole dimensions. The keyhole depth profiles and the width profiles are shown in (d) and (e). Note that the timestamps in (a-c) are the time since the laser was initiated. The DXR videos (Supplementary Video S1, S2, and S3) can be found in the [supplementary material](#). Bold solid lines in (d) and (e) are 5 point moving averages.

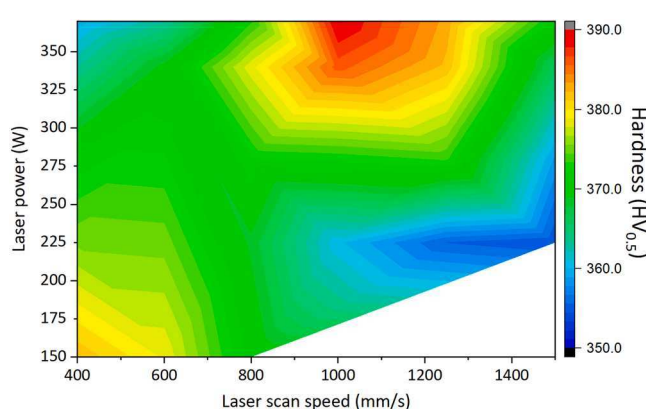


**Fig. 15.** Vickers microhardness variation based on the processing parameters of the LB-PBF processed Ti-6Al-4V alloy. Data was collected on the samples manufactured using fine powder with a constant hatch spacing of 120  $\mu\text{m}$ .

- Parts with a relative density of > 99.5% were produced using a build rate of 1.5–2 times of the nominal production rate and lower energy density (30–60 J/mm<sup>3</sup> in HDH powder) compared to GA powders and standard EOS M290 parameters (~75 J/mm<sup>3</sup>). By increasing the build rate, parts are produced faster using less energy which will lower the cost of production even further.
- Microstructure and phase analysis indicated that acicular  $\alpha'$  martensite was the main phase in LB-PBF Ti-6Al-4V parts owing to the high cooling rates. Traces fractions of  $\beta$  phase (about 1–4%) with nano-granular morphology were also detected despite the extremely high cooling rate during solidification of the melt pool.
- Grain morphology in LB-PBF Ti-6Al-4V parts changed from regional equiaxed to fully columnar and then distorted columnar by increasing laser scan speed at a constant laser power. The change in grain morphology occurred because of melt pool shape change and heat transfer disturbance which affect the chance of grain regrowth and new grains nucleation.

- *In situ synchrotron x-ray imaging* showed that coarse HDH powder (75–175  $\mu\text{m}$ ) caused less packing density and higher laser shadowing effect which resulted in higher variation in keyhole depth. Fine HDH powder (50–125  $\mu\text{m}$ ) behaved similar to GA powder (20–63  $\mu\text{m}$ ), both in keyhole depth and width fluctuations. This suggests that, by using non-spherical powder with an optimized PSD, laser shadowing can be mitigated.
- Mechanical testing showed dependency of Vickers microhardness to process parameters and resultant microstructure of the LB-PBF Ti-6Al-4V in which the highest value of  $\sim 390 \text{ HV}_{0.5}$  was attained for samples with a density of  $> 99.8\%$ .

## CRediT authorship contribution statement

**Mohammadreza Asherloo:** Writing – original draft, Visualization, Methodology, Investigation, Formal analysis, Data curation. **Ziheng Wu:** Writing – original draft, Visualization, Investigation, Formal analysis, Data curation. **Melody H. Delpazir:** Formal analysis, Data curation, Investigation, Formal analysis. **Eyob Ghebrejesus:** Formal analysis. **Sara Fryzlewicz:** Formal analysis. **Runbo Jiang:** Investigation, Formal analysis. **Benjamin Gould:** Writing – review & editing, Formal analysis. **Mike Heim:** Formal analysis, Data curation. **Dave Nelson:** Resources. **Mike Marruci:** Resources. **Muktesh Paliwal:** Writing – review & editing, Resources, Investigation. **Anthony D. Rollett:** Writing – review & editing, Supervision, Methodology, Resources, Funding acquisition, Conceptualization. **Amir Mostafaei:** Writing – review & editing, Supervision, Resources, Project administration, Methodology, Investigation, Funding acquisition, Conceptualization.

## Declaration of Competing Interest

The authors declare that they have no known competing financial interests or personal relationships that could have appeared to influence the work reported in this paper.

## Acknowledgments

AM would like to acknowledge the startup funding from the Department of Mechanical, Materials and Aerospace Engineering and Armour College of Engineering at Illinois Institute of Technology at Chicago, Illinois. This work is supported, in part, by the Pennsylvania Infrastructure Technology Alliance, a partnership of Carnegie Mellon, Lehigh University, and the Commonwealth of Pennsylvania's Department of Community and Economic Development (DCED). The authors recognize Reading Alloys (formerly affiliated with AMETEK Inc., now a part of Kymera International) for providing the powder used in this work. The authors acknowledge the support of the NextManufacturing Center and the use of the Materials Characterization Facility, supported by grant MCF-677785, at Carnegie Mellon University. This research used resources of the Advanced Photon Source, a US Department of Energy (DOE) Office of Science User Facility operated for the DOE Office of Science by Argonne National Laboratory under Contract No. DE-AC02-06CH11357 in addition to supporting through Laboratory Directed Research and Development (LDRD) funding from Argonne National Laboratory under the same contract. Dr. Tao Sun, Dr. Niranjan Parab, Dr. Cang Zhao, and all the 32-ID beamline staff at the Advanced Photon Source are thanked for assisting in the acquisition of the DXR data. Undergraduate student researchers (EG and SF) were supported by the National Science Foundation - Research Experience for Undergraduates under award DMR 2050916.

## Appendix A. Supporting information

Supplementary data associated with this article can be found in the online version at [doi:10.1016/j.addma.2022.102875](https://doi.org/10.1016/j.addma.2022.102875).

## References

- [1] W. Ding, G. Chen, M. Qin, Y. He, X. Qu, Low-cost Ti powders for additive manufacturing treated by fluidized bed, *Powder Technol.* 350 (2019) 117–122.
- [2] W. Ding, Z. Wang, G. Chen, W. Cai, C. Zhang, Q. Tao, X. Qu, M. Qin, Oxidation behavior of low-cost CP-Ti powders for additive manufacturing via fluidization, *Corros. Sci.* 178 (2021), 109080.
- [3] Y.P. Dong, Y.L. Li, S.Y. Zhou, Y.H. Zhou, M.S. Dargusch, H.X. Peng, M. Yan, Cost-affordable Ti-6Al-4V for additive manufacturing: Powder modification, compositional modulation and laser in-situ alloying, *Addit. Manuf.* (2020), 101699.
- [4] M.J. Donachie, Titanium: a technical guide, 2000.
- [5] G. Chen, S.Y. Zhao, P. Tan, J. Wang, C.S. Xiang, H.P. Tang, A comparative study of Ti-6Al-4V powders for additive manufacturing by gas atomization, plasma rotating electrode process and plasma atomization, *Powder Technol.* 333 (2018) 38–46.
- [6] Y.Y. Sun, S. Gulizia, C.H. Oh, C. Doblin, Y.F. Yang, M. Qian, Manipulation and characterization of a novel titanium powder precursor for additive manufacturing applications, *JOM* 67 (2015) 564–572.
- [7] W. Ding, G. Chen, M. Qin, Y. He, X. Qu, Low-cost Ti powders for additive manufacturing treated by fluidized bed, *Powder Technol.* 350 (2019) 117–122.
- [8] S.P. Narra, Z. Wu, R. Patel, J. Capone, M. Paliwal, J. Beuth, A. Rollett, Use of Non-Spherical Hydride-Dehydride (HDH) Powder in Powder Bed Fusion Additive Manufacturing, *Addit. Manuf.* 34 (2020), 101188.
- [9] A. Rogalsky, I. Rishmawi, L. Brock, M. Vlasea, Low cost irregular feed stock for laser powder bed fusion, *J. Manuf. Process.* 35 (2018) 446–456.
- [10] R. Cunningham, A. Nicolas, J. Madsen, E. Fodran, E. Anagnostou, M.D. Sangid, A. D. Rollett, Analyzing the effects of powder and post-processing on porosity and properties of electron beam melted Ti-6Al-4V, *Mater. Res. Lett.* 5 (2017) 516–525.
- [11] N.D. Parab, J.E. Barnes, C. Zhao, R.W. Cunningham, A.D. Rollett, T. Sun, Real time observation of binder jetting printing process using high-speed X-ray imaging, *Sci. Rep.* (2019) 28–30.
- [12] A. Mostafaei, C. Zhao, Y. He, S. Reza Ghiasi, B. Shi, S. Shao, N. Shamsaei, Z. Wu, N. Kouravem, T. Sun, J. Pauza, J.V. Gordon, B. Webler, N.D. Parab, M. Asherloo, Q. Guo, L. Chen, A.D. Rollett, Defects and anomalies in powder bed fusion metal additive manufacturing, *Curr. Opin. Solid State Mater. Sci.* 26 (2022), 100974.
- [13] F. Medina, Reducing metal alloy powder costs for use in powder bed fusion additive manufacturing: Improving the economics for production, The University of Texas at El Paso, 2013.
- [14] R. Li, Y. Shi, Z. Wang, L. Wang, J. Liu, W. Jiang, Densification behavior of gas and water atomized 316L stainless steel powder during selective laser melting, *Appl. Surf. Sci.* 256 (2010) 4350–4356.
- [15] J. Varela, E. Arrieta, M. Paliwal, M. Marucci, J.H. Sandoval, J.A. Gonzalez, B. McWilliams, L.E. Murr, R.B. Wicker, F. Medina, Investigation of Microstructure and Mechanical Properties for Ti-6Al-4V Alloy Parts Produced Using Non-Spherical Precursor Powder by Laser Powder Bed Fusion, in: *Materials*, 14, Basel,, 2021, p. 3028.
- [16] ASTM B348, Standard Specification for Titanium and Titanium Alloy Bars and Billets 02 (04).
- [17] Z. Wu, M. Asherloo, R. Jiang, M.H. Delpazir, N. Sivakumar, M. Paliwal, J. Capone, B. Gould, A. Rollett, A. Mostafaei, Study of Printability and Porosity Formation in Laser Powder Bed Fusion Built Hydride-Dehydride (HDH) Ti-6Al-4V, *Addit. Manuf.* 47 (2021) 102323.
- [18] C.A. Schneider, W.S. Rasband, K.W. Eliceiri, NIH Image to ImageJ: 25 years of image analysis, *Nat. Methods* 9 (2012) 671–675.
- [19] L. Scime, Methods for the Expansion of Additive Manufacturing Process Space and the Development of In-Situ Process Monitoring Methodologies, *Carnegie Mellon Univ.*, 2018.
- [20] I. Yadroitsev, I. Yadroitsev, 3 - A step-by-step guide to the L-PBF process, in: I. Yadroitsev, I. Yadroitsev, A. du Plessis, E.B.T.-F. of L.P.B.F. of M. MacDonald (Eds.), *Addit. Manuf. Mater. Technol.*, Elsevier, 2021: pp. 39–77.
- [21] R. Al-Roush, K.A. Alshibli, Distribution of local void ratio in porous media systems from 3D X-ray microtomography images, *Phys. A Stat. Mech. Its Appl.* 361 (2006) 441–456.
- [22] K.F. H, P. Dayakar, G. Jens, K. Nikolay, M. Ingo, High-Resolution Neutron and X-Ray Imaging of Granular Materials, *J. Geotech. Geoenviron. Eng.* 139 (2013) 715–723.
- [23] R. Russell, D. Wells, J. Waller, B. Poorganji, E. Ott, T. Nakagawa, H. Sandoval, N. Shamsaei, M. Seifi, Qualification and Certification of Metal Additive Manufactured Hardware for Aerospace Applications, Elsevier Inc., 2019.
- [24] E. Wycisk, A. Solbach, S. Siddique, D. Herzog, F. Walther, C. Emmelmann, Effects of defects in laser additive manufactured Ti-6Al-4V on fatigue properties, *Phys. Procedia* 56 (2014) 371–378.
- [25] M. Tang, P.C. Pistorius, J.L. Beuth, Prediction of lack-of-fusion porosity for powder bed fusion, *Addit. Manuf.* 14 (2017) 39–48.
- [26] H. Gong, K. Rafi, H. Gu, T. Starr, B. Stucker, Analysis of defect generation in Ti-6Al-4V parts made using powder bed fusion additive manufacturing processes, *Addit. Manuf.* 1 (2014) 87–98.
- [27] T. Mukherjee, T. DebRoy, Mitigation of lack of fusion defects in powder bed fusion additive manufacturing, *J. Manuf. Process.* 36 (2018) 442–449.
- [28] S. Coeck, M. Bisht, J. Plas, F. Verbiest, Prediction of lack of fusion porosity in selective laser melting based on melt pool monitoring data, *Addit. Manuf.* 25 (2019) 347–356.
- [29] K.G. Prashanth, S. Scudino, T. Maity, J. Das, J. Eckert, Is the energy density a reliable parameter for materials synthesis by selective laser melting? *Mater. Res. Lett.* 5 (2017) 386–390.

# PROJECT SIX

# Laser Powder Bed Fusion of Ti-6Al-4V Alloy

<sup>1</sup>Eyob Ghebrejesus, <sup>2</sup>Amir Mostafaei

<sup>1</sup> Author, BSc. Aerospace Engineering, Illinois Tech  
<sup>2</sup> Advisor, Phd. Material Science, Illinois Tech

National Science Foundation Research in collaboration with Illinois Tech  
Department of Materials and Additive Manufacturing  
10 W 35th St Chicago, IL 60616

August 12, 2021

---

## Abstract

Additive manufacturing (AM) is the process of joining materials to make objects from three-dimensional (3D) model data, usually layer upon layer, as opposed to subtractive manufacturing methodologies. It includes various near-net shaping processes that are capable of building complex 3D geometries directly from raw materials, which require little post processing. This report looks at several types of materials printed using additive manufacturing. The materials used are Ti-64, Inconel-718 and Stainless Steel. The purpose of this report is to explore how Laser Powder Bed Fusion transformed the manufacturing process of different materials. This discipline of process engineering summarizes the broad range of processes, where particles are synthesized, tailored, separated or are used as supporting agent. The characterization of these processes and of the particles thus is key for a detailed understanding. As particles are three-dimensional objects, their morphology as well as the macroscopic structures formed by the particles should be characterized using three-dimensional methods. Using methods of lower dimension often is bound to a loss of information such as a particle size distribution based on a single equivalent diameter, a pore size distribution of a specimen without having the spatial information of the pore network or the stereological bias known in the field of conventional microscopy. Particle technology as sub-discipline of process engineering summarizes the broad range of processes, where particles are synthesized, tailored, separated or are used as supporting agent. The characterization of these processes and of the particles thus is key for a detailed understanding. As particles are three-dimensional objects, their morphology as well as the macroscopic structures formed by the particles should be characterized using three-dimensional methods. Using methods of lower dimension often is bound to a loss of information such as a particle size distribution based on a single equivalent diameter, a pore size distribution of a specimen without having the spatial information of the pore network or the stereological bias known in the field of conventional microscopy.

---

**Keywords:** AM, EBSD, LPBF, Ti-64, SEM, SLM, XDR, XRD, Microscopy, Keyholes, Porosity

## 1 Introduction

Additive manufacturing (AM), also known as 3D printing, is a transformative approach to industrial production that enables the creation of lighter, stronger parts and systems. It is yet, another technological advancement made possible by the transition from analog to digital processes. In recent decades, communications, imaging, architecture, and engineering have all undergone their own digital revolutions. Now, AM can bring digital flexibility and efficiency to manufacturing operations. It utilizes data computer-aided-design (CAD) software or 3D object scanners to direct hardware to deposit material, layer upon layer, in precise geometric shapes. As its name implies, additive manufacturing adds a material to create an object. By contrast, when you create an object by traditional means, it is often necessary to remove material through milling, machin-

ing, carving, shaping or other means. Although the terms "3D printing" and "rapid prototyping" are casually used to discuss additive manufacturing, each process is actually a subset of additive manufacturing. While additive manufacturing seems new to many, it has actually been around for several decades. In the right applications, additive manufacturing delivers a perfect trifecta of improved performance, complex geometries, and simplified fabrication. As a result, opportunities abound for those who actively embrace additive manufacturing whether in terms of finance, material strength and or uses. In this laboratory-based research we looked at three different materials. They are Titanium-64 alloy, Stainless Steel and Inconel-718 Nickel superalloy. With each to its advantages we'll cover what the basic steps for sample design and printing, sample preparation and characterization.

## 1.1 What is Ti-6Al-4V alloy?

Ti6Al4V alloy, also known as Ti-64, is an  $\alpha$  plus  $\beta$  titanium alloy with high strength, low density, high fracture toughness, excellent corrosion resistance and superior biocompatibility. Recognized as the most popular titanium alloy, Ti6Al4V occupies almost a half of the market share of titanium products used in the world today [1]. Ti6Al4V alloy was originally developed for aircraft structural applications in the 1950s.

The formation of  $\alpha$  prime martensite phase is beneficially produced by the rapid cooling through diffusionless transformation while  $\alpha + \beta$  transformation is a diffusional process. Conventionally, Ti-6Al-4V consists of a lamellar structure allowing a high strength with slightly reduced ductility. Refinement of the micro-structure results in a higher yield stress. However, after SLM, the micro-structure of as-built Ti-6Al-4V commonly consists of a fine  $\alpha$  martensitic micro-structure. The high cooling rates during Selective Laser Melting (SLM) result in the formation of the acicular (lamellar)  $\alpha$  martensitic phase in Ti6Al4V. Cross-sectional images collected along the SLM building direction show the presence of long columnar grains of prior beta phase (Figure 1. A and B) courtesy of Zhang [2]. Strongly textured structures can lead to significant anisotropic mechanical properties, causing different mechanical responses to external loading along different sample orientations.

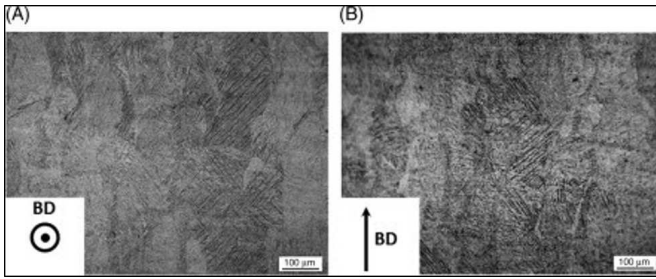


Figure 1: Cross-sectional images collected using SLM.

## 1.2 Mechanical Properties of Processed Ti-6Al-4V

SLM produces parts with finer microstructures, increasing the mechanical strength (compared to cast Ti-6Al-4V or even sometimes to wrought products). Reported strength values range from about 1000 to 1400 MPa, a 50% increase over wrought products: with corresponding elongations ranging from 25 to 4.4%, respectively. Corresponding hardness values can range between HRC 37 to 54. For example, the coefficient of variation, which represents the ratio of the standard deviation to the average, was up to 48 per cent for elongation at break. Thus, the difference in the mechanical properties of the AM processed samples and the wide scatter among the mechanical properties

reported by the different sources, highlight the issue of repeatability and reliability of the mechanical properties of the AM-processed Ti-6Al-4V alloys. According to the standard specifications for wrought Ti-6Al-4V (ELI) and cast Ti-6Al-4V alloys for surgical implant applications (ASTM F136-13 and ASTM F1108-14), the elongation of the material should be at least 8 percent. The content of interstitials has a substantial influence on the mechanical properties of Ti-6Al-4V. As indicated an oxygen content higher than 0.2 wt.% leads to a higher strength and a lower ductility in the Ti-6Al-4V alloy. A decrease in oxygen and nitrogen content improves the ductility, fracture toughness, stress-corrosion resistance, and resistance against crack growth. As published in the literature, the UTS for SLM Ti-6Al-4V (ELI) horizontal samples varied from 1206 to 1267 MPa.

## 1.3 Industrial Uses of Ti-64

This lightweight and yet strong alloy saves weight in highly loaded structures and is hence extremely suitable for jet engines, gas turbines and many air frame components. While the aerospace industry still dominates the Ti6Al4V demand, other application fields such as marine, automobile, energy, chemical and biomedical industries have also found its wide acceptance during the last half a century. The low density, high strength, high corrosion resistance and biocompatibility are attractive characteristics of Ti6Al4V for applications such as bridges and dental implants. Its applications have also been extended to the marine and chemical industries due to its high corrosion resistance to most corrosive acids and alkalis.

However, despite the high demand, manufacture of Ti6Al4V products is always challenging due to its poor thermal conductivity, the propensity to strain hardening and active chemical reactivity to oxygen.

## 1.4 Traditional Manufacturing of Ti-64

Conventional manufacture of Ti6Al4V products relies on forging, casting and rolling of bulk feedstock materials, followed by subsequent machining to final shapes and dimensions. These traditional manufacturing processes always inevitably result in a large amount of material waste, high manufacturing cost and long lead time. Some of the traditional methods are:

*Forging:* A manufacturing process involving the shaping of a metal through hammering, pressing, or rolling. These compressive forces are delivered with a hammer or die.

*Casting:* This is a manufacturing process used by the forging industry to produce an object (often metal) of a specific desired shape. This is achieved by pouring hot molten metal into a mold that contains a hollow cavity of the exact required shape.

*Extrusion:* It's a process used to create objects of a fixed cross-sectional profile. The two main advantages of this process over other manufacturing processes are its ability

to create very complex cross-sections, and to work materials that are brittle, because the material only encounters compressive and shear stresses, such as aluminum, by forcing it to flow through a shaped opening in a die. Extruded material emerges as an elongated piece with the same profile as the die opening.

*Coating:* The coating process consists of applying a coating material to a moving web of flexible substrate. The carrier substrate may be paper, film, or aluminum foil and the resulting material's additional properties will vary depending on the required application and on the material's end-use. Many industrial coating processes involve the application of a thin film of functional material to a substrate. Industrial coatings are engineered barriers that protect parts from a wide variety of damages and extreme environments

*Secondary manufacturing:* processes are those processes that are performed after the initial manufacturing process like injection molding, CNC machining production, and so on. As the name implies, these processes involve performing additional work on parts or materials that have already been subjected to a primary machining process. There are many types of secondary machining processes; these can remove unwanted material from a part, refine an existing feature, or produce some other type of enhancement beyond the scope of primary machining. Those processes typically are like welding, grinding, coating, and polishing.

## 1.5 Additive Manufacturing Technologies

Compared to traditional manufacturing methods, the most significant advantage of AM is its free form fabrication of complex parts directly from feedstock materials without involving traditional manufacturing methods such as extrusion, forging, casting and secondary machining processes to achieve desired shapes. The near-net shaping capability makes AM a cost effective technique since it minimizes wasted material. There are numerous types of AM widely used in present day. Some of those are:

*Directed Energy Deposition (DED):* In the Direct energy deposition process, the laser beam creates a molten pool, into which the powder material is delivered via argon gas and locally injected to fuse and solidify into a bead. After building one layer, the laser and powder feeding head is raised in Z direction with a preset height and starts building a subsequent layer. The DED process is usually conducted in an inert environment filled with the argon gas where the oxygen level can be controlled to below 5–10 ppm. After deposition, the unused blown out powders can be recycled.

*Selective Energy Melting (SLM):* An additive manufacturing process in which preplaced fine metal powder is melted by using a high-power laser to generate a layer. Layer by layer, powder is preplaced and melted to generate a part. The technique is also termed powder-bed fusion. During this process, significant remelting of surrounding tracks and layers normally takes place.

*Electron Beam Melting (EBM):* This is a Rapid Proton capture process, developed and commercialized by Arcam AB in Sweden; it produces fully dense metal parts directly from metal powder, having the characteristic properties of the target material. The EBM system builds structures from the bottom up by scanning the focused electron beam to selectively melt specific powder areas. It reads data from a 3D CAD model and lays down successive layers of powdered material. The process continues until the last layer of the part is built. It takes place under vacuum, which makes it a highly suitable process to fabricate structures using reactive materials that cannot be exposed to the atmosphere. The EBM system is an electron optical system similar to an SEM60 or an EB melting system. The EBM process can build a minimum layer thickness of 0.05mm and it has a tolerance capability of  $\pm 0.4$  mm.

*Metal Injection Molding (MIM):* Metal injection molding is a manufacturing method that combines traditional PM with plastic injection molding. Over the past decade it has established itself as a competitive manufacturing process for small precision components that would be costly to produce by alternative methods. It can be used to produce comparatively small parts with complex shapes from almost any type of material such as metals, ceramics, inter-metallic compounds, and composites (German, 1984). Recently MIM has been studied not only for hard metals, but also for materials such as titanium, copper, and aluminum (German and Bose, 1997). Unlike in the case of PM, MIM requires mixing metal powders with a large amount of polymeric binder. After this the organic constituents are removed in a de-binding step such as solvent extraction or pyrolysis. The brown body is held in the molded form only by metal powder after de-binding. This de-binding process and powder forming mechanism is unique to the MIM process.

## 2 Procedure

### 2.1 Designing Samples

Before printing the samples, you need to design, select the best powder and parameter settings for printing. Designing is usually done using different types of CAD software on a computer. For the Ti-64 samples 31 samples are designed as seen in Figure 2 and Figure 3 using Netfab Autodesk 2020. Each of these samples have different parameter settings, like power, speed and or pre heat temperature. For the 31 samples we printed all of them were preheated to 200°C. The common feature of these AM processes is the utilization of geometrical data contained in a 3D computer aided design (CAD) file, which is sliced into layers with a defined thickness. While designing the samples, it's best to carefully place each sample with in the base-plates so as to avoid any miss steps by the laser power. Carefully check and note down the appropriate settings and sample placement before proceeding to print.

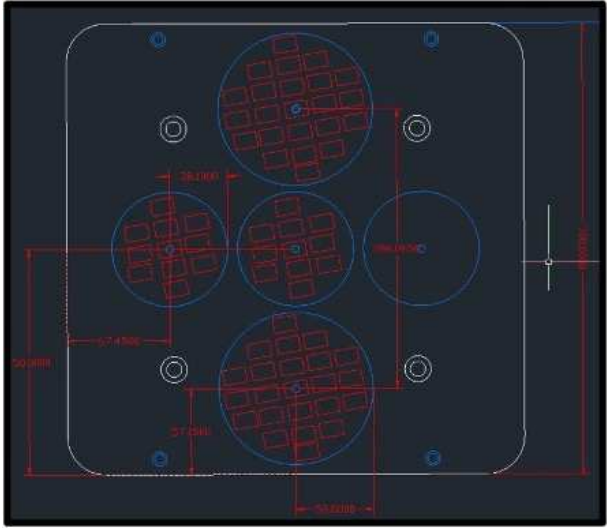


Figure 2: Designing Samples.

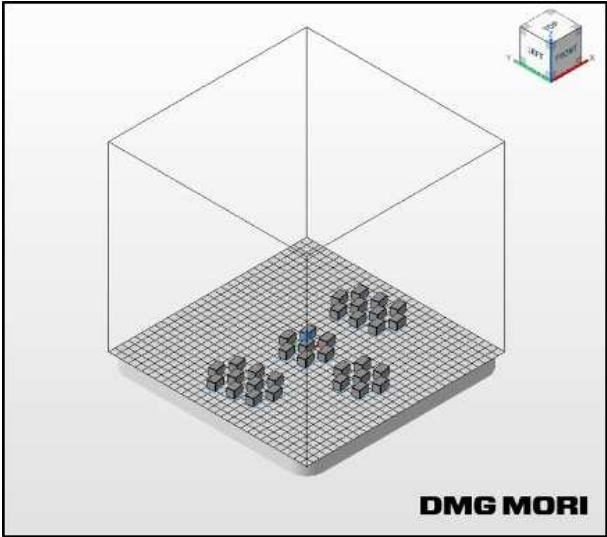


Figure 3: Location of Samples on Base-plate.

After designing the sample layout using software Autodesk Netfab, the settings are uploaded to the LASERTEC 30 SLM in the lab. This machine is a laser-based powder printer that melts and prints the desired sample according to the given parameters. The Powder used is of two types: irregular and regular Ti-64 powder. The goal of the research is to study if the shape of the powder has effect in the mechanical and chemical properties of the Ti-64 samples. All the 31 samples have either a different power setting or scan speed threshold (see Table 1). Those sample parameters are graphed and presented in Figure 4. The plot shows the samples with their respective parameter settings. For example, sample 1 has a laser power setting of 150W and a scan speed of 400mm/s. Similarly, sample 27 has a power 370W and 1500mm/s.

Table 1: Sample Scan Speed and Power values

Sample No	Scan Speed (mm/s)	Laser Power (W)
1	400	150
2	400	225
3	400	280
4	400	340
5	400	370
6	600	150
7	600	225
8	600	280
9	600	340
10	600	370
11	800	150
12	800	225
13	800	280
14	800	340
15	800	370
16	1000	225
17	1000	280
18	1000	340
19	1000	370
20	1250	225
21	1250	280
22	1250	340
23	1250	370
24	1500	225
25	1500	280
26	1500	340
27	1500	370
28	1000	385
29	1250	385
30	800	385
31	1500	385

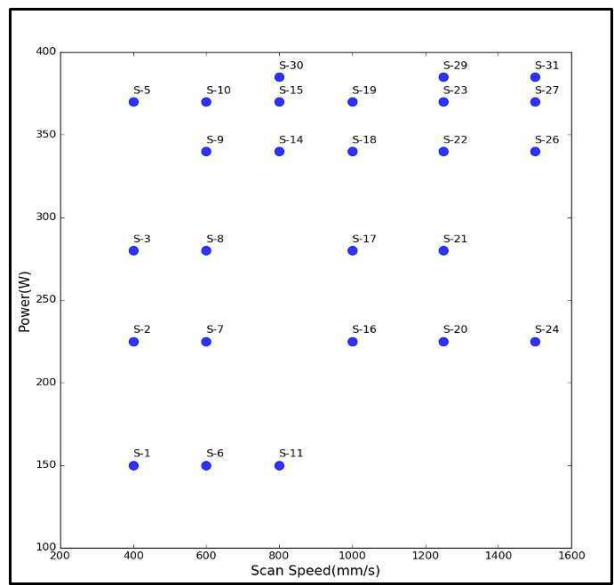


Figure 4: Power vs Scanspeed Plot (S denotes Sample).

The various scan speed and SLM laser power values in Table 1 allows us to study and monitor how laser power and speed affects additive manufacturing. At a letter section, the porosity is compared for each sample and graphed accordingly. It is also good to use more sample parameter in order to avoid sample bias and get accurate results. Having more sample means we can anticipate some samples not being printed due to technical or mechanical issues raised by the SLM machine.

## 2.2 Printing Samples

Printing samples is done using the Lasertec SLM 30 Machine. It usually takes 4 to 5 hours to print 30 or more samples depending on the parameter settings. It also needs to be checked for preheating process. Preheat is just the warming up the melting chamber to a desired temperature in order to study how the layers are formed and to relieve some stress in powder binding. If a printing process is required for a print process, it should be noted and assessed whilst studying results of the samples later. Useful things before printing is to upload the sample data, rename all the samples, cleaning the baseplates, bring down the oxygen level below 0.08%, check the argon gas levels and sealing the melting chamber. Following the sliced pattern, a focused, high-power laser or electron beam scans and melts the precursor powders, forming a molten pool. As the heating source moves away, the molten pool cools down quickly and solidifies to form a track bead. This process is repeated to successively build new layers until a final geometry is completed.

Once printing is done, all the previous actions should be redone in order to keep the machine to it's initial settings and be ready for cleaning. After the samples are printed (see Figure 5 below) they are taken to a post processing lab to be cut into smaller parts using an Electric Discharge Machining (EDM). EDM is powered through a high electric current that is discharged through a voltage difference in order to cut, split and trim sample parts with high precision. Each sample is cut into two or more parts, so that each is used for different studies. For example, one-part can be used to study Microscopy and Corrosion testing, while the second can be used for FEM and EBSD analysis or even tensile testing as well. Additionally keeping cut-samples in the long run also helps to trace back our studies and replicate it without having to print new ones. This mechanism allows us to save Ti-64 powder.

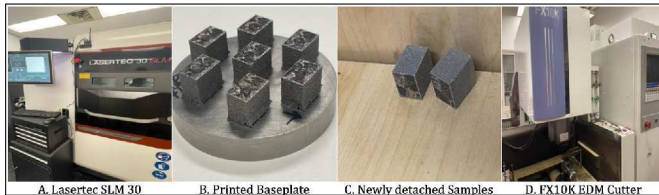


Figure 5: Printing, detaching, and cutting samples.

## 2.3 Mounting

The next step is to mount the samples so that they are ready for grinding and polishing. Those three steps are necessary in order to take Microscopy, study scratches, check porosity and any other analysis required. Mounting is the just the process of putting the getting part of the sample in a holder resin which makes it easier to grind and polish the sample. There are two types of Mounting see Figure 6 below. Compression or hot mounting presses are used to form and cure compression mounting compounds around a sample. The pressure and heat applied is typically not a problem with most metal alloy, ceramic, glass or inorganic samples. Cold mounting equipment is used to mount samples for microscopy or other analysis using cold or liquid resins. Cold mounting resins are typically a two-part system. A sample is placed in a cold mounting ring mold or dam, mold cup, or rubber molds and then the cold mounting resin is poured around the sample and cured. Some mold rings remain with the sample and cannot be reused. Silicone rubber molds are reusable because the mounting sample can be removed. Curing typically occurs at ambient or room temperatures. Usually engraving is done after mounting the sample. Refer to Figure 6-D to see how engraving is done. The idea is to label your samples so that you can differentiate them easily. Engraving is preferred than writing on your labels using a marker, because the label doesn't wear off easily while grinding or polishing.

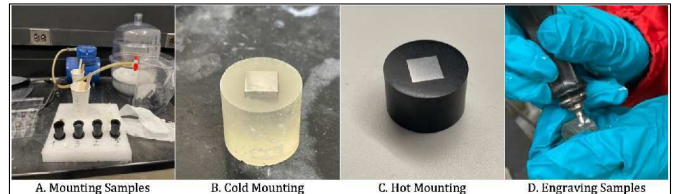


Figure 6: Mounting and labeling.

## 2.4 Grinding Samples

Grinding is a machining process that's used to remove material from a workpiece via a grinding wheel. As the grinding wheel turns, it cuts material off the workpiece while creating a smooth surface texture in the process. A mechanical process using a rotating grinding wheel made from abrasive material containing small particles of grit ranging from fine to coarse see Figure 7-(A and B). The wheel revolves around a central axis, making contact with the surface of the workpiece, while the particles act as cutting tools that cut chips from the material. There two ways to grind a sample, manual and automatic. These are usually selected based on necessity and efficiency. Grinding needs a sandpaper (grinding paper) with a specific grit size. The grit of sandpapers is a rating of the size of abrasive materials on the sandpaper. The higher grit number is

equivalent to a finer abrasive, which creates smoother surface finishes. Lower grit numbers represent coarser abrasives that scrape off materials much quicker. For those 31 samples printed we started at 240, 500, 600, 800, and then 1200 at the end. You grind each sample until it's smooth, with no scratches and is ready for polishing. Note that a scratch made at a higher grid can only be removed by going one or two steps back to a lower grit number. Thus, if you made a scratch at 1200 grit-size, only an 800 or 600 can remove that scratch. Grinding takes the most time in sample preparation and is extremely tedious.

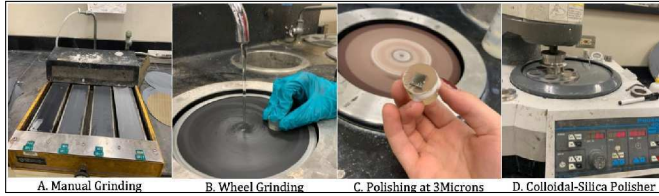


Figure 7: Sample grinding and polishing Process

## 2.5 Polishing Samples

Polishing is the process of creating a smooth and shiny surface by rubbing it or by applying a chemical treatment, leaving a clean surface with a significant specular reflection. In some materials, polishing is also able to reduce diffuse reflection to minimal values. Technically polishing refers to processes that use an abrasive that is glued to the work wheel, while buffing uses a loose abrasive applied to the work wheel. The two main reasons for polishing are to remove considerable amounts of metal or nonmetallic and smooth a particular surface. Figure 7-(C and D) are prime examples of polishing. Similarly, for polishing is based on the grit size of the polisher paper. We have 9micron, 3microns, 1microns and 0.05microns at last. The lower the number the finer the polishing paper is, and thus the smoother your sample becomes. Mostly polishing is done on a wheel machine. However, at the last process we have a colloidal silica based automatic polisher to finalize the sample polisher. After each grinding and polishing one is supposed to wash the sample using distilled water, methanol, and isopropanol consecutively to clean the sample. Then carefully sonicate the sample using ethanol or methanol for about 3 minutes. Sonication is just the act of applying sound energy to agitate particles in a sample, for various purposes such as the extraction of multiple compounds from plants, microalgae, and seaweeds. In this laboratory, it is usually applied using an ultrasonic bath or an ultrasonic probe, colloquially known as a Sonicator.

Now that the samples are done, they're all ready for analysis whether it's Microscopy, SEM or EBSD. Note that sometimes the samples can get scratched due to hand placement, touching, or scrapping against any surface. You need to be careful to not scratch it. But if at point they

get scratched follow the same process for grinding and polishing in order to smoothen the surface again.

## 3 Results and Analysis

After the samples are prepared, we move to the first analysis that is Microscopy. We look at sample scratches, porosity and other defects using microscopy. Porosity refers to the level of solidity achieved in an additively made metal part, that is, whether there are cavities or holes between the layers of a sample part. During printing the laser is used to melt a layer of metal powder to the point where the powder liquefies and adheres to an earlier melted layer. Usually, this process results in very dense parts, typically 98% dense or more. However, there are times when the melt is not complete, resulting in hollows or cavities, also referred to as porosity. The two types of porosity are lack of fusion porosity and gas porosity. The fundamental origin of lack-of-fusion porosity is insufficient overlap of successive melt pools. The approach allows rapid prediction of the effects of changes in processing parameters (beam power and beam speed, hatch spacing and layer thickness) on part porosity. On the other hand, gas porosity occurs because the molten metal can hold a large amount of dissolved gas, unlike the solid form. This occurs when the molten metal is cooled down too quickly. That causes the gases to be trapped and thus they form bubble like circle dark spots on the sample. Gas porosity can be eliminated through good design, better parameter settings, and sometimes using hot isostatic process. The goal of microscopy is to optimize the processing parameters in order to reduce porosity as much as possible. Now this can be whether gas porosity or lack of fusion porosity. The main goal of this research is to come up with the best possible parameter setting for printing. The research aims to avoid porosity as much as possible. Because porosity can create little defects which in return become a big problem during manufacturing. Porosity can remain an issue even after doing every possible action to avoid it. Traditionally a major issue has to do with the printer itself, die-cast components, microscopic holes form within a part's body during the AM process. Though invisible to the eye, they reduce component density, potentially leading to cracks, leaks, and fatigue. In applications with pressure differentials or requirements to be air or fluid tight, for example in cooling systems, this can be an especially critical issue.

### 3.1 Microscopy

Looking down a reflection microscope we see the light reflected off a sample. The contrast can arise in different ways. Transmission light microscopes are used to look at thin sections – the specimen must transmit the light. The specimen is mounted and placed on the stage; begin by slowly increasing the power of the light source until there is a bright spot visible on the sample. With the lowest mag-

nification lens in place focus using the coarse focus knob: without looking down the microscope, lower the objective lens close to the specimen surface, and then use the coarse focus knob to slowly raise it until the circle of light on the specimen appears reasonably sharp. Now, looking through the eyepiece, adjust the coarse focus control. When looking down the eyepiece and using coarse focus, we should only ever adjust so as to move the sample away from the objective. To increase the magnification, slide the rotatable nosepiece around (ensuring the lens does not touch the specimen) and then re-focus using the fine focus (it should take very little adjustment!). Once a representative area is found and focused a digital camera can be used to take a photo and a sketch can be made. After taking the images, stitching, and fusing is needed. This is done usually through a third-party software called ImageJ or Fiji-ImageJ. It's a public domain Java image processing program. ImageJ is used to display, annotate, edit, calibrate, measure, analyze, process, print, and save raster (row and column) image data. ImageJ is used in various other scientific disciplines as well. It has the potential to be a powerful tool for any field that benefits from image visualization, processing, and analysis: earth sciences, astronomy, fluid dynamics, computer vision, signal processing, etc. Based, on the selection type, calculates and displays either area statistics, line lengths and angles, or point coordinates. Area statistics are calculated if there is no selection or if a sub-region of the image has been selected using one of the first four tools in the toolbar.

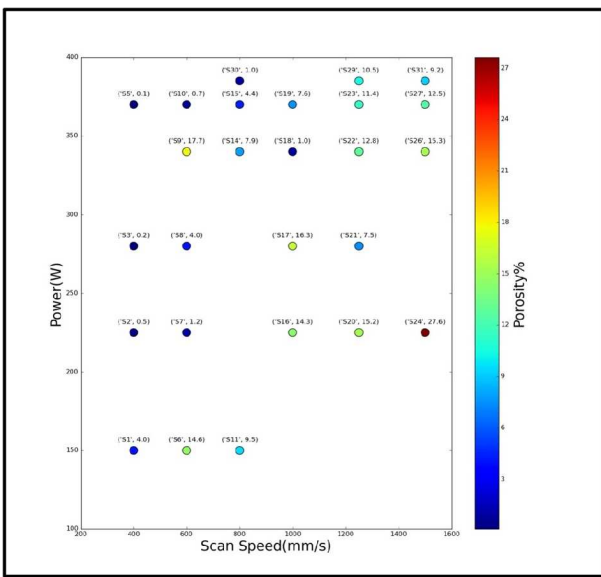


Figure 8: Porosity % using Microscopy.

Out of the 31 samples printed, we were able to do ImageJ analysis on 26 of the samples. Five of the samples came out badly due to the technical issues as discussed earlier. We looked at the porosity and density area against the parameter (Speed and Power) settings we set initially for these

26 samples. The results are plotted on Figure 8. The plot is provided using a free third-party software Python. As usual the codes are provided on the official GitHub for this project and can be referred at any time. The colors indicate the amount of porosity in the samples. Red is used as a higher indication of porosity, while blue is the least. Each point on the plot represents a sample number and the amount of porosity it contains. For example Sample 24 (S24, 27.6) is found to contain the most porosity which we intend to avoid. It shows that at a higher laser scan speed there's lack of fusion porosity forming on the layers of the samples. And when there's a lower laser-power involved with higher scan speed the greater the porosity %. A porosity of 27% for a sample is usually unwanted, and best if avoided.

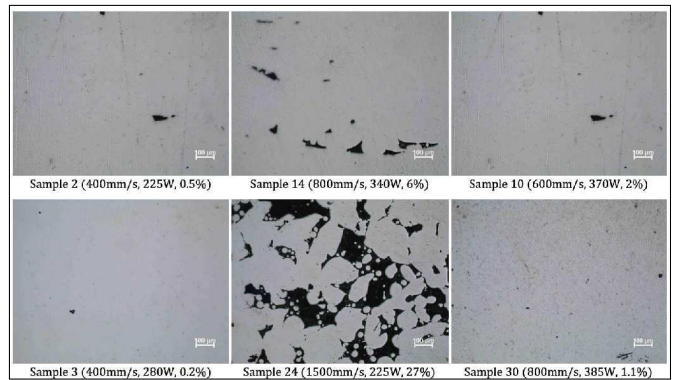


Figure 9: Surface porosity comparison.

We can see the surface comparison in Figure 9 very well. The idea of porosity is illustrated by frames of images from the selected given sample. One can notice that the higher scan speed leads to lack of fusion porosity. Comparing Sample 24 with Sample 2, there's an obvious relation between scan speed and porosity. Thus, the microscopy analysis can tell us which parameters to avoid (in this case a 1500mm/s and 225W) and which ones to select as for the best printing results. It shows the best parameter settings are found on the center of plotted graph in Figure 8. Furthermore, one can see the blue light samples around the mid-top center of the plot have relatively low porosity when compared. Once done with microscopy, we looked at X-ray Diffraction analysis, Scanning Electron Microscope, Field Emission -SEM, Corrosion testing, Mechanical testing, Digital X-ray Radiography analysis.

### 3.2 Scanning Electron Microscope

A scanning electron microscope (SEM) scans a focused electron beam over a surface to create an image. The electrons in the beam interact with the sample, producing various signals that can be used to obtain information about the surface topography and composition. Because of its great depth of focus, a scanning electron microscope is the

EM analog of a stereo light microscope. It provides detailed images of the surfaces of cells and whole organisms that are not possible by normal microscope [3]. It can also be used for particle counting and size determination, and for process control. It is termed a scanning electron microscope because the image is formed by scanning a focused electron beam onto the surface of the specimen in a raster pattern. In the lab there are two types SEM's. One is the standard SEM and the second is the Field Emission SEM (FE-SEM). For the analysis of FE-SEM we used as built Ti-64 sample with Hot Isostatic Pressure (HIP) treatment. Figure 10 shows the results of FE-SEM provided by the research lab.

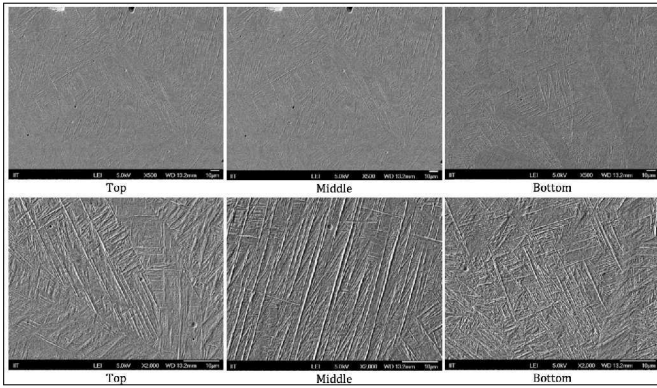


Figure 10: SEM images First row images have 500x magnification, while the second row have 2000x.

The SEM images are taken from top to bottom in a vertical cut. Three images are taken generally: top, middle, and bottom. As shown in the above figure 10, the first row is images takes at 500x magnification. Although we can't see the sharp lines, but we can see the surface of the sample in much detail. However, the second row shows us the phases of the sample material even. They are magnified at a scale of 2000x. Clear white sharp lines are observed in the sample. Those are the alpha prime ( $\alpha'$ ) phases of Ti-6Al-4V. They give the sample it's strength. Essentially an SEM images can tell you about the mechanical properties of the sample at hand. And in this case the SLM printed Ti-64 samples have similar strength values as those traditionally produced samples.

### 3.3 Dynamic X-ray Radiography

The third analysis conducted was the Dynamic X-ray Radiography. DXR is used to measure Keyholes (see Figure 11. Courtesy of C. Zhao [4] ) and other properties of a sample. One way to minimize the effects of boundary layers along walls on the measured kinematics is the use of X-ray radiography, the building block of X-ray CT. For example, X-ray radiography has long been used to inspect density variations in a variety of geoscientific problems, including inferences about the existence of discontinuities in

sandstones and clays in stationary samples and measuring density in granular materials. We were able to obtain DXR images of Ti-64 printed using an irregular powder at the Argonne National Laboratory in Illinois. Keyholes are a small key shaped holes in a printed sample. They're caused by a strong recoil pressure from the rapid evaporation of metal pushing the melted liquid down. This creates a deep and narrow cavity called a keyhole. Sometimes keyholes can largely enhance laser absorption and improve energy efficiency. However, usually the keyhole walls constantly fluctuate and collapse that creating pores and leads to defects. This occurs when bubbles of gas get trapped underneath the surface a part constructed during the metal additive manufacturing process, resulting in the formation of relatively spherical pores under the surface of the part. This is opposed to other types of porosity, which can form from incomplete melting of the powder material or improper adhesion of two layers of material.

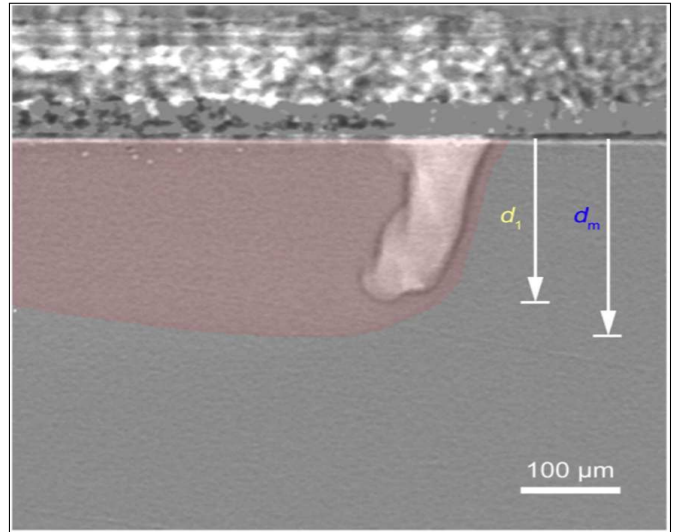


Figure 11: A keyhole observed using DXR.

In total 5 samples were sent to Argonne to be printed. All 5 samples have same laser power of 350W and a frequency frame rate of 50kHz but with different scan speeds as seen in Table 1. The scan speed ranges from 400mm/s – 1200 mm/s. The purpose of XRD analysis is to see how much scan speed alone has an effect in the creation of the keyhole, and how large or deep the keyholes are generally. A complete data sheet is provided at the appendix of this report. A handful explanation of the graph codes is also posted on GitHub.

To compare the severity of keyhole porosity formation, we used area under the surface of the sample with ImageJ and measured the area fraction which displayed keyhole porosity. Measuring Keyhole depth is a little different from measuring porosity. One would have to individually measure the depth until each tiff file frame is finished. And the longer the longer the sample length, the more measuring it

Table 2: Average keyhole depth

Sample No:	Scanspeed (mm/s)	Average depth ( $\mu m$ )	Variance
1	400	303.50	23.35
2	500	264.12	13.54
3	600	222.12	11.33
4	700	144.94	8.57
5	1200	46.29	7.90

requires on ImageJ. The high-speed x-ray imaging makes it possible to observe the pore formation process within the keyhole. Regardless of laser power and the presence or absence of powder, pore formation occurs when the bottom tip of a letter ‘J’ shaped keyhole was pinched off, released at high speed toward the wake of the laser beam, and trapped by the solidification front. With decreasing laser power, the keyhole porosity boundary becomes increasingly sensitive to scan speed, particularly in the presence of powder, and appeared to asymptote to a threshold in power. As seen in Figure 12 the sample with 400mm/s contains big fluctuation but longer average keyhole depth. On the contrary the sample with 1200mm/s was found to have shorter constant keyhole depth. This would only mean one thing i.e., as the scan speed increases, the average depth of the keyhole decreased. In addition to that the variation of keyhole depth increased strongly with decreasing scan speed as seen in Table 2. Compared to sample 1, sample 5 had a much better variance on the average of the keyhole depth. That indicates the accuracy while measuring the keyhole depth. The less fluctuation theirs is the smaller the variance. This is an obvious read in the Figure 12. The blue lines sample 1 have more difference between each point than there’s for red points in sample 5.

Compared with bare plate samples, in which such pores tend to merge quickly into the subsequent growing keyhole and disappear, the larger keyhole fluctuations in powder bed samples create sufficient waiting time for the pores. These pores are nearly stationary after pinching off the keyhole and suspended inside the melt pool (or potentially accelerated by the local melt flow through forces such as drag away from the keyhole) to be pinned by the advancing solidification front. Typically, at a constant laser power, keyhole pores form only when the keyhole depth is larger than a threshold, as depicted in the graph in the previous slide. This threshold increases, statistically, with scan speed and laser power in distinct power-law forms respectively. Similarly, an irregular shaped powder leads into a smaller depth keyhole. This is beneficial when comparing the cost of regular vs. irregular powder of Ti-64 alloy. That would mean the production of Ti-64 alloys will much cheaper, defect free and less prone to fatigue creeps.

In the keyhole porosity regime and far away from the keyhole porosity boundary, large pores (i.e., pore size comparable to keyhole length) can be trapped directly by the solidification front while or after pinching off the keyhole.

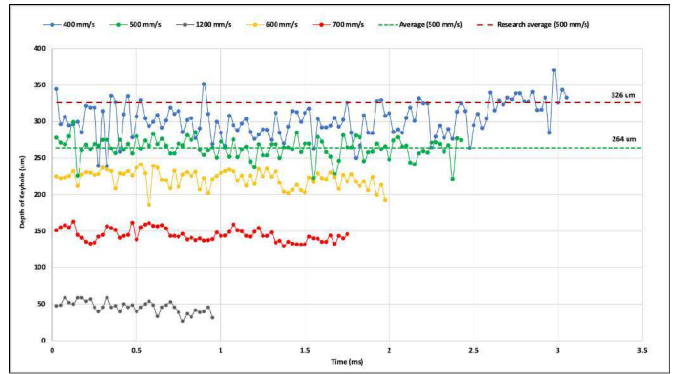


Figure 12: Keyhole depth vs Time.

In this sort of cases, acoustic waves may still exist, but may not play a critical role in driving the pore formation and motion (pore splitting is still possible) because the far side of the pore to the keyhole is pinned by the solidified structure. There’s also the concept of acoustic waves in keyhole formation. Acoustic waves could generate from the collision of keyhole walls, the crashing of liquid on the melt pool boundary. For the measurement of acoustic waves, coupling real-time passive acoustic sensing with x-ray imaging may allow one to identify the characteristic signals of those waves relevant to the keyhole pore formation [4]. Indirectly, ultrahigh-speed x-ray diffraction using synchrotron or future high-energy high-repetition-rate free-electron laser sources may also

### 3.4 X-ray Diffraction (XRD)

X-ray diffraction (XRD) is a nondestructive technique that provides detailed information about the crystallographic structure, chemical composition, and physical properties of materials. It is a technique used to find out the nature of the materials as crystalline or amorphous. It will define the quantification of cementitious materials [5]. It also provides information on structures, phases, preferred crystal orientations (texture), and other structural parameters, such as average grain size, crystallinity, strain, and crystal defects. XRD peaks are produced by constructive interference of a monochromatic beam of X-rays scattered at specific angles from each set of lattice planes in a sample. The peak intensities are determined by the atomic positions within the lattice planes. Consequently, the XRD pattern is the fingerprint of periodic atomic arrangements in a given material. An online search of a standard database for X-ray powder diffraction patterns enables quick phase identification for a large variety of crystalline samples. This means that structural changes induced in a crystalline material by blending with other materials can be monitored using the XRD technique. For this research a nickel superalloy named Inconel-718 was subjected to an XRD analysis. The sample was horizontally cut hipped at 200Mpa for 90minutes (see Figure

13). Inconel 718 is a high strength nickel base superalloy used for cryogenic temperatures up to long term service at 1200°F. The super alloy is used for gas turbine engine parts, firearms production, liquid fuel rocket motor components, springs, fasteners and cryogenic tanks. The idea of this analysis was to understand and graph XRD data using MATLAB in order to determine the samples character fingerprint.

This XRD relation is given by Bragg's Law as:

$$n\lambda = 2d \sin \theta \quad (1)$$

where:

- n is an integer
- $\lambda$  is the wavelength of the x-ray,
- d is the spacing of the crystal layers (path difference),
- $\theta$  is the incident angle (the angle between incident ray and the scatter plane)

Equation 1 is commonly known as Bragg's Law. The law states that when the x-ray is incident onto a crystal surface, its angle of incidence, will reflect back with a same angle of scattering,  $\theta$ . And, when the path difference,  $d$  is equal to a whole number,  $n$  of wavelength, a constructive interference will occur.

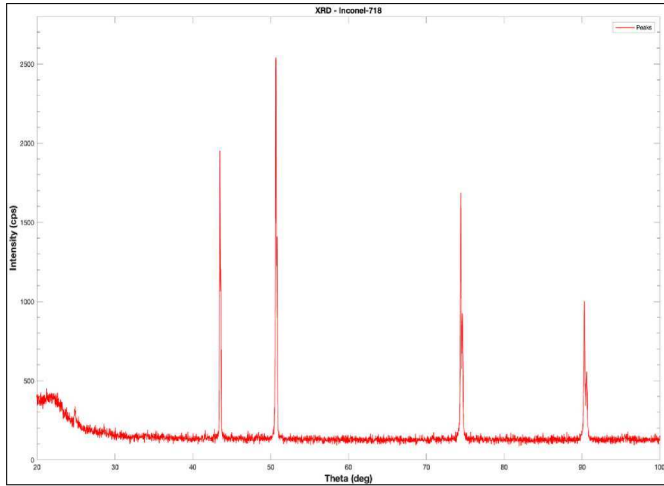


Figure 13: Inconel-718 Hipped at 200MPa for 90 min.

For this super alloy there are four main peaks, and very small peaks associated with the sample in Figure 13. The main peak occurs around 55 degrees for an intensity of 2880 cps, but we need to divide the angle by two and our ideal angle is actually 27.5 degrees.

### 3.5 Electron Backscatter Diffraction (EBSD)

Electron Backscatter Diffraction (EBSD) is a scanning electron microscope (SEM) based technique that gives

crystallographic information about the microstructure of a sample. In EBSD, a stationary electron beam interacts with a tilted crystalline sample and the diffracted electrons form a pattern that can be detected with a fluorescent screen. The diffraction pattern is characteristic of the crystal structure and orientation in the sample region where it was generated. Hence the diffraction pattern can be used to determine the crystal orientation, discriminate between crystallography of different phases, characterize grain boundaries, and provide information about the local crystalline perfection. EBSD has become a well-established accessory for the SEM, which is used to provide crystallographic information routinely [6]. As a result, EBSD is now being applied in numerous different application areas to assist in materials characterization, as shown in the graph. For this research, an EBSD analysis was done for the Inconel-718 hipped at 200MPa for 90minutes. But this time the sample was vertically cut in order to study its phases. A total of 4 sample properties were observed through the EBSD. Using EBSD we were able to study the grain boundary, and surface angles across the sample.

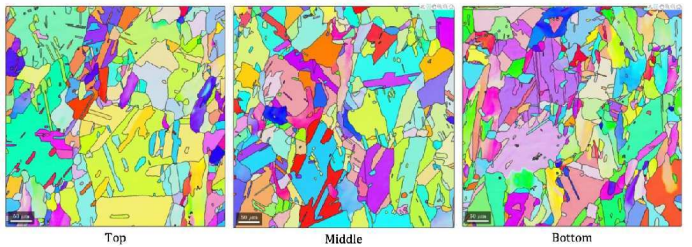


Figure 14: Crystal Orientation map of Inc-718 EBSD

The first three images being analyzed are the crystal orientation map of Inc-718. Figure 14 illustrates the orientations. These maps are derived by EBSD, are often displayed in so-called inverse pole figure (IPF) coloring. These maps (often three maps are displayed for reference direction X, Y and Z) really reflect the locally discovered orientation. They insert additional symmetries which reflect a higher symmetry and therefore perhaps another not-symmetry-equivalent crystal orientation. A grain is a three-dimensional crystalline volume within a specimen that differs in crystallographic orientation from its surroundings but internally has little variation. Grain size is an important characteristic used in understanding the development, engineering, and potential failure in materials. EBSD has a lot of advantages and has become an attractive manufacturing method to produce the super alloys. The experimental results, the beam scanning speed did show notable effects on the preferred orientation of the phase in the Z-plane which presents a relatively strong texture. However, with the increase of the beam speed, the intensity of the texture in the Z-plane decreases first and then increases slightly. Generally, the parts did not show out-

standing anisotropic characteristics in hardness and elastic modulus. The Inc-718 did present the highest properties (Vickers hardness and elastic modulus) between the four parts, which results from its finest microstructure and the weakest texture. In grain boundary engineering it can

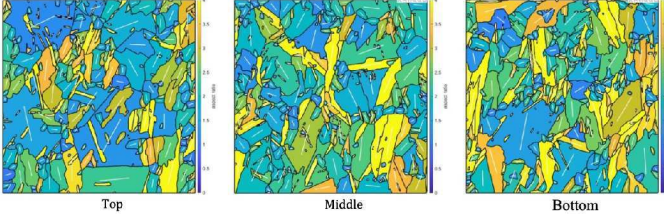


Figure 15: Preferred orientation map of Inc-718 EBSD

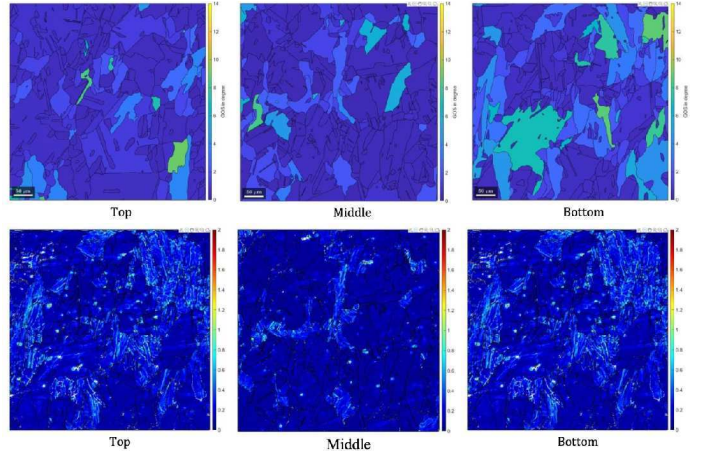


Figure 17: Grain Orientation Spread of Inc-718 EBSD

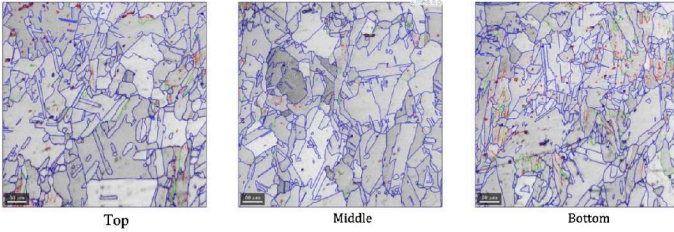


Figure 16: Grain boundaries of Inc-718 EBSD

be important to enhance or reduce the relative abundance of certain grain boundary types in order to optimize the properties of the final material. EBSD is well suited to extract this type of information as it gives both statistical and spatial information about the grain boundaries. Figures 15 and 16 show us the grain boundaries of Inc-718. For that sample, some smooth boundaries are seen in the center, most of them close to a circle. The more circular the boundary the better the strength of the sample is. This meant the sample can withstand cracks, and helps minimizing bending, and sudden fracture.

Figure 17 first row is the Kernel Average Misorientation (KAM), and the second row is Grain Average Misorientation (GAM). The idea to use these local orientations for other applications later arose since first it became obvious that one can link the local position AND the orientation to extract additional but still not evaluated information like the definition of grains as "volumes" of identical orientations. Kernel average misorientation (KAM) during electron backscatter diffraction (EBSD) analysis can be used as a measure of local grain misorientation. KAM quantifies the average misorientation around a measurement point with respect to a defined set of nearest neighbor points. Similarly the normal and inverted poles of INC-718 is mapped in Figure 18.

## 4 Conclusion

Laser powder bed fusion is a dominant metal 3D printing technology. However, porosity defects remain a challenge for fatigue-sensitive applications. Some porosity is associated with deep and narrow vapor depressions called keyholes, which occur under high-power, low-scan speed laser melting conditions. In this paper, the recent progress on Ti6Al4V fabricated by three mostly developed additive manufacturing (AM) techniques-directed energy deposition (DED), selective laser melting (SLM) and electron beam melting (EBM)-is thoroughly investigated and compared. High-speed x-ray imaging enables operando observation of the detailed formation process of pores in Ti-6Al-4V caused by a critical instability at the keyhole tip. A research by conducted by C. Zhao's team showed [4] similar results to ours, and they found that the boundary of the keyhole porosity regime in power-velocity space is sharp and smooth, varying only slightly between the bare plate and powder bed. The critical keyhole instability generates acoustic waves in the melt pool that provide additional yet vital driving force for the pores near the keyhole tip to move away from the keyhole and become trapped as defects. Fundamental knowledge is provided for the creation of links between processing parameters, resultant microstructures and associated mechanical properties. Room temperature tensile and fatigue properties are also reviewed and compared to traditionally manufactured Ti6Al4V parts. The presence of defects in as-built AM Ti6Al4V components and the influences of these defects on mechanical performances are also critically discussed.

The research also found that porosity increases with higher scan speed but lower laser power. Lack of fusion porosity was observed on samples printed for the Ti-64 samples. Furthermore, Keyhole depth are related with scan speed in the opposite manner. Faster scan speeds reduce the creation of melt pool and show the keyhole depth

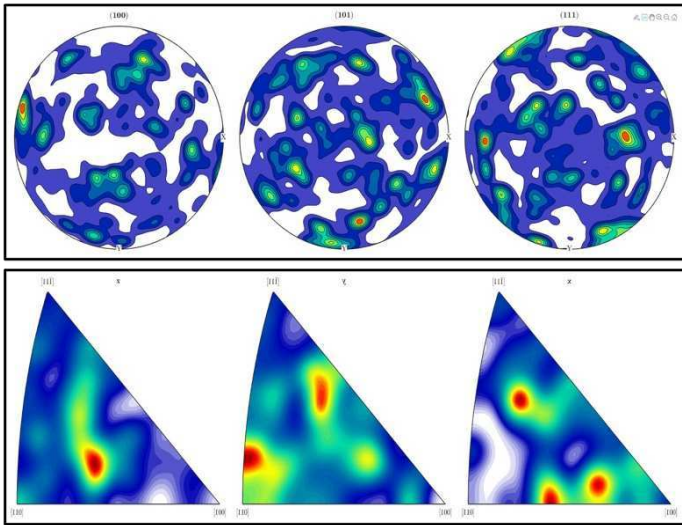


Figure 18: Normal and Inverted poles of Inc-718

is short enough. The propagation of an internal fatigue crack in Ti-6Al-4V was non-destructively observed by synchrotron radiation imaging to clarify the crack growth rate in very high cycle fatigue. The results show irregular powder does have an advantage in decreasing the keyhole depth and increase the strength of the sample. Figure 11 also shows samples printed using an irregular powder are less prone to fatigue crack and produce slighter lesser gas porous compared to regular powder.

This paper aims at illustrating the potential of X-ray tomography for studying the mechanical behavior of materials through various experiments. Typical experimental are the ones which use laboratory and synchrotron X ray sources as shown in the report. Advantages and limitations of all types of sources are presented. Dedicated experimental devices which allow deformation and/or temperature changes to be applied to various types of materials are described. Examples of results of in situ mechanical experiments are presented and discussed in a manner of graphs and images.

For this superalloy there are four main peaks, and very small peaks associated with the sample in Figure 12. The main one occurs around 55 degrees. But since this is twice the theta value, therefore we need to divide it by two. Thus, the actual diffraction angle for the biggest is actually 27.5 degrees. For sample Inc-718, some smooth boundaries are seen in the center, most of them close to a circle. The more circular the boundary the better the strength of the sample is. This meant the sample can withstand cracks, and helps minimizing bending, and sudden fracture. The overall goal of this research was to learn and understand the uses of X-ray imaging in additive manufacturing technology. It provides a great deal of knowledge, hands on experience, and technology to

conduct a scientific experiment in the institute. This was only possible through the funds from the National Science Foundation. This research is a great achievement and an eye-opening journey from the start to finish.

## References

- [1] S. Liu and Y. C. Shin, “Additive manufacturing of Ti6Al4V alloy: A review,” *Materials and Design*, vol. 164, p. 107552, 2019, ISSN: 18734197. DOI: 10.1016/j.matdes.2018.107552. [Online]. Available: <https://doi.org/10.1016/j.matdes.2018.107552>.
- [2] B. Zhang, R. Seede, L. Xue, K. C. Atli, C. Zhang, A. Whitt, I. Karaman, R. Arroyave, and A. Elwany, “An efficient framework for printability assessment in Laser Powder Bed Fusion metal additive manufacturing,” *Additive Manufacturing*, vol. 46, p. 102018, 2021, ISSN: 22148604. DOI: 10.1016/j.addma.2021.102018. [Online]. Available: <https://doi.org/10.1016/j.addma.2021.102018>.
- [3] T. Leißner, A. Diener, E. Löwer, R. Ditscherlein, K. Krüger, A. Kwade, and U. A. Peuker, “3D ex-situ and in-situ X-ray CT process studies in particle technology – A perspective,” *Advanced Powder Technology*, vol. 31, no. 1, pp. 78–86, 2020, ISSN: 15685527. DOI: 10.1016/j.apt.2019.09.038.
- [4] C. Zhao, N. D. Parab, X. Li, K. Fezzaa, W. Tan, A. D. Rollett, and T. Sun, “Critical instability at moving keyhole tip generates porosity in laser melting,” *Science*, vol. 370, no. 6520, pp. 1080–1086, 2020, ISSN: 10959203. DOI: 10.1126/science.abd1587.
- [5] F. Yoshinaka, T. Nakamura, S. Nakayama, D. Shiozawa, Y. Nakai, and K. Uesugi, “Non-destructive observation of internal fatigue crack growth in Ti-6Al-4V by using synchrotron radiation  $\mu$ CT imaging,” *International Journal of Fatigue*, vol. 93, pp. 397–405, 2016, ISSN: 0142-1123. DOI: <https://doi.org/10.1016/j.ijfatigue.2016.05.028>. [Online]. Available: <https://www.sciencedirect.com/science/article/pii/S0142112316301360>.
- [6] X. Wang and K. Chou, “EBSD study of beam speed effects on Ti-6Al-4V alloy by powder bed electron beam additive manufacturing,” *Journal of Alloys and Compounds*, vol. 748, pp. 236–244, Jun. 2018, ISSN: 09258388. DOI: 10.1016/j.jallcom.2018.03.173.